UC Berkeley
UC Berkeley Electronic Theses and Dissertations

Title

Design, Functionalization, and Evolution of Metal-Organic Frameworks

Permalink

https://escholarship.org/uc/item/8w9887fj

Author

Wang, Haoze

Publication Date

2022

Peer reviewed|Thesis/dissertation

eScholarship.org Powered by the California Digital Library
University of California

Design, Functionalization, and Evolution of Metal-Organic Frameworks

by

Haoze Wang

A dissertation submitted in partial satisfaction of the

requirements for the degree of

Doctor of Philosophy

in

Chemistry

in the

Graduate Division

of the

University of California, Berkeley

Committee in charge:

Professor Omar M. Yaghi, Chair
Professor Kenneth N. Raymond
Professor Jeffrey A. Reimer

Spring 2022

Abstract

Design, Functionalization, and Evolution

of Metal-Organic Frameworks

by

Haoze Wang

Doctor of Philosophy in Chemistry

University of California, Berkeley

Professor Omar M. Yaghi, Chair

Chapter 1: This chapter presented the introduction to the structural design and functionalization of reticular chemistry and pore chemistry of metal-organic frameworks (MOFs). The pores in MOFs can be functionalized by placing chemical entities along the backbone and within the backbone. This chemistry is enabled by the architectural, thermal and chemical robustness of the frameworks and the ability to characterize them by many diffraction and spectroscopic techniques. Pore chemistry, functionalization chemistry and strategies, their applications, and reading and writing functionality sequences in MOFs are discussed.

Chapter 2: In this chapter, I described a new post-synthetic functionalization strategy of MOFs: a metal docking strategy utilizing the precise spatial arrangement of organic struts as metal chelating sites in MOF-303 [$Al(OH)(C_5H_2O_4N_2)$]. Pairs of uncoordinated N-atoms on adjacent pyrazole dicarboxylate linkers distributed along the rod-shaped Al–O secondary building units in MOF-303 were used to chelate Cu(I) and Ag(I) with atomic precision and yield the metalated Cu- and Ag-MOF-303 compounds [$(CuCl)_{0.50}$-$Al(OH)(C_5H_2O_4N_2)$ and $(AgNO_3)_{0.49}$-$Al(OH)(C_5H_2O_4N_2)$]. The coordination geometries of Cu(I) and Ag(I) were examined using 3D electron diffraction and extended X-ray absorption fine structure spectroscopy techniques. The resulting metalated MOFs showed pore sizes matching the size of Xe, thus allowing for binding of Xe from Xe/Kr mixtures with high capacity and selectivity. In particular, Ag-MOF-303 exhibited Xe uptake of 59 $cm^3\ cm^{-3}$ at 298 K and 0.2 bar with a selectivity of 10.4, placing it among the highest performing MOFs. It also gave up to 100% improvement of the dynamic separation performance in comparison to pristine MOF-303. This metalation strategy represents a new strategy for engineering MOFs to give high-performance gas separations.

Chapter 3: MOFs with absolute structures are of particular interest as the asymmetry of their crystal structures enables wide applications from asymmetric catalysis to enantioselective separation. Previous reports on the synthetic strategies toward MOFs with absolute structures always required the use of chiral precursors or chiral templates, however, it is not always easy to obtain enantiopure starting materials. In this chapter, a new non-centrosymmetric MOF, MOF-829, synthesized from aluminium salt and achiral organic linker was described. Further comparisons are made between MOF-829 and a reported Al-based chiral MOF (MOF-520) that is composed of the same metal ion and linker, and similarly synthesized without using chiral compounds. The

configurations of the building units, the absolute structures of both MOFs, and their topologies were investigated in detail. I found that (i) topology is one of the determining factors in the formation of non-centrosymmetric MOFs; (ii) the formation of chiral MOFs further requires the directionality of chiral linkers but more importantly chiral secondary building units (SBUs), which can be realized by fine tuning of the synthetic conditions. I envision that both synthetic exploration of chiral SBUs and the design of non-centrosymmetric topologies will open a new direction in the design of MOFs with absolute structures.

Chapter 4: Zeolitic imidazolate frameworks (ZIFs) is a subclass of MOFs, built from tetrahedral nodes connected through imidazolate linkers. The structures of ZIFs are characteristic of a variety of large, zeolite-like cages that are covalently connected with neighboring cages and fused in 3-dimensional space. In contrast to molecular cages, the fuse of cages results in extraordinary architectural and chemical stability for the passage of gases and molecules throughout cages and for carrying out chemical reactions within these cages while keeping the cages intact. While the field of ZIFs has seen rapid development over the past decade, with hundreds of ZIF structures built from dozens of different cages of varying composition, size, and shapes reported, rational approaches to their design are largely unknown. This chapter summarized a vast number of cages formed in reported ZIFs, then demenstrated how the thermodynamic factors and traditional guest-templating strategies from zeolites influence the formation of cages. I also highlight how the link-link interactions perform in the ZIF formation mechanism and serve as a means to target the formation of frameworks containing cages of specific sizes with structures exhibiting a level of complexity as yet unachieved in discrete coordination cages.

Chapter 5: When applying sorption isotherms to the study of crystalline materials, it is often assumed that the measured bulk sample represents each individual crystal, and thus the performance of the powder as a whole describes the intrinsic properties of a unit cell. However, crystals are not all equivalent, even if they are synthesized from the same materials in the same batch; crystallites exhibit a distribution of sizes, morphologies, surface textures, and defect levels, all contributing in an unknown way to adsorption behavior. This chapter presented a spectroscopic and imaging approach to sorption isotherms at the single-crystal level for the first time. A metal-organic framework, MOF-801, was chosen as the object of the study, which has shown great performance in water harvesting from atmosphere in arid climates. The uptake of water by MOF-801 is recorded for single crystals and quantified as a function of vapor pressure (isotherms), time (kinetics), and location (imaging), through the combination of in situ Raman spectroscopy and polarization-sensitive coherent anti-Stokes Raman scattering (pCARS) imaging. The results showed that in MOF-801 crystal, water moves ~20 times faster than in the bulk. This represents the upper limit for water harvesting devices containing MOF-801 could produce up to 3.8 L of water per hour per kilogram of MOF, a vast improvement over the previously reported 2.8 L per day.

Chapter 6: MOFs are typically viewed as solids that have fixed volumes and shapes with atoms that are bound tightly to each other that makes them resistant to change. This chapter presented that MOFs can respond to the external environments and change. Building units of MOFs can move in and out of MOFs freely just like in the “solution” system. The composition, pore chemistry, and even structure of MOFs will change accordingly. Thus, the MOFs can be viewed as living solids and the evolution of MOFs can happen.

Acknowledgements

I would like to express my deepest and sincerest gratitude to my supervisor, Prof. Omar M. Yaghi. His continues support, motivation, enthusiasm, and vision have deeply inspired me and provide me with invaluable guidance throughout my graduate research. He is an open-minded person who is always energetic on his research and supportive on his students. He provided me with freedom and infrastructures to focus on projects that I am interested in and encouraged me to do creative researches. When I was frustrated from experiments, he was never tired of discussing with me to strengthen not only my projects but also my mind. His mentorship let me realize my potential that I did not know and tackle the most challenging ideas and projects. He taught me how to be a good scientist who is uncompromising on scientific standard and also how to be a good person. His firm belief in me gives me courage and confidence to overcome difficulties, which is a lifelong gift for me. It is my honor to be his student and to be in Yaghi Lab.

I also want to thank Prof.Yue-Biao Zhang, Prof. Evelyn Ploetz, and Prof. Stefan Wuttke for their supports during our collaborations. There are numerous discussions between us and I was inspired by their ideas and gained lots of knowledge from them. Thank you all!

I would like to thank Prof. Kenneth N. Raymond, Prof. Jeffrey A. Reimer, Prof. John Arnold, and Prof. Jonathan Rittle for serving as my qualifying exam committees. Thank you for providing me with advice, knowledge, and helpful discussions to be a qualified researcher. I also want to thank Prof. Kenneth N. Raymond and Prof. Jeffrey A. Reimer for serving as my thesis committee members and reviewing this thesis.

I would like to thank Dr. Zhe Ji and Dr. Jingjing Yang for their help to build up my research skills and critical thinking. When I joined the Yaghi Lab, they provide me with help and knowledge without asking for return. Thanks for your beliefs in my abilities. I also want to thank Dr. Yuzhong Liu and Dr. Christian S. Diercks for their great help and encouragement. I learned a lot from them to be a researcher. Additionally, I want to express thanks to Dr. Xiaokun Pei and Dr. Hao Lyu for their technical supports and helpful discussions of my research.

I want to thank all my collaborators and Yaghi family memebers. It would not be possible for me to carry out my research projects without your help. I would like to express my thanks to Prof. Davide M. Proserpio, Dr. Wentao Xu, Dr. Zhaolin Shi, Dr. Markus J. Kalmutzki, Dr. Bunyarat Rungtaweevoranit, Mr Tu. Sun, Mr. Zach Zheng, Mr. Nikita Hanikel, Mr. S. Ephraim Neumann, Mr. Mathew Burigana, Ms. Fangying Jin, Mr. Zihui Zhou, Mr. Kaiyu Wang, Mr. Zichao Rong, Mr. Kelvin Lee, Mr. Ali Alawadhi, Dr. Xing Han, Dr. Tianqiong Ma, Dr. Daria Kurandina, Dr. Woochul Song, Dr. Chuanshuai Li, Dr. Cornelius Gropp, Dr. Chenfei Zhao, Dr. Eugene Kapustin, Mr. Oscar Iu-Fan Chen, Mr. Haozhe Li, and Dr. Lac Ha Nguyen.

Finally, I want to acknowledge my parents, family and friends. Thank my parents for bring me in this world and teaching me to be a good person. My father and mother always stand behind me and make me fearless to the challenges in my whole life. They raised me as a person who never gives up and always look on the bright side. My grandparents are always there for me and support me for my dreams. They taught me to be kind to things and people around me. This is the most precious gift they gave me. My cousins share my pains and joys with me and always encouraging me to move forward. I also want to thank all my family members and friends.

Table of Contents

Chapter 1. Design, Functionalization, and Pore Chemistry of Metal-Organic Frameworks 1
1.1 Introduction 2
1.2 Functionalization and Pore Chemistry of MOFs 2
1.3 Pore-Functionalization Strategies 3
1.4 The Conceptual Basis for Functionality Positioning 4
1.4.1 Site Isolation 4
1.4.2 Site Coupling 5
1.4.3 Site Cooperation 6
1.5 Construction of MOF Backbone 7
1.5.1 Retro-Synthetic Reticular Design. 8
1.5.2 *De Novo* Reticular Design. 8
1.6 Methods for Functionalization of the Pores 9
1.6.1 Pre-Synthetic Functionalization 9
1.6.2 Post-Synthetic Functionalization 9
1.6.3 Covalent Attachment of Functional Units 9
1.6.4 Exchange of Building Units 11
1.6.5 Functionality Addition at Structural Defects 11
1.6.6 Functionality Addition at Structural Defects 11
1.6.7 Introduction of Mechanical Interlocking in the Backbone 11
1.7 Applications of Functionalized MOFs 12
1.7.1 Guest Binding with High Specificity and Affinity 12
1.7.2 Catalysis 16
1.7.3 Functionalities and Pores for Ion and Electron Transport 20
1.7.4 Pores Functionalized for Fluorescence, Light Harvesting, and Energy Transfer 22
1.7.5 Functionalization for Tuning Pore Dynamics 24
1.7.6 Molecularly Designed Porous Interfaces 26
1.8 Writing and Reading Functionality Sequences in MOF Pores 29
1.9 References 32
Chapter 2. Docking of Cu(I) and Ag(I) in Metal-Organic Frameworks for Adsorption and Separation of Xenon 37
2.1 Introduction 38
2.2 Results and Discussion 38

2.2.1 Preparation and Characterization of Metalated MOF-303 38
2.2.2 Adsorption and Separation of Xe from Xe/Kr Mixture of MOF-303 and Metalated MOF-303 41
2.3 Conclusion 42
2.4 Supporting Information 43
2.4.1 Synthesis and Characterization of Materials 43
2.4.2 Gas Adsorption Analyses 45
2.4.3 Energy Dispersive Spectroscopy Mapping 52
2.4.4 Electron Diffraction Tomography 53
2.4.5 X-ray Absorption Spectroscopy Analyses 63
2.4.6 Xenon Uptake, Adsorption Selectivity, and Heat of Adsorption 65
2.4.7 Breakthrough Measurements 75
2.4.8 ^{129}Xe NMR Measurements 77
2.5 References 78
Chapter 3. Design of MOFs with Absolute Structures 83
3.1 Introduction 84
3.2 Experimental Section 84
3.2.1 Materials and Methods 84
3.2.2 Synthetic Procedure 85
3.2.3 Determination and Refinement of the Single-Crystal X-ray Structure 85
3.3 Results and Discussions 87
3.3.1 Synthesis and Structure of MOF-829 and MOF-520 87
3.3.2 Absolute Structure of MOF-520 88
3.3.3 Absolute Structure of MOF-829 89
3.3.4 The Relationship between the Topologies and the Absolute Structures 90
3.4 Conclusion 91
3.5 References 93
Chapter 4. Large Cages of Zeolitic Imidazolate Frameworks 96
4.1 Introduction 97
4.2 Origins of the Stability of Extended Tetrahedral Structures 98
4.3 Design of ZIFs Through Link-Link Interactions 100
4.4 Diversity of ZIFs Structures and Cages 104
4.5 Intrinsic Advantages of Fused Cages 113
4.6 Conclusion and Outlook 114
4.7 Supporting Information 115

4.8 References 118
Chapter 5. Water Harvesting at the Single Crystal Level 121
5.1 Introduction 122
5.2 Methods and Results 122
5.2.1 Determine Water Uptake in MOF-801 Crystals via Raman spectroscopy 123
5.2.2 Determine Water Uptake in MOF-801 Crystals via Raman spectroscopy 126
5.3 Materials and Characterizations 129
5.3.1 Hyperspectral Raman Imaging at A Controlled Relative Humidity 129
5.3.2 Quantification of Water Uptake 131
5.3.3 Raman-Based Single-Crystal Isotherms and Sorption Kinetics 133
5.3.4 MOF-801 synthesis and material characterization 134
5.3.4.2.2 Scanning Electron-Microscopy (SEM) 135
5.3.4.2.3 Sorption measurements for determining isotherms and kinetic curves in bulk 135
5.3.5 MOF-801 synthesis and material characterization 136
5.4 Conclusion 136
5.5 Supporting Information 137
5.5.1 Uptake Mechanism Description and Fit Model 137
5.5.2 Quantitative Water Uptake and Kinetics of MOF-801 via Raman Spectroscopy 141
5.5.3 SC-XRD on Polycrystalline MOF-801 Particles 150
5.6 References 156
Chapter 6. Evolution of MOFs: Living Solids 158
6.1 Introduction 159
6.2 Results and Discussions 159
6.2.1 Synthesis of UiO-67 and organic linkers 159
6.2.2 Evolution of UiO-67 162
6.2.3 Composition of MOFs after Evolution 163
6.2.4 Guest Selectivity in Living Solids 163
6.3 Conclusion 164
6.4 References 165

Chapter 1. Design, Functionalization, and Pore Chemistry of Metal-Organic Frameworks

Portions of this chapter have been published in:
Ji, Z.; Wang, H.; Canossa, S.; Wuttke, S.; Yaghi, O. M. Pore Chemistry of Metal-Organic Frameworks. *Adv. Funct. Mater.* **2020**, *30*, 202000238.

1.1 Introduction

Metal-organic frameworks (MOFs) are a class of porous, crystalline, and extended structures assembled from secondary building units (SBUs) and organic linkers.[1,2] This class of materials has attracted significant research attention and seen extensive growth due to their high surface areas, structural tunability, as well as wide potential applications.[2,3] MOFs have high structural diversities because the SBUs and organic linkers can be changed and modified, giving rise to tens of thousands of MOFs with various pore metrics and functionalities. The pores are essentially important for the design and functionalization of MOFs. Pores in MOFs can be functionalized by placing chemical entities along the backbone and within the backbone. This chemistry is enabled by the architectural, thermal and chemical robustness of the frameworks and the ability to characterize them by many diffraction and spectroscopic techniques. Framework structures of MOFs serve as versatile platforms for functionalization chemistry to be performed in their interior with the same precision typically practiced in molecular chemistry. This is further enabled by the fact that: (a) The strong bonds making up the backbone of the framework imparts the robustness needed for chemical modifications to be performed post-synthetically without losing the integrity of the structure or the pores, (b) frameworks with pores of sufficiently large size can be designed to allow access to their interior by various guests and reagents to harness their pore chemistry, (c) rich organic and inorganic chemistry can be applied in the functionalization and modification of the pores, and (d) persistent crystallinity of these frameworks vastly facilitates their characterization before and after pore functionalization.

1.2 Functionalization and Pore Chemistry of MOFs

The functionalization chemistry of MOFs discussed in this section targets the modification of pores to achieve new framework properties. We consider, for example, new bond formation, exchange of counter ions, and encapsulation of nanoparticles, as a process of functionalization. Some of these involve complex multi-step chemical reactions or simple removal of solvent from the pores. We articulate the functionalization of MOFs based on the following criteria: (a) being an unnecessary outcome of reticulation; (b) not leading to structure collapse when replaced or removed; (c) being deliberately installed in either pre-synthetic or post-synthetic manner; (d) leading to a specific function. In all cases, the functionalization of MOFs designs the chemical environment of their pores, where every moiety is positioned, manipulated, and addressed for crafting a well-defined, high performing machinery — Designed pore chemistry.

Pore chemistry addresses the precise control over the position and spatial arrangement of the installed functionalities guided by the framework backbone. The separation of functionalities across the backbone makes these chemical sites isolated and function in parallel, while placing functionalities in neighboring positions within a pore introduces functionality-functionality coupling behavior, dependent on their relative orientation and distance. When functionalities of different chemical identities are distributed over the entire pore space, this heterogeneity in distribution, electron density, and geometrical shapes creates a ‘forest’ covering the internal surface of framework backbone, where diverse chemical synergies may emerge. By tracing the trajectory of a guest molecule, which travels across framework interior and thereby passes through consecutive pores, the varying environment experienced by this molecule constitutes a chemical sequence of high dimensionality.

In this chapter, we focus on this pore chemistry and describe the installation of functionalities for achieving different configurations in positioning, including site isolation, coupling, and

cooperation. This is furthered by a brief introduction to frameworks' backbone construction and functionalization chemistry, which provides guidance to the precise control of functionality positioning. Finally, we specify the wide-ranging functions achieved by tuning pore environment, including catalysis, gas adsorption and separation, electron and ion conductivity, and many other processes, with an emphasis on the physical nature underpinning these applications and how site-specific properties are utilized. We note that this review is meant to be illustrative of the rich pore chemistry that can result from chemical modifications rather than provide comprehensive treatment of this topic.

1.3 Pore-Functionalization Strategies

One practical example that can be useful in developing pore chemistry is to install chloro(triphenylphosphine)gold(I) in the hexagonal channel of IRMOF-74-II[3] (Figure 1.1). The motivation to pin down this catalytic unit on the internal surface of MOF pore is to enhance its catalytic cyclability. The immobilization of the metal complex can efficiently prevent its degradation, which is favored in solution where the free motion of the metal-phosphine intermediates leads to the generation of metal particles through disproportionation reactions.[4] Therefore, the metal complexes appended onto framework backbone become isolated from each other and each single unit can perform independently—*site isolation*. An additional advantage of using MOFs as the immobile phase is that their highly porous nature allows for the facile transport of substrates for accessing the active centers.

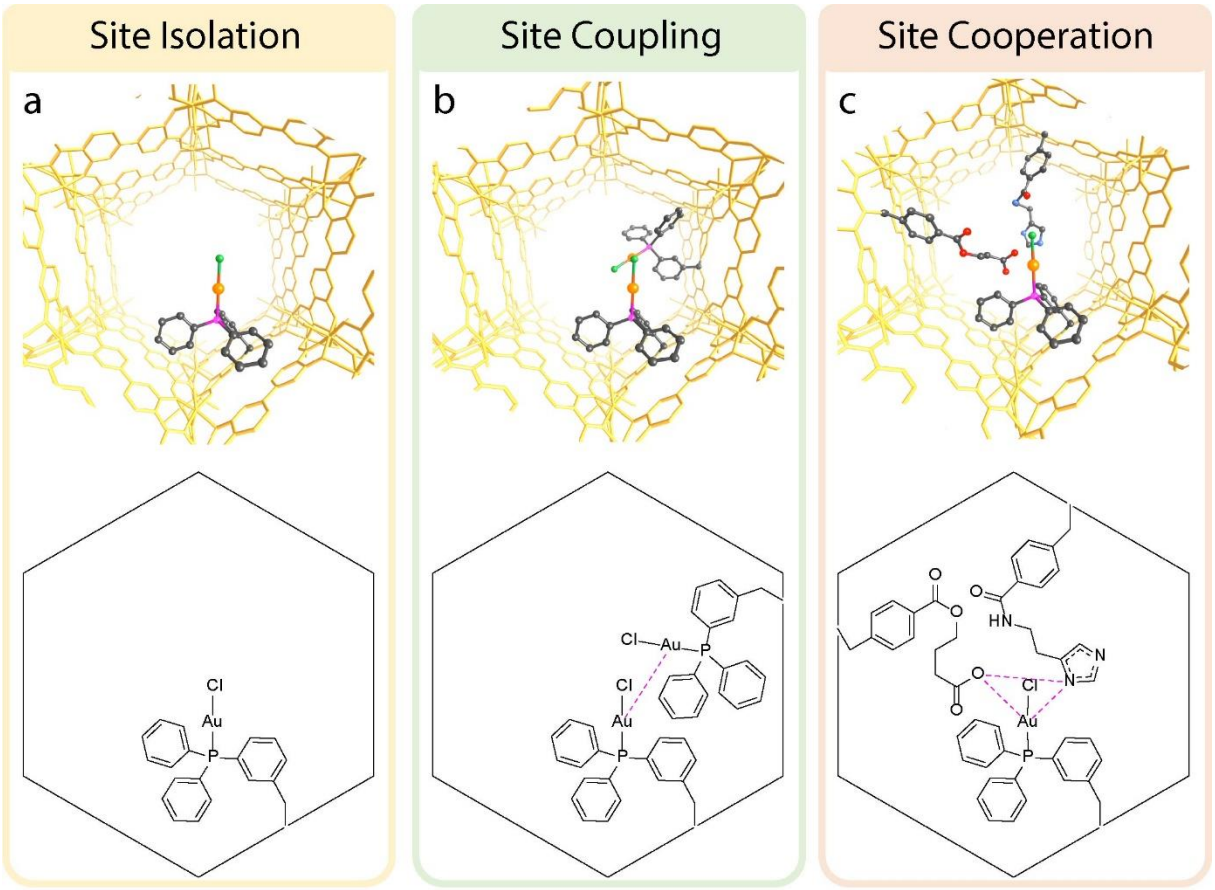


Figure 1.1. Pore functionalization strategies illustrated by the installation of chloro(triphenylphosphine)gold(I) in the hexagonal channel of IRMOF-74-II. The metal-phosphine complexes are appended onto the MOF backbone, being isolated (a), coupled (b), or cooperative with organic functionalities in close proximity (c). The backbone of IRMOF-74-II is presented in yellow sticks. The functionalities are illustrated in the ball-and-stick model. Color code: Au, orange; Cl, green; P, magenta; C, grey; O, red; N, blue. H atoms are omitted for clarity. The magenta dash lines in molecular structures indicate intermolecular interactions between functionalities.

The site isolation strategy leads to separation of the desired functionalities, while maintaining their presence in sufficient quantities owing to the repetitive arrangement of pores in MOF structures. An ideal result of such functionalization therefore is to uniformly spread this metal complex over the whole internal surface of IRMOF-74-II. When its density continues to increase, inevitably two molecules will sit in proximity of each other and their chemical interactions become possible (Figure 1.1b). In this case, the electrostatic interactions between two complexes enforce significant charge redistribution, or they form a gold-gold interaction when their distance is appropriate.[5] The installed functionalities thus are no longer isolated but instead generate a new chemical environment or new chemical species. The two neighboring gold centers can potentially activate a single substrate at the same time, resulting in breaking strong bonds within that substrate. For this reason, functionalities belonging to the same type are sometimes intentionally placed at neighboring sites and we term this functionalization strategy as *site coupling*.

Inspired by metalloenzymes in nature, it becomes interesting to install distinct functionalities, especially organic ones in the primary or the secondary coordination spheres of the gold-phosphine complex. It is envisioned that carboxylate and imidazolate, for instance, can tune the reactivity of this metal complex by either direct coordination or electrostatic interactions (Figure 1.1c). In general, the use of multiple kind of functionalities for achieving a property that cannot be accessed by a single functionality can be described by the term *site cooperation*. The molecular definitiveness and the architectural robustness of the MOF structure make the framework backbone a scaffold for the precise positioning of functionalities at designed locations and orientations. The rich functionalization chemistry of MOFs further provides a large design space with high chemical diversity. Reticular chemistry distinguishes itself from polymer chemistry in the fact that variation and manipulation of functional groups has negligible structural impact on the backbone. This independency prevents the limitation in functionalities that a given framework can bear, and provides access to a large library of pore chemistry.

1.4 The Conceptual Basis for Functionality Positioning

1.4.1 Site Isolation

Framework backbones are treated as a pin board onto which functionality moieties are appended (Figure 1.2). The resulting chemically modified frameworks thus inherit the properties of discrete molecules bearing the same functional groups. This strategy bridges the gap between homogenous and heterogeneous systems by loading molecules such as catalysts and dyes onto solids. Compared with other matrix materials, MOFs provide high porosities, enabling the attachment of numerous functional units and having them exposed to an extensive internal surface poised to interact with incoming guests. One advantage of pinning functional groups onto frameworks is that small molecules that tend to cluster in solution and thus lose their functionality can be fixed to a backbone, resulting in their permanent spatial separation.[4] Pinning molecules onto frameworks additionally facilitates recycling, as laborious procedures such as column chromatography are replaced by simple washing techniques. Through site isolation, species that are incompatible with

each other can now be combined into one pot given that they are compartmentalized into different pores.[6] In such system, cascade catalysis can take place sequentially in distinct domains, where the product of one reaction serves as the precursor for another. The exchange of mass and energy between domains within a single crystal provides access to a sophisticated system that is driven out of equilibrium, self-maintaining, and responsive to environmental stress.

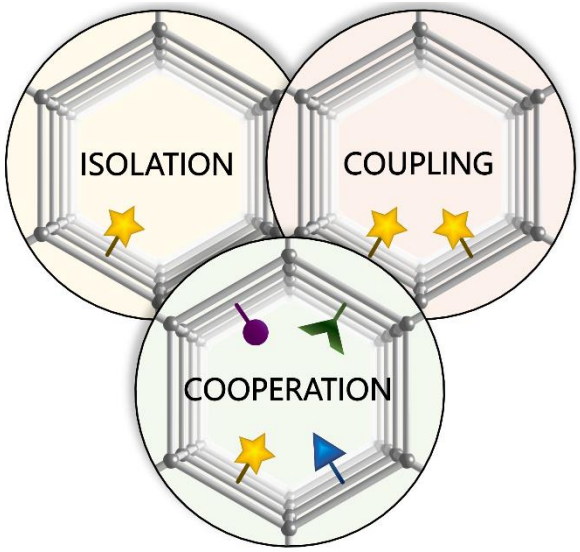


Figure 1.2 Three pore-functionalization strategies for positioning functionalities for their isolation, coupling, and cooperation. The MOF backbones are presented in grey and the functionalities are shown in colorful objects.

1.4.2 Site Coupling

The pre-synthesized framework backbone can serve as a scaffold for placing multiple functional groups (of the same type) in adjacent positions to accomplish a common task (coupled behaviors, Figure 1.2). Functionalities that are far apart across the backbone ('moving' across the backbone from one site to the other through chemical bonds), can be brought close in 3D space. This principle is exemplified by the structure of sulfated MOF-808.[7] If one goes from the terminal O atom of one chelating SO_4 group to that of another neighboring SO_4, the shortest path through chemical bonds is 23.34 Å in length, encompassing two metal-containing building units, one organic linker, and 14 bonds in total, while the Euclidean distance between these two O atoms is in fact only 2.57 Å. The alignment of functionalities into close positions, guided by framework backbone, can be designed and implemented with atomic precision. This geometrical control enables concerted performance that cannot be accessed by one functionality alone.

A homo-coupling reaction can be accelerated by bringing functionalities that are amenable to this reaction in proximity.[8] When these moieties are preorganized in a reaction-ready configuration, the entropy loss in passing through the transition state can be reduced. Compared with dispersing such molecules in solution, anchoring in vicinity onto a framework scaffold significantly increases their local effective concentration, further driving the reaction forward.[5] Other than catalysis, using the principle of site coupling imparts through-space interactions between the arranged chemical species, thus leading to, for instance, facile electron hopping over a short distance. When these functionalities can interact with a single guest molecule from its multiple sites, the multivalent interaction can enhance the host-guest affinity. It is envisioned that fast transport of guest

molecules across framework pores can be enabled if there exist multiple binding sites arranged in a compact configuration and bridged by shallow energy wells.

1.4.3 Site Cooperation

The third strategy entails the synergistic effect by functionalities of varying types (Figure 1.2). The concept of decorating a variety of multiple functionalities onto an otherwise periodic backbone is not too dissimilar from how nature arranges nucleobases along the phosphate-sugar scaffold of DNA, or how residues are propped up on polypeptide scaffold enclosing an enzyme pocket. Typically, building synthetic structures by mixing multiple precursors results in phase separation. However, this is not the case in reticular chemistry, where an ordered backbone serves as a robust platform that allows for variation in functionalization. One way of building systems with cooperative functions and rich information is to install functionalities of different types on the symmetric related positions within a pore and among pores, a strategy we termed multivariate chemistry.[9] Multivariate chemistry can be performed by using organic linkers with the same geometrical parameters and linking groups, but different appended substituents. This was demonstrated by the incorporation of up to eight distinct linkers bearing different functional groups into a single crystal of MOF-5.

Multivariate functionalization is carried out through using judiciously chosen combinations of functionalities for achieving their desired spatial arrangement; typically driven by free energy minimization during synthesis. It is noted that multivariate frameworks are still an outcome of design: A plan is made and followed by synthetic efforts, which may or may not result in what was targeted at the outset, but it represents a useful step in understanding what the next step should be towards achieving the targeted design. Such iterative method allows multivariate systems to evolve into optimized structures and thus are distinguished from other chemical architectures where such flexibility is absent. These architectures may have limited choices of placing functionalities (*e.g.* using only symmetric unrelated positions with a pore of framework), and human bias imposed onto an all-pre-determined design can constrain the search away from global optima.

Cooperation can also take place between functionalities that are connected to linkers coexisting in a crystal yet not symmetrically related, *e.g.* a three-connected linker and a two-connected linker in MOF-210.[10] This strategy can also be facilitated by installing metal species and organic functionalities that are close in their positions and function cooperatively, or even effected by interacting a building unit with the surrounding framework scaffold. For example, the conformational restrictions imposed by the framework backbone can tune the photophysical behavior of a confined chromophore.[11] In all of these cases, functionalities of different type are positioned in 3D space and cooperate through the heterogeneous chemical environment created by them.

In contrast to site coupling, site cooperation extends the scope of functionalities that can work together in the pore of a framework. As such, reticular chemistry offers the platform to generate a wide array of multicomponent structures by varying the composition, ratio, and arrangement of functional groups on the backbone. In this way the resulting multicomponent system can outperform the simple linear sum of its constituents and may very well display synergistic effects. To accommodate the varying surface electrostatics of guest molecules, combining multiple functionalities, each providing unique geometry and charge configuration, enables building of a binding pocket with shape and charge complementary to those of the guest. When using multiple

functionalities for binding the transition state of a substrate, the activation barrier can be significantly lowered by the cumulative contribution from every binding site. Functionalities that are not involved in direct chemical bonding can also play an important role by modulating electric field, gating the entry of substrate, or aligning substrate in specific orientations.

1.5 Construction of MOF Backbone

When larger derivatives of the gold-phosphine complex are involved in pore functionalization, they will require the use of MOFs with correspondingly larger pore sizes. The expanded form of the framework should not only accommodate bulky functionalities but also keep their distances

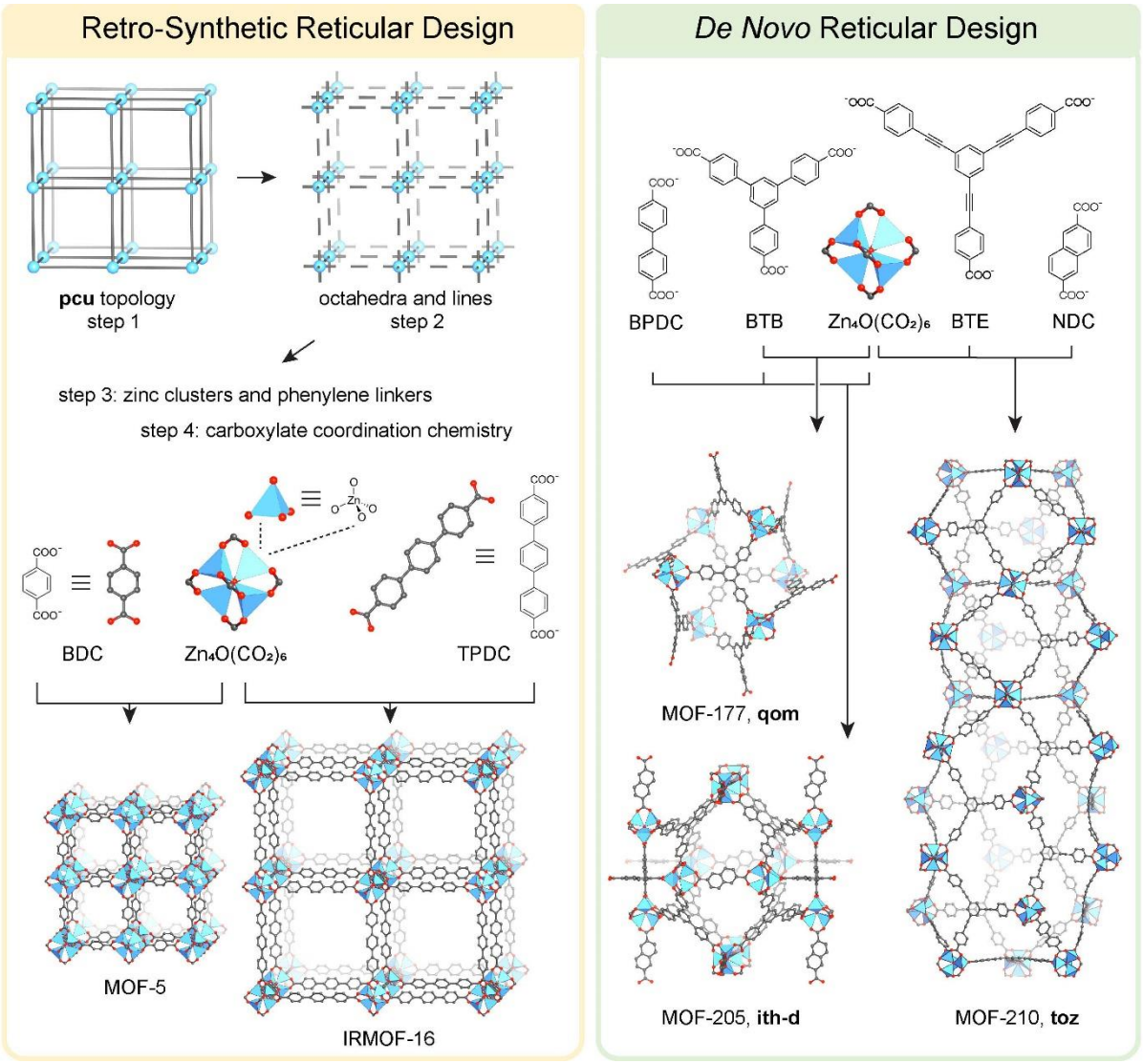


Figure 1.3. Retro-synthetic reticular design and *de novo* reticular design. In retro-synthetic reticular design, a target structure type is defined and then specified into chemical details. *De novo* reticular design on the other hand starts with judiciously chosen building units and addresses their linking into unknown structure types. Color code: Zn, blue; O, red; C, grey. H atoms are omitted for clarity.

the same as those between the less bulky counterparts so that to achieve a constant coupling effect. On the other hand, designers may want to place the neighboring functionalities at different distances and orientations in order to investigate how the geometrical parameters can determine their coupling/cooperation behavior. This may require a framework scaffold of a completely different structure type. Overall, a fine control over the relative position of functionalities requires the global structural control in framework backbone construction. By leveraging methodologies and tools of molecular synthesis, reticular chemists significantly enrich the synthetic pool by bringing the sophistication of covalent chemistry from discrete molecules to extended structures. To achieve this, the building-unit approach has been applied to build frameworks, by which the connectivity, size, and shape of molecular building units predetermine the geometry of the targeted structures.

Two general strategies for reticular design are being practiced (Figure 1.3): retro-synthetic and *de novo*. In the retrosynthetic strategy, a structure type of a specific topology is identified and used as blueprint. It is then deconstructed into its fundamental geometrical units, and these units are matched to the corresponding molecular building blocks. In contrast, in the *de novo* strategy, judiciously chosen molecular building blocks are linked together to explore unknown topological outcomes. By using the geometrical, chemical and compositional features of inorganic building units to direct their linking, this strategy has been heavily applied to extend the structure scope of reticular chemistry.

1.5.1 Retro-Synthetic Reticular Design.

This is performed by using four sequential steps (Figure 1.3, left). (*i*) A target topology (**pcu**) is chosen as the blueprint for the construction of the desired framework. (*ii*) The chosen topology is then deconstructed into its underlying geometric units (octahedra and lines) by breaking edges between vertices. Without altering the connectivity of these geometrical units, the lengths, angles, and dihedral angles can be varied to target specific structural features (e.g. longer lines for larger pores). (*iii*) Molecular equivalents of the geometric units that are synthetically accessible are then identified. These molecules serve as building blocks for the construction of the target framework. It is crucial that during this process the size, shape, and connectivity of the building units remain unchanged to ensure that the linkages exclusively form at the predetermined positions. Molecules constructed from aromatic rings are prevalent in use as linkers of MOFs, and metal clusters with rigid coordination spheres serve as metal-containing building units. In this case, we choose $Zn_4O(-CO_2)_6$, benzenedicarboxylate (BDC), and p-terphenyl-4,4’-dicarboxylate (TPDC) to fulfill the geometrical requirements.[12,13] (*iv*) Finally, the chemical nature of the linkage connecting metal-containing clusters and linkers here is identified as carboxylate. Other options of linkages are exemplified by the coordination chemistries of sulfonate, phosphonate, catecholate, diamino, disulfido, imidazolate, pyrazolate, and triazolate moieties.[14]

1.5.2 *De Novo* Reticular Design.

The vast unknown space of framework topologies can be explored by tailoring inorganic building units, organic linkers, and their linkage chemistries. In this context, the $Zn_4O(-CO_2)_6$ was used to connect with the trigonal organic linker (4,4’,4’’-benzene-1,3,5-triyl-tribenzoate, BTB) and a net (**qom**) was discovered instead of the expected highly symmetric one (**pyr**) being produced (Figure 3b). To make other MOFs of distinct nets, combinations of organic linkers of mixed connectivity were used for linking the same tetra-zinc units. When 2,6-naphthalenedicarboxylate (NDC) and biphenyl-4,4’-dicarboxylate (BPDC) are combined with BTB and 4,4’,4’’-(benzene-1,3,5-triyl-

tris(ethyne-2,1-diyl))tribenzoate (BTE), respectively, two new highly porous structures (MOF-205 and MOF-210) were discovered.[10] In contrast to organic linkers that serve as preformed building blocks which remain intact during the reticulation process, the inorganic building units are produced *in situ* and can vary in their shape and connectivity depending on the specific linkage chemistry. The design and discovery of MOF-910 epitomizes this approach; the choice of a heterotritopic linker bearing three distinct types of functional group (benzoate, semiquinonate, and 2-pyridone) facilitates the formation of helical rod metal-containing building units rather than the common straight ones.[15]

1.6 Methods for Functionalization of the Pores

When the relative position of the gold-phosphine complexes and the type of framework backbone, the next step is to specify the functionalization chemistry that is used for installing this species onto the framework scaffold. The synthesis and functionalization of MOFs represent two distinct stages of the construction. Although this distinction holds at a conceptual level, real functionalization approaches do not necessarily involve a modification of an already assembled framework. Indeed, functionalities are often present as native groups carried by the building units as part of MOF formation. To classify these two kinds of approaches, pre-synthetic functionalization refers to the modification of the building block that is performed prior to the framework synthesis. Post-synthetic functionalization pertains to modification reactions conducted on an already formed MOF.

1.6.1 Pre-Synthetic Functionalization

One advantage of pinning functional groups onto frameworks pre-synthetically is that the incorporation of functionalities is ensured by their presence on the building blocks,[16] thus eliminating complications linked to functionalization reactions' yield and kinetics. Even challenging reactions can be used for functionalization as the small-molecule product can be purified. This strategy effectively avoids the lack in quantitative control sometimes present in post-synthetic functionalization. It is noted that the ratio of each functionality present in the synthesized framework may differ from that in the reaction mixture, since every building block's reactivity is influenced by the appended functional groups.

1.6.2 Post-Synthetic Functionalization

In order to attach functionalities to the backbone, the synthetic approach known as post-synthetic functionalization has been implemented to complement pre-synthetic synthesis.[17] One advantage of reticular chemistry is that the functionalization of frameworks can be performed in the same way as the functionalization of discrete building units. The molecular nature of frameworks enables a rich chemistry of post-synthetic functionalization to take place on the periodic scaffold, either by exchange of its constituents or by introducing new moieties at reactive sites.

1.6.3 Covalent Attachment of Functional Units

Functionalization by formation of covalent bonds is by far the most explored approach to integrate non-native chemical groups into MOFs (Figure 1.4a).[18] One of its main advantages is the stability of the attachment of the introduced functionalities and the possibility to employ a vast library of chemical reactions to identify the most suitable one according to the stability of the material. The covalent bond formation approach is based on the presence of reactive sites in the framework. The most commonly used reactive groups for such transformations include amine,[19] aldehyde,[20] azide,[21] and unsaturated coordination sites.[22] MOFs without any reactive sites are particularly

challenging in this respect. Interesting examples are the use of the inorganic cluster as an anchoring point for chemical bond formation[23] or even the aromatic linker as modification point to introduce functional groups (*e.g.* nitro group) that can be further functionalized.[24]

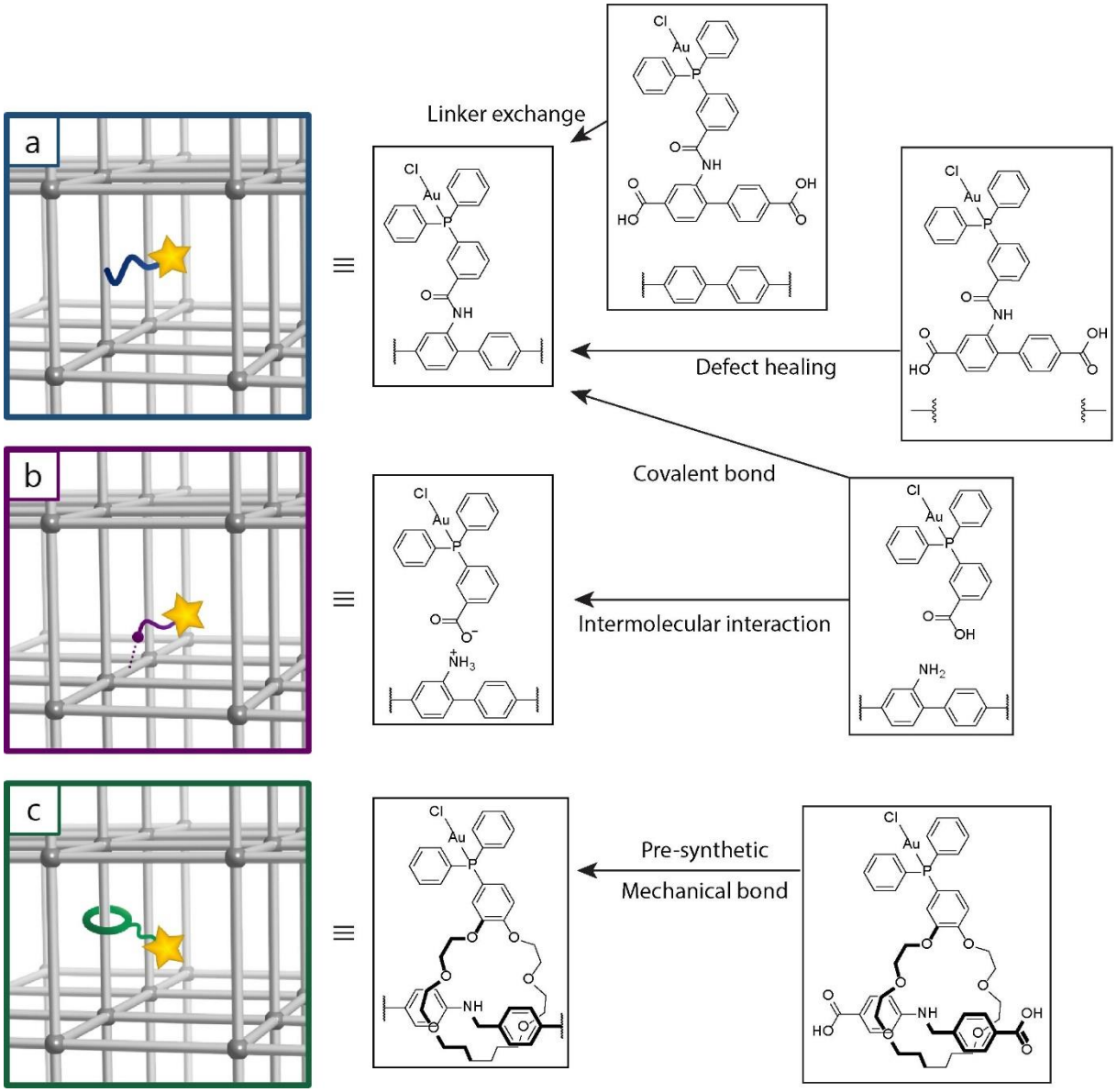


Figure 1.4. The chemistry of functionalizing a MOF in pcu net with chloro(triphenylphosphine)gold(I). (a) Covalent attachment can be achieved by grafting functionalites to the reactive moieties on the backbone though the formation of amide. Alternatively, linker molecules bearing the gold-phosphine complex can post-synthetically replace the native ones or occupy missing-linker defects. (b) Intermolecular interaction can be used for the adsorption of negatively charged gold-phosphine complex to the positively charged backbone. (c) Mechanical interlocking attaches the gold-phosphine complex to the linker molecule permanently. Such functionalized linker can be used for MOF synthesis and thus bring this functionality to the MOF backbone in a pre-synthetic manner. The backbone of the MOF is illustrated in grey. The target gold-phosphine functionality is represented as a yellow star. Its attachments to the backbone in the form of covalent bond, intermolecular interactions, and mechanical interlocking are drawn in blue, purple, and green.

1.6.4 Exchange of Building Units

Through linker exchange, the original organic linkers in the crystallized frameworks can be substituted by others that possess different functional groups (Figure 1.4a).[25] This process is enabled by the dynamic nature of the linkage, during which the incoming linker traverses the framework structures by diffusion and competes with the built-in linkers through continuously forming and breaking coordination bonds. Performing linker exchange allows for the incorporation of linker molecules that are incompatible with synthetic conditions used for the formation of the MOF. Transmetalation occurs when metal cations in the as-synthesized framework are replaced post-synthetically by different metal species.[26] In so doing, the incorporated metal cations are forced into the coordination environment of their predecessors, which may be energetically unfavourable when in solution.

1.6.5 Functionality Addition at Structural Defects

Another possibility of pore functionalisation is to take advantage of the lack of components within the backbone, i.e. the presence of structural defects. The occurrence of these defects implies the presence of linker-terminated or node-terminated sites. As the reactivity of such exposed moieties has not been expressed during the MOF's synthesis, these sites are available for post-synthetic functionalisation reactions and can be decorated with chemical groups of interest (Figure 1.4a). The most studied functionalisation of a defect until now focused on missing linker defects in UiO-66. Its framework can be engineered to have short monocarboxylate "capping" species replacing the terephthalate linkers to obtain missing linker defects available for functionalization.[27] Most importantly, these defective sites have been also introduced on purpose and used to incorporate different linkers by "sequential linker installation".[28]

1.6.6 Functionality Addition at Structural Defects

Despite being intrinsically weaker, intermolecular interactions have the unique advantage of offering a much higher cooperativity (Figure 1.4b). While the number of bonds that a given atom can establish is limited by its valence in the state it is found, molecules and ions can be designed to allow manifold cooperative interactions with complementary species, which can result in very high binding energies. This possibility allows for the design of reversible functionalization reactions, so that the functional groups can be removed or substituted with minor damage or alteration to the framework itself, and likely with quantitative yields. Intermolecular interactions include π–π stacking between organic linkers and guest molecules.[29] Coulombic interactions can be established between charged framework backbone and counterions residing in the pore.[30] The presence of hydrogen bond donors or acceptors in MOF backbone can recognize the matching partners with relatively high affinity.[31]

1.6.7 Introduction of Mechanical Interlocking in the Backbone

One last approach is mechanical interlocking of molecules within the backbone, where chemical bonds are not responsible for the installation of a novel functionality (Figure 1.4c). In this category, the force which keeps the introduced species in their location is the simple interatomic impenetrability that comes into play when a species is nested in a cavity due to steric hindrance or "tied" to part of the framework by its own structure. An interesting difference of this type of docking compared to the first two functionalisation methods is that the introduced species maintain a much higher mobility and, in certain conditions, can slide or rotate about the framework backbone and adopt different orientations or positions. This lowers the spatial constraints of the

functionalisation sites and endows the pore with a unique type of functional group dynamics, where it can be taken advantage of to tune guest permeation or reaction kinetics by dynamically mitigating the pore accessibility. Impressive examples are a molecular shuttle (an interlocked macrocyclic ring is able to move back and forth between two recognition sites) interlocked with MOF backbone,[32] a catenated strut in a catenated MOF,[33] and macrocyclic wheels[34] (*i.e.* crown ethers). The future development of such 'robust dynamics'[35] can transfer precisely designed molecular dynamics to solid state.

1.7 Applications of Functionalized MOFs

1.7.1 Guest Binding with High Specificity and Affinity

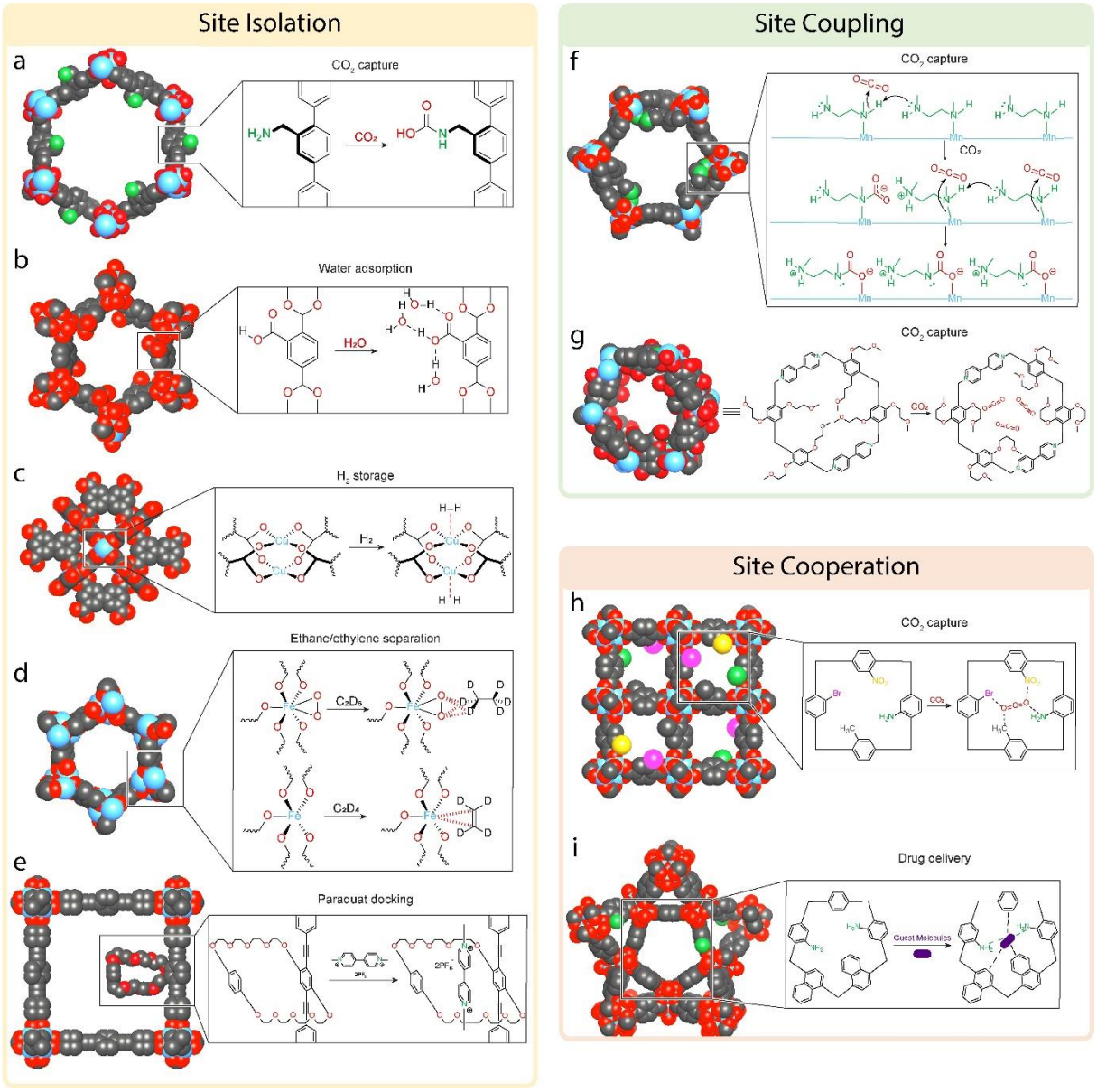


Figure 1.5. Site-specific functionalization of pores for guest binding. Through site isolation, functionalities work independently: the amine group for CO_2 capture (a); the carboxylate group for water adsorption (b); the open metal sites for H_2 storage (c) and ethane/ethylene separation (d); the macrocyclic crown ether for paraquat docking (e). Through site coupling, functionalities of the same type bind to guests

in collaborative ways: diamine (f) and alkyl ethers (g) gate the adsorption of CO_2. Through site cooperation, functionalities of different types bind to guests in collaborative ways: mixing methyl, amine, bromo, and nitro groups in one framework for CO_2 capture, outperforming the sum of every homogeneous component (h); mixing amine and benzene groups for tuning drug release rate (i). Color code: metal, blue; C, grey; O, red; N, green; Br, magenta. In (h), the nitro groups are represented by yellow spheres for clarity. H atoms are omitted for clarity.

Proteins carry out molecular recognition by using their evolved binding pocket to discriminate guest molecules of diverse structures with high selectivity and affinity. The strong host-guest binding packages over all the interactions between an array of amino acid residues appended on the peptide scaffold and all the regions of the substrate exposed to the pocket. The rich chemical diversity of functional groups attached to the amino acids ensures that every region of varying electrostatics and geometries across substrate surface is precisely addressed and thus energetically stabilized. The cooperation and the precise spatial alignment of the pocket functionalities provide insights into the design of artificial pores for guest binding. In this regard, MOFs provide a versatile platform for building binding sites with structural complexity approaching to that of protein pockets. The molecule-level definitiveness of functionalities along with the flexibility in choosing their chemical nature and spatial positions create binding sites of desired energy. A strong binding is beneficial for the adsorption of guest at a low concentration (or relative pressure), while it may complicate desorption, and therefore an optimized binding energy should be targeted. Here, framework pores can be specifically functionalized to meet the demand of a particular application setting. In the following content, we discuss the use of different functionalization strategies—site isolation, site coupling, and site cooperation—to accommodate different guest species (Figure 1.5).

1.7.1.1 Guest Capture on Isolated Sites

Compared to traditional adsorbent materials, being able to anchor accessible polar functional groups (*e.g.* Lewis bases) in high density makes MOFs promising candidates for CO_2 separation. Each of these binding sites can interact with CO_2 independently, and give rise to excellent CO_2 adsorption capacity and selectivity over other gases, such as N_2, CH_4, and H_2O. In an attempt to incorporate Lewis base moieties into MOFs, an amine-functionalized terephenylene linker was utilized to build IRMOF-74-III-CH_2NH_2 (Figure 1.5a).[36] With the presence of amine groups, CO_2 was chemisorbed to form carbamic acid and ammonium carbamate under dry and wet conditions, respectively. Recently, this effort has been continued by increasing the density of amino groups in the same MOF structure. Two primary alkylamine functionalities were covalently tethered to each linker of IRMOF-74-III.[37] Compared with its monoamine counterpart, IRMOF-74-III-$(CH_2NH_2)_2$ collected 2.33 times the amount of CO_2 per gram of material in a low pressure range (<100 Torr), indicative of the effectiveness for site isolating functional groups having strong binding affinity within framework pores.

MOFs also show promise in water adsorption, owing to their structural diversity and functionalization tunability for adjusting pore size and hydrophilicity, parameters that are crucial for their water-sorption performance. The chemical type of functional groups strongly affects hydrophilicity of the pores, and thus the position of inflection point α in water sorption isotherm. For studying this effect, the pristine benzenedicarboxylate (BDC) linker in MIL-101(Cr) was functionalized with −COOH (**1**) (Figure 1.5b), −NHCOCHCHCOOH (**2**), $-NH_2$ (**3**), $-NHCH_2CH_2CH_2SO_3H$ (**4**), $-NHCONHCH_3$ (**5**), and $-NO_2$ (**6**).[38] Water adsorption isotherms of these MOFs revealed that the introduction of hydrophilic functional moieties (**1**, **2**, **3**, and **4**) shift α to lower pressures, while hydrophobic functional group **5** shifts α to a higher pressure compared

with that of the original MIL-101(Cr). The shift caused by hydroneutral moiety **6** on α is negligible as expected.

Unlike CO_2 and H_2O, H_2 storage in MOFs remains an outstanding challenge due to the difficulty in polarizing H_2 molecules to create attractive interactions. To approach this problem, open metal sites of relatively strong affinity to H_2 becomes a promising target. The axial positions of the paddle-wheel type [$Cu_2(\text{-}CO_2)_4$] building unit are originally occupied by coordinating solvent molecules. These can be removed by evacuation without compromising the integrity of the framework structure, thus leading to the formation of open metal sites. In this regard, a wide variety of MOFs with open metal sites have been synthesized for optimizing H_2 uptake. In 2005, MOF-505 synthesized from Cu(II) paddle-wheel secondary building units and 3,3',5,5'-biphenyltetracarboxylate was for the first time studied for H_2 storage using open metal sites (Figure Figure 1.5c).[39] In the presence of open metal sites, MOF-505 adsorbed at the time an exceptional 2.47 wt% H_2 at 750 Torr and 77 K.

Incorporating foreign cations into frameworks as additional binding sites provides another useful tool to enhance H_2 uptake. In the structure of the MOF Mn-BTT, the positively charged counterions residing in the pore were post-synthetically exchanged with transition metal-ions (*i.e.* Fe^{2+}, Co^{2+}, Ni^{2+}, Cu^{2+}, and Zn^{2+}).[40] The newly introduced metal-ions served as effective binding sites, possibly by forming coordination bonds with H_2, and exhibited improved H_2 capacity.

Immobilization of open metal sites within MOFs also helps selectively extract gas molecules from their mixtures. Early efforts achieved preferable adsorption of CO_2 against methane and the separation of harmful gases with MOF-74 replete with open metal sites.[41] The separation of light hydrocarbons is also of great interest. Featuring a high density of open Fe(II) coordination sites, Fe_2(dobdc) exhibited excellent performance for the separation of C_2H_4/CH_4 and C_3H_6/C_3H_8 mixtures (Figure 1.5d).[42] The strong affinity for unsaturated hydrocarbons with respect to saturated ones was evidenced by the initial steep rise in the isotherms. Additionally, the uptake of these gases at 1 bar approached stoichiometric quantity, suggesting that every Fe(II) site adsorbs one gas molecule. Neutron powder diffraction experiments indicated that these unsaturated hydrocarbons display side-on binding mode, with Fe-C distances varying in the range of 2.42(2)–2.60(2) Å. These distances are much shorter than those in the case of C_2H_6 and CH_4 (~3 Å), suggesting stronger interactions between MOFs and unsaturated hydrocarbons. The C_2H_4/CH_4 and C_3H_6/C_3H_8 permeation selectivities were calculated to sit in the range of 13–20 and 14–16, respectively.

Purifying ethylene from ethane contamination is of industrial importance and requires an abnormal binding site that favours saturated hydrocarbon against unsaturated ones. Inspired by natural metalloenzymes and synthetic catalysts for C(sp3)-H activation, an Fe(III)-peroxo sites in the MOF [$Fe_2(O_2)$dobdc] was created to preferentially bind ethane over ethylene (Figure 1.5d).[43] The adsorption measurement showed that $Fe_2(O_2)$dobdc not only has a relatively high ethane uptake but also exhibits the highest ethane/ethylene selectivity among all porous materials.

Other than binding gas molecules, MOFs can also be functionalized to capture specific species from its solution using their docking sites. Macrocyclic crown ethers which act as electron-rich receptors can specifically recognize electron-deficient substrates and yield corresponding pseudorotaxane complexes. By incorporating 34- and 36-membered macrocyclic polyethers in the construction of organic linkers, MOF-1001, MOF-1001A and MOF-1002 are capable of capturing paraquat cations in a stereoelectronically controlled fashion (Figure 1.5e).[44] Every one of these

receptors is accessible for docking paraquat cations, as evidenced by X-ray diffraction and by solid- and solution-phase NMR spectroscopic studies.

1.7.1.2 Carbon Dioxide Capture through Site Coupling

In the context of MOF-based CO_2 adsorption, step-shaped isotherm is favourable for realizing a large working capacity operated under a narrow window of pressure swing. This has been achieved by the coordinative functionalization of open metal sites with diamines and the resulting coupling behaviour between two adjacent amine sites (Figure 1.5f).[45] For each diamine molecule, one end is bonded to unsaturated metal centres and the other end is dangling in the channel for CO_2 adsorption. Spectroscopic, diffraction and computational studies showed that the sharp adsorption step is attributed to a unique coupling mechanism, involving the insertion of CO_2 into metal-amine bond by forming ammonium carbonate chains. In addition, the position of the step in the adsorption isotherm can be altered by the change of temperature, the type of metal species, and the structure of appended diamines.

When pores of the framework are modified with alkyl ether chains, the resulting MOF can display novel profiles of guest molecule binding and separation, owing to the coupling effect between side chains in the pore. For example, methoxyethoxy groups on organic linkers interact with each other to form a closed molecular gate that prevents nitrogen molecules from entering the pore (Figure 1.5g).[46] As a result, the uptake of CO_2 at 273 K and 1 bar is ~500 times higher than that of N_2, which can be attributed to the larger polarizability of CO_2 which leads to a stronger interaction with the methoxyethoxy groups for opening the gate.

1.7.1.3 Gas Separations by Site Cooperation in Multicomponent Frameworks

Multivariate MOFs, which are constructed by multiple organic linkers with the same geometrical parameters and linking groups, but different appended substituents provide the opportunity to enable site cooperation for guest binding. In 2010, up to eight organic linkers with distinct functionalities have been successfully incorporated into MOF-5.[9] The arrangement of these linkers and the cooperative effects between specific combinations of functionalities made the multivariate system outperform the simple linear sum of its discrete components. Particularly multivariate MOF-5-EHI, composed of three distinct linkers, displayed up to 400% better selectivity for CO_2 over CO than pristine MOF-5 (Figure 1.5h).

The design of multivariate MOFs permits the variation in the composition and ratio of functional groups without changing the underlying topology. The cooperation among functional sites with varying ratios generates a series of continuum energy states that can be used to tune the release rate of guest in a precise manner and over a wide range. Multivariate MIL-101(Fe) constructed by BDC linkers with distinct functional groups (−H, $-NH_2$, and $-C_4H_4$) were used to demonstrate this principle (Figure 1.5i).[47] Three guest molecules (ibuprofen, rhodamine B, and doxorubicin) were incorporated into this series of MOFs and their release rate were found finely tuned by varying the ratio of functional groups. Particularly, the time of release for doxorubicin can be programmed from 17 to 29 days. Additionally, the co-release of multiple guest molecules (rhodamine/ibuprofen and doxorubicin/ibuprofen) was accomplished by adjusting the ratio of the paired-up functional groups in the MOFs. The obtained continuum in coding energy levels holds potential in using multivariate MOFs for drug delivery systems with predictable guest release kinetics. The power of this site-cooperative approach cannot be realized by a physical mixture of discrete linkers.

1.7.2 Catalysis

Guest molecules residing in the pore can be activated for lowering their energetic barrier to make new bonds. Such catalytic processes rely on the interaction between the substrate and the active site, which stabilizes the transition state and steer the catalytic transformation towards specific products, thereby providing reaction acceleration and selectivity. A strong framework-guest interaction gives an additional enhancement to substrate selectivity, when foreign molecules other than the target one that can participate in side-reactions, are prevented from staying at the active site for a time window sufficient for entering the reaction coordinate. Fostering a pore environment that favours the binding of the ground state of substrate does not necessarily undermines the reduction in activation energy, as long as the chemical bond to be broken is less stabilized than the molecule as a whole. Nevertheless, the major function of active sites is still transition state stabilization and the strategies in building such sites within framework pores are detailed in the following sections.

1.7.2.1 Isolated Active Sites

The most common practice in building active sites within framework pores is to install a single chemical moiety that significantly lowers the activation energy. Open metal sites are capable of this task through their facile coordination with substrate, acting as Lewis acid centres for accepting electrons from substrates. These open metal sites can be readily produced from the synthesis of many framework structures. Following the first mentioning of open metal sites, [48] crystal structure of open metal sites was for the first time reported for MOF-12.[49] In these cases, the linkage of metal nodes only uses partial coordination sites, leaving the remaining ones occupied by dangling solvent molecules. The removal of these solvent molecules through evacuation thus creates open metal sites suitable for catalysis. This is contrasted to the low-coordination metal complexes where bulky ligands for protection from decomposition are needed. Open metal sites in MOFs have low steric hindrance for incoming substrates than their homogenous analogues, as the energy deficit in stabilizing open metal sites has been paid off by the rigid framework backbone. Indeed, the first effort in using open metal sites for catalysis is demonstrated by Cu(II) of HKUST-1 (Figure 1.6, a1) in the cyanosilylation of benzaldehyde and the isomerization of terpene derivatives.[50] Further studies explored other open metal sites, such as Mn (II),[51] Cr(III),[52] Fe (II),[53] and Zr (IV),[54] which are isolated across the framework backbone for performing catalysis in high efficiency and stability.

For framework structures that do not have open metal sites on the backbone, foreign catalytic metal species can be installed through functionalization. Organic linkers containing metal docking moieties, such as 2-phenylpyridine (Figure 1.6, a2),[55] 2,2'-bipyridine (Figure 1.6, a3),[55,56] 1,1'-bi-2-naphthol (Figure 1.6, a4),[57] phenanthroline (Figure 1.6, a5),[58] phosphine (Figure 1.6, a6),[4] and porphyrin (Figure 1.6, a7).[59] Inorganic clusters in MOFs have also been used for bonding extra metal species, *e.g.* bridged through O (Figure 1.6, a8) or N atoms (Figure 1.6, a9) in the cluster.[60] Metal complexes can been encapsulated within the framework pore by Coulombic interaction and trapped due to steric hindrance thus preventing their leakage into solution and the degradative self-dimerization (Figure 1.6, a10).[61] Other than catalytic metal species, organic functionalities that are capable of catalysis have been employed through site isolation. These include amide (Figure 1.6, a11),[62] carboxylic acid (Figure 1.6, a12),[63] proline (Figure 1.6, a13),[64] 1,1′-bi-2-naphthol (Figure 1.6, a14),[65] urea (Figure 1.6, a15),[66] and thiourea (Figure 1.6, a16).[67] When two type of active sites are each isolated within distinct frameworks, but combined into one pot, two intrinsically incompatible catalysts can thus work in parallel for enabling continuous chemical transformations.

Such cascade catalysis was demonstrated by site isolation of TEMPO and MacMillan's catalyst in framework cages (Figure 1.6, a17).[8]

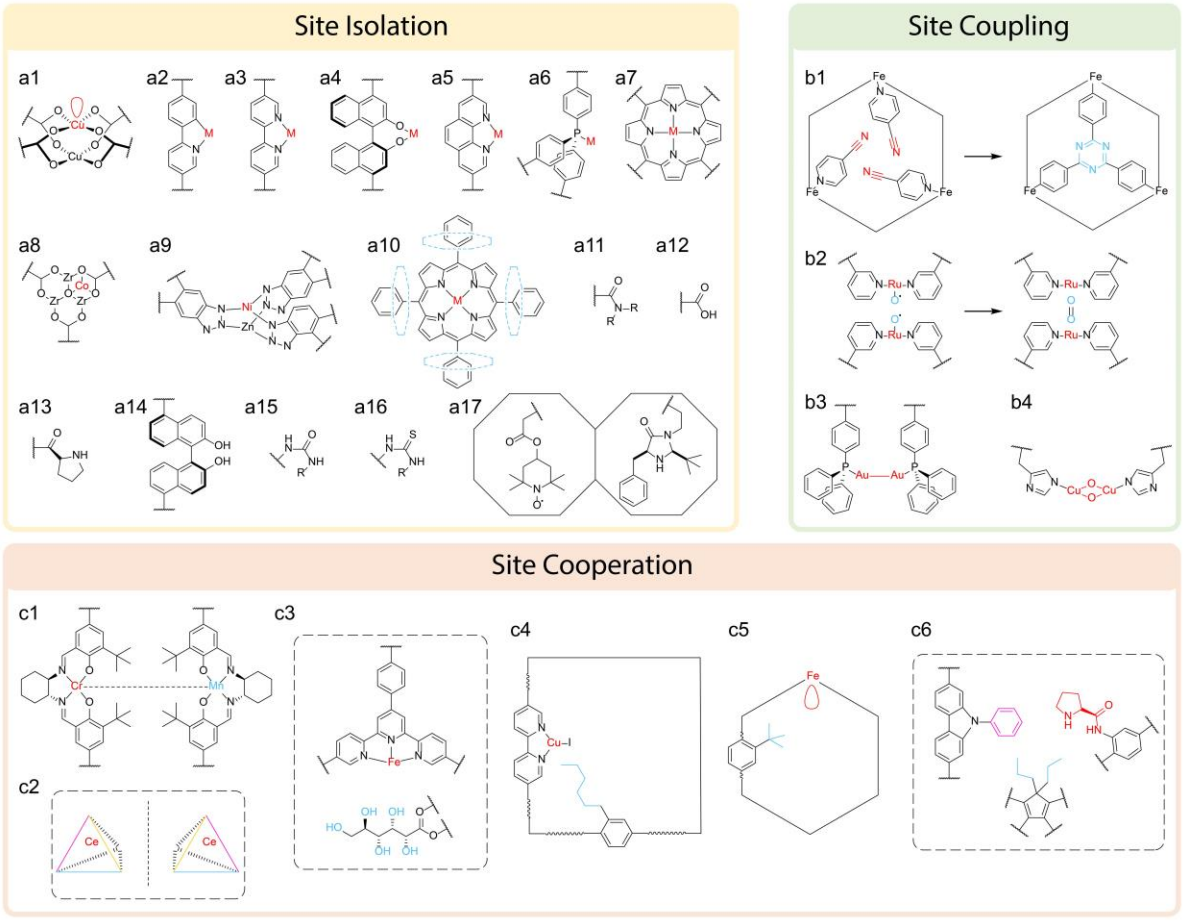


Figure 1.6. Site-specific functionalization for building active sites. Isolated catalytic units include open metal sites on metal clusters (a1), metalated organic linkers (a2-7), extra metals attached to existing metal clusters (a8, a9), a molecular catalyst trapped in the pore (a10), organocatalysts appended on framework backbone (a10-16), and two otherwise incompatible molecule catalysts each compartmented in framework cage catalysing cascade reactions (a17). Coupled catalytic units include three open metal sites in a triangular shape for pre-orient substrates for their coupling reactions (b1) and the neighboring metal species for activating together one substrate (b2-4). Placing different types of catalytic units in proximity imparts the cooperation between different metallosalens (c1), cerium centers and their chiral backbone (c2), metal species and the neighboring organic functional groups (c3-5), and between different organic moieties (c6).

1.7.2.2 Coupled Metal-Ions

Coupling reaction between the moieties that are placed at neighbouring sites can be accelerated due to the reduction in entropy loss during passage through the reaction coordinate. While the appropriate geometry necessary for entering the transition state demands a time-consuming sampling through diffusion and rotation of precursor molecules in solution, the preorganization of the reactive precursors guided by framework scaffold confines reaction-ready states in place. This strategy was presented in the framework guided [2+2+2] cyclotrimerization (Figure 1.6, b1).[68] In the structure of the ground state, three molecules of 4-cyanopyridine are anchored on the backbone of MIL-88B through Fe-pyridine coordination bonds. Their cyano groups are therefore aligned

toward the centre of the pore in a triangular shape. This constrained geometry enforced by the framework scaffold effects an otherwise sluggish [2+2+2] cyclotrimerization reaction. A prerequisite for using site coupling for catalysis is to have a reversible bonding between the substrates and the framework, such that the product of the coupling reaction can leave the active site and make room for the entry of substrates for the next turnover. Although product removal becomes energy demanding due to its multivalent bonding with the framework, further efforts in destabilizing product binding by geometric mismatch for instance will accomplish a real catalyst.

Other than recruiting substrates in proximity, bringing multiple catalytic species together, for example metal centres, can lead to significant activation of reaction precursors, exceeding that enabled by a single species alone. This has been observed in encapsulating an otherwise inactive AuCl complex in framework cages for catalysing intramolecular C-O and C-C bond-forming cyclization reactions.[5] When the AuCl complex densely occupies the pore space to a high local concentration, up to 1.1 M, the generated Au-Au interactions (Figure 1.6, b3) endow a high reactivity and selectivity, which is inaccessible to homogenous catalysis where catalyst concentration is typically kept in the range of 10^{-3} to 10^{-6} M. The principle of coupling multiple metal centres for catalysis is further presented in the encapsulation of 12 Ru complexes inside a framework cage.[69] These metal centres are placed at close positions for facilitating dinuclear pathway for oxygen bond formation (Figure 1.6, b2), thus enhancing water oxidation rate by two orders of magnitude. In this process, each Ru actives one O atom followed by the coupling of two metal-oxyl radicals. Without framework preorganization, such dinuclear coupling becomes diffusion limited and consequently slow. In another example, bis(μ-oxo) dicopper species are created through their coordination with metal-binding ligands propped up by framework scaffold (Figure 1.6, b4).[70] The structure of MOF-808 was judiciously selected as it possesses the chemical and geometrical parameters allowing two imidazole-containing ligand at neighbouring sites to sandwich a dicopper cluster. This construct mimics the active site of methane monooxygenase and is found to display high selectivity for methane oxidation to methanol.

1.7.2.3 Multicomponent Systems for Synergistic Catalysis

In the scenario of site isolation, we emphasize the predominant component contributing the most to lowering activation barrier. Typically, this is a single chemical moiety that can be recognized and conceptually separated from the rest of the framework pore. However, this does not mean that the surrounding pore environment has no contribution to accelerating reaction rates. Any change in local electrostatic field, arising from charge redistribution or different solvent compositions, results in the variation of activation energy. This inevitably occurs when taking a catalyst from solution to the confined environment of framework pore. The strategy of site isolation applies when the contribution from the pore environment is trivial. For those catalytic sites where pore environment plays a crucial role or is deliberately designed and functionalized for promoting the reaction in parallel with other catalytic units, we term this strategy site cooperation. Site cooperation addresses the cooperation of catalytic partners different in chemical nature, thus extend beyond the scope of site coupling to encompass a wide variety of elements where each contributes substantially to multicomponent catalysis.

Incorporating multiple actives sites for their cooperation can be achieved when distinct metal centres are mixed into one framework. These catalytic species occupy the symmetrically identical positions due to the same connectivity and geometric parameters they assume, but play diverse chemical roles in catalysis. Such multivariate system is embodied by a series of MOF constructed by up to three different chiral metallosalen struts.[71] The 2-fold interpenetration of the framework

backbone brings metallosalen units into proximity (Figure 1.6, c1) and effects their cooperation in catalysis. It was found that the ternary heterogeneity of Co, Mn, and Cr centres displayed higher activities and enantioselectivities than those of the homogeneous mixtures for a variety of asymmetric sequential alkene epoxidation/epoxide ring-opening reactions. A cooperative mechanism was proposed that Cr(salen) serves as a Lewis acid to activate the epoxide, while the adjacent metal centres of other types enhance the nucleophilicity of the other reaction partner.

Catalytic activity of metal centres can be tuned by the structure type of the framework backbone. When a substrate approaches the metal active site, the neighbouring framework components impose geometric and electrostatic constraints that can modulate the energy of its reaction pathway. This effect becomes prominent when an asymmetric reaction is carried out in two enantiomeric frameworks that are identical except for being the mirror image with respect to each other. Accordingly, the chirality of the local environment of the metal active site is determined by that of the overarching scaffold and displays enantioselectivity in catalysing for instance cyanosilylation of aldehydes by a cerium chiral MOF (Figure 1.6, c2).[72]

A more versatile strategy to tune the chemical environment of metal catalytic centre is to attach functionalities at adjacent positions to the framework scaffold. By modifying a monolayer of MOF with monocarboxylic acids, the local hydrophobicity/hydrophilicity of the neighbouring Fe(terpyridine) active site can be finely tuned (Figure 1.6, c3), thus enabling selective photocatalytic oxidation of tetrahydrofuran.[73] The pristine MOF catalyst produces 2-hydroxy tetrahydrofuran as a byproduct. This is due to incomplete oxidation and the premature release of this by product from the active site without further oxidation into the target product butyrolactone. The functionalization with gluconic acid, a molecule of a high affinity to 2-hydroxy tetrahydrofuran, promotes its retaining in the hydrophilic environment of the metal centre for complete oxidation. In another example, by adopting the strategy of sequential linker installation, each pore of PCN-700 was decorated by a metal centre and an organic moiety which are precisely positioned (Figure 1.6, c4).[74] The organic functional group serve as a modulator that can fine tune the size selectivity of aerobic oxidation of alcohol by discriminating bulky substrates. The tuning of environment around metal site was also demonstrated in MOF-74 (Fe) analogues.[75] By installing nonpolar functional groups near the Fe site (Figure 1.6, c5), a hydrophobic pore environment favours the oxidation of cyclohexane to cyclohexanol against cyclohexanone and an order of magnitude increase in turnover number.

Furthermore, site cooperation can be implemented using solely organic functionalities. The precise spatial arrangement of functional moieties guided by framework scaffold can be used for creating a finely tailored catalytic pocket. A preliminary result shows that mixed functionalities installed in the pores of IRMOF-74-III can mimic the active sites of the enzyme tobacco etch virus endopeptidase.[76] By covalently attaching tripeptides to the organic struts through tandem multi-step post-synthetic modification, a complexity of residual groups coded by amino acid sequences as well as guided by the spatial scaffolding of the framework leads to sequence-specific peptide bond cleavage. This work showed the promise of embedding the principle of enzyme machinery into framework design by appending functional groups on an architectural scaffold to create an enclosed pore replete with chemical functionalities. A multicomponent framework MUF-77 provides a platform to place three functionalities in precise locations to circumvent disorder (Figure 1.6, c6).[77] Prolinyl groups known to be catalytically active toward asymmetric aldol reactions were selected as the catalytic unit, along with two other organic groups playing the role of selectivity modulator. The modulator units, even remote from the active site, have a decisive

impact on the reaction rate and the obtained enantiomeric excess. The modulated spatial environment around the proline catalyst can even override its innate stereochemical preference and discriminate between different reaction channels available to a given substrate.[78]

1.7.3 Functionalities and Pores for Ion and Electron Transport

Moving proton and metal ions across framework pores has been of particular scientific and technological interest. In electrolysis, the collective movement of these ionic species across a membrane, driven by external power, feed the separated half-cell reactions for producing valuable chemicals. On the other hand, ion transport through electrolyte during battery discharge allows the shuttling of electrons along an external circuit, generating electric current on demand. The implementation of solid electrolyte, with framework structures as a promising candidate, eliminates the hazard of housing flammable liquids and provides higher cation transference number (the ratio of the electric current derived from the cation to the total electric current) and mechanical strength. We are not digging into technological specifications, but rather focusing on how pore environments are designed and functionalized to facilitate the transport of Li^+ cation. Our discussion is further briefly extended to electrical conduction in MOFs using similar functionalization strategies.

There are in general two pathways for Li^+ to transport within a framework, either through hopping between sites distributed on the backbone or through pore space in solvated form. In both scenarios, the negative charge should be trapped as much as possible in order to maximize the transference number of Li^+. The immobilized negative charge thus becomes the site of the highest affinity to Li^+ among the whole structure due to Coulombic interaction. Whether the Li^+ is transported in neat or as solvated, these negatively charged sites act as 'toll gates' on the highway of Li^+, slowing down its transport by trapping the temporarily bound Li^+ for longer retention time compared with other non-bounding sites along the trajectory. The binding energy of these sites therefore plays a major role in determining cation mobility of the material. The ideal structure features shallow energy wells in high density such that Li^+ can facilely hop from one site to the other in short distances, leading to enhanced transport kinetics. The large number of negative charges supported by a unit volume of framework structure also means that a higher Li^+ concentration can be achieved, further promoting conductivity. Therefore, site coupling has been widely adopted as the functionalization strategy for making a high density of negatively charged hopping sites of minimal binding affinity to Li^+. Anionic functionalities, serving as the hopping sites are expected to locate close to each other and belong to the same type for the formation of an energy landscape of relatively uniform depths.

One way to anchor negative charge in the pore is to coordinate an anionic ligand onto open metal sites. By taking advantage of the coordinatively unsaturated Mg^{2+} sites in MOF-74, the authors add LiO^iPr in electrolyte solution for its uptake.[79] The alkoxide anions preferentially bind by coordination, pining themselves on the backbone (Figure 1.7a) while leaving the Li^+ cation more free to move along the channels. In another example, the open Zr^{4+} sites were created by dehydration of the zirconium cluster, a building unit of the MOF UiO-66, and reacted with LiO^tBu, consequently occupied by the alkoxide anion (Figure 1.7c).[80] It was suggested that the negative charge is shielded by the bulky aliphatic group, resulting in a weaker interaction with the charge-balancing Li^+ ion. A MOF capable of reversible phase transition from an anionic phase to a neutral one allows for the coordination of a variety of anions (Figure 1.7b). Soaking the MOF MIT-20d in LiCl, LiBr, and $LiBF_4$ solution afforded frameworks with different stationary anion, leading to

tuneable mobility of Li^+ along the framework channel. It was observed that increasing softness of the anion correlated well with increasing Li^+ conductivity.[81]

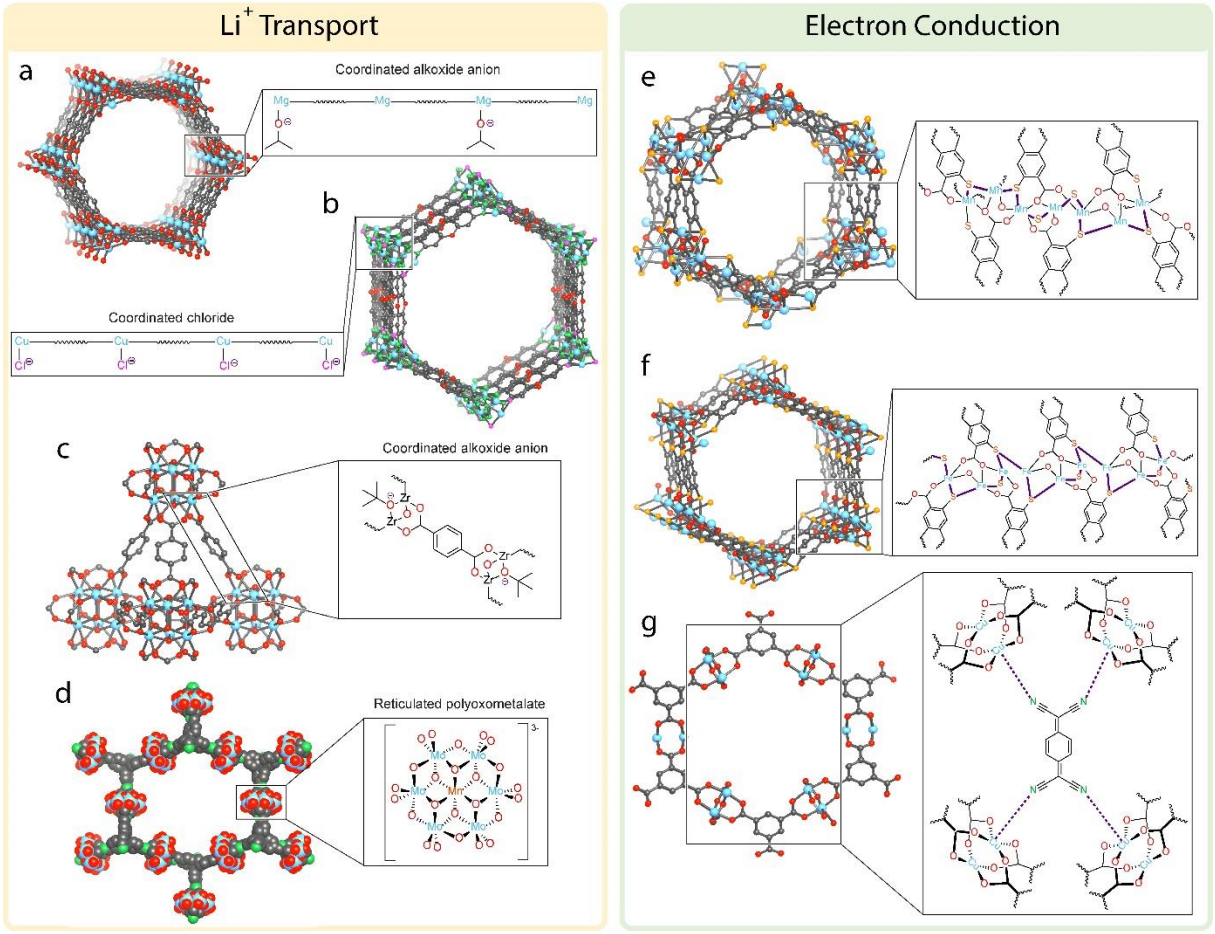


Figure 1.7. Pore functionalization for constructing ion and electron transport pathways. For having Li^+ as the only mobile entity, anions are immobilized by coordination to open metal sites of the Mg (a) and Cu (b) rods, by ligand substituting on Zr clusters (c), or by the direct reticulation of anionic building units (d). To facilitate orbital overlapping, one dimensional Mn-S (e) and Fe-S (f) chains are crafted; framework pore is infiltrated with TCNQ for building a continuous electron transport pathway (g). Color code: metal, blue; C, grey; O, red; N, green; Cl, magenta; S, orange. The framework structure in (d) is illustrated in the space-filling model for clarity. Other structures are illustrated in ball-and-stick model. H atoms are omitted for clarity.

Conversely, anions can serve as a building unit for framework construction, thus integrated directly into the structure and permanently immobilized. This strategy largely removes the risk of losing the anionic ligand, ensuring a high transference number of Li^+ cation. As long as the integrity of the framework structure is retained, the connected anionic unit remains stationary, which otherwise might release from the open metal sites into the electrolyte when the coordination is not strong enough to prevent the exchange with solvent. This was recently achieved by an intrinsically anionic three-dimensional MOF-688 synthesized by connecting ditopic amino functionalized polyoxometalate with organic linkers through imine condensation (Figure 1.7d).[30] The cation

filling the pore can be exchanged with Li^+ and balanced by the anionic framework. The highly charged Anderson type polyoxometalates and their three-fold interpenetration afford a high density of hopping sites distributed among the framework structure. Each negative charge is widely dispersed over the whole polyoxometalate cluster, instead of accumulating at specific atoms, thus exhibiting a low Li^+ binding energy. Indeed, the resulting material displays high ionic conductivity and high Li^+ transference number, making it a competing solid-state electrode, as demonstrated in a prototype lithium metal battery.

For electron conduction, many researchers focus on developing framework backbones as electron transport pathway with high charge mobility. A pre-functionalization strategy turned a previously insulating backbone into a relatively conductive one by replacing the phenol group in the organic linker with the thiophenol group.[82] The resulting Mn_2(DSBDC), a thiolated analogue of MOF-74, features infinite one-dimensional Mn-S chains (Figure 1.7e) and thus display high charge mobility. A further exchange of the Mn^{2+} building unit with Fe^{2+} (Figure 1.7f) resulted in a 6 orders of magnitude higher electrical conductivity, which can be attributed to the loosely bound Fe^{2+} β-spin electrons.[83] In addition, framework scaffolds can template the construction of charge transport pathways using conjugated guest molecules, as exemplified by HKUST-1 infiltrated with tetracyanoquinodimethane (TCNQ).[84] The pores within HKUST-1 were filled with TCNQ molecules anchored to the open Cu^{2+} sites of the backbone (Figure 1.7g). The formation of a charge transfer complex between Cu^{2+} and TCNQ and their extension into a continuous pathway guided by the framework provide a six orders of magnitude enhancement in electrical conductivity.

1.7.4 Pores Functionalized for Fluorescence, Light Harvesting, and Energy Transfer

The functionalized pore environment can be used for manipulating the photophysical behaviour of the incorporated dye, leading to its desired performance in photoluminescence, light harvesting, and energy transfer. The reticulation of fluorescent dyes results in the incorporation of a high concentration of luminophores in solid state, leading to strong light emission. Another advantage of using the ordered framework scaffold is that the distance between dye molecules can be well controlled in order to prevent undesired quenching. The fluorescence of a dye molecule can be tuned by the geometric constraint and electric field imposed by the neighbouring functional groups appended to the framework backbone, and reciprocally be used as the probe to reveal the distribution of local functionalities and structure defects.

Research using artificially engineered porous scaffold to tune the fluorescence response of chromophores was carried out for biomimicry of green fluorescent protein (GFP).[11] A chromophore with a benzylidene imidazolidinone core was attached by covalent bond to the framework backbone (Figure 1.8.1a) and exhibited a similar emission profile of GFP, in contrast to its unlinked, non-emissive counterpart. Spectroscopy studies demonstrated that the conformational restrictions imposed on the trapped chromophores by the rigid framework scaffold, which is reminiscent to the β-barrel structure of GFP, suppresses non-radiative pathways. It was envisioned that further tenability of fluorescence response can be achieved by modulating the pore microenvironment.

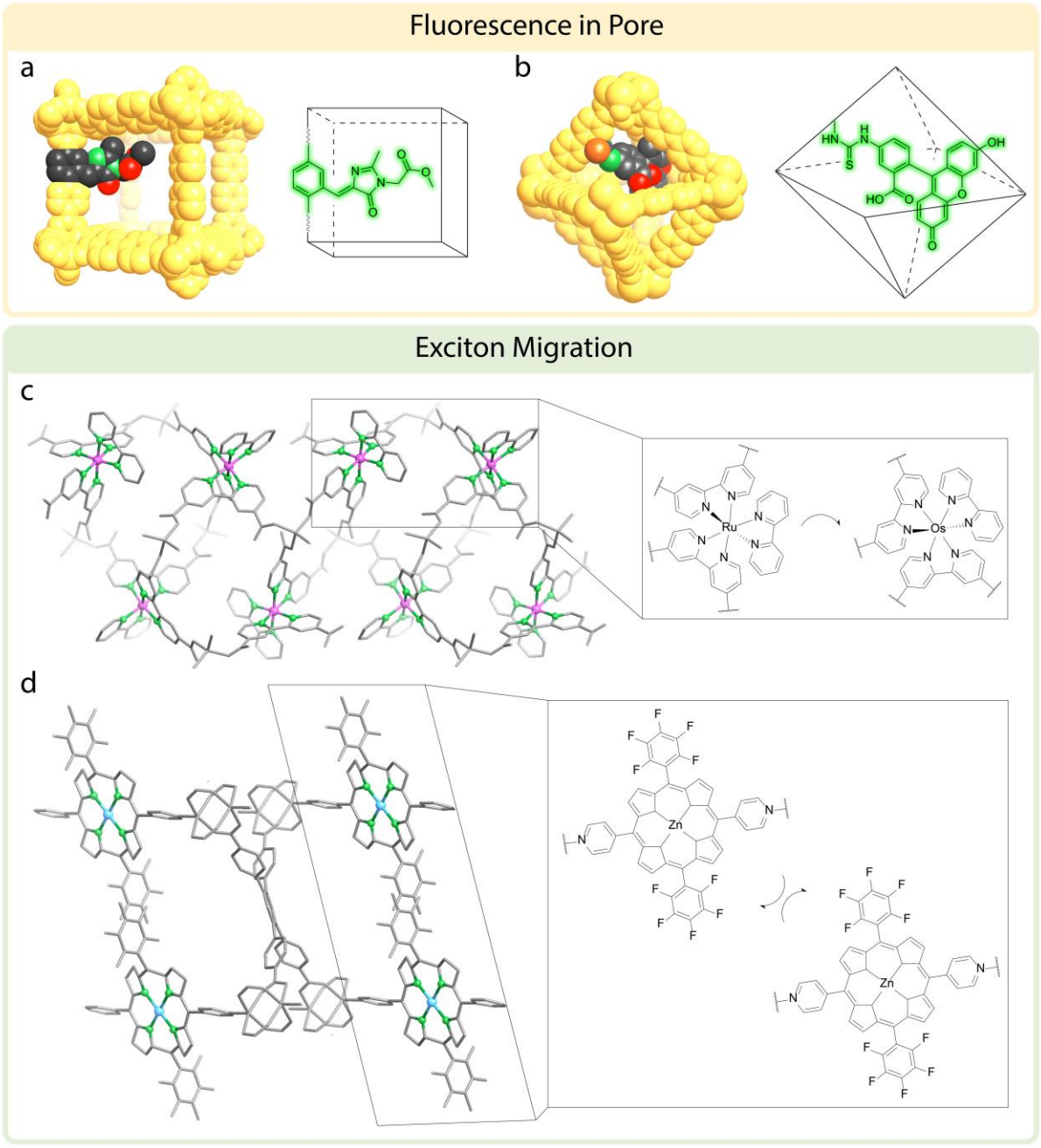


Figure 1.8. Pore functionalization for facilitating fluorescence and energy transfer. (a) A benzylidene imidazolidinone chromophore confined in a cubic pore. (b) Fluorescein confined in a octahedron pore containing a missing edge defect. (c) Triplet-triplet energy transfer between reticulated Ru and Os complexes through the Dexter mechanism. (d) Anisotropic alignment of the reticulated Zn-porphyrin for the Förster energy transfer. Color code: backbone encompassing chromophores, yellow; C, grey; O, red; N, green; S, orange; Ru/Os, magenta; Zn, blue. H atoms are omitted for clarity.

On the other hand, a fluorescent dye can be employed for probing the local chemical environment when its fluorescence profile can be interpreted as physical metrics for gauging the structural features of the host material. For example, fluorescent dye modified linkers were incorporated into the UiO-67 framework (Figure 1.8.1b) and fluorescence lifetime analysis revealed a correlation

between fluorescence quenching and the level of local defects, aspects not detectable with standard bulk characterization techniques.[85] The mapping of the spatial arrangement of defects and multivariate functional groups residing in bulk samples as well as single crystals uncovered chemical diversity present in MOF structures, highlighting the potential of fluorescence based methods in decoding the chemical states of complex porous materials.

An alternative pathway for the dye to be released from the electronic excited state is to relay the energy to neighbouring dye molecules. In fact, this energy transfer process is best practiced in the light harvesting complex. A broad range of solar energy can be harvested by an array of antenna pigment molecules due to their non-overlapping absorption spectra, and shuttled by resonance energy transfer to a reaction centre for photosynthesis. The position, orientation, and distribution of pigment molecules are delicately crafted by nature for maximizing the efficiency of the energy transfer in between. The coordination of hundreds of pigment molecules housed by each antenna complex to one reaction centre ensures that the total kinetics of light harvesting matches with those of the associated photosynthetic reactions, thereby maximizing the efficiency in transforming the energy from light into that stored in chemicals. The prospect of building such systems in artificial materials drives researchers to position chromophores onto framework backbone.[86] The chemical and spatial precision that can be achieved in functionalizing framework pores allow the design of defined energy transfer pathway, connecting light harvesting units with the downstream charge separation centre, charge transfer chains, and finally a reaction centre; altogether integrated into a single framework.

The precise arrangement of donor and acceptor chromophores in MOFs make them an attractive platform for studying long range energy transfer. The Dexter mechanism plays a dominant role in the case of triplet-triplet energy transfer and is used for describing the energy relay in a MOF containing both Ru and Os complex on the organic linker (Figure 1.8.1c).[87] The excited Ru complex exhibit phosphorescence that is not quenched due to energy migration to the Os trapping sites. Luminescence quenching studies of in another work indicated that the excited states of Ru complex rapidly migrate over hundreds of nanometer before reaching the MOF-solution interface with efficiency of a near unity.[88]

When energy transfer is based on dipole-dipole interaction between chromophores and thereby the Förster mechanism becomes spin-allowed for transfer longer distances. This is exemplified by MOFs containing porphyrin-based building units (Figure 1.8.1d). [89] As the constituent porphyrin units occupy the pillar positions of the pillar-layer structure, the intra-layer energy transfer is favoured in accordance with the short distance between porphyrin units in lateral direction. Fluorescence quenching experiments and theoretical calculations indicated that the photogenerated exciton migrates over a net distance of up to 45 porphyrin units. The resulting long distance and anisotropic energy transfer provides insight into the rational design of framework structures for guiding directional energy transfer across pores and reaching artificial photocatalytic active sites.

1.7.5 Functionalization for Tuning Pore Dynamics

One advantage of MOFs is the ability to tune the individual building blocks and interactions between them to endow the parent framework with flexibility and dynamics. Conceptually, the term flexibility has been used to describe the change in pore volume, including expansion/shrinkage or opening/closing, triggered by external stimuli. While pore dynamics in a lot of cases result from the constituent metal sites that has a flexible coordination sphere, their

responsiveness can be modulated through the functionalization of organic linkers. A library of functionalized BDC (fu-BDC) linkers bearing alkoxy side chains of varying chain lengths dangling from different positions of the benzene core were used as the building unit for constructing pillar-layer MOFs $[Zn_2(fu\text{-}BDC)_2(dabco)]_n$ (dabco = 1,4-diazabicyclo[2.2.2]octane).[90] The pristine MOF with unfunctionalized organic linker only exhibited weak dynamic behaviour; however, the pore of the functionalized frameworks experienced a drastic and reversible change from wide to narrow upon the insertion and removal of guest molecules (*N,N'*-dimethylformaldehyde, CO_2, and ethanol, Figure 1.9a). The framework with relatively hydrophobic pore featuring the bulky butoxy substituent showed the highest phase-transition pressure and a prominent hysteresis. In contrast, the framework modified with the short ethoxy substituent displayed a low phase-transition pressure and a relatively small hysteresis. The different dynamic behaviours of pores are attributed to the dangling side chains on the fu-BDC linkers that can interact with each other as well as with incoming guest molecules in the pore. This work provides an approach to rationally tailoring the structural dynamics and responsiveness of MOFs.

Another comprehensive study on the influence of functional groups on pore dynamics has been conducted with MIL-53(Al).[91] Five functionalized BDC linkers (substituted with -Cl, -Br, $-CH_3$, $-NO_2$, and $-(OH)_2$, respectively) were incorporated in the structure of MIL-53(Al). The characterization of these MOF analogues indicated that the modification of pore environment with diverse functional groups results in different dynamic behaviours (Figure 1.9b). The volume of micropore that is H_2O accessible in as-synthesized MIL-53(Al) analogues were measured and the largest value was obtained from MIL-53(Al)-$(OH)_2$ due to its hydrophilic pore environment. When the pores were filled with N_2, the sequence of pore size became largely reversed: MIL-53(Al)-NO_2 > MIL-53(Al)-Cl = MIL-53(Al)-CH_3 > MIL-53(Al)-Br > MIL-53(Al)-$(OH)_2$. The smaller value obtained from MIL-53(Al)-Br compared with those from MIL-53(Al)-Cl and MIL-53(Al)-CH_3 can be attributed to the larger steric hindrance of -Br group, prohibiting the entry and coverage of N_2. The drastic decrease in micropore volume for MIL-53(Al)-$(OH)_2$ is facilitated by the interactions between -(OH) side chains in the pore when hydrophobic guests can no longer compete for hydrogen bonds.

Besides tuning the flexibility of pores by using differently functionalized organic linkers, dynamic behaviours of the same linker can be induced by external physicochemical stimuli. In order to control the pore dynamics of the framework, a photoactive azobenzene-functionalized BDC linker was chosen for constructing PCN-123, a photoresponsive MOF with tunable CO_2 uptake.[92] This linker can switch its configuration from *trans* to *cis* upon light irradiation and reverse under heat (Figure 1.9c). The fresh MOF was made from the linker in *tran* configuration, and adsorbed a significant amount of CO_2. UV irradiation triggered the switch of azobenzene configuration, leading to a decreased uptake of CO_2 in accompany with the shrinkage of pore volume. Such phase transformation can be recovered by incubation at ambient conditions for a period of long time or a gentle heating if necessary. Through the control of linker configuration by physicochemical treatment, the pore structure and environment can be adjusted and regulated, and thus modulate its dynamic behaviour.

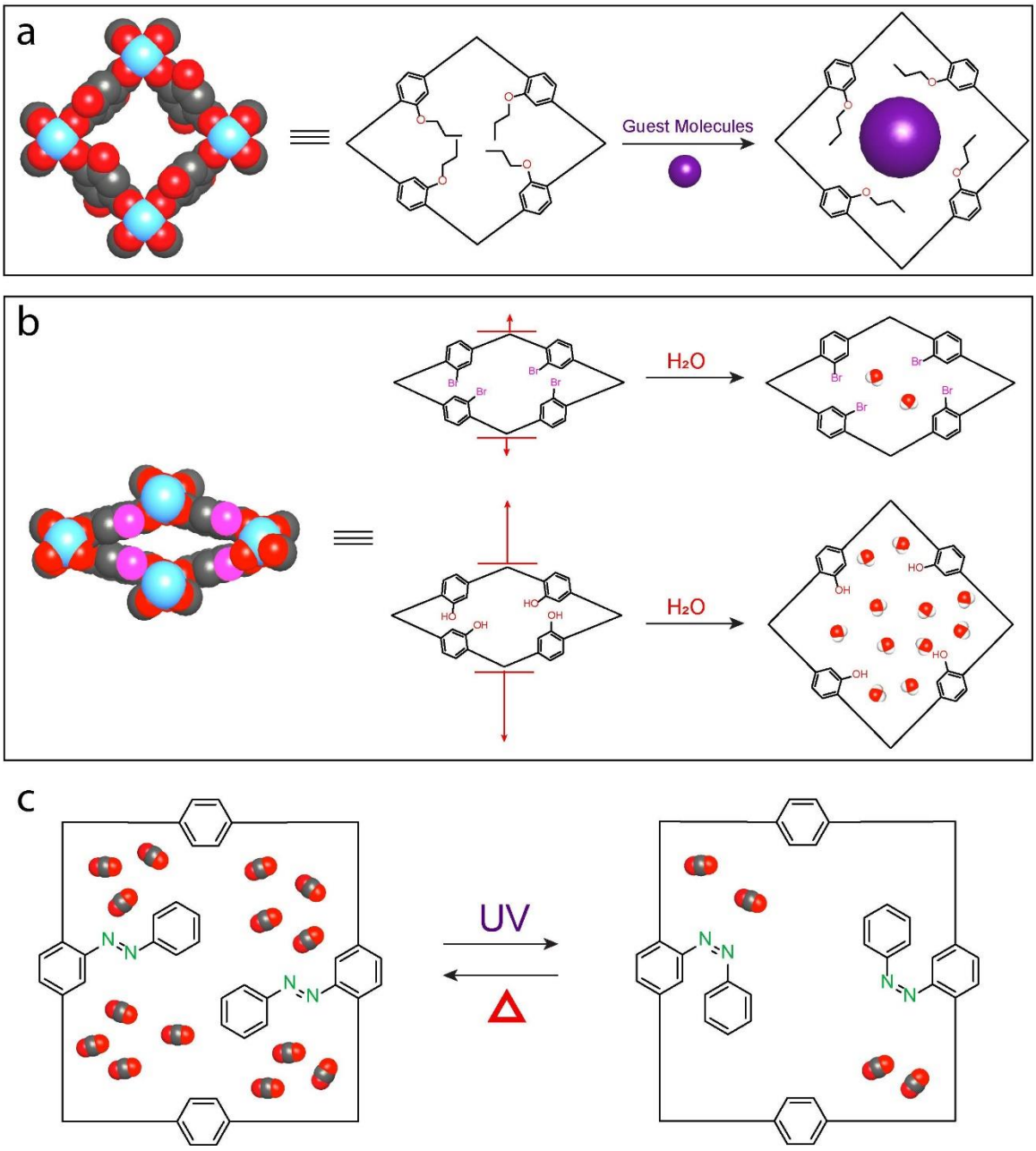


Figure 1.9. Functionalization for tuning pore dynamics. (a) The butoxy groups that can interact with each other and with guest molecules activate the dynamic properties of the pore. (b) Hydroxyl groups effect a larger pore-size increase upon water uptake compared with Br groups. (c) The photoactive azobenzene can switch between cis and trans configurations for modulating the uptake of CO_2. Color code: metal, blue; O, red; C, grey; Br, magenta. H atoms are omitted for clarity except for those in water molecules.

1.7.6 Molecularly Designed Porous Interfaces

The design of pore chemical environment can be used for tuning the chemophysical properties of a foreign material that is interfaced with MOFs. On the surface of the foreign material, the attached framework structures offer a unique interface distinctive from the typical solid-solid or solid-liquid interface, where either the dense structure (*e.g.* metal oxide support) does not permit rich chemical

modification, or mobile solvent molecules are passively oriented for energy minimizing rather than pre-organized for creating specific chemical environments. An architectural scaffold for placing functionalities in the immediate space above the surface atoms of the foreign material allows for a fine tuning of its performances. The interfacial gap between the two components is segregated into domains by protruding moieties that are involved in attachment. Each domain therefore is consisting of half of the pore contributed by the framework structure and closed by the foreign material on the other side. In this section, we examine the functionalization chemistry in the 'half pore' and its role in modulating the behaviour of the interfaced foreign material.

In view of attaching inorganic nanoparticles on the surface of MOFs, activity and selectivity of these heterogeneous catalysts are highly dependent on the chemical environment of the half pore. One of widely used strategy for controlling the catalytic performance of inorganic nanoparticles is to tune the type and ratio of functionalities dangling from the organic linkers used for MOF synthesis. Different functional sites in half pore can provide diverse interactions with interfaced nanoparticles for achieving different catalytic performances. Pt nanoparticles were fully encapsulated in UiO-66 (Pt⊂UiO-66) and its derivatives with functionalized organic linkers (bdc-SO_3H, bdc-SO_3^-, bdc-NH_3^+, and bdc-NH_2) and studied for catalytic methylcyclopentane conversion.[93] The chemical environment around Pt nanoparticles can be systematically controlled by incorporating bdc-SO_3H, bdc-SO_3^-, bdc-NH_3^+, and bdc-NH_2 separately (denoted as UiO-66-S, UiO-66-S*, UiO-66-N, and UiO-66-N*) or together (denoted as UiO-66-SN, UiO-66-S*N, and UiO-66-S*N*) in the framework UiO-66 (Figure 1.10a). Pt⊂UiO-66-S showed the highest selectivity of 62.4% for cyclohexane without generating the undesirable acyclic isomers. This catalytic activity was doubled compared with Pt⊂UiO-66, and the enhancement can be attributed to synergistic interplay between Pt nanoparticles and the sulfonic acid in half pore serving as strong acidic sites. In contrast, Pt⊂UiO-66-N exhibited a low selectivity of 10.6% for cyclohexane while displayed enhanced selectivity for the acyclic isomer to 38.6%. When combining two organic functionalities in Pt⊂UiO-66-SN, no cyclohexane was produced and the main product was benzene with a selectivity of 51.7%.

Another way of improving the selectivity of catalysts is to use open metal sites on the interfaced frameworks to exert intermolecular interactions with substrates for discriminating different reaction pathways. These open metal sites usually act as Lewis acid sites which can activate targeted chemical bonds in substrates and thereby lower the energy barrier of the desired chemical transformation. To illustrate this, Pt nanoparticles were sandwiched between an inner core and an outer shell both made of MIL-101 (Fe^{3+} or Cr^{3+}), and used as the catalyst to convert α,β-unsaturated aldehydes towards unsaturated alcohols with high selectivity and efficiency.[94] Although both the C=O and C=C groups are potential hydrogenation targets, the interaction between the C=O bond and the Fe^{3+} or Cr^{3+} unsaturated metal sites (Figure 1.10b) makes the formation of alcohol products energetically favored. Interestingly, the catalytic activity of Pt nanoparticles interfaced with MIL-101(Fe) was lower than the counterpart interfaced with MIL-101(Cr), while the selectivity was much higher, owing to the interfacial electron-transfer effect. This result shows the possibility to tune the activity and selectivity of catalysts by changing the type of open metal sites inside the half pore.

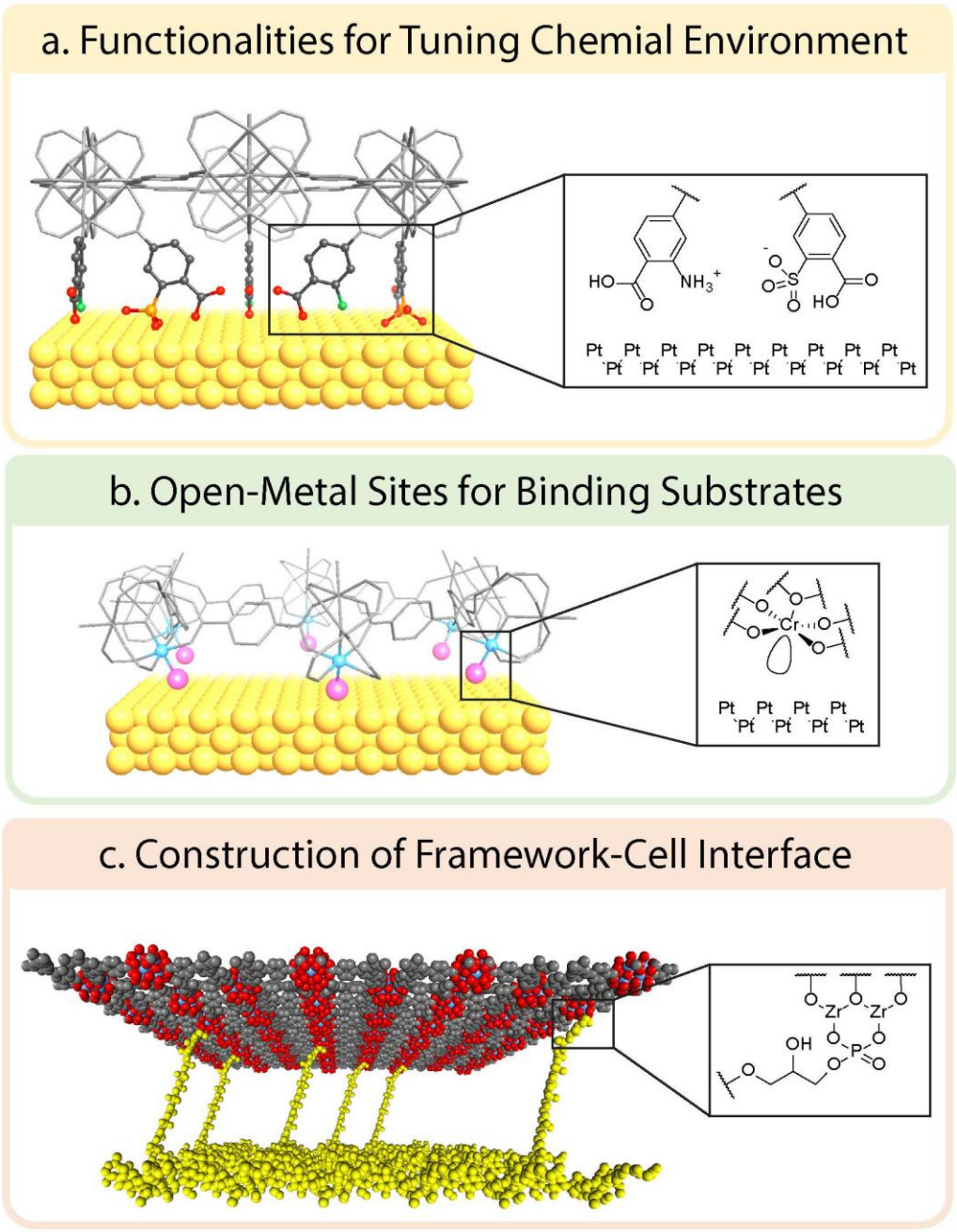


Figure 1.10. The functionalized, porous interface between frameworks and porous materials. (a) Organic functionalities appended on the framework backbone for tuning the environment of catalytic Pt surface. (b) Open metal sites for docking substrates in specific orientations with respect to catalytic Pt surface. (c) The polymeric phosphate units dangling from the bacterial cell wall coordinate to the unsaturated metal sites of Zr clusters on a MOF monolayer.

Constructing an abiotic-biotic interface between framework structures and living cells in addition provides the access to modulating life with artificial materials. When the anaerobic bacteria *Morella thermoacetica* is uniformly wrapped with a MOF monolayer of nanometer thickness, their inherent susceptibility to O_2 and reactive oxygen species that are inevitably generated on anodes during the artificial photosynthesis was overcome.[95] The cytoprotection is endowed by the MOF-

catalyzed decomposition of reactive oxygen species accumulated on the cell surface, with an activity 600 times higher than that of zirconia nanoparticles, thus reducing the death of the strictly anaerobic bacteria by fivefold in air. The artificially enhanced tolerance to O_2 enabled the MOF-wrapped bacteria to continuously produce acetate from CO_2 fixation under oxidative stress. The chemical structure of the MOF-bacteria interface was determined as the coordination of phosphate units dangling from the cell surface to zirconium clusters on the MOF layer (Figure 1.10c). The reversibility of the MOF-bacteria bonding gives rise to the dynamic nature of MOF wrapping, allowing for cell elongation and separation without permanently losing the MOF enclosure.

1.8 Writing and Reading Functionality Sequences in MOF Pores

Recent years have witnessed a gradual shift of research interest from site isolation to site coupling and cooperation for addressing challenges that cannot be solved simply by a single functionality. Technological advancement has been accelerated by using multiple functional groups that can cooperate synergistically where the whole outperforms the sum of its parts. This has been a motivation in the field of reticular chemistry for building frameworks with deliberate control over the position, arrangement, and the chemical identity of functional groups inside the pore. Their efforts in anchoring chemical functionalities onto the backbone with atomic spatial resolution exploit the advantage of framework scaffold on precise positioning. Although significant achievements have been made in site coupling and site cooperation, it is noted that the number of types of functionality participating into their collaborative operation is still limited, typically varying between 2 and 3, not by the intrinsic attributes of frameworks, but by researchers' will. We envision that the future of pore chemistry lies in combining functionalities within the same pore with higher density, higher chemical variety, and higher positioning precision. Ultimately, these functionalities are arranged into specific sequences spreading over the three-dimensional internal surface of the pore. Such functionality sequence can also propagate along multiple pores and form a channel that is made up by an array of heterogeneous chemical environments.

Appending variable functionalities on rigid backbone resembles the way nature stores genetic information in DNA molecules where the sugar-phosphate backbone acts as the scaffold of double helixes, while the unique arrangement of nucleic bases bound covalently to the backbone encodes the sequence of information that can be passed down to daughter molecules through replication and transcription. An artificial pore replete with chemical functionalities is reminiscent of enzyme pocket where the positioning of amino acid residuals is optimized through evolution for decreasing activation barrier (Figure 1.11). It becomes intriguing to find out whether such functionality sequence can be installed, programmed, and evolved in framework pores. Along these lines, developing methodologies to both write and read this chemical information from and onto architecture backbone allows for the ultimate accomplishment in programing materials on demand. As a result, sequences of functionalities decorating the framework backbone can be programed to create unique pore environments, which are addressable by guest molecules, rich in chemical information, and customizable for targeted applications.

Writing sequences. Programing sequence-dependent functions into materials requires the generation of meaningful sequences in frameworks, a field of research that is in its infancy. Preliminary results toward the rational design of multicomponent materials show that a simple change of linker ratio does not necessarily result in a new product. In the structure of MOF-2000, the ratio of the two incorporated linkers remains 2:1 even though this value is varied by an order of magnitude in the starting solution.[96] Advancement in controlling the distribution of functional groups was achieved in multivariate MOF-5, where the choice of combinations of linkers affords

distinct patterns of functional group apportionment.[97] In both cases, however, the distribution of functional groups cannot be controlled at the molecular level, and the obtained patterns of such distribution cannot be tuned independently from the composition of linkers precluding the writing of any arbitrary sequences. The adaptation of solid-state polypeptide synthesis to the construction of metal-organic complex arrays begins to address this challenge by linking constituent metal-containing building blocks in a consecutive way [98]. Alternatively, building units of different types each can be used as the anchoring point for a unique component of the sequence when mixed into a single framework structure.[99] This requires the discovery of multicomponent MOF structures and the number of components determines the length of the sequence that they can constituted. Inspired by how Nature replicate information in DNA, potential solution to the sequence writing challenge may take advantage of a template framework that carries preexisting sequences, which can be copied into the functionality sequence of another framework.

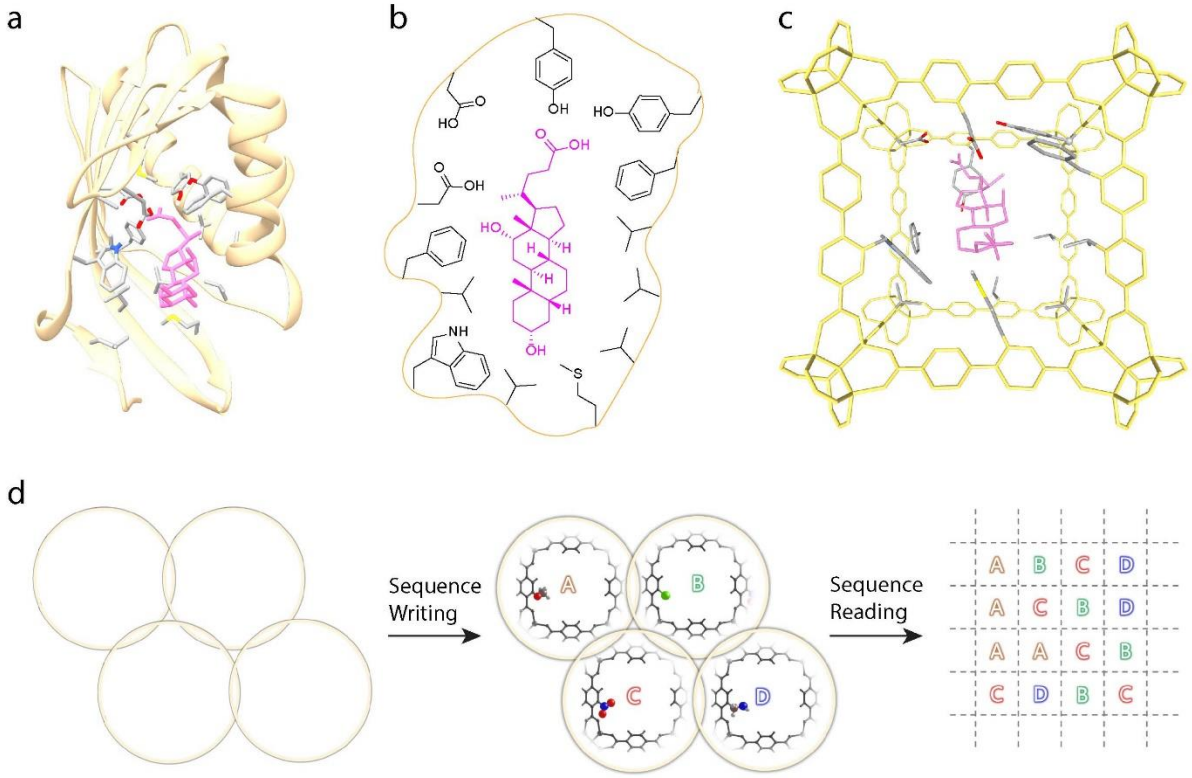


Figure 1.11. Approaching the structural complexity and sophistication of enzymes by functionalized frameworks. (a) The pocket of an enzyme ketosteroid isomerase complexed with a substrate deoxycholic acid (magenta). The polypeptide scaffold is depicted in yellow. Residues involved in substrate interaction are shown. (b) The chemical structure of the substrate and the relevant residues. (c) Functionalities are installed on the backbone of IRMOF-10 (yellow) for accommodating the binding of deoxycholic acid (magenta). Color code for the residues and functionalities: C, grey; O, red; N, blue; S, yellow. (d) Schematic illustration of functionality-sequence writing and reading by using synthetic tools and characterization techniques.

Reading sequences. Unlike the facility in reading DNA sequences enabled by efficient biochemical technologies, the difficulty in the mapping of spatial distribution of functional groups appended on the ordered framework arise from the fact that characterization techniques synthetic

chemists routinely perform rely on the statistical averaging of resonances emanating from the bulk sample. In order to probe the local environment of functional groups, solid-state NMR and molecular dynamic simulation were applied to identify random, alternating, and various cluster forms of the apportionments of organic functional groups.[97] Another work deciphered the arrangement of mixed metals among inorganic building units by measuring X-ray photoelectron spectroscopy [100]. Additionally, fluorescent dyes that can penetrate into the framework and sample along the pore coverage were imaged, and the lifetime analysis revealed the defect distribution and chemical diversity in the crystal.[85] Though these methods show promise, it is noted that the spatial resolution achieved has not been high enough to read the sequence of functionalities at the molecular level. Revolutionary development in finding tools to sequence the channel of frameworks molecule by molecule are highly desired, and we encourage more research efforts in this direction. Both methodological and technological breakthroughs in reading such chemical information with high fidelity will be a revolutionary step towards the sequencing of an increasingly complex pore environment.

1.9 References

1. Yaghi, O. M.; Kalmutzki, M. J.; Diercks, C. S. *Introduction to Reticular Chemistry: Metal-Organic Frameworks and Covalent Organic Frameworks*, Wiley-VCH, Weinheim, **2019**.
2. Furukawa, H.; Cordova, K. E.; O'Keeffe, M.; Yaghi, O. M. *Science* **2013**, *341*, 1230444.
3. Deng, H.; Grunder, S.; Cordova, K. E.; Valente, C.; Furukawa, H.; Hmadeh, M.; Gándara, F.; Whalley, A. C.; Liu, Z.; Asahina, S.; Kazumori, H.; O'Keeffe, M.; Terasaki, O.; Stoddart, J. F.; Yaghi, O. M. *Science* **2012**, *336*, 1018–1023.
4. Sawano, T.; Lin, Z. K.; Boures, D.; An, B.; Wang, C.; Lin, W. *J. Am. Chem. Soc.* **2016**, *138*, 9783–9786.
5. Gramage-Doria, R.; Hessels, J.; Leenders, S. H. A. M.; Troppner, O.; Durr, M.; Ivanovic-Burmazovic, I.; Reek, J. N. H. *Angew. Chem. Int. Ed.* **2014**, 53, 13380–13384.
6. Ueda, Y.; Ito, H.; Fujita, D.; Fujita, M. *J. Am. Chem. Soc.* **2017**, *139*, 6090–6093.
7. Jiang, J. C.; Gandara, F.; Zhang, Y. B.; Na, K.; Yaghi, O. M.; Klemperer, W. G. *J. Am. Chem. Soc.* **2014**, *136*, 12844–12847.
8. Wei, Y. S.; Zhang, M.; Liao, P. Q.; Lin, R. B.; Li, T. Y.; Shao, G.; Zhang, J. P.; Chen, X. M. *Nat. Comm.* **2015**, *6*, 8348.
9. Deng, H.; Doonan, C. J.; Furukawa, H.; Ferreira, R. B.; Towne, J.; Knobler, C. B.; Wang, B.; Yaghi, O. M. *Science* **2010**, *327*, 846–850.
10. Furukawa, H.; Ko, N.; Go, Y. B.; Aratani, N.; Choi, S. B.; Choi, E.; Yazaydin, A. O.; Snurr, R. Q.; O'Keeffe, M.; Kim, J.; Yaghi, O. M. *Science* **2010**, *329*, 424–428.
11. Williams, D. E.; Dolgopolova, E. A.; Pellechia, P. J.; Palukoshka, A.; Wilson, T. J.; Tan, R.; Maier, J. M.; Greytak, A. B.; Smith, M. D.; Krause, J. A.; Shustova, N. B. *J. Am. Chem. Soc.* **2015**, *137*, 2223–2226.
12. Li, H.; Eddaoudi, M.; O'Keeffe, M.; Yaghi, O. M. *Nature* **1999**, *402*, 276–279.
13. Eddaoudi, M.; Kim, J.; Rosi, N.; Vodak, D.; Wachter, J.; O'Keeffe, M.; Yaghi, O. M. *Science* **2002**, *295*, 469–472.
14. Jiang, J.; Zhao, Y.; Yaghi, O. M. *J. Am. Chem. Soc.* **2016**, *138*, 3255–3265.
15. Catarineu, N. R.; Schoedel, A.; Urban, P.; Morla, M. B.; Trickett, C. A.; Yaghi, O. M. *J. Am. Chem. Soc.* **2016**, *138*, 10826–10829.
16. Yaghi, O. M. *Abstr. Pap. Am. Chem. Soc.* **2002**, *223*, A35.
17. Wang, Z. Q.; Cohen, S. M. *Chem. Soc. Rev.* **2009**, *38*, 1315–1329.
18. Cohen, S. M. *J. Am. Chem. Soc.* **2017**, *139*, 2855–2863.
19. Wang, Z. Q.; Cohen, S. M. *J. Am. Chem. Soc.* **2007**, *129*, 12368–12369.
20. Burrows, A. D.; Frost, C. G.; Mahon, M. F.; Richardson, C. *Angew. Chem. Int. Ed.* **2008**, *47*, 8482–8486.
21. Goto, Y.; Sato, H.; Shinkai, S.; Sada, K. *J. Am. Chem. Soc.* **2008**, *130*, 14354–14355.

22. Hwang, Y. K.; Hong, D. Y.; Chang, J. S.; Jhung, S. H.; Seo, Y. K.; Kim, J.; Vimont, A.; Daturi, M.; Serre, C.; Ferey, G. *Angew. Chem. Int. Ed.* **2008**, *47*, 4144–4148.

23. Meilikhov, M.; Yusenko, K.; Fischer, R. A. *J. Am. Chem. Soc.* **2009**, *131*, 9644–9645.

24. Bernt, S.; Guillerm, V.; Serre, C.; Stock, N. *Chem. Comm.* **2011**, *47*, 2838–2840.

25. Deria, P.; Mondloch, J. E.; Karagiaridi, O.; Bury, W.; Hupp, J. T.; Farha, O. K. *Chem. Soc. Rev.* **2014**, *43*, 5896–5912.

26. Brozek, C. K.; Dinca, M. *Chem. Soc. Rev.* **2014**, *43*, 5456–5467.

27. Shearer, G. C.; Vitillo, J. G.; Bordiga, S.; Svelle, S.; Olsbye, U.; Lillerud, K. P. *Chem. Mater.* **2016**, *28*, 7190–7193.

28. Yuan, S.; Lu, W. G.; Chen, Y. P.; Zhang, Q.; Liu, T. F.; Feng, D. W.; Wang, X.; Qin, J. S.; Zhou, H. C. *J. Am. Chem. Soc.* **2015**, *137*, 3177–3180.

29. Akpinar, I.; Drout, R. J.; Islamoglu, T.; Kato, S.; Lyu, J.; Farha, O. K. *ACS Appl. Mater. Interfaces* **2019**, *11*, 6097–6103.

30. Xu, W.; Pei, X.; Diercks, C. S.; Lyu, H.; Ji, Z.; Yaghi, O. M. *J. Am. Chem. Soc.* **2019**, *141*, 17522–17526.

31. Cai, H.; Li, M.; Lin, X.; Chen, W.; Chen, G.; Huang, X.; Li, D. *Angew. Chem. Int. Ed.* **2015**, *54*, 10454–10459.

32. Zhu, K.; O'Keefe, C.; Vukotic, V. N.; Schurko, R. W.; Loeb, S. J. *Nat. Chem.* **2015**, *7*, 514–519.

33. Li, Q.; Sue, C.-H.; Basu, S.; Shveyd, A. K.; Zhang, W.; Barin, G.; Fang, L.; Sarjeant, A. A.; Stoddart, J. F.; Yaghi, O. M. *Angew. Chem. Int. Ed.* **2010**, *49*, 6751–6755.

34. a) Vukotic, V. N.; O'Keefe, C. A.; Zhu, K.; Harris, K. J.; To, C.; Schurko, R. W.; Loeb, S. J. *J. Am. Chem. Soc.* **2015**, *137*, 9643–9651; b) Zhu, K.; Vukotic, V. N.; O'Keefe, C. A.; Schurko, R. W.; Loeb, S. J. *J. Am. Chem. Soc.* **2014**, *136*, 7403–7409.

35. Deng, H.; Olson, M. A.; Stoddart, J. F.; Yaghi, O. M. *Nat. Chem.* **2010**, *2*, 439–443.

36. Fracaroli, A. M.; Furukawa, H.; Suzuki, M.; Dodd, M.; Okajima, S.; Gandara, F.; Reimer, J. A.; Yaghi, O. M. *J. Am. Chem. Soc.* **2014**, *136*, 8863–8866.

37. Faig, R. W.; Popp, T. M. O.; Fracaroli, A. M.; Kapustin, E. A.; Kalmutzki, M. J.; Altamimi, R. M.; Fathieh, F.; Reimer, J. A.; Yaghi, O. M. *J. Am. Chem. Soc.* **2017**, *139*, 12125–12128.

38. a) Akiyama, G.; Matsuda, R.; Sato, H.; Hori, A.; Takata, M.; Kitagawa, S. *Micropor. Mesopor. Mat.* **2012**, *157*, 89–93; b) Ko, N.; Choi, P. G.; Hong, J.; Yeo, M.; Sung, S.; Cordova, K. E.; Park, H. J.; Yang, J. K.; Kim, J. *J. Mater. Chem. A* **2015**, *3*, 2057–2064; c) Khutia, A.; Rammelberg, H. U.; Schmidt, T.; Henninger, S.; Janiak, C. *Chem. Mater.* **2013**, *25*, 790–798.

39. Chen, B.; Ockwig, N. W.; Millward, A. R.; Contreras, D. S.; Yaghi, O. M. *Angew. Chem. Int. Ed.* **2005**, *44*, 4745–4749.

40. Dinca, M.; Long, J. R. *J. Am. Chem. Soc.* **2007**, *129*, 11172–11176.

41. a) Britt, D.; Furukawa, H.; Wang, B.; Glover, T. G.; Yaghi, O. M. *Proc. Natl. Acad. Sci. U. S. A.* **2009**, *106*, 20637–20640; b) Britt, D.; Tranchemontagne, D.; Yaghi, O. M. *Proc. Natl. Acad. Sci. U. S. A.* **2008**, *105*, 11623–11627.

42. Bloch, E. D.; Queen, W. L.; Krishna, R.; Zadrozny, J. M.; Brown, C. M.; Long, J. R. *Science* **2012**, *335*, 1606–1610.

43. Li, L.; Lin, R.; Krishna, R.; Li, H.; Xiang, S.; Wu, H.; Li, J.; Zhou, W.; Chen, B. *Science* **2018**, *362*, 443–446.

44. Li, Q.; Zhang, W.; Miljanic, O.; Sue, C.-H.; Zhao, Y.; Liu, L.; Knobler, C.; Stoddart, J. F.; Yaghi, O. M. *Science* **2009**, *325*, 855–859.

45. McDonald, T. M.; Mason, J. A.; Kong, X.; Bloch, E. D.; Gygi, D.; Dani, A.; Crocella, V.; Giordanino, F.; Odoh, S. O.; Drisdell, W. S.; Vlaisavljevich, B.; Dzubak, A. L.; Poloni, R.; Schnell, S. K.; Planas, N.; Lee, K.; Pascal, T.; Wan, L. F.; Prendergast, D.; Neaton, J. B.; Smit, B.; Kortright, J. B.; Gagliardi, L.; Bordiga, S.; Reimer, J. A.; Long, J. R. *Nature* **2015**, *519*, 303–308.

46. Henke, S.; Fischer, R. A. *J. Am. Chem. Soc.* **2011**, *133*, 2064–2067.

47. Dong, Z.; Sun, Y.; Chu, J.; Zhang, X.; Deng, H. *J. Am. Chem. Soc.* **2017**, *139*, 14209–14216.

48. Yaghi, O. M.; Li, H.; Groy, T. *J. Am. Chem. Soc.* **1996**, *118*, 9096–9101.

49. Chen, B.; Eddaoudi, M.; Reineke, T.; Kampf, J.; O'Keeffe, M.; Yaghi, O. M. *J. Am. Chem. Soc.* **2000**, *122*, 11559–11560.

50. Schlichte, K.; Kratzke, T.; Kaskel, S. *Micropor. Mesopor. Mat.* **2004**, *73*, 81–88.

51. Horike, S.; Dinca, M.; Tamaki, K.; Long, J. R. *J. Am. Chem. Soc.* **2008**, *130*, 5854–5855.

52. Henschel, A.; Gedrich, K.; Kraehnert, R.; Kaskel, S. *Chem. Comm.* **2008**, 4192–4194.

53. Xiao, D.; Bloch, E. D.; Mason, J. A.; Queen, W. L.; Hudson, M. R.; Planas, N.; Borycz, J.; Dzubak, A. L.; Verma, P.; Lee, K.; Bonino, F.; Crocella, V.; Yano, J.; Bordiga, S.; Truhlar, D. G.; Gagliardi, L.; Brown, C. M.; Long, J. R. *Nat. Chem.* **2014**, *6*, 590–595.

54. Mondloch, J. E.; Katz, M. J.; Isley, W. C.; Ghosh, P.; Liao, P. L.; Bury, W.; Wagner, G.; Hall, M. G.; DeCoste, J. B.; Peterson, G. W.; Snurr, R. Q.; Cramer, C. J.; Hupp, J. T.; Farha, O. K. *Nat. Mater.* **2015**, *14*, 512–516.

55. Wang, C.; Xie, Z.; deKrafft, K. E.; Lin, W. *J. Am. Chem. Soc.* **2011**, *133*, 13445–13454.

56. Zhang, T.; Manna, K.; Lin, W. *J. Am. Chem. Soc.* **2016**, *138*, 3241–3249.

57. Wu, C.; Hu, A.; Zhang, L.; Lin, W. *J. Am. Chem. Soc.* **2005**, *127*, 8940–8941.

58. Manna, K.; Zhang, T.; Greene, F. X.; Lin, W. *J. Am. Chem. Soc.* **2015**, *137*, 2665–2673.

59. Feng, D.; Gu, Z.; Li, J.; Jiang, H.; Wei, Z.; Zhou, H. *Angew. Chem. Int. Ed.* **2012**, *51*, 10307–10310.

60. a) Manna, K.; Ji, P.; Lin, Z.; Greene, F. X.; Urban, A.; Thacker, N. C.; Lin, W. *Nat. Comm.* **2016**, *7*, 12610; b) Metzger, E. D.; Brozek, C. K.; Comito, R. J.; Dinca, M. *ACS Cent. Sci.* **2016**, *2*, 148–153.

61. Alkordi, M.; Liu, Y.; Larsen, R. W.; Eubank, J. F.; Eddaoudi, M. *J. Am. Chem. Soc.* **2008**, *130*, 12639–12641.

62. Hasegawa, S.; Horike, S.; Matsuda, R.; Furukawa, S.; Mochizuki, K.; Kinoshita, Y.; Kitagawa, S. *J. Am. Chem. Soc.* **2007**, *129*, 2607–2614.

63. a) Garibay, S. J.; Wang, Z.; Cohen, S. M. *Inorg. Chem.* **2010**, *49*, 8086–8091; b) Ingleson, M. J.; Barrio, J. P.; Bacsa, J.; Dickinson, C.; Park, H.; Rosseinsky, M. J. *Chem. Comm.* **2008**, 1287–1289.

64. a) Banerjee, M.; Das, S.; Yoon, M.; Choi, H. J.; Hyun, M. H.; Park, S. M.; Seo, G.; Kim, K. *J. Am. Chem. Soc.* **2009**, *131*, 7524–7525; b) Lun, D. J.; Waterhouse, G. I. N.; Telfer, S. G. *J. Am. Chem. Soc.* **2011**, *133*, 5806–5809.

65. K. Tanaka, S. Oda, M. Shiro, *Chem. Comm.* **2008**, 820–822.

66. Dong, X.; Liu, T.; Hu, Y.; Liu, X.; Che, C.-M. *Chem. Comm.* **2013**, *49*, 7681–7683.

67. Luan, Y.; Zheng, N.; Qi, Y.; Tang, J.; Wang, G. *Catal. Sci. Technol.* **2014**, *4*, 925–929.

68. Wei, Y.-S.; Zhang, M.; Liao, P.-Q.; Lin, R.-B.; Li, T.-Y.; Shao, G.; Zhang, J.-P.; Chen, X.-M. *Nat. Commun.* **2015**, *6*, 8348.

69. Yu, F.; Poole, D.; Mathew, S.; Yan, N.; Hessels, J.; Orth, N.; Ivanovic-Burmazovic, I.; Reek, J. N. H. *Angew. Chem. Int. Ed.* **2018**, *57*, 11247–11251.

70. Baek, J.; Rungtaweevoranit, B.; Pei, X.; Park, M.; Fakra, S. C.; Liu, Y.; Matheu, R.; Alshmimri, S. A.; Alshehri, S.; Trickett, C. A.; Somorjai, G. A.; Yaghi, O. M. *J. Am. Chem. Soc.* **2018**, *140*, 18208–18216.

71. Xia, Q.; Li, Z.; Tan, C.; Liu, Y.; Gong, W.; Cui, Y. *J. Am. Chem. Soc.* **2017**, *139*, 8259–8266.

72. Dang, D.; Wu, P.; He, C.; Xie, Z.; Duan, C. *J. Am. Chem. Soc.* **2010**, *132*, 14321–14323.

73. Shi, W.; Cao, L.; Zhang, H.; Zhou, X.; An, B.; Lin, Z.; Dai, R.; Li, J.; Wang, C.; Lin, W. *Angew. Chem. Int. Ed.* **2017**, *56*, 9704–9709.

74. Yuan, S.; Chen, Y.; Qin, J.; Lu, W.; Zou, L.; Zhang, Q.; Wang, X.; Sun, X.; Zhou, H. *J. Am. Chem. Soc.* **2016**, *138*, 8912–8919.

75. Xiao, D. J.; Oktawiec, J.; Milner, P. J.; Long, J. R. *J. Am. Chem. Soc.* **2016**, *138*, 14371–14379.

76. Fracaroli, A. M.; Siman, P.; Nagib, D. A.; Suzuki, M.; Furukawa, H.; Toste, F. D.; Yaghi, O. M. *J. Am. Chem. Soc.* **2016**, *138*, 8352–8355.

77. Liu, L.; Zhou, T.; Telfer, S. G. *J. Am. Chem. Soc.* **2017**, *139*, 13936–13943.

78. Zhou, T.; Auer, B.; Lee, S. J.; Telfer, S. G. *J. Am. Chem. Soc.* **2019**, *141*, 1577–1582.

79. Wiers, B. M.; Foo, M. L.; Balsara, N. P.; Long, J. R. *J. Am. Chem. Soc.* **2011**, *133*, 14522–14525.

80. Ameloot, R.; Aubrey, M.; Wiers, B. M.; Gomora-Figueroa, A. P.; Patel, S. N.; Balsara, N. P.; Long, J. R. *Chem.: Eur. J* **2013**, *19*, 5533–5536.

81. Park, S. S.; Tulchinsky, Y.; Dinca, M. *J. Am. Chem. Soc.* **2017**, *139*, 13260–13263.

82. Sun, L.; Miyakai, T.; Seki, S.; Dinca, M. *J. Am. Chem. Soc.* **2013**, *135*, 8185–8188.

83. Sun, L.; Hendon, C. H.; Minier, M. A.; Walsh, A.; Dinca, M. *J. Am. Chem. Soc.* **2015**, *137*, 6164–6167.

84. Talin, A. A.; Centrone, A.; Ford, A. C.; Foster, M. E.; Stavila, V.; Haney, P.; Kinney, R. A.; Szalai, V.; Gabaly, F. El; Yoon, H. P.; Leonard, F.; Allendorf, M. D. *Science* **2014**, *343*, 66–69.

85. Schrimpf, W.; Jiang, J.; Ji, Z.; Hirschle, P.; Lamb, D. C.; Yaghi, O. M.; Wuttke, S. *Nat. Comm.* **2018**, *9*, 1647.

86. Zhang, T.; Lin, W. *Chem. Soc. Rev.* **2014**, *43*, 5982–5993.

87. a) Kent, C. A.; Mehl, B. P.; Ma, L.; Papanikolas, J. M.; Meyer, T. J.; Lin, W. *J. Am. Chem. Soc.* **2010**, *132*, 12767–12769; b) Lin, J.; Hu, X.; Zhang, P.; Van Rynbach, A.; Beratan, D. N.; Kent, C. A.; Mehl, B. P.; Papanikolas, J. M.; Meyer, T. J.; Lin, W.; Skourtis, S. S.; Constantinou, M. *J. Phys. Chem. C* **2013**, *117*, 22250–22259.

88. Kent, C. A.; Liu, D.; Ma, L.; Papanikolas, J. M.; Meyer, T. J.; Lin, W. *J. Am. Chem. Soc.* **2011**, *133*, 12940–12943.

89. Son, H. J.; Jin, S. Y.; Patwardhan, S.; Wezenberg, S. J.; Jeong, N. C.; So, M.; Wilmer, C. E.; Sarjeant, A. A.; Schatz, G. C.; Snurr, R. Q.; Farha, O. K.; Wiederrecht, G. P.; Hupp, J. T. *J. Am. Chem. Soc.* **2013**, *135*, 862–869.

90. Henke, S.; Schneemann, A.; Wutscher, A.; Fischer, R. A. *J. Am. Chem. Soc.* **2012**, *134*, 9464–9474.

91. Biswas, S.; Ahnfeldt, T.; Stock, N. *Inorg. Chem.* **2011**, *50*, 9518–9526.

92. Park, J.; Yuan, D.; Pham, K. T.; Li, J. R.; Yakovenko, A.; Zhou, H. *J. Am. Chem. Soc.* **2012**, *134*, 99–102.

93. Choi, K. M.; Na, K.; Somorjai, G. A.; Yaghi, O. M. *J. Am. Chem. Soc.* **2015**, *137*, 7810–7816.

94. Zhao, M.; Yuan, K.; Wang, Y.; Li, G.; Guo, J.; Gu, L.; Hu, W.; Zhao, H.; Tang, Z. *Nature* **2016**, *539*, 76–80.

95. Ji, Z.; Zhang, H.; Liu, H.; Yaghi, O. M.; Yang, P. *Proc. Natl. Acad. Sci. U. S. A.* **2018**, *115*, 10582–10587.

96. Sue, A. C.-H.; Mannige, R. V.; Deng, H.; Cao, D.; Wang, C.; Gandara, F.; Stoddart, J. F.; Whitelam, S.; Yaghi, O. M. *Proc. Natl. Acad. Sci. U. S. A.* **2015**, *112*, 5591–5596.

97. Kong, X.; Deng, H.; Yan, F.; Kim, J.; Swisher, J. A.; Smit, B.; Yaghi, O. M.; Reimer, J. A. *Science* **2013**, *341*, 882–885.

98. Sukul, P. K.; Bose, P.; Takei, T.; Yaghi, O. M.; He, Y.; Lee, M.; Tashiro, K. *Chem. Comm.* **2016**, *52*, 1579–1581.

99. Tu, B.; Pang, Q.; Ning, E.; Yan, W.; Qi, Y.; Wu, D.; Li, Q. *J. Am. Chem. Soc.* **2015**, *137*, 13456–13459.

100. Liu, Q.; Cong, H.; Deng, H. *J. Am. Chem. Soc.* **2016**, *138*, 13822–13825.

Chapter 2. Docking of Cu(I) and Ag(I) in Metal-Organic Frameworks for Adsorption and Separation of Xenon

Portions of this chapter have been published in:
Wang, H.; Shi, Z.; Yang, J.; Sun, T.; Rungtaweevoranit, B.; Lyu, H.; Zhang, Y.-B.; Yaghi, O. M. *Angew. Chem. Int. Ed.* **2021**, *60*, 3417–3421.

2.1 Introduction

Embedding external metal ions into metal-organic frameworks (MOFs)[1] allows access to functional MOFs with enhanced and new properties.[2] Typically, this has been done by anchoring external metal ions on (i) secondary building units (SBUs)[3] or (ii) organic struts.[4] The latter requires the use of organic struts that bear auxiliary chelating groups such as bipyridyl (Figure 2.1a),[5] or post-synthetic functionalization of organic struts to introduce chelating sites (Figure 2.1b).[6] More recently, a molecular vise approach has been demonstrated by partially replacing tetratopic linkers with tritopic linkers to create "defective" binding sites (Figure 2.1c).[7] Herein, we present a new metalation strategy that utilizes the precise spatial arrangement of organic struts in a MOF to create metal chelating sites (Figure 2.1d), in a manner reminiscent of metalloenzymes having defined spatial arrangement of multiple binding functionalities.[8] We show that in MOF-303 [$Al(OH)(C_5H_2O_4N_2)$][9] constructed from Al^{3+} and 1*H*-pyrazole-3,5-dicarboxylate (PZDC) linkers, the adjacent pair of uncoordinated N-atoms of the pyrazole dicarboxylates along the rod-shaped Al–O SBUs could be used to precisely chelate additional Cu(I) and Ag(I) to yield the metalated Cu- and Ag-MOF-303 compounds [$(CuCl)_{0.50}$-$Al(OH)(C_5H_2O_4N_2)$ and $(AgNO_3)_{0.49}$-$Al(OH)(C_5H_2O_4N_2)$] with near complete incorporation efficiency (Figure 2.1e). We reveal their coordination geometry through 3D electron diffraction[10] and extended X-ray absorption fine structure spectroscopy.

The metalated MOFs remain porous, and show reduced pore sizes of 5.5 Å for Cu-MOF-303 and 5.2 Å for Ag-MOF-303, respectively, compared to that of the pristine MOF-303 (8.7 Å). We further show that these two MOFs exhibited high capacity and selectivity for Xe separation. Specifically, Ag-MOF-303 showed a high Xe uptake of 59 $cm^3\ cm^{-3}$ at 298 K and 0.2 bar with a selectivity of 10.4, which are 2.1 and 1.6 times as high as those of pure MOF-303 (28 $cm^3\ cm^{-3}$ and 6.6), respectively, and ranks among the highest MOFs (record performance of 74 $cm^3\ cm^{-3}$ and 16.7 for NJU-Bai7). Furthermore, we show up to 100% improvement of the dynamic separation performance in comparison with that of the pristine MOF-303 for the efficient, steady, and recyclable separation of Xe from Kr.

2.2 Results and Discussion

2.2.1 Preparation and Characterization of Metalated MOF-303

MOF-303 was synthesized from an aqueous solution of $AlCl_3 \cdot 6H_2O$ and PZDC at 100 °C according to an adapted literature procedure (Section S1 in SI).[9] Its phase purity and crystallinity were confirmed by powder X-ray diffraction (PXRD) (Figures S2.27). Metalation of MOF-303 with Cu(I) or Ag(I) was accomplished by immersing the pristine crystals in hot acetonitrile solutions (70 °C) of CuCl or $AgNO_3$ for 2 days (Section S2.4.1 in S2.4). Combined PXRD (Figures S2.28–32) and scanning electron microscopy (SEM) (Figures S2.15–16) of these samples revealed retention of crystallinity after metalation, where the scanning electron micrographs indicated a homogenous single crystal morphology.

Metal loading in Cu- and Ag-MOF-303 was determined by inductively coupled plasma−optical emission spectrometry (ICP-OES) and their chemical formulae were evaluated by elemental analysis to be $(CuCl)_{0.50}$-$Al(OH)(C_5H_2O_4N_2)$ and $(AgNO_3)_{0.49}$-$Al(OH)(C_5H_2O_4N_2)$ for Cu- and Ag-MOF-303, respectively (Section S2.4.1 in S2.4). Energy dispersive spectroscopy (EDS) revealed uniform distribution of Cu and Ag ions throughout the MOF crystals (Figures S2.15–16).

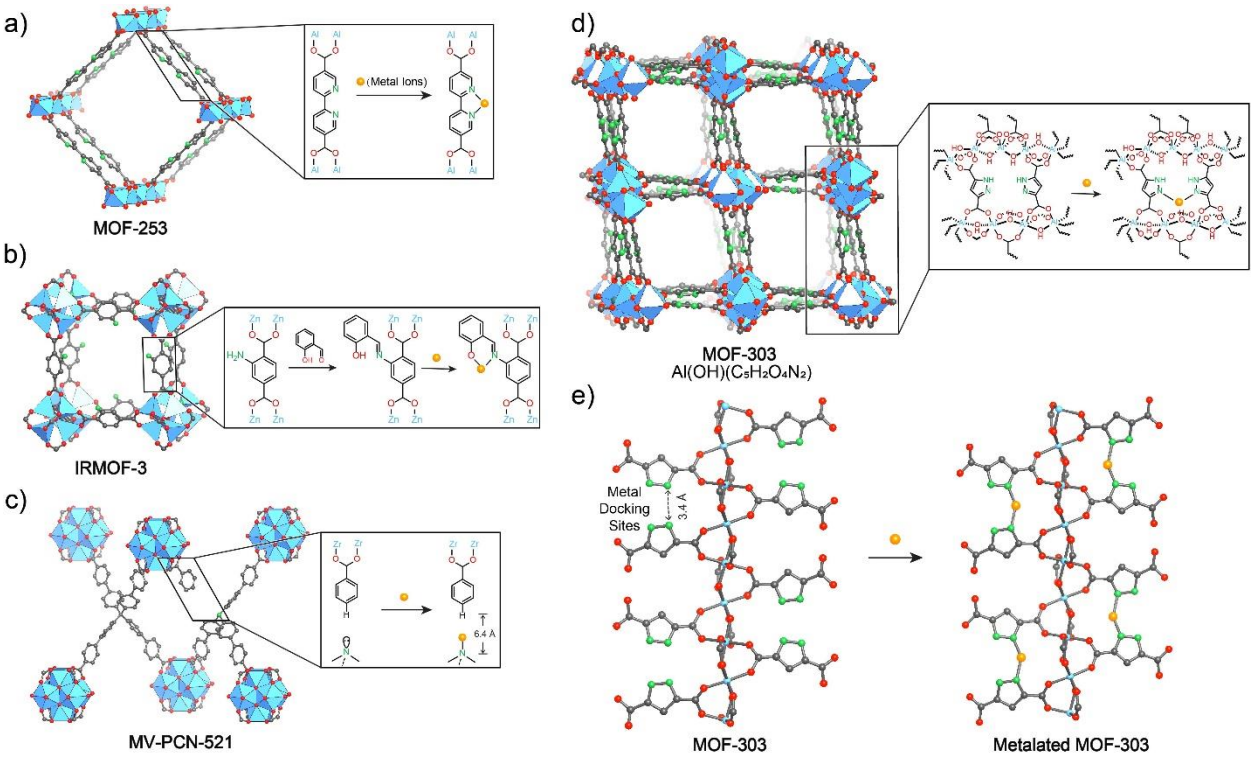


Figure 2.1. a) Metalation of MOFs on organic struts bearing auxiliary chelating groups, exemplified by introducing additional metal ions to MOF-253 structures. b) Metalation of MOFs on organic struts with post-synthetically introduced chelating sites, illustrated by adding metals to IRMOF-3. c) Metal binding sites generated by the molecular vise approach in MV-PCN-521. d) A new metalation strategy of MOFs by using spatial arrangement of organic struts as novel metal chelating sites in the MOF matrix, illustrated by adding additional metals in MOF-303. e) Metal docking sites created by pairs of uncoordinated N-atoms on adjacent pyrazole dicarboxylate linkers distributed along the rod-shaped one-dimensional Al–O SBUs in MOF-303. Color code: C, gray; O, red; N, green; Zr, Zn, Al, blue; potential additional metal ions, yellow. H atoms are omitted for clarity.

Structures of the pristine and Cu(I) and Ag(I) metalated MOF-303 were determined by 3D electron diffraction tomography (EDT) (Figures 2.2d–2.2f and S2.17–22).[11] MOF-303, Cu-, and Ag-MOF-303 crystallized in the monoclinic $P2_1/c$ space group with unit cell parameters of a = 12.3 Å, b = 15.4 Å, c = 14.3 Å, $\alpha = \gamma = 90°$, $\beta = 101.5°$, V = 2654.3 $Å^3$; a = 12.7 Å, b = 15.0 Å, c = 14.3 Å, $\beta = 102.0°$, V = 2664.6 $Å^3$; and a = 12.7 Å, b = 15.5 Å, c = 14.2 Å, $\beta = 101.7°$, V = 2737.2 $Å^3$, respectively (Tables S2.1–3). In MOF-303, the octahedrally coordinated Al(III) are bound by four bridging carboxyl groups and two bridging hydroxyl groups to form corner-sharing −Al−O−Al− SBUs. These SBUs are connected by PZDC linkers to give a 3D framework with rhombic channels orientated along the a-axis (Figure 2.1d). The pyrazole rings of two adjacent linkers adopt an edge-to-edge arrangement with N–N distances of 3.4 Å (Figures 2.1e and 2.2b), rendering MOF-303 a unique platform to bind additional metal ions. This was confirmed by the crystal structures of Cu- and Ag-MOF-303, in which we observed the chelation of both metal ions by the N atoms of adjacent PZDC linkers. In Cu-MOF-303, the additional Cu(I) were coordinated by two adjacent PZDC linkers with Cu−N bond lengths of 1.9 Å and 2.1 Å, respectively, resulting in the N–N distances of 3.6 Å (Figure 2.2a).

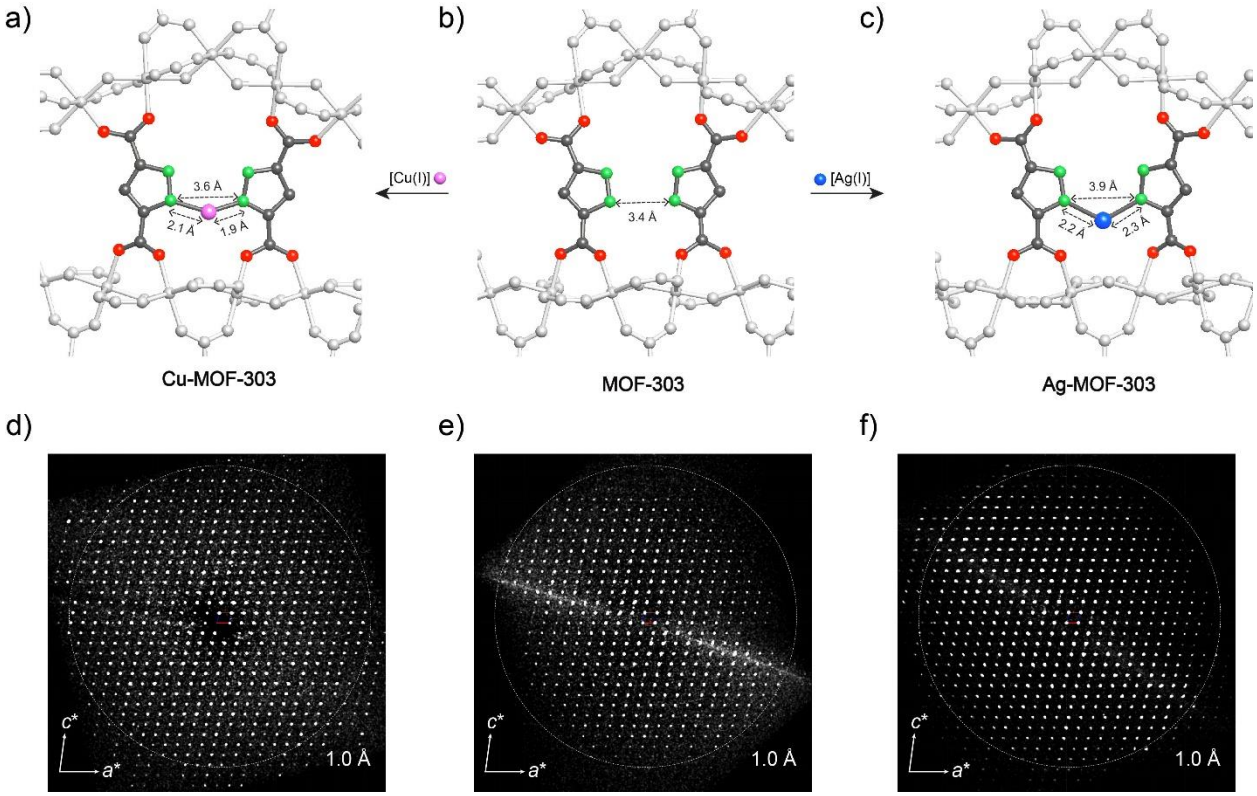


Figure 2.2. a) Cu-MOF-303 structure as determined from 3D EDT with Cu(I) ions chelated by N-atoms from two adjacent PZDC linkers. b) MOF-303 structure as determined from 3D EDT with pyrazole-based metal docking sites between adjacent PZDC linkers. c) Ag-MOF-303 structure as determined from 3D EDT with Ag(I) ions chelated by N-atoms from two adjacent PZDC linkers. d) The projection of the reconstructed three-dimensional reciprocal lattice of Cu-MOF-303 along the [010] direction. e) The projection of the reconstructed three-dimensional reciprocal lattice of MOF-303 along the [010] direction. f) The projection of the reconstructed three-dimensional reciprocal lattice of Ag-MOF-303 along the [010] direction. Circles represent the resolution of 1.0 Å. Color code: C, gray; O, red; N, green; Al, blue; Cu, pink; Ag, dark blue. H atoms are omitted for clarity.

The valence of the Cu center and its local coordination sphere were confirmed by the X-ray absorption near edge structure (XANES) and extended X-ray absorption fine structure (EXAFS) spectroscopies, respectively (Section S2.4.5 in SI). An absorption peak at 8984 eV corresponding to the Cu(I) 1s $\rightarrow$ 4p + L shakedown transition was observed in the pre-edge region of XANES.[12] A CuN_2Cl core structure was assigned to fit the EXAFS spectrum, which indicated Cu−N and Cu−Cl bond lengths of 1.92 and 2.14 Å, respectively, and is in accordance with the literature.[13] For Ag-MOF-303, we also obtained high-resolution EDT data that showed Ag(I) ions chelated by two N atoms from adjacent PZDC linkers with Ag−N bond distances of 2.2 and 2.3 Å, respectively (Figure 2.2c). Compared to the pristine MOF-303, the retained structural symmetry and slightly changed lattice constants of Cu- and Ag-MOF-303 indicated the modularity of MOF-303 as a robust platform for docking additional metal ions.

Porosity of MOF-303, Cu-, and Ag-MOF-303 was examined by their N_2 and Ar sorption isotherms. The Brunauer-Emmett-Teller (BET) surface area and pore diameter were measured to be of 1343, 860, and 716 $m^2\ g^{-1}$ (Figures S2.8–14); 8.7, 5.5 and 5.2 Å, respectively (Figures S2.4–7). Reduced

porosity in metalated Cu- and Ag-MOF-303 arises from the increase of their molecular weights and reduced pore sizes.

2.2.2 Adsorption and Separation of Xe from Xe/Kr Mixture of MOF-303 and Metalated MOF-303

To investigate the impact of metalation in MOF-303, we explored their use for Xe/Kr separation. Xe/Kr separation is an industrially important yet energy intensive process.[14] In this context, adsorptive separation by porous zeolites and MOFs[15] is a promising direction compared to traditional cryogenic distillation. Given the larger polarizability of Xe (40.4×10^{25} cm^{-3}) compared to Kr (24.8×10^{25} cm^{-3}),[16] the introduction of polar functional groups (-OH, -NH_2, -F, -Cl, -Br, and -I),[17] anions (CrO_4^{2-}, ZrF_6^{2-}, and $NbOF_5^{2-}$),[18] and metal sites (Co, Ni, Ag, etc)[19] to polarize Xe for enhanced framework–Xe interactions represents an effective strategy to improve uptake and selectivity of Xe.

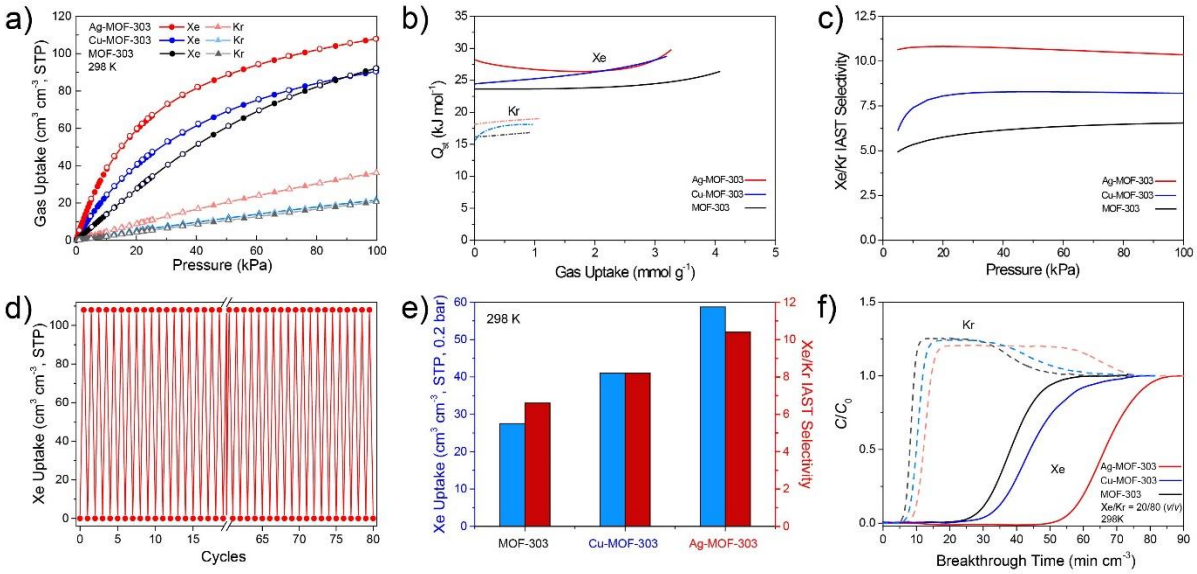


Figure 2.3. a) Xe and Kr sorption isotherms for MOF-303, Cu-, and Ag-MOF-303 measured at 298 K. Filled and open circles represent adsorption and desorption data, respectively. b) Isosteric heat of adsorption (Qst) for Xe/Kr of MOF-303, Cu-, and Ag-MOF-303. c) Calculated IAST selectivity at 298 K for a 20/80 Xe/Kr mixture in MOF-303, Cu-, and Ag-MOF-303 to be 6.6, 8.2, and 10.4, respectively. d) Xe adsorption-desorption cycling data represented with volumetric uptake for Ag-MOF-303 measured at 298 K. Adsorption-desorption cycling measurements were conducted without additional activation of Ag-MOF-303, between the cycles the sample was regenerated by evacuation at 298 K, demonstrating mild regeneration conditions and cyclic stability of 80 Xe adsorption cycles. e) Comparison of Xe separation performance between MOF-303, Cu-, and Ag-MOF-303. Metalation of MOFs showed significant improvement in Xe uptake capacity and Xe/Kr selectivity. f) Experimental breakthrough curves for a binary Xe/Kr mixture [20/80 (v/v)] at 298 K and 1.1 bar showing the separation performance of MOF-303, Cu-, and Ag-MOF-303. STP: standard temperature and pressure. Solid and dashed lines refer to Xe and Kr, respectively.

We first measured the low-pressure (0–100 kPa) Xe and Kr adsorption isotherms of MOF-303, Cu-, and Ag-MOF-303 at 273, 283, and 298 K, respectively (Figures 2.3a and S2.39–41). Compared to the pristine MOF-303, the Xe uptake capacity at 298 K and 0.2 bar of the Cu- and Ag-MOF-303 were increased from 28 cm^3 cm^{-3} to 41 cm^3 cm^{-3} and 59 cm^3 cm^{-3}, respectively

(Figure 2.3e). The Xe/Kr (*v*/*v* = 20/80) selectivity based on the ideal adsorbed solution theory (IAST) was improved from 6.6 to 8.2 and 10.4, respectively (Figures 2.3c and 2.3e). This significant performance improvement in Cu- and Ag-loaded MOF-303 compared to pristine MOF-303 emphasized the importance of metalation. Such high uptake remains consistent throughout 80 cycles of adsorption-desorption experiments (Figure 2.3d) and ranks among the highest measured for MOFs (record performance of 74 cm^3 cm^{-3} and 16.7 for NJU-Bai7) (Table S2.5).

The significant improvements in Cu- and Ag-MOF-303 were attributed to the enhanced framework–Xe interactions due to metalation. To probe these interactions, we measured the ^{129}Xe NMR spectra under isobaric Xe pressures at 293 K in MOF-303, Cu-, and Ag-MOF-303 (Figure S2.49). The chemical shifts of ^{129}Xe of MOF-303, Cu-, and Ag-MOF-303 appeared at 93.68, 103.53, and 105.50 ppm, respectively. This trend in downfield shifts indicates greater electron de-shielding effects in metalated MOF-303, and thus suggested stronger framework–Xe interactions. This result is also in line with the calculated Q_{st} for the three compounds (23.7, 24.4, and 28.2 kJ mol^{-1}, respectively, Figure 2.3b). The broader linewidths (full width at half maximum, FWHM) of Cu-MOF-303 (11.60 ppm) and Ag-MOF-303 (11.89 ppm) can be attributed to the more heterogeneous pore environments in comparison with pristine MOF-303 (5.79 ppm).

To examine the practical performance of metalated MOFs for extracting Xe from Xe/Kr mixtures, we conducted fixed-bed breakthrough experiments with a representative inlet gas mixture [Xe/Kr = 20/80 (v/v)]. A 540 mg sample of Ag-MOF-303 was packed in a column through which the Xe/Kr mixture passed through (Scheme S2.1). As shown in Figure 2.3f, the Ag-MOF-303 bed held at capacities of Xe of 3000 s cm^{-3} and capacities of Kr of 600 s cm^{-3}. The large difference in the breakthrough time between Xe and Kr confirmed the performance of Ag-MOF-303 in Xe/Kr separations. In comparison with the pristine MOF-303, Cu- and Ag-MOF-303 exhibited greatly enhanced separation performance for Xe/Kr, with an improved retention time for Xe by 100% in Ag-MOF-303. The metalated MOF-303 could easily be regenerated by purging an inert Ar flow, after which the dynamic adsorption capacity remained unchanged throughout the measurements (65 cycles) (Figure S2.48).

2.3 Conclusion

In summary, we presented a unique metal docking strategy in MOFs that makes use of the precise spatial arrangement of organic linkers distributed along a rod-shaped SBU as metal chelating sites. This approach uses simple organic linkers, does not require the installation of additional binding sites, and gives access to metalated MOF-303 with high Xe capacity and separation performance.

2.4 Supporting Information

2.4.1 Synthesis and Characterization of Materials

Chemicals. Aluminum chloride hexahydrate ($AlCl_3 \cdot 6H_2O$), 1*H*-pyrazole-3,5-dicarboxylic acid, sodium hydroxide and all solvents, unless otherwise specified, were purchased from Sigma-Aldrich and used as received.

Analytical techniques and instruments. Powder X-ray diffraction (PXRD) patterns were recorded using a Bruker D8 Advance diffractometer (λ = 1.54 Å, Cu Kα). Inductively coupled plasma−optical emission spectrometry (ICP-OES) experiments were carried out on a Perkin Elmer Optima 7000 Spectrometer. Elemental microanalyses (EA) were performed in the Microanalytical Laboratory at the College of Chemistry, UC Berkeley using a Perkin Elmer 2400 Series II CHNS elemental analyzer. Thermogravimetric analysis (TGA) curves were recorded on a TA Q500 thermal analysis system under nitrogen flow at 40 mL min^{-1}, ramping at 5 ˚C per minute from room temperature to 800 ˚C. Scanning electron microscopy (SEM) images were recorded on a FEI Quanta 3D FEG scanning electron microscope with an accelerating voltage of 10 kV and a working distance of 10.8 mm. Energy-dispersive X-ray spectroscopy (EDS) data were collected using an Oxford X-Max EDS system at an acceleration voltage of 10 kV.

Preparation of MOF-303: 3,5-pyrazoledicarboxylic acid monohydrate (7.50 g, 43.1 mmol) and NaOH (2.60 g, 65 mmol) were dissolved in deionized water (750 mL). The resulting mixture was sonicated for 10 min and heated for 30 min in a pre-heated oven at 100 °C until the solution was clear. Afterwards, $AlCl_3 \cdot 6H_2O$ (10.4 g, 43.1 mmol) was added to the solution. Any precipitate was dissolved with vigorous shaking. The hot reaction mixture was put in a pre-heated oven at 100 °C, where it was kept for 15 hours. The crystals formed were collected and washed with water three times per day for two days. The white solid was subsequently washed with methanol (anhydrous, Macron Fine Chemicals) for two days, three times per day and dried in air. Further, the product was activated under dynamic vacuum at room temperature for 6 hours until the pressure was below 100 mbar. After that, the MOF sample was heated at 100 ºC for 6 hours, and then at 150 ºC for another 6 hours to yield activated MOF-303 crystals (3.6 g).

Preparation of Cu-MOF-303: A 20 mL vial was loaded with MOF-303 (110 mg, 55.6 mmol), CuCl (55 mg, 55.6 mmol), and 11 mL of CH_3CN in the glovebox under Ar. The reaction was heated at 70 ºC for 48 hours, yielding yellow crystals at the bottom of the vial. The metalated material was washed with 10 mL of fresh CH_3CN for 3 times. The resulting Cu-MOF-303 was activated under dynamic vacuum at room temperature for 4 hours, and then at 120 ºC for 12 hours. Elemental analysis calcd. (%) for $C_5H_3O_5N_2AlCu_{0.5}Cl_{0.5}$: C 24.26, H 1.22, N 11.32; found: C 24.23, H 1.21, N 11.35. ICP-OES calcd. (mol mol^{-1}) for $C_5H_3O_5N_2AlCu_{0.5}Cl_{0.5}$: Al : Cu = 1 : 0.5; found: Al : Cu = 1 : 0.5.

Preparation of Ag-MOF-303: A 20 mL vial was loaded with MOF-303 (120 mg, 60.6 mmol), $AgNO_3$ (112 mg, 65.9 mmol), and 6 mL of CH_3CN in the glovebox. The reaction was heated at 70 ºC for 48 hours, yielding white solids at the bottom of the vial. The product was isolated by filtration and washed with 10 mL of fresh CH_3CN for 3 times. The resulting Ag-MOF-303 was activated under dynamic vacuum at room temperature for 2 hours, and then at 120 ºC for 12 hours. Elemental analysis: calcd. (%) for $C_5H_3O_{6.47}N_{2.49}AlAg_{0.49}$: C 21.35, H 1.07, N 12.40; found: C 21.51, H 1.22, N 12.11. ICP-OES calcd. (mol mol^{-1}) for $C_5H_3O_{6.47}N_{2.49}AlAg_{0.49}$: Al : Ag = 1 : 0.49; found: Al : Ag = 1 : 0.49.

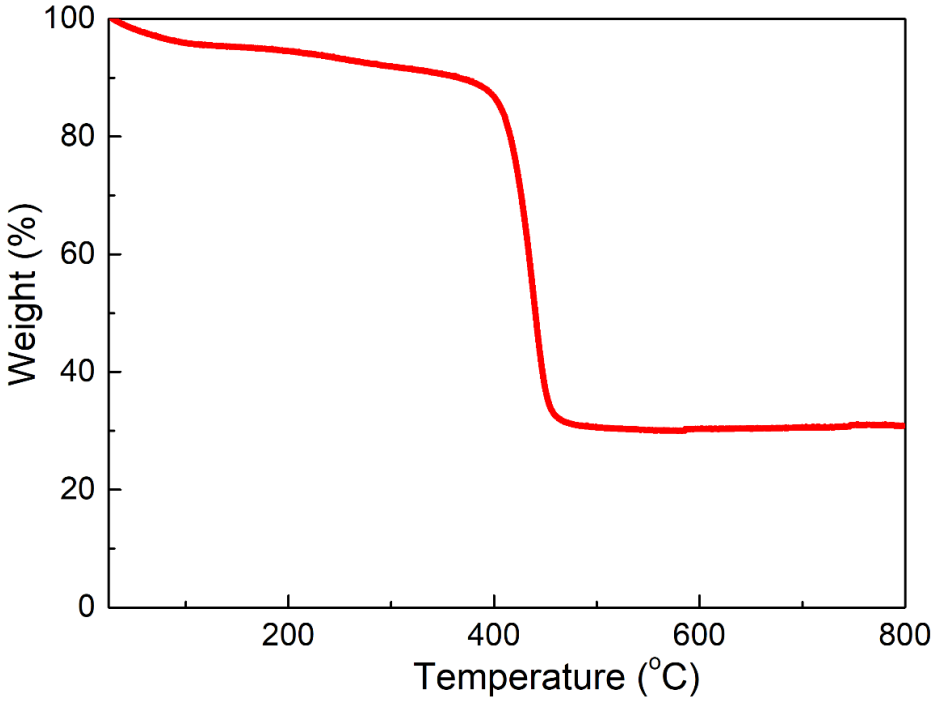


Figure S2.1. TGA trace of Cu-MOF-303. The sample was dried under dynamic vacuum overnight at 120 °C prior to the analysis.

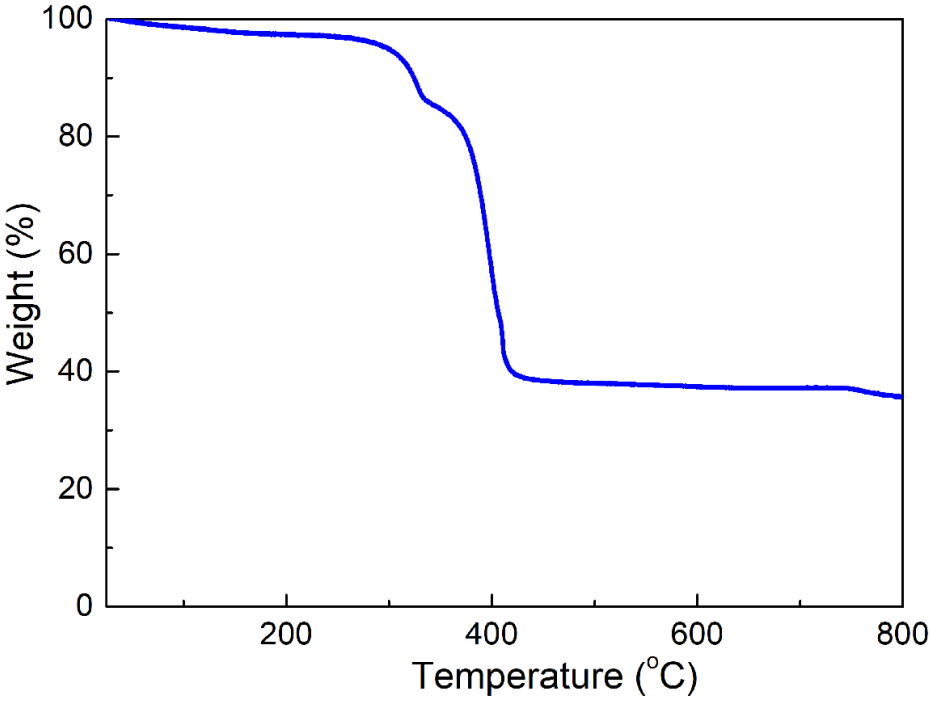


Figure S2.2. TGA trace of Ag-MOF-303. The sample was dried under dynamic vacuum overnight at 120 °C prior to the analysis.

2.4.2 Gas Adsorption Analyses

Gas adsorption measurements of N_2 (77 K), Ar (87 K) and Xe, Kr (atmospheric temperatures) were carried out on a two-port microporosity and specific surface area analyzer (Quantachrome, Autosorb IQ), a three-port Microtrac BELsorp Max or a four-port Microtrac BELsorp Max II gas sorption analyzer. Liquid nitrogen or argon bath was used for the temperatures controlled at 77 K or 87 K, respectively. A dewar connected to a Julabo F12-E0 isothermal bath filled with an ethylene glycol aqueous solution (*v*/*v* = 1:3), for which the temperature error is within ± 0.02 °C, was used to keep the temperature at 273, 283, and 298 K, respectively. Ultrahigh-purity (>99.999%) N_2, Ar, Xe, Kr, and He in compressed gas cylinders were used throughout all experiments. Samples were dried under dynamic vacuum overnight at 120 °C prior to the analyses. MOF-303, Cu-, and Ag-MOF-303 were prepared and measured after fully activated under dynamic vacuum at 120 ºC for 12 hours.

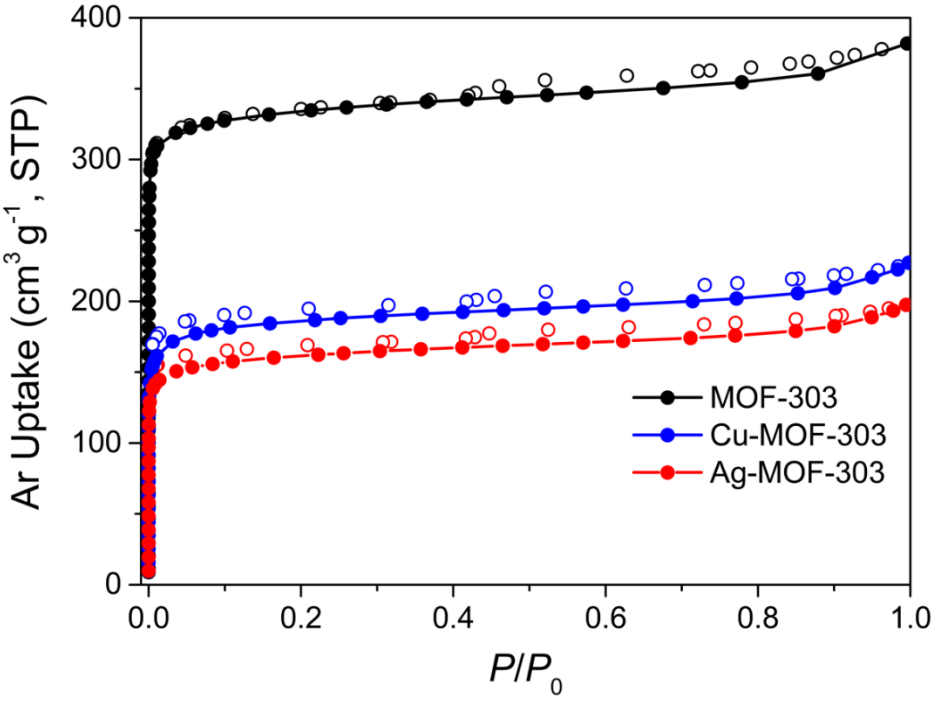


Figure S2.3. Argon sorption isotherms of MOF-303, Cu-, and Ag-MOF-303 measured at 87 K. Filled and open circles represent adsorption and desorption data, respectively. *P*: partial pressure of argon, P_0 = 1 atm. STP: standard temperature and pressure.

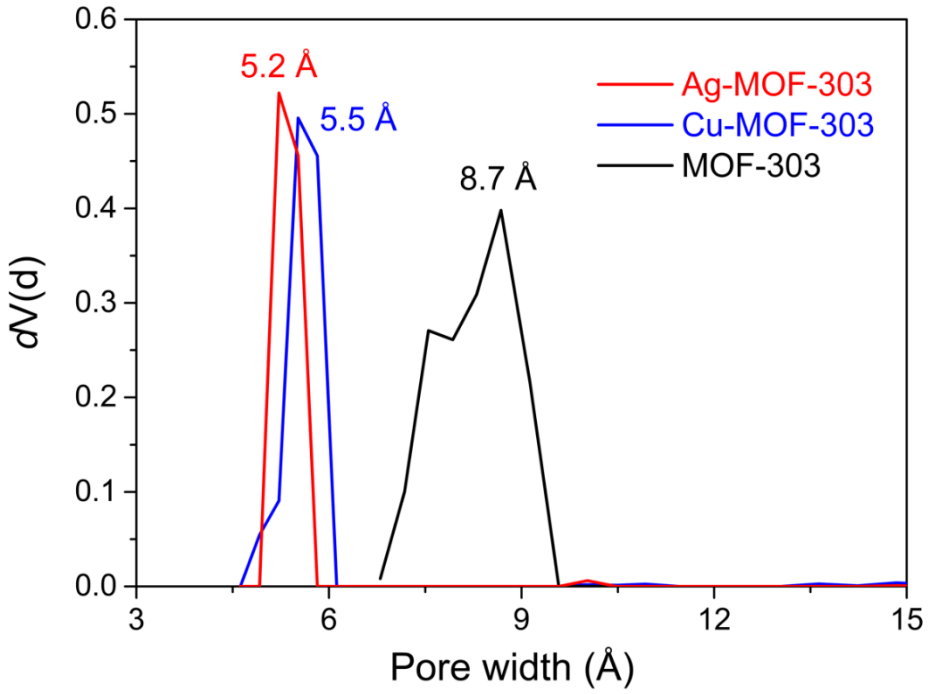


Figure S2.4. Comparison of pore size distribution (PSD) of MOF-303 and its metalated compounds. PSD is derived from NLDFT (sphere/cylinder pores on zeolite) model by fitting their Ar adsorption isotherms at 87 K.

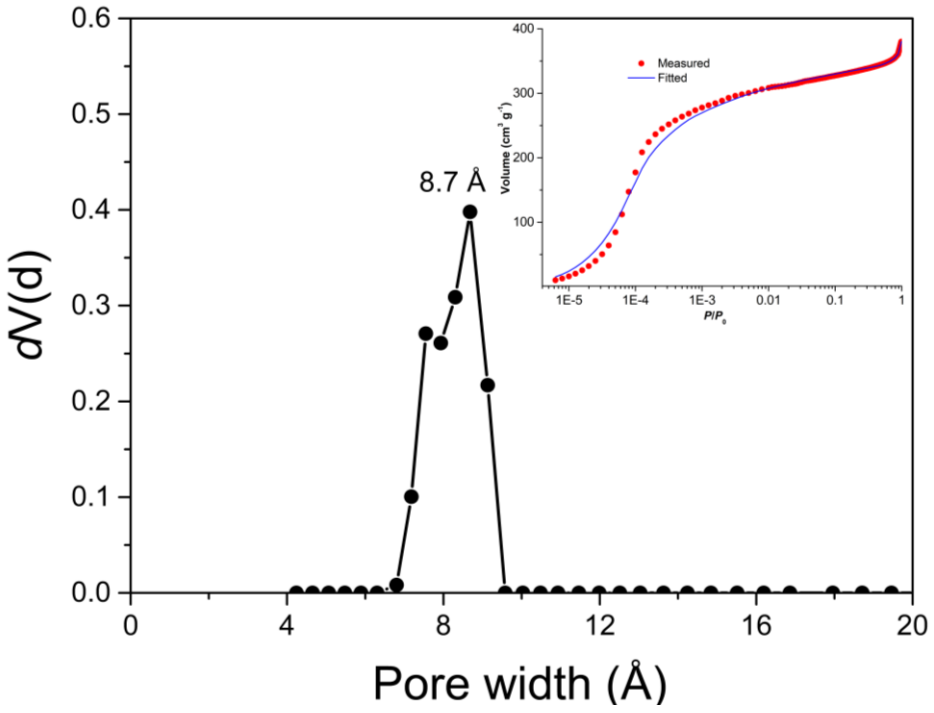


Figure S2.5. The pore size distribution of MOF-303 derived from the NLDFT (sphere/cylinder pores on zeolite) fitting of its Ar adsorption isotherm at 87 K with minimal fitting error (1.039%).

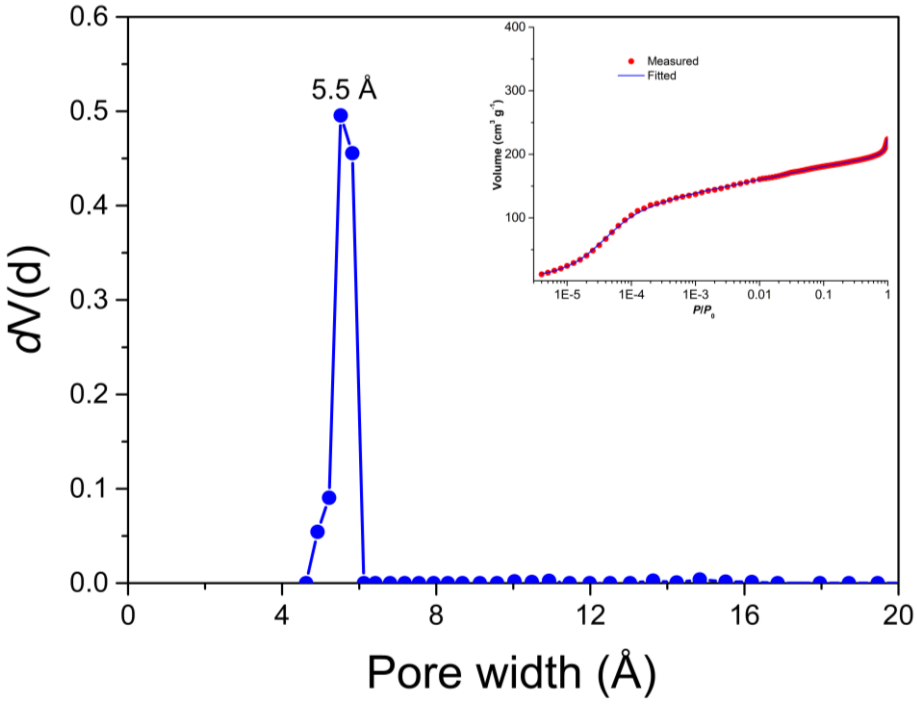


Figure S2.6. The pore size distribution of Cu-MOF-303 derived from the NLDFT (cylinder pores on zeolite) fitting of its Ar adsorption isotherm at 87 K with minimal fitting error (0.182%).

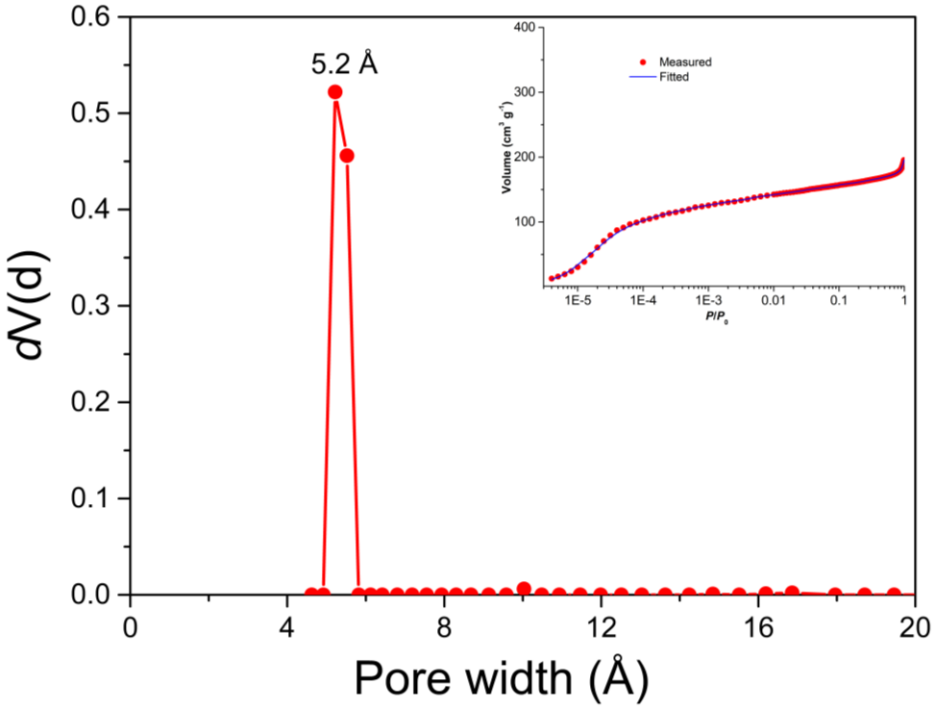


Figure S2.7. The pore size distribution of Ag-MOF-303 derived from the NLDFT (cylinder pores on zeolite) fitting of its Ar adsorption isotherm at 87 K with minimal fitting error (0.266%).

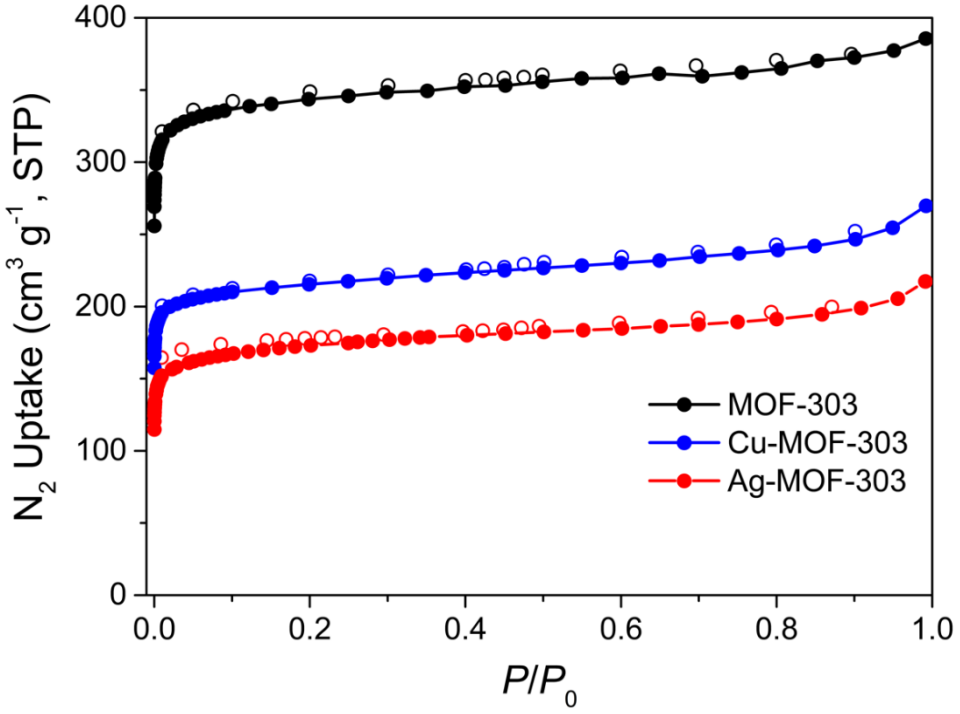


Figure S2.8. N_2 sorption isotherms at 77 K of MOF-303 and its metalated compounds. *P*: partial pressure of nitrogen, P_0 = 1 atm. STP: standard temperature and pressure.

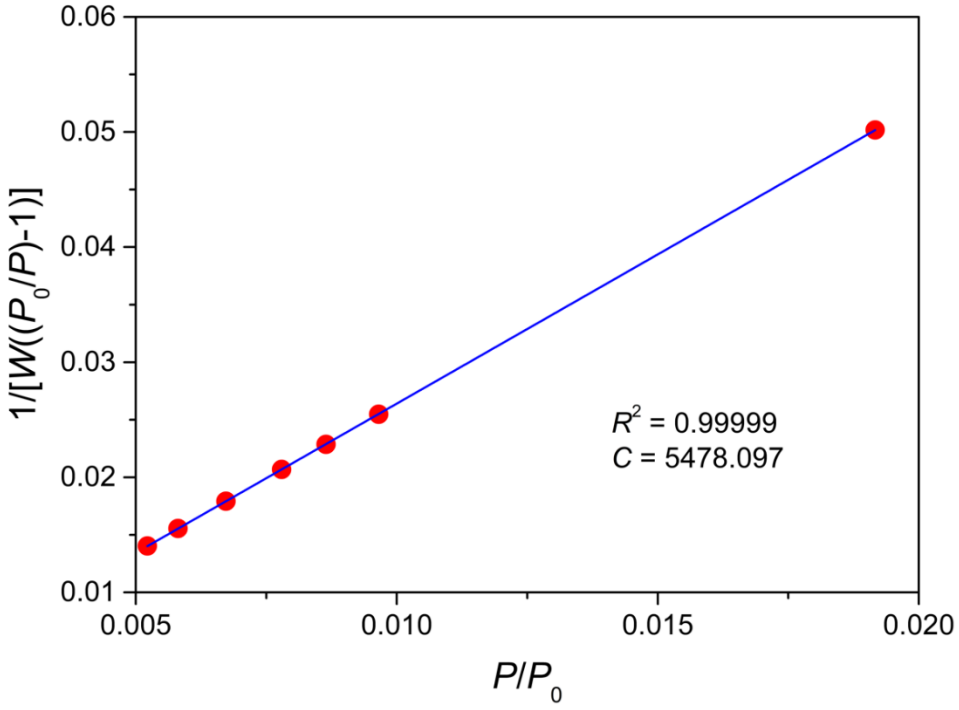


Figure S2.9. Multiple point BET plot of MOF-303 gives a specific surface area of 1343 $m^2 g^{-1}$. *P*: partial pressure of nitrogen, P_0 = 1 atm.

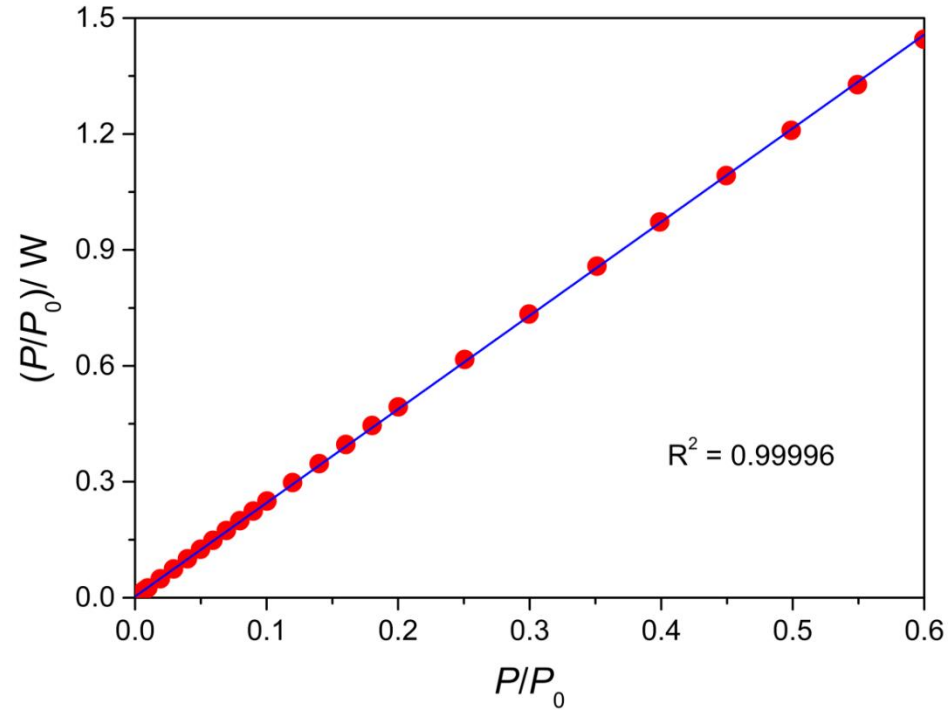


Figure S2.10. Langmuir plot of MOF-303 giving a specific surface area of 1437 m^2 g^{-1}. *P*: partial pressure of nitrogen, P_0 = 1 atm.

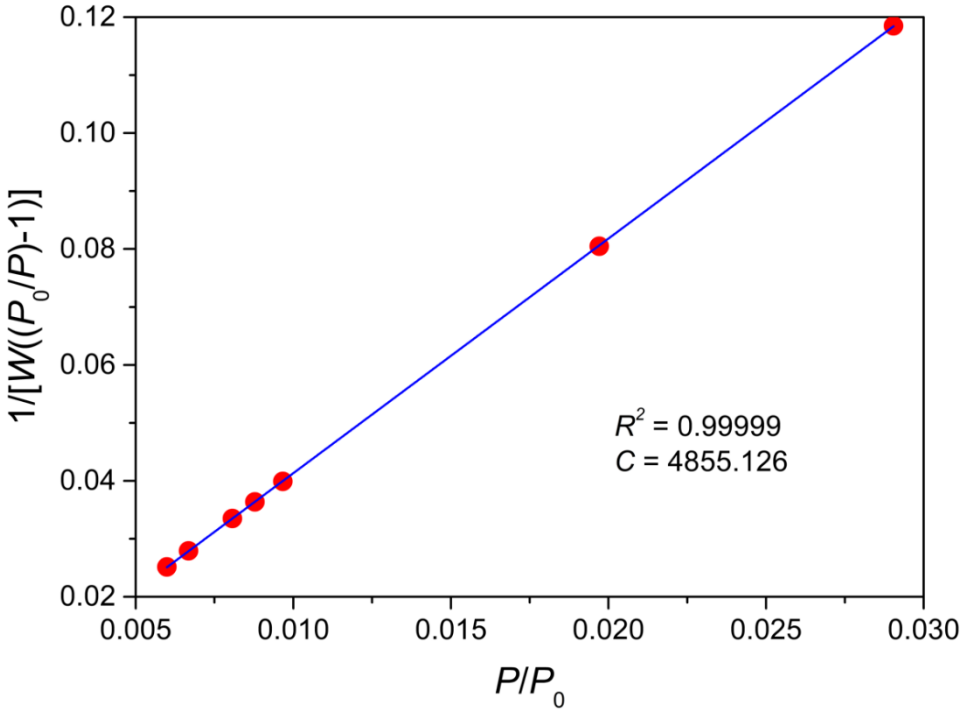


Figure S2.11. Multiple point BET plot of Cu-MOF-303 gives a specific surface area of 860 m^2 g^{-1}. *P*: partial pressure of nitrogen, P_0 = 1 atm.

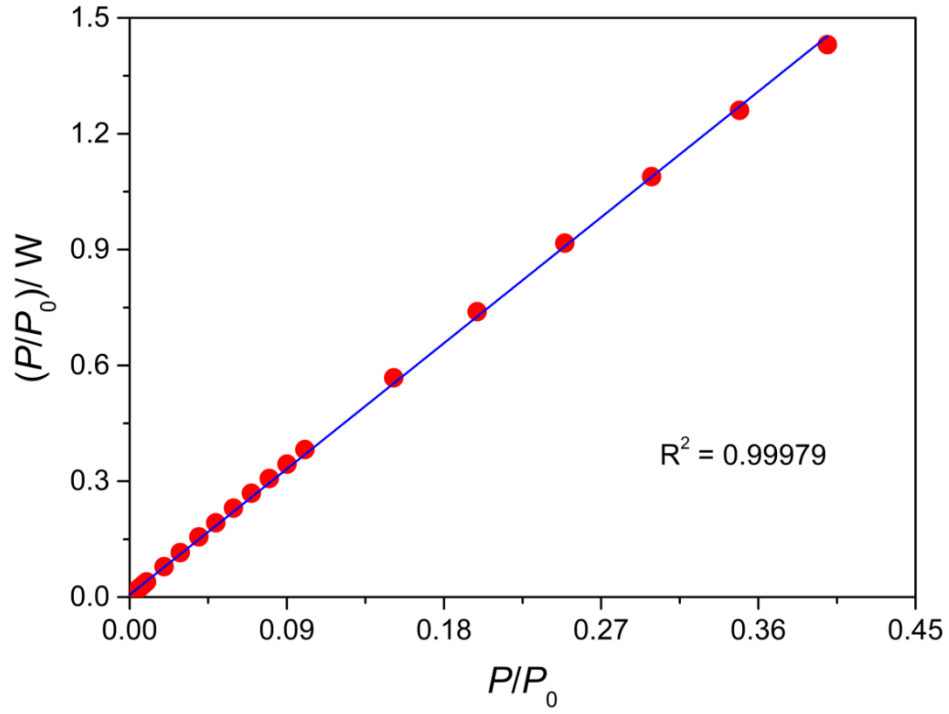


Figure S2.12. Langmuir plot of Cu-MOF-303 giving a specific surface area of 962 m^2 g^{-1}. *P*: partial pressure of nitrogen, P_0 = 1 atm.

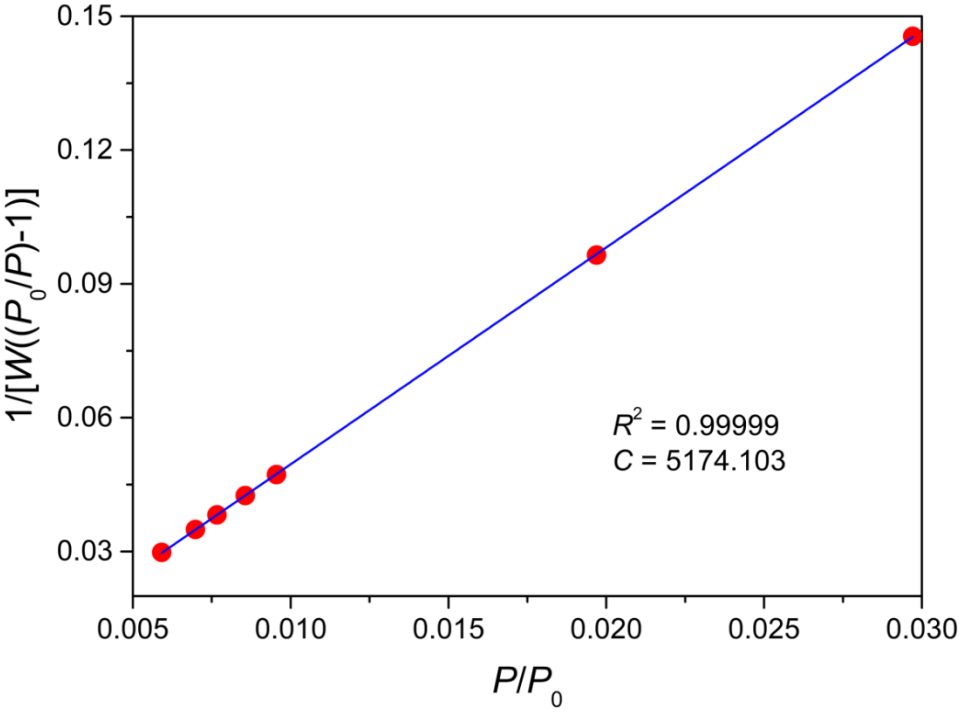


Figure S2.13. Multiple point BET plot of Ag-MOF-303 gives a specific surface area of 716 m^2 g^{-1}. *P*: partial pressure of nitrogen, P_0 = 1 atm.

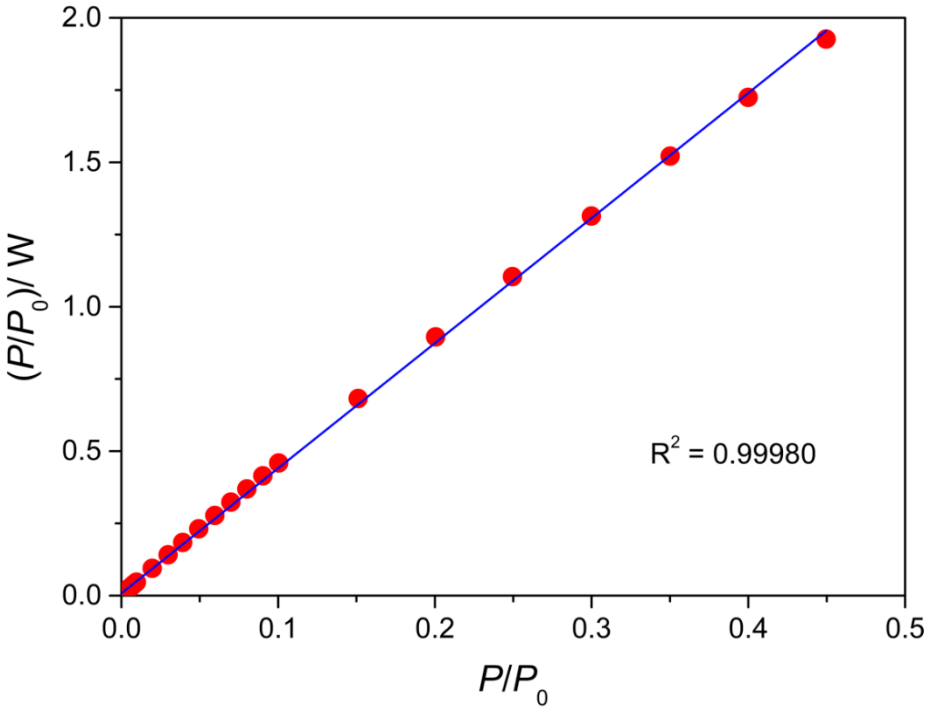


Figure S2.14. Langmuir plot of Ag-MOF-303 giving a specific surface area of 804 m^2 g^{-1}. *P*: partial pressure of nitrogen, P_0 = 1 atm.

2.4.3 Energy Dispersive Spectroscopy Mapping

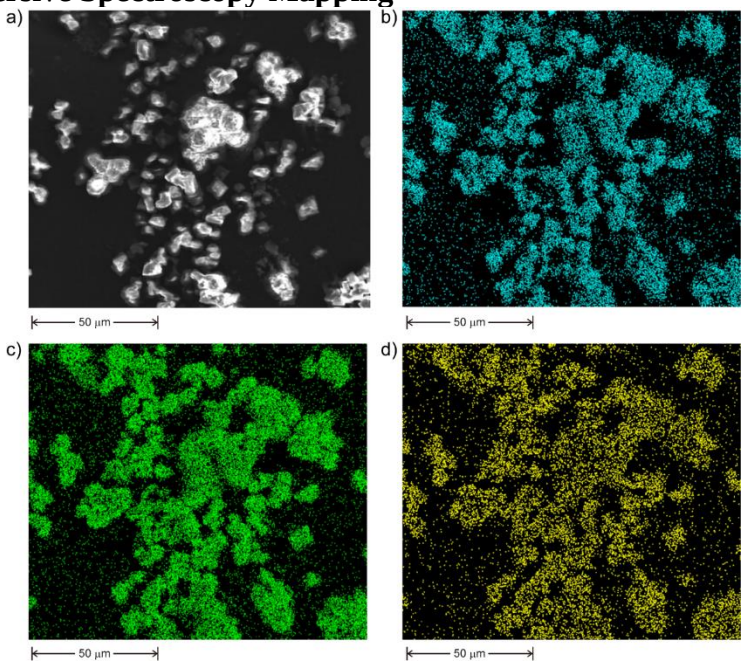


Figure S2.15. SEM EDS elemental mapping of a representative area of Cu-MOF-303 dispersed on a carbon tape. The (a) secondary electron image, (b) Cu Lα map, (c) Al Kα map, and (d) Cl Kα map support that Cu species are uniformly distributed among the MOF crystals. Color code for elements: Cu, blue; Al, green; Cl, yellow.

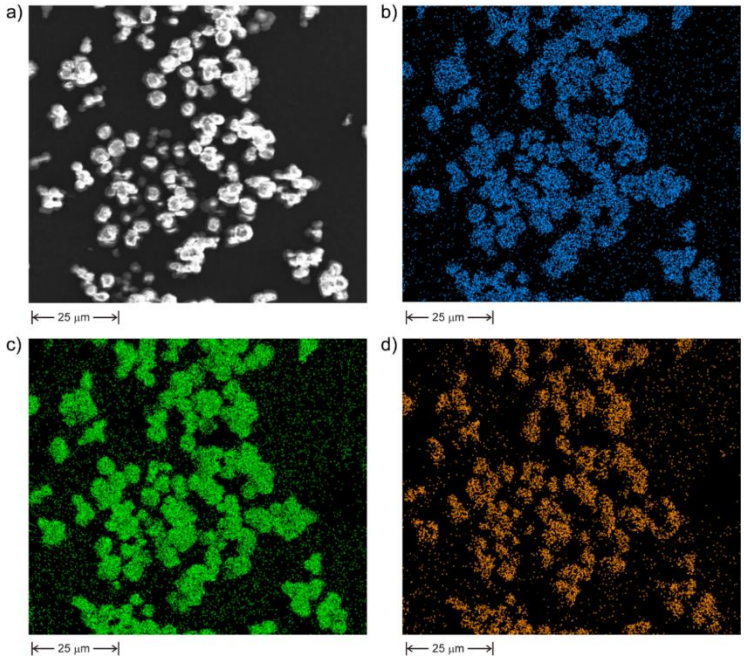


Figure S2.16. SEM EDS elemental mapping of a representative area of Ag-MOF-303 dispersed on a carbon tape. The (a) secondary electron image, (b) Ag Lα map, (c) Al Kα map, and (d) N Kα map support that Ag species are uniformly distributed among the MOF crystals. Color code for elements: Ag, dark blue; Al, green; N, orange.

2.4.4 Electron Diffraction Tomography

Transmission Electron Microscope (TEM): A JEOL 2100 Plus transmission electron microscope was used to collect EDT data set operating at an acceleration voltage of 200 kV. A TVIPS (FX416) CMOS camera was used for high signal-to-noise ratio EDT data acquisition. A JEOL Model-21010 high tilt sample holder was used to collect EDT data.

Sample preparation of MOF-303, Cu-, and Ag-MOF-303: The as-synthesized sample were crushed with mortar and then the milled powder was dispersed with methanol. The suspension liquid was further treated with sonication for 5 minutes. Then one droplet of the suspension was transferred onto a carbon film supported copper grid. The carbon grid was air-dried for 2 hours. A pump station was then used to fully remove guest molecules. The prepared TEM grid was transferred onto a high tilt sample holder for EDT data collection. All three samples were prepared in consistent protocols.

EDT data collection and analysis: To reduce electron beam damage, EDT data were collected in a continuous rotation mode with the camera working in video mode. In this way, the collection time of one dataset was significantly decreased to 5~10 min. The electron beam was fully spread into a parallel condition to reduce beam dose. The electron diffraction patterns of single frames were collected in selected-area electron diffraction (SAED) mode. The data collection parameters were optimized to adopt a spot size of 4 and an exposure time of 0.5 s. The EDT data of MOF-303, Cu-, and Ag-MOF-303 were collected with tilt ranges from −56.3° to 53.9°, −48.9° to 61.2° and −57.0° to 58.2° with an average step of 0.191°, 0.193° and 0.193°, respectively. The reconstructed reciprocal lattice of all three dataset suggested a primitive monoclinic Bravais lattice. The unit cell parameters determined from each dataset were, MOF-303: a = 12.3 Å, b = 15.4 Å; c = 14.3 Å; β = 101.5˚; V = 2654.3 Å^3; Cu-MOF-303: a = 12.7 Å, b = 15.0 Å; c = 14.3 Å; β = 102.0˚; V = 2664.6 Å^3; Ag-MOF-303: a = 12.7 Å, b = 15.5 Å; c = 14.1 Å; β = 101.7˚; V = 2737.2 Å^3. The space group of three materials is confirmed as $P2_1/c$ (no.14) in the structural determination. The processed EDT data of MOF-303 shows a resolution up to 1.0 Å and the resolution of Cu- and Ag-MOF-303 dataset are higher than 1.0 Å. *Ab initio* structure solution of all three structures were finished by using direct method[20] implemented in SIR2014.[21] The structure refinement was finished by using SHELX[22] in Olex2 packages.[23]

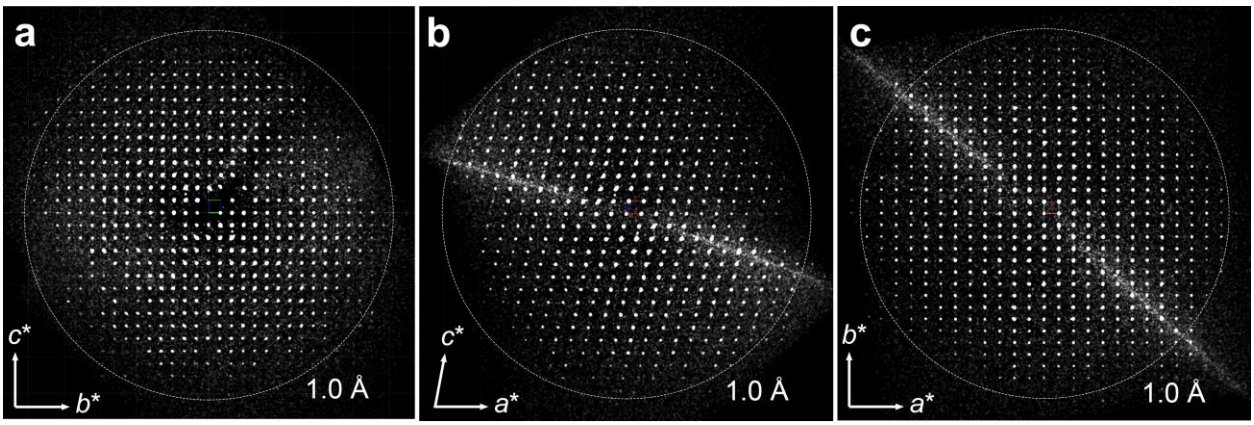


Figure S2.17. Projections of the reconstructed three-dimensional reciprocal lattice of MOF-303 along (a) [100], (b) [010] and (c) [001] directions, respectively. To show the weak diffraction more clearly, the intensity values of all pixels have been taken the square root value. The reconstructed reciprocal lattice shows a primitive monoclinic Bravais lattice. The resolution of the whole dataset is limited to 1.0 Å.

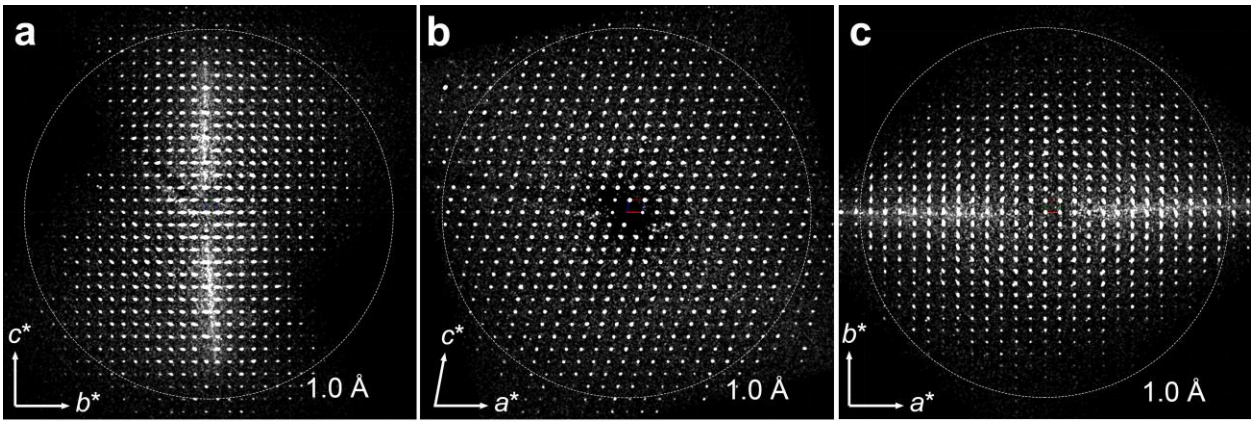


Figure S2.18. Projections of the reconstructed three-dimensional reciprocal lattice of Cu-MOF-303 along (a) [100], (b) [010] and (c) [001] directions, respectively. To show the weak diffraction points more clearly, the intensity values of all pixels have been taken the square root value. The reconstructed reciprocal lattice shows a primitive monoclinic Bravais lattice. The resolution of the whole dataset is better than 1.0 Å.

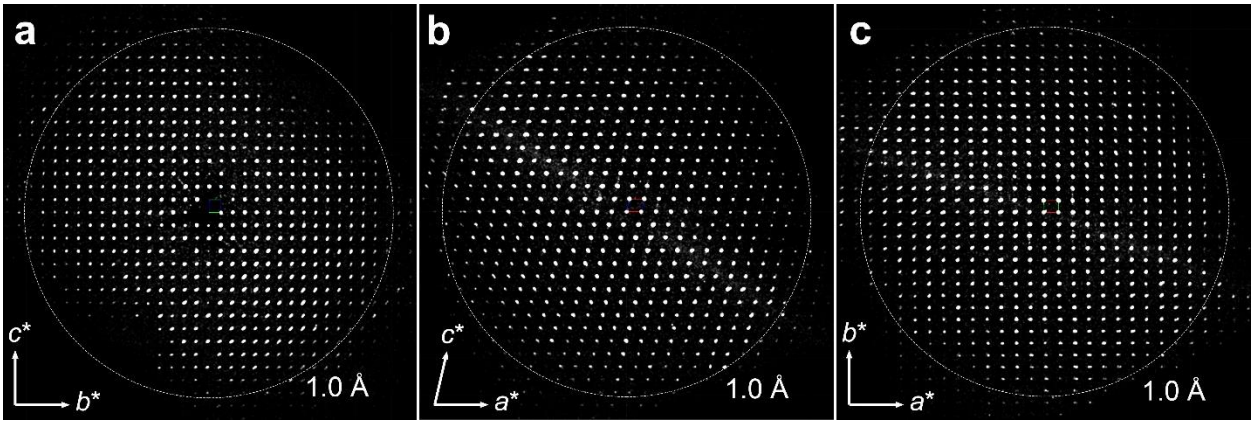


Figure S2.19. Projections of the reconstructed three-dimensional reciprocal lattice of Ag-MOF-303 along (a) [100], (b) [010] and (c) [001] directions, respectively. The reconstructed reciprocal lattice shows a primitive monoclinic Bravais lattice. The resolution of the whole dataset is up to 1.0 Å.

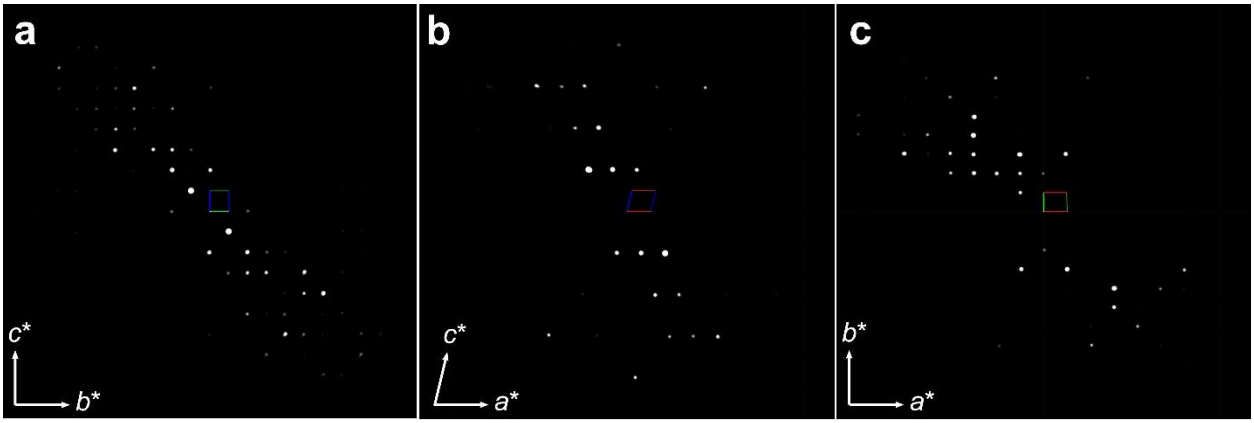


Figure S2.20. The slices cut from reconstructed three-dimensional reciprocal lattice of 3D EDT data of MOF-303. (a) (0*kl*), (b) (*h*0*l*) and (c) (*hk*0). The observed reflection conditions were summarized as *h*0*l*, *l* = 2*n*, 0*k*0: *k* = 2*n*, and 00*l*: *l* = 2*n*, which suggested the only possible space group: $P2_1/c$ (no.14).

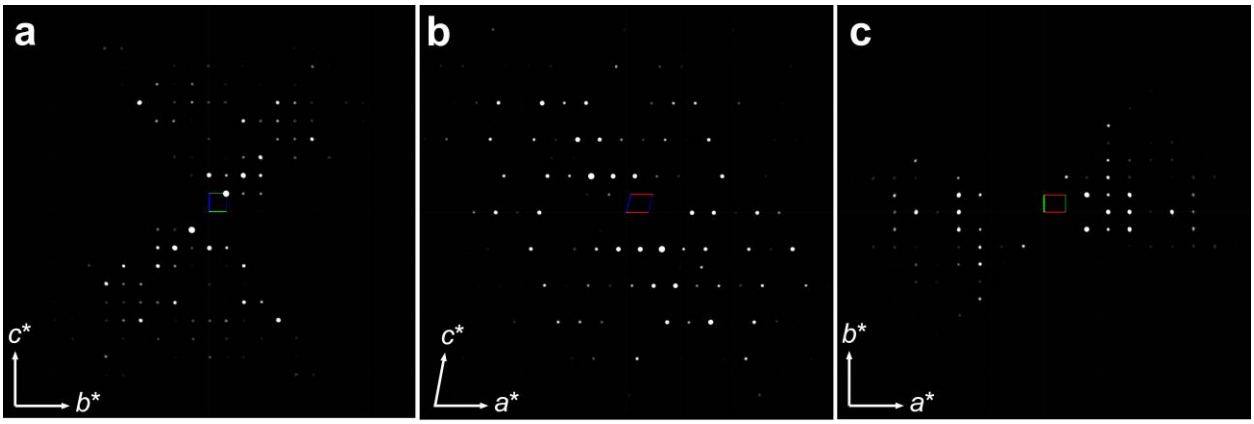


Figure S2.21. The slices cut from reconstructed three-dimensional reciprocal lattice of 3D EDT data of Cu-MOF-303. (a) (0*kl*), (b) (*h*0*l*) and (c) (*hk*0). The observed reflection conditions were summarized as *h*0*l*, 00*l*: *l* = 2*n*, which suggested the possible space groups: *Pc* (no.7) *or* $P2_1/c$ (no.14). We confirmed the space group as $P2_1/c$ in the structural determination.

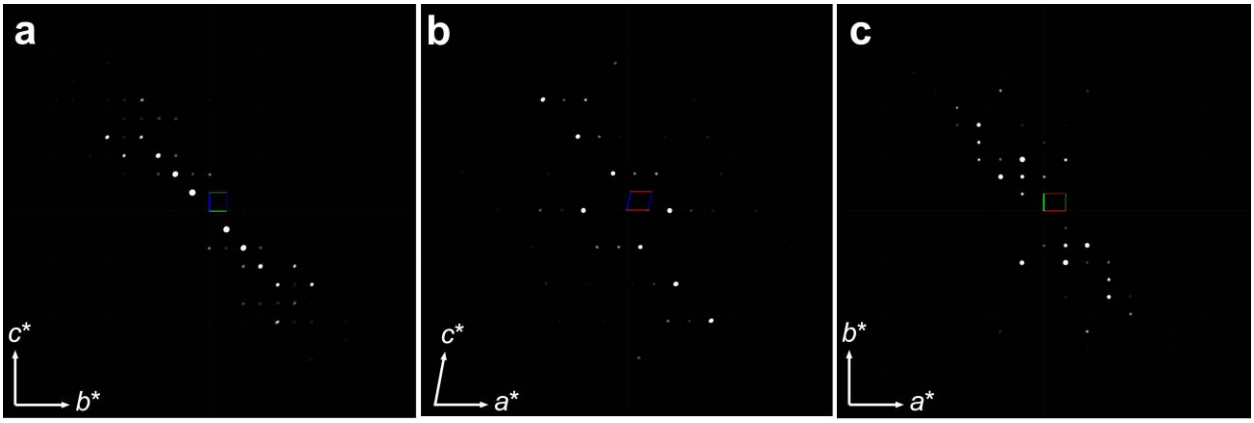


Figure S2.22. The slices cut from reconstructed three-dimensional reciprocal lattice of 3D EDT data of Ag-MOF-303. (a) (0*kl*), (b) (*h*0*l*) and (c) (*hk*0). The observed reflection conditions were summarized as *h*0*l*, 00*l*: *l* = 2*n*, 0*k*0: *k* = 2*n*, which suggested the only possible space group: $P2_1/c$ (no.14).

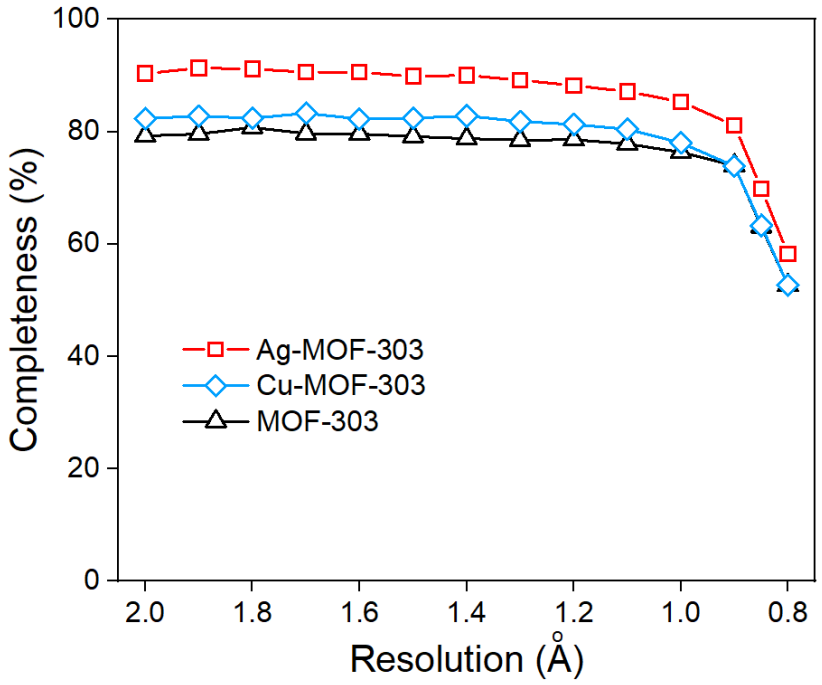


Figure S2.23. The completeness of 3D EDT data set of MOF-303, Cu-, and Ag-MOF-303 against resolution.

Table S2. 1. The structure solution and refinement statistic of MOF-303

MOF-303	
Data collection	Continuous mode
Molecular	$C_{20}H_{12}Al_4N_8O_{20}$
Tilt range(º)	110.2
Radiation source	200 kV Electron
Wavelength (Å)	0.025079
Space group	$P2_1/c$
a (Å)	12.3
b (Å)	15.4
c (Å)	14.3
β (°)	101.5
V (Å^3)	2654.3
Resolution (Å)	1.0
R_{int} (%)	28.41
Completeness (%)	76.6
Total reflections	5513
Unique reflections	2119
S	1.096
R_1(%)	17.88
wR_2(%)	42.58

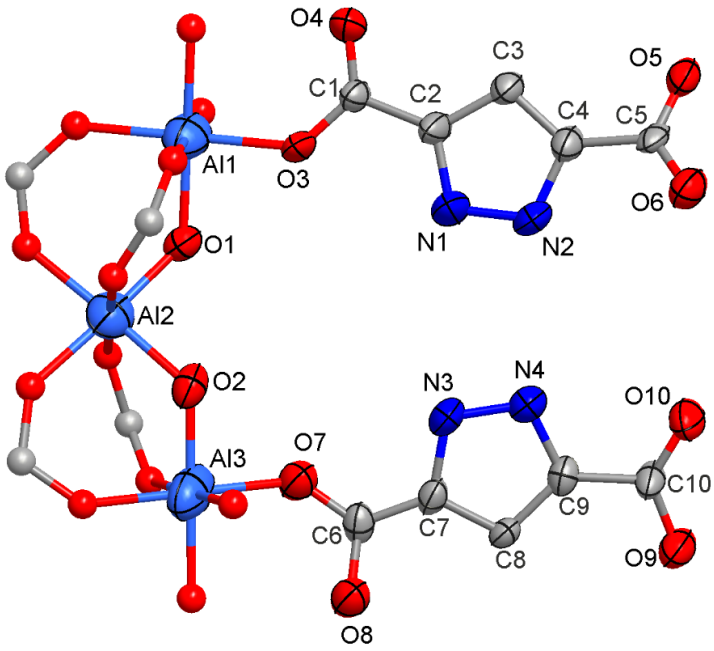


Figure S2.24. Asymmetric unit in the single-crystal structure of MOF-303. Thermal ellipsoids are drawn with 30% probability. H atoms are omitted for clarity.

Table S2.2. The 3D electron diffraction structure solution and refinement statistic of Cu-MOF-303.

Cu-MOF-303	
Data collection	Continuous mode
Molecular	$C_{20}H_8Al_4Cu_{0.5}N_8O_{20}$
Tilt range(º)	110.1
Radiation source	200 kV Electron
Wavelength (Å)	0.025079
Space group	$P2_1/c$
a (Å)	12.7
b (Å)	15.0
c (Å)	14.3
β (°)	102.0
V (Å^3)	2664.6
Resolution (Å)	1.0
R_{int} (%)	20.71
Completeness (%)	78.9
Total reflections	5556
Unique reflections	2199
S	1.078
R_1(%)	19.04
wR_2(%)	44.67

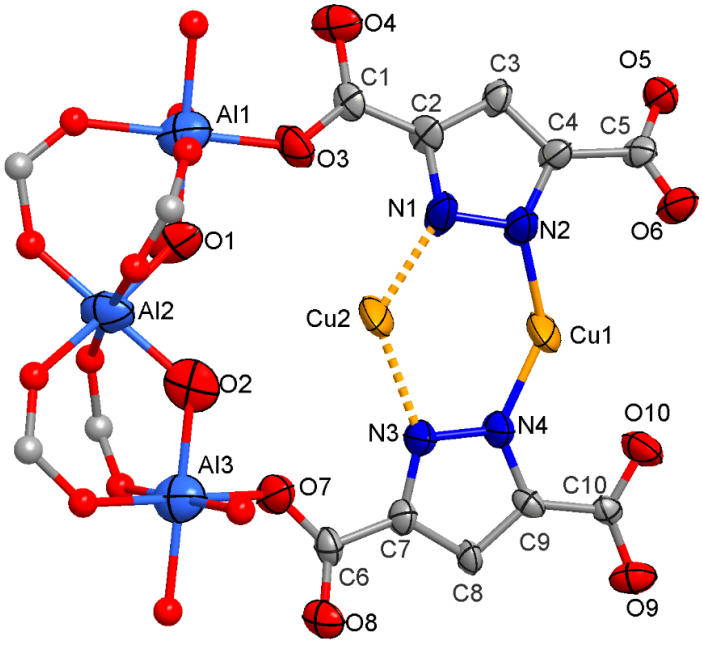


Figure S2.25. Asymmetric unit in the single-crystal structure of Cu-MOF-303. Thermal ellipsoids are drawn with 30% probability. H atoms are omitted for clarity.

Table S3. The 3D electron diffraction structure solution and refinement statistic of Ag-MOF-303.

Ag-MOF-303	
Data collection	Continuous mode
Molecular	$C_{20}H_8Ag_{0.5}Al_4N_8O_{20}$
Tilt range(º)	115.2
Radiation source	200 kV Electron
Wavelength (Å)	0.025079
Space group	$P2_1/c$
a (Å)	12.7
b (Å)	15.5
c (Å)	14.2
β (°)	101.7
V (Å^3)	2737.2
Resolution (Å)	1.0
R_{int} (%)	16.71
Completeness (%)	85.5
Total reflections	5425
Unique reflections	2441
S	1.073
R_1(%)	19.16
wR_2(%)	44.57

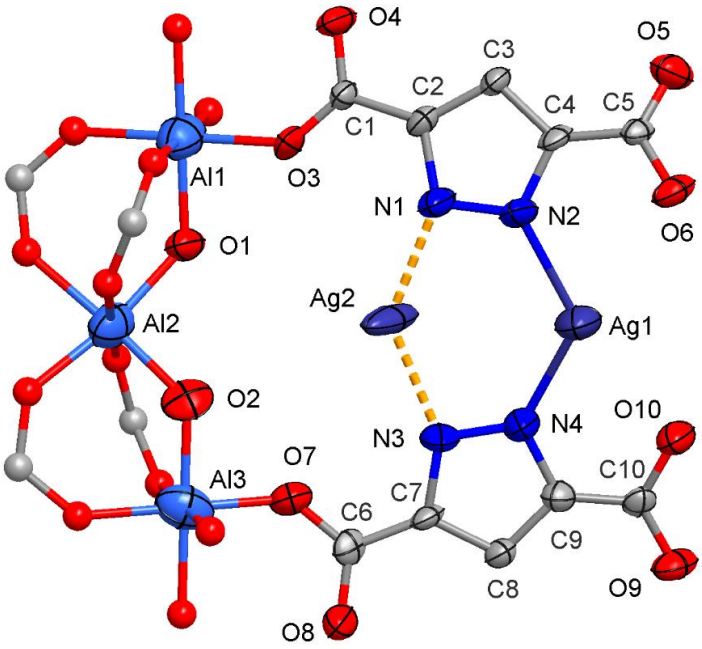


Figure S2.26. Asymmetric unit in the single-crystal structure of Ag-MOF-303. Thermal ellipsoids are drawn with 30% probability. H atoms are omitted for clarity.

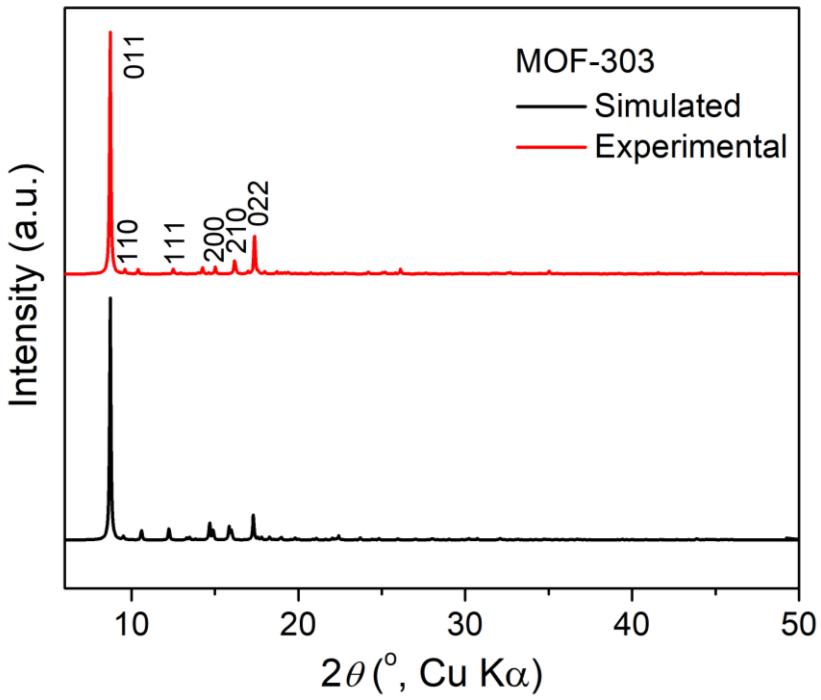


Figure S2.27. Experimental (red) and simulated (black) PXRD patterns for MOF-303.

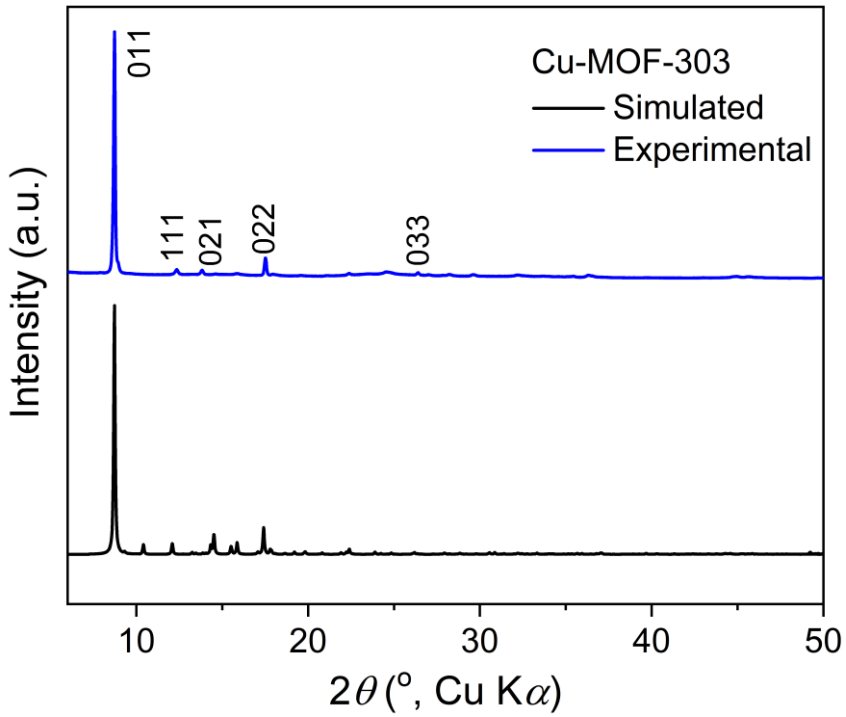


Figure S2.28. Experimental (blue) and simulated (black) PXRD patterns for Cu-MOF-303.

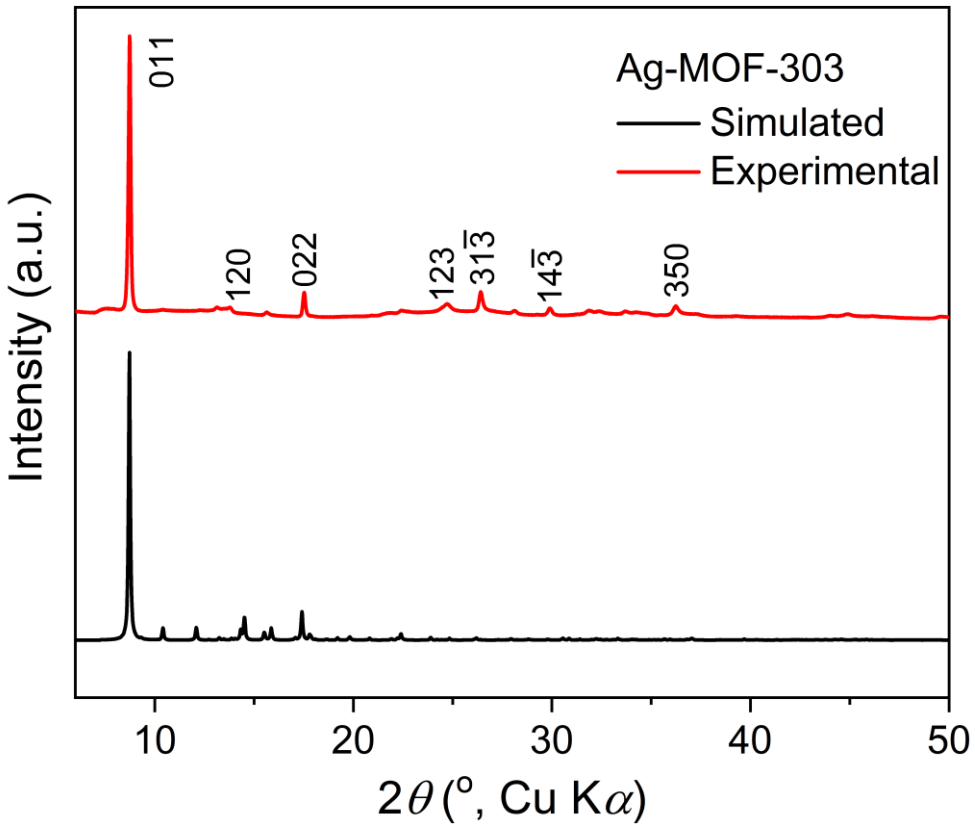


Figure S2.29. Experimental (red) and simulated (black) PXRD patterns for Ag-MOF-303.

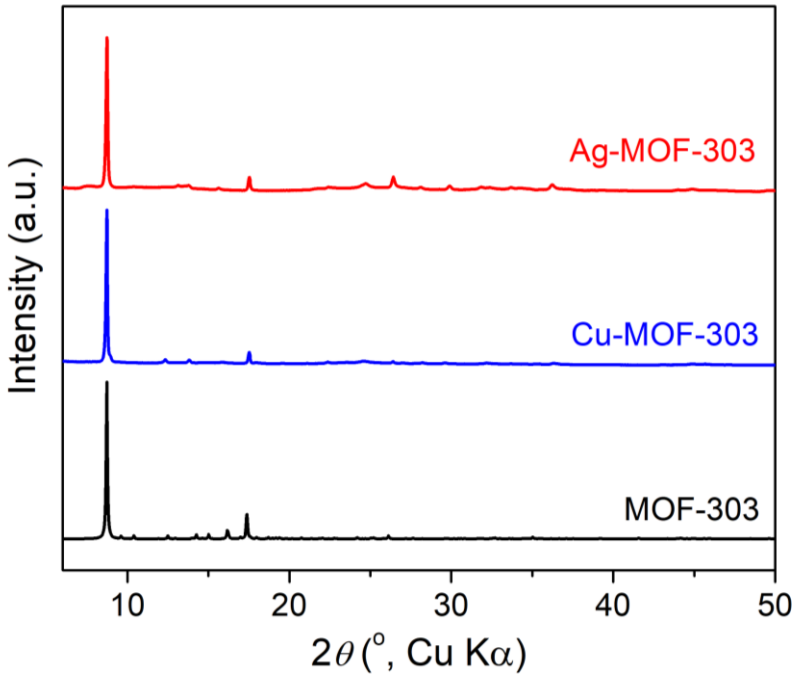


Figure S2.30. PXRD patterns of MOF-303, Cu-, and Ag-MOF-303.

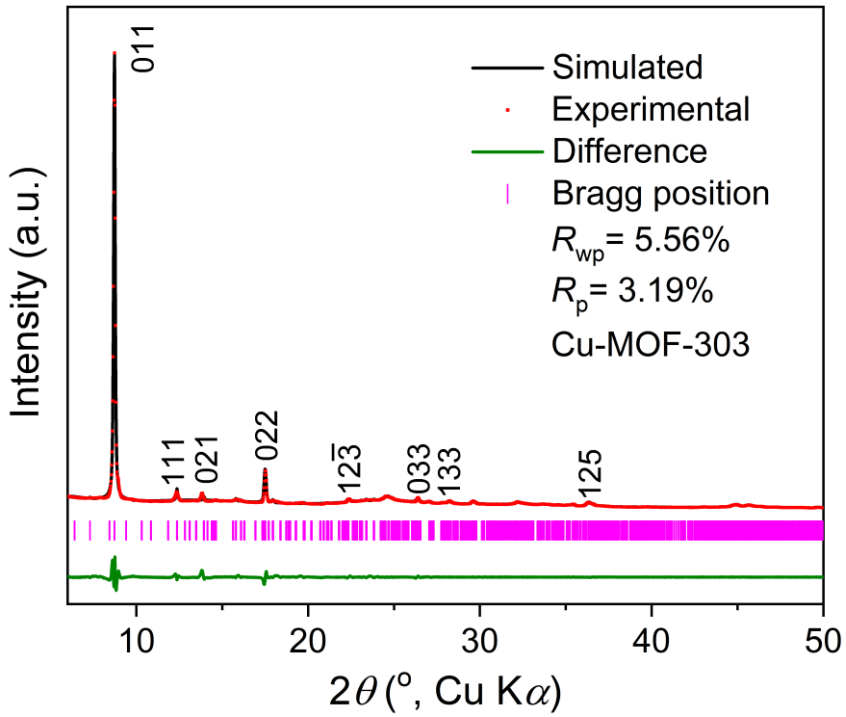


Figure S2.31. PXRD pattern and Pawley fitting of Cu-MOF-303.

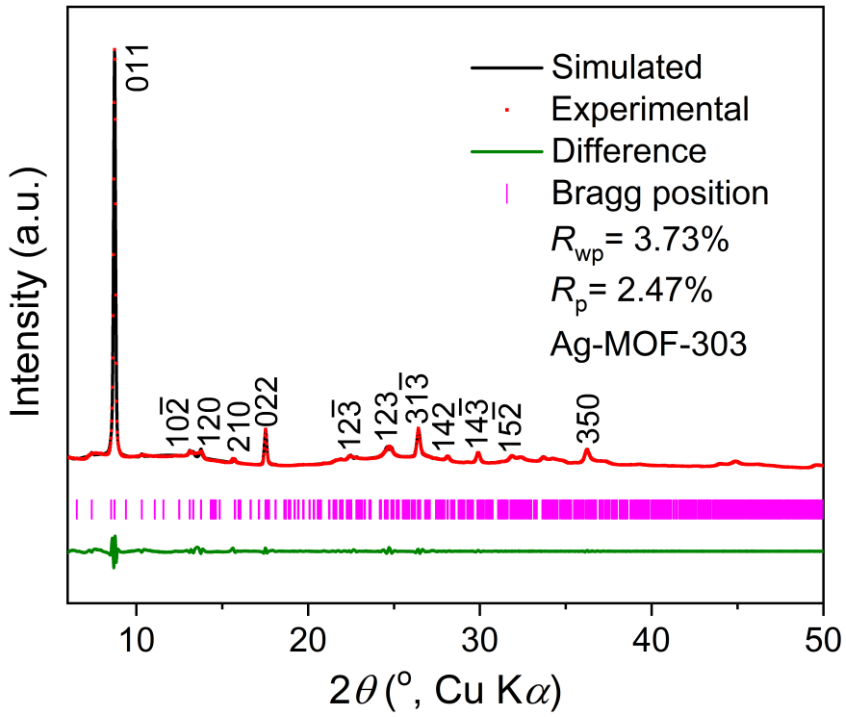


Figure S2.32. PXRD pattern and Pawley fitting of Ag-MOF-303.

2.4.5 X-ray Absorption Spectroscopy Analyses

Cu K-edge X-ray absorption spectroscopy data were collected at the Advanced Light Source (ALS) bending-magnet beamline 10.3.2 (2.1−17 keV) with the storage ring operating at 500 mA and 1.9 GeV, using a Si(111) monochromator and adjustable pre-monochromator slits.[24] All data were collected at room temperature (24 °C) in fluorescence mode at the Cu K-edge (8980.48 eV). The incoming X-ray intensity (I_0) was measured in an ion chamber and the fluorescence emission with a seven element LN_2 cooled Ge solid state detector (Canberra) using XIA electronics. A Cu foil was used to calibrate the monochromator, with 1st derivative maximum set at 8980.48 eV and an internal I_0 glitch (present in all spectra) was used to calibrate the data.[25]

Cu K-edge XANES spectra were recorded in fluorescence mode by continuously scanning the Si (111) monochromator (Quick XAS mode) from 8880 to 9020 eV, with 0.3 eV steps in the XANES region. All data were processed using the LabVIEW custom BL 10.3.2 software to perform dead time correction, energy calibration, and glitch removal with detailed procedure described elsewhere.[26] XANES spectra were processed with Athena software to find first derivative peak (E_0), pre-edge background subtraction and post-edge normalization, and to align and merge the spectra.[27] EXAFS spectra were recorded up to 565 eV above the edge (8836−9982 eV, i.e., up to $k \approx 16$ Å^{-1}) and 11 scans were averaged. EXAFS spectra of samples were reduced with k^1-, k^2-, and k^3-weighting, out to $k = 11$ Å^{-1}, and analyzed via shell-by-shell fitting using the FEFF6l code and the Artemis software where it yields minima in variances.[27-28]

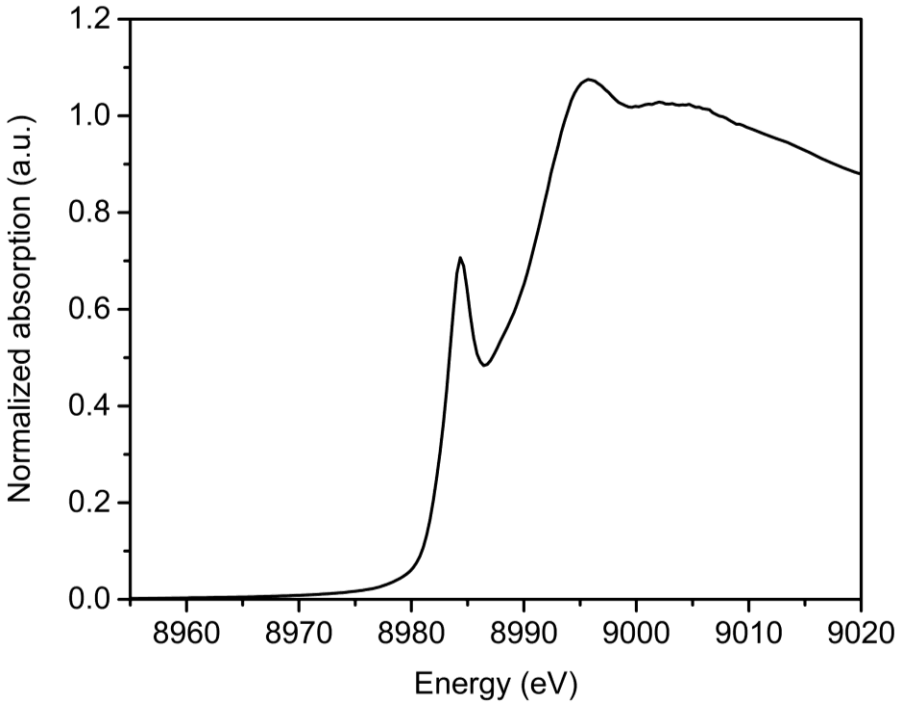


Figure S2.33. Cu K-edge XANES spectrum of Cu-MOF-303.

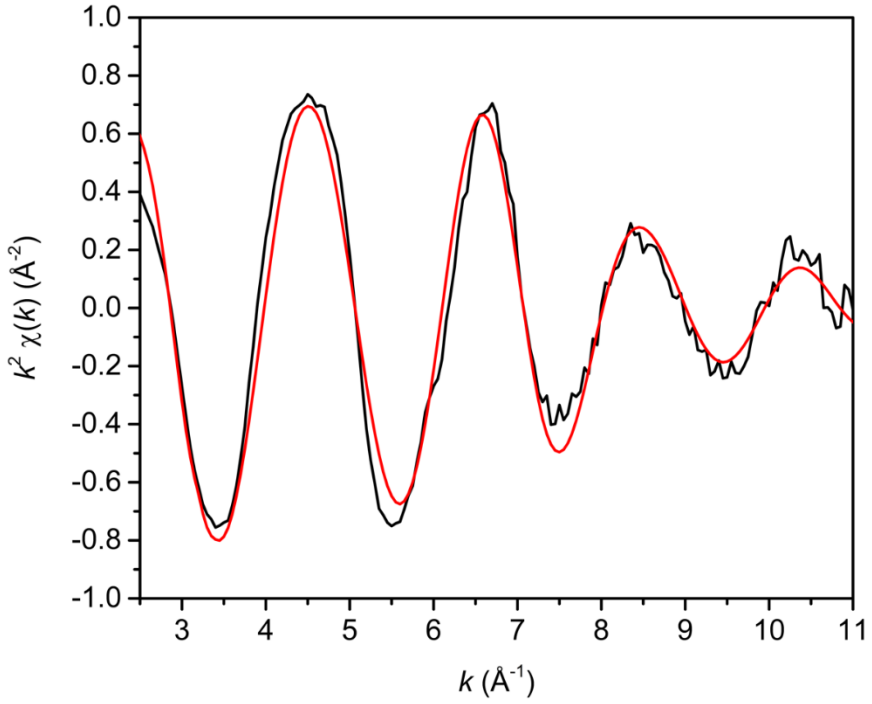


Figure S2.34. k^2-weighted EXAFS spectra of Cu-MOF-303 (black line) and best fit (red line) in *k*-space. Fitting was conducted using N scatter. Fit range: 2.5 < k < 11.0 $Å^{-1}$; fit window: Hanning.

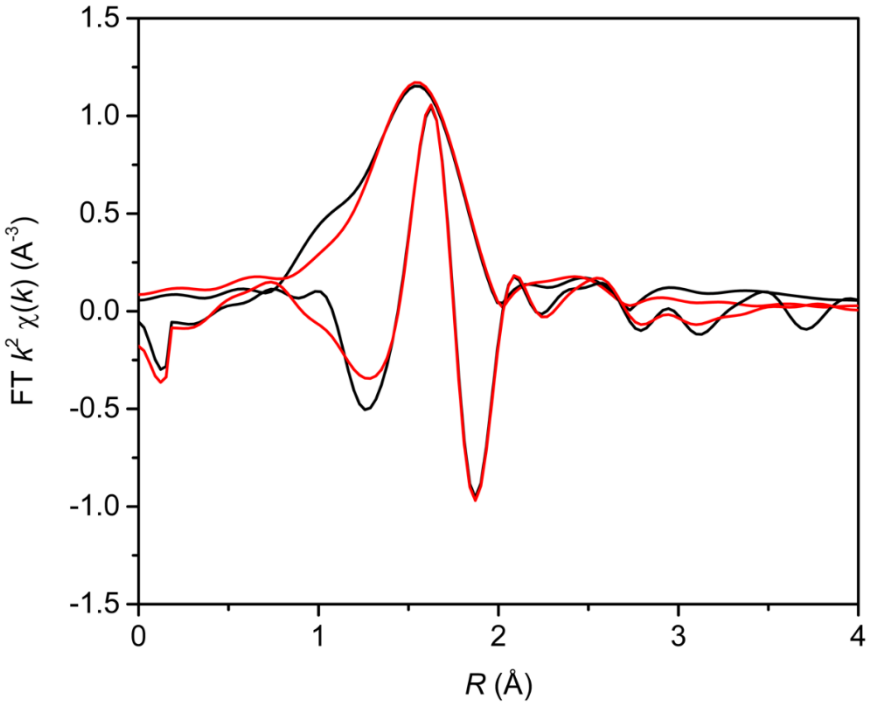


Figure S2.35. Fourier transformed EXAFS spectra of Cu-MOF-303 (black line) and best fit (red line) in *R*-space. Fitting was conducted using N scatter. Fit range: 1.0 < R < 3.2 Å; fit window: Hanning.

Table S4. EXAFS fitting results for Cu-MOF-303: [a]Ab = absorber; Sc = scatterer. [b]Coordination number. [c]Distance (Å). [d]Debye-Waller factor (Å^2). [e]A measure of mean square sum of the misfit at each data point. [f]SS = single scattering. Fitting was conducted using N scatter. Fit range: 2.5 < k < 11.0 Å^{-1}; 1.0 < R < 3.2 Å; fit window: Hanning. N_{idp} = 11.7. N_{var} = 8.

Ab-Sc pair[a]	CN[b]	R[c]	DWF[d]	R-factor[e]
Cu–N SS[f]	1.82±0.55	1.92±0.04	0.0027±0.0047	
Cu–Cl SS	0.91±0.28	2.14±0.02	0.0049±0.0053	0.014
Cu···O SS	0.70±0.18	2.84±0.05	0.0027±0.0064	

2.4.6 Xenon Uptake, Adsorption Selectivity, and Heat of Adsorption

The adsorption isotherms for Xe and Kr in Cu- and Ag-MOF-303 were measured at 273 K, 283 K, and 298 K. The single component-isotherm data were fitted with the single-site or dual-site Langmuir-Freundlich model:

$$\frac{n}{N} = \frac{b_1 p^{\frac{1}{t_1}}}{1 + b_1 p^{\frac{1}{t_1}}} + \frac{b_2 p^{\frac{1}{t_2}}}{1 + b_2 p^{\frac{1}{t_2}}}$$

where n is the amount adsorbed in mmol g^{-1}, p is the pressure in Pa, N is the saturation capacity in mmol g^{-1}, and t is the heterogeneity parameter of adsorbents. b is the temperature-dependent parameter in kPa^{-1}:

$$b = b_0 \exp\left(\frac{E}{RT}\right)$$

The fitting parameters of Langmuir-Freundlich model were shown in the fitting figure.

The selectivity of preferential adsorption of Xe over Kr in a mixture containing Xe and Kr can be defined as:

$$S_{Xe/Kr} = \frac{x_{Xe}}{x_{Kr}} \Big/ \frac{y_{Xe}}{y_{Kr}}$$

where x_{Xe} and x_{Kr} are the equilibrated adsorption capacity of Xe and Kr, respectively; and y_{Xe} and y_{Kr} are the molar fractions of Xe and Kr in gas phase, respectively. The calculations of x_{Xe} and x_{Kr} were based on the Ideal Adsorbed Solution Theory (IAST) of Myers and Prausnitz.[29]

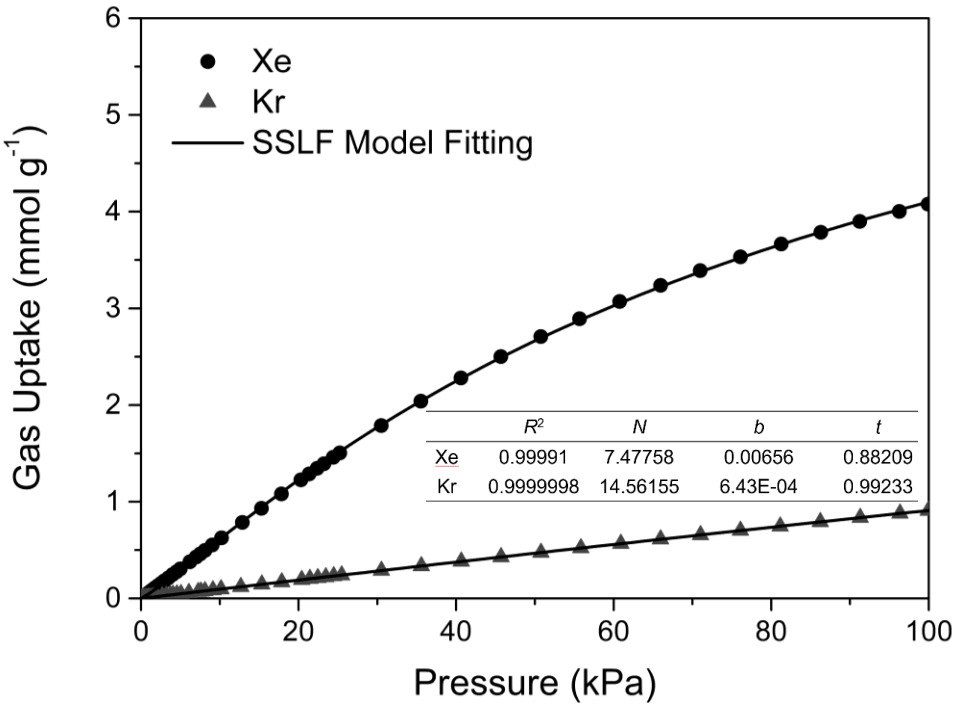


Figure S2.36. Single-site Langmuir-Freundlich Model fitting (lines) of the Xe and Kr adsorption isotherms (points) for MOF-303 measured at 298 K.

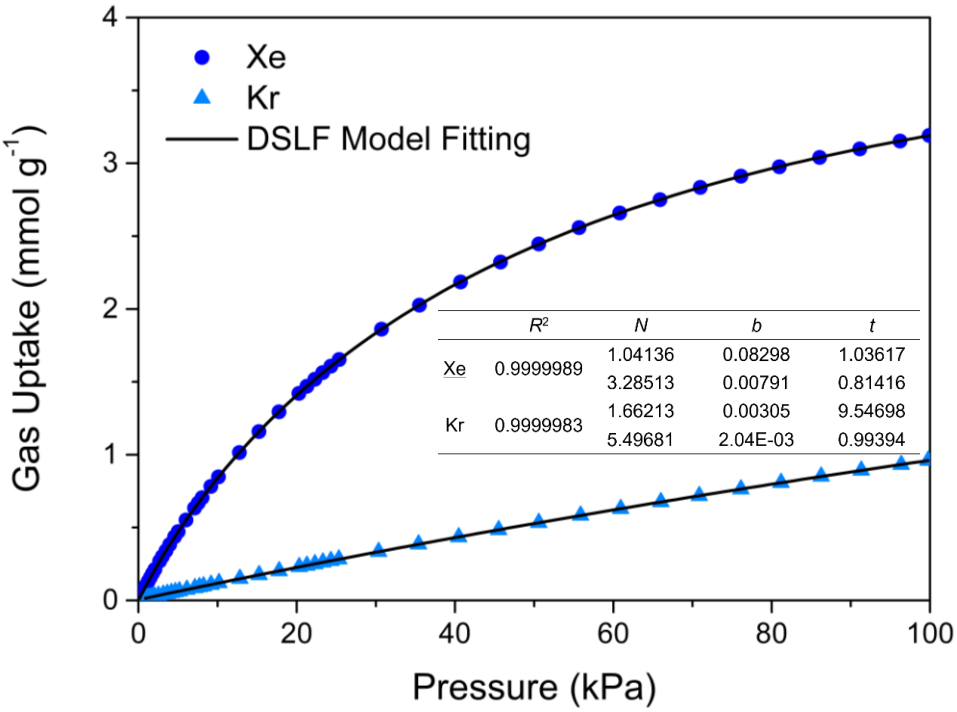


Figure S2.37. Dual-site Langmuir-Freundlich Model fitting (lines) of the Xe and Kr adsorption isotherms (points) for Cu-MOF-303 measured at 298 K.

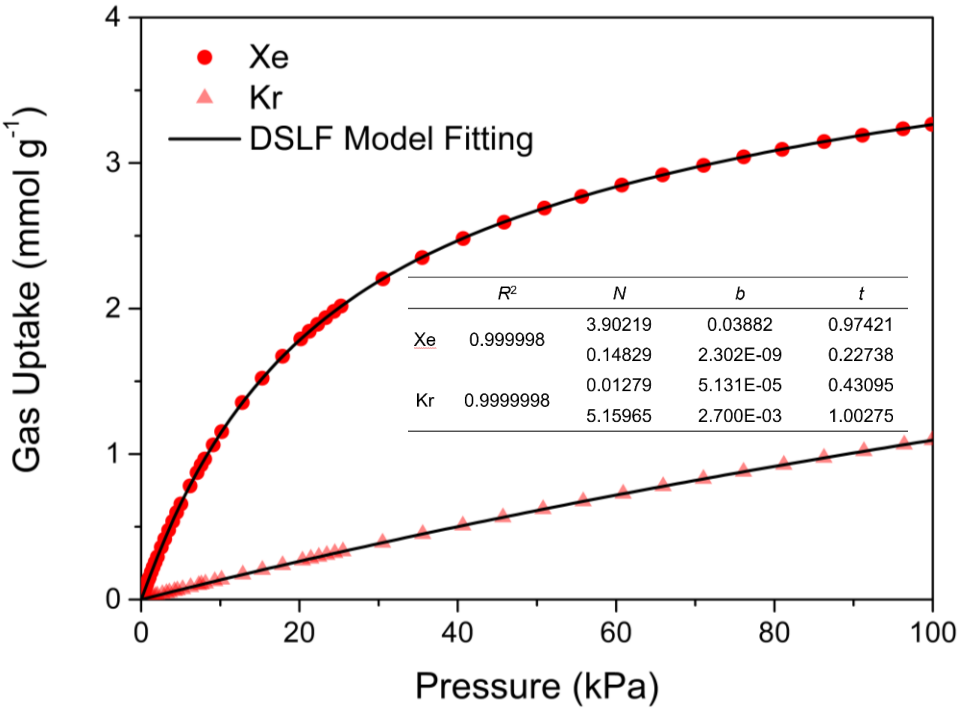


Figure S2.38. Dual-site Langmuir-Freundlich Model fitting (lines) of the Xe and Kr adsorption isotherms (points) for Ag-MOF-303 measured at 298 K.

Isosteric heats of adsorption (Q_{st}) is used to evaluate the adsorption affinity between gas molecules and adsorbent materials. The Clausius-Clapeyron equation and single-site Tóth Model method are used to calculate the Q_{st}.[11] Q_{st} is defined as:

$$Q_{st} = -RT^2\left(\frac{\partial lnP}{\partial T}\right)_{n_a}$$

where n_a (mmol g^{-1}) is the amount of adsorbed gas, T (K) is the temperature, P (kPa) is the pressure, Q_{st} (kJ mol^{-1}) is the isosteric heat of adsorption.

Single-site Tóth Model equations as follows, where n is the amount adsorbed in mmol g^{-1}, p is the pressure in Pa, N is the saturation capacity in mmol g^{-1}, b is the parameter in Pa^{-1}, and t is the heterogeneity parameter of adsorbents.[30]

$$\frac{n}{N} = \frac{bp}{[1+(bp)^t]^{\frac{1}{t}}}$$

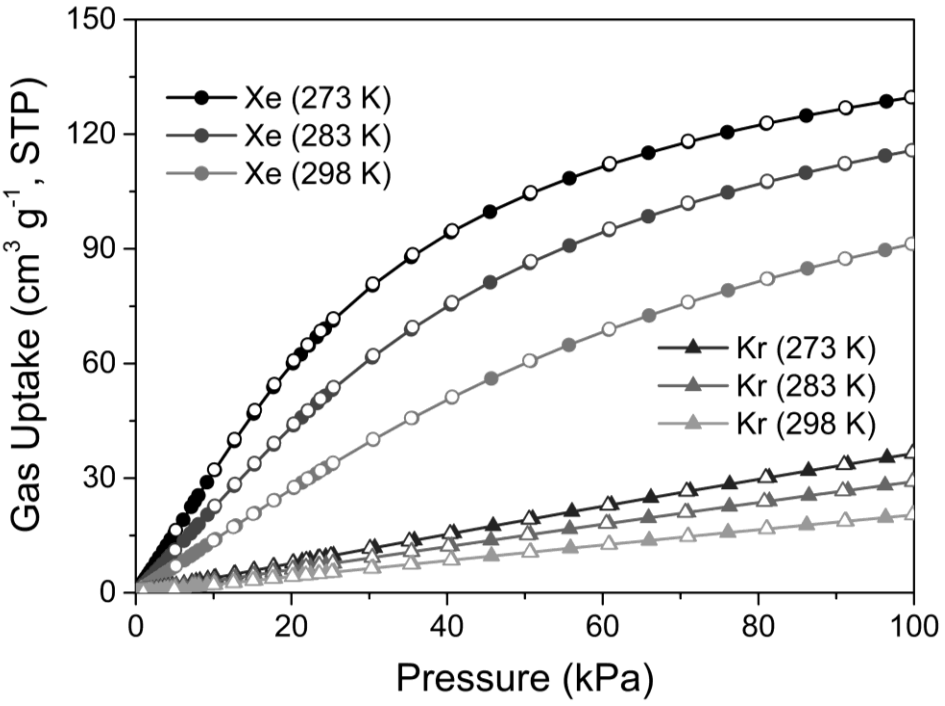


Figure S2.39. Xe and Kr sorption isotherms of MOF-303 at 273, 283, and 298 K. Filled and open circles represent adsorption and desorption data, respectively. STP: standard temperature and pressure.

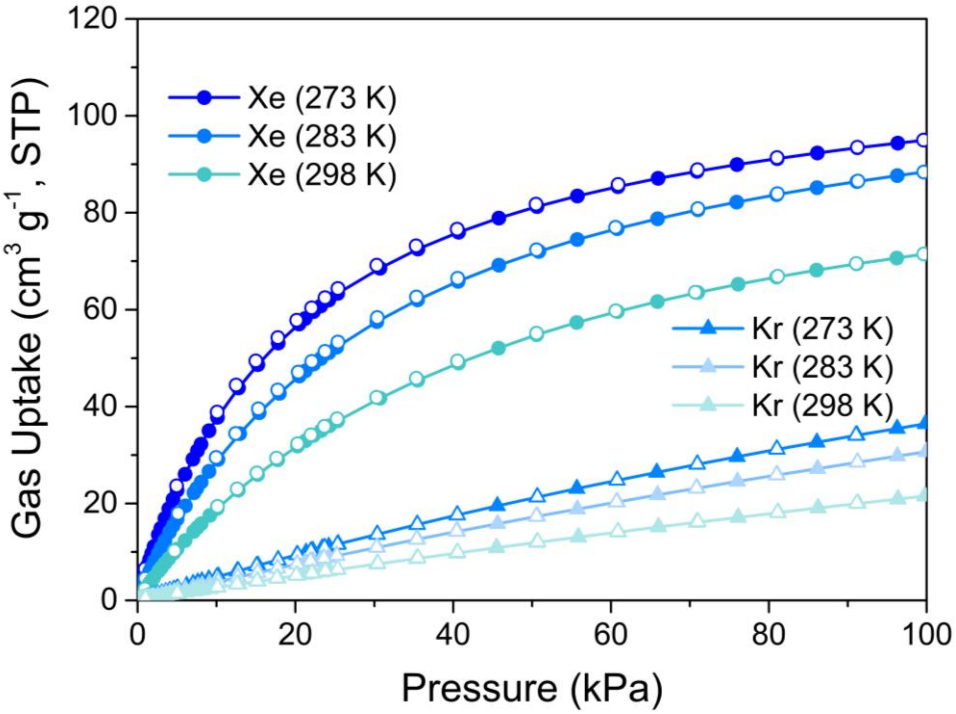


Figure S2.40. Xe and Kr sorption isotherms of Cu-MOF-303 at 273, 283, and 298 K. Filled and open circles represent adsorption and desorption data, respectively. STP: standard temperature and pressure.

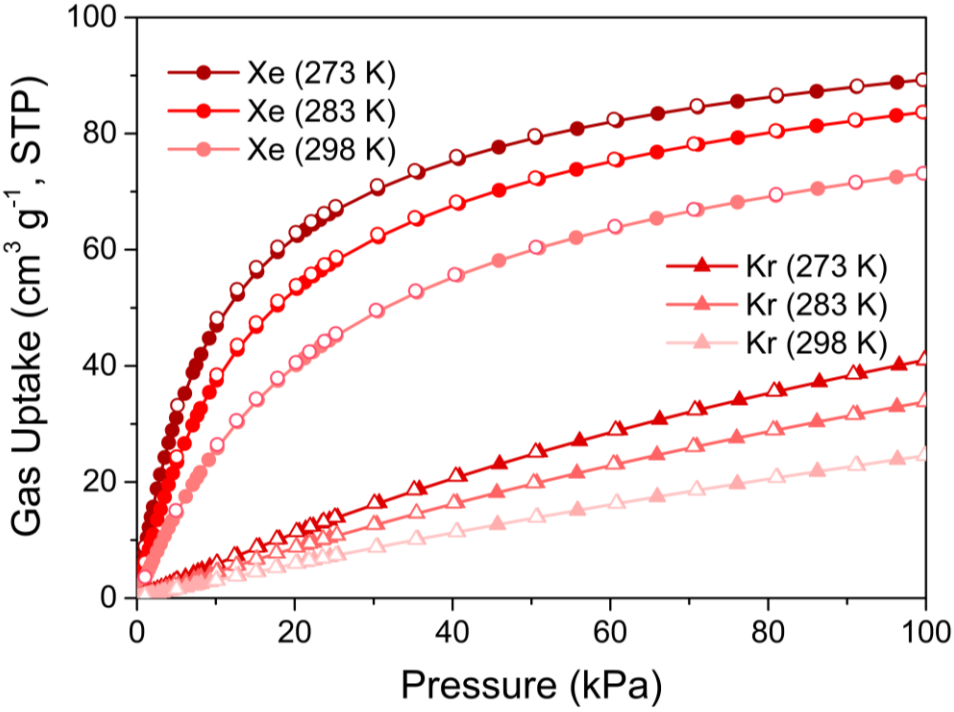
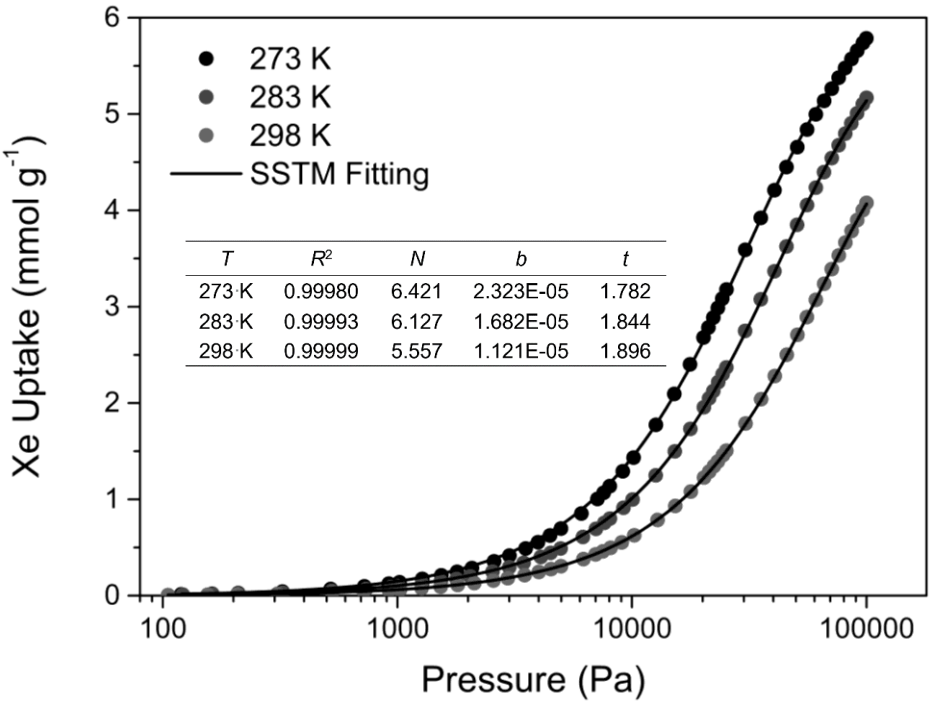


Figure S2.41. Xe and Kr sorption isotherms of Ag-MOF-303 at 273, 283, and 298 K. Filled and open circles represent adsorption and desorption data, respectively. STP: standard temperature and pressure.



T	R^2	N	b	t
273 K	0.99980	6.421	2.323E-05	1.782
283 K	0.99993	6.127	1.682E-05	1.844
298 K	0.99999	5.557	1.121E-05	1.896

Figure S42. Single-site Tóth Model fitting (lines) of the MOF-303 Xe adsorption isotherms (points) measured at 273, 283, and 298 K.

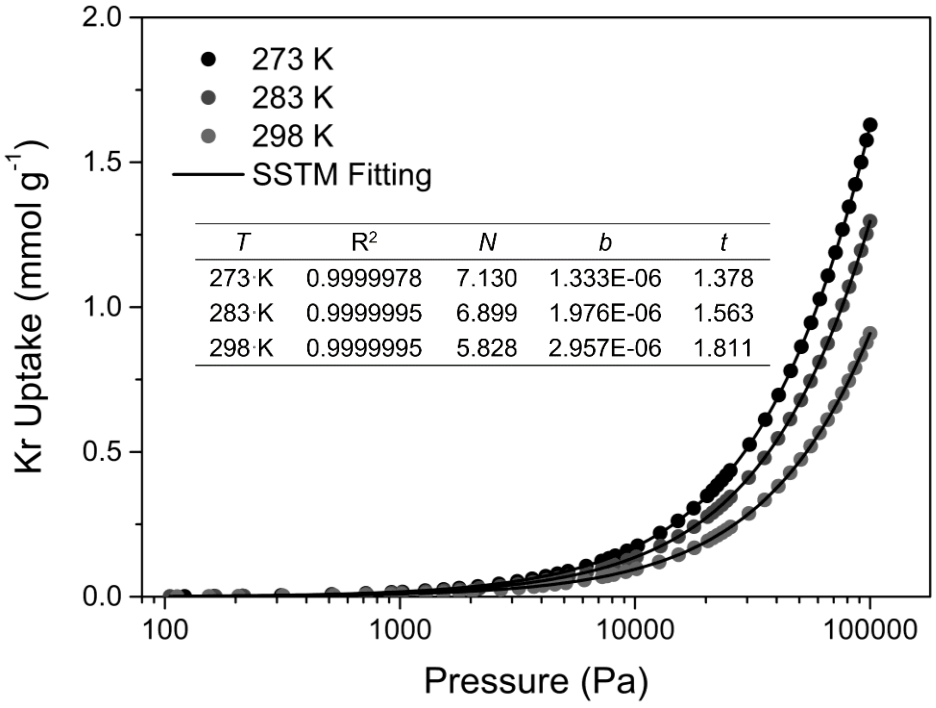


Figure S2.43. Single-site Tóth Model fitting (lines) of the MOF-303 Kr adsorption isotherms (points) measured at 273, 283, and 298 K.

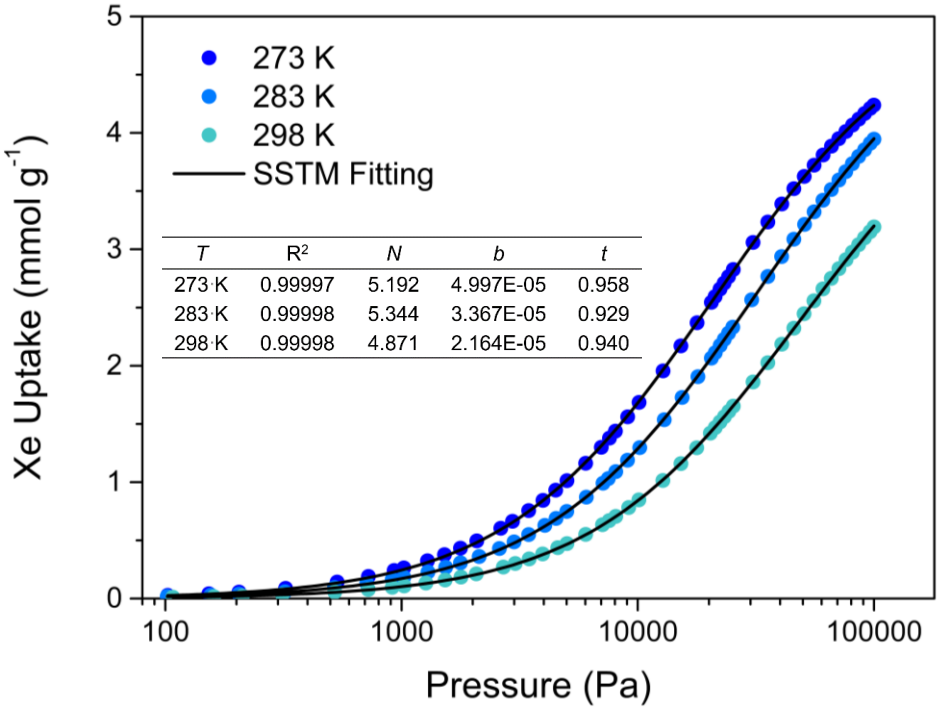


Figure S2.44. Single-site Tóth Model fitting (lines) of the Cu-MOF-303 Xe adsorption isotherms (points) measured at 273, 283, and 298 K.

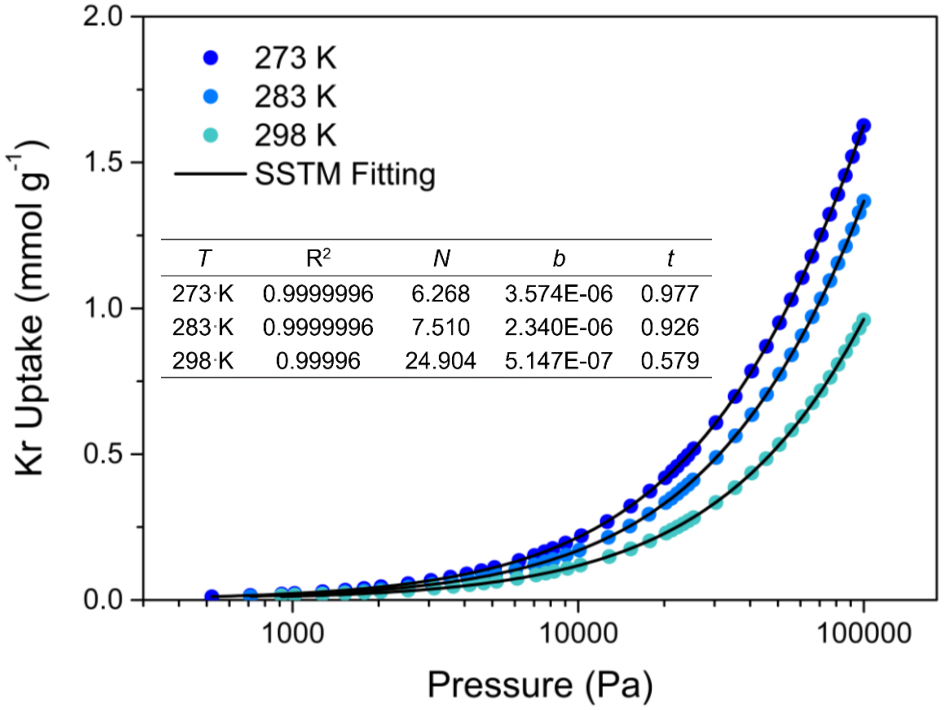


Figure S2.45. Single-site Tóth Model fitting (lines) of the Cu-MOF-303 Kr adsorption isotherms (points) measured at 273, 283, and 298 K.

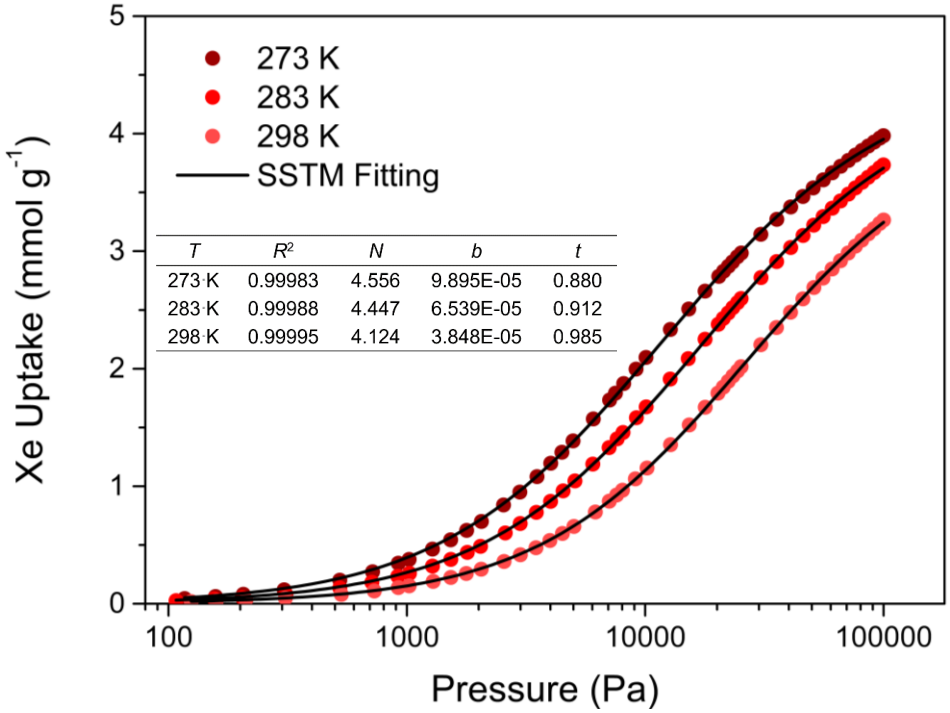


Figure S2.46. Single-site Tóth Model fitting (lines) of the Ag-MOF-303 Xe adsorption isotherms (points) measured at 273, 283, and 298 K.

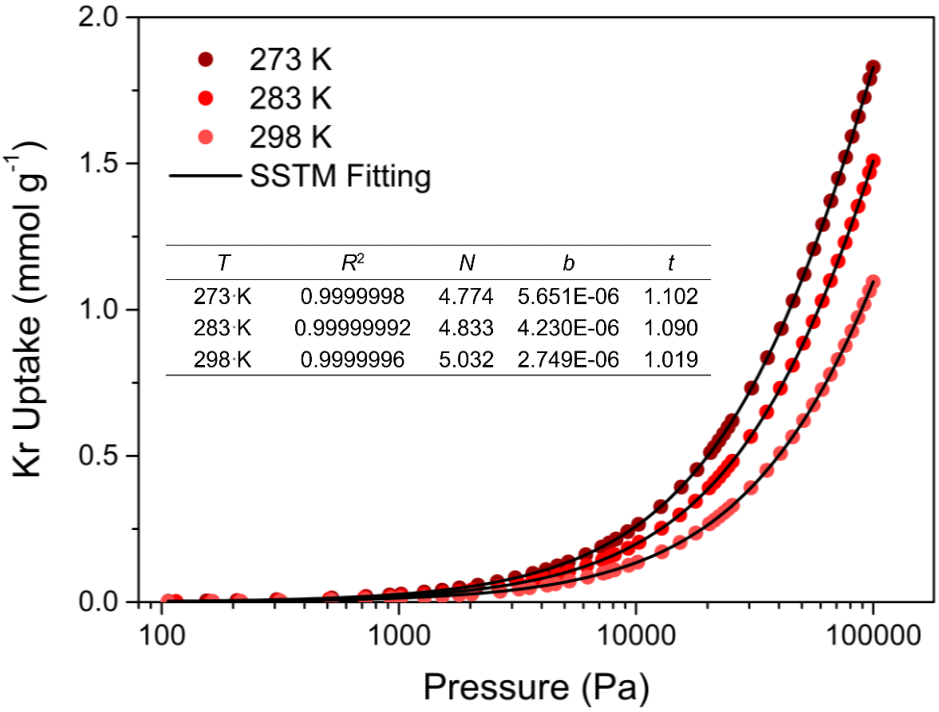


Figure S2.47. Single-site Tóth Model fitting (lines) of the Ag-MOF-303 Kr adsorption isotherms (points) measured at 273, 283, and 298 K.

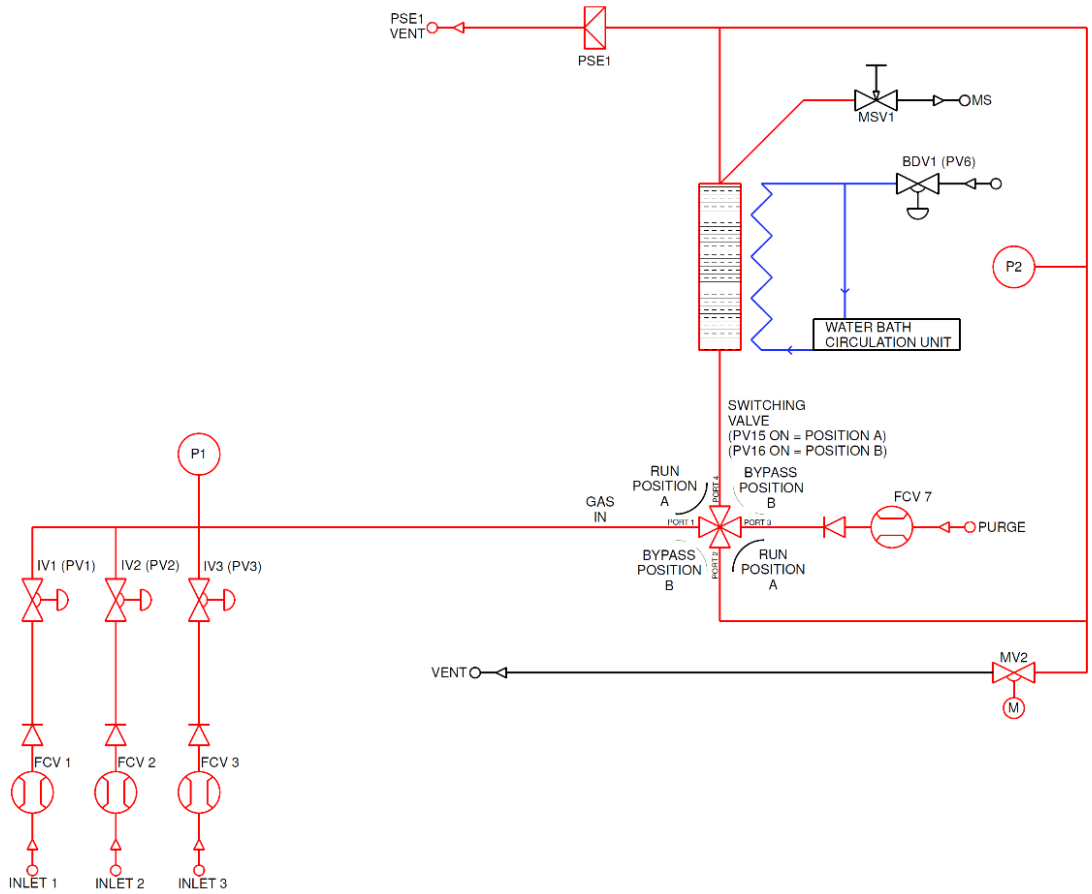
Table S2.5. Comparison of Xe capture properties in this work with benchmark materials.

	PSD	Uptake		Selectivity	Density	Q_{st}	Strategies	Ref.
		1 bar	0.2 bar					
	nm	$cm^3 cm^{-3}$	$cm^3 cm^{-3}$		$g\ cm^{-3}$	$kJ\ mol^{-1}$		
MOFs								
MOF-Cu-H (NJU-Bai7)	0.44	91	74	16.7[a]	1.27	33.4	Ultramicropore	31
$Zn(ox)_{0.5}(trz)$	0.63	97	73	10.2[a]	1.59	29.0	Ultramicropore	32
$(Ni/Co)_2$(m-dobdc)	1.1	146/157	68	10.1/11.8[a]	1.17	28.3/27.3	Open metal site	33
SIFSIX-3-Zn	0.38	110	66	9.2[a]	1.59	30.0	Ultramicropore	34
Ag-MOF-303	0.52	108	**59**	**10.4**[a]	1.44	28.2	**Metalation**	This chapter
$Co_3C_8H_2O_{10}$	~0.42	66	58	69.7[a]	2.20	43.6	Polar functional group	35
$Co_3(HCOO)_6$	0.5	80	55	12[b]	1.82	28.0	Ultramicropore	36
Ag@MOF-74-Ni	N.A.	129	55	6.8	1.19	N.A.	Ag nanoparticles	37
NKMOF-1-Ni	0.54	85	53	5.2[a]	1.75	34.2	Open metal site	38
MIL-120	0.54*0.47	70	50	9.6[a]	1.57	31.5	Ultramicropore	39
MOF-505	0.48	49	49	8.00[c]	0.99	N.A.	Open metal site	40
SIFSIX-3-Fe	0.37	83	47	N.A.	1.52	27.4	Dynamics	41
CaSDB (SBMOF-1)	0.5	51	44	20.5[d]	1.55	37.0	Ultramicropore	42
Cu-MOF-303	0.55	91	**41**	**8.2**[a]	1.27	24.4	**Metalation**	This chapter
Zr-Fum-Me	0.52, 0.55	74	40	11.7[a]	1.73	30.9	Polar functional group	43
SBMOF-2	0.65	76	39	10[a]	1.19	26.4	Polar functional group	44
SIFSIX-3-Cu	0.37	76	36	4.81[e]	1.61	N.A.	Ultramicropore	45
NU-403-PSDH	0.86, 1.0	72	35	6.36[a]	1.42	26.0	Postsynthetic defect	46
Zr-Fum (MOF-801)	0.66, 0.69	69	32	8.3[a]	1.63	25.3	Ultramicropore	43
CROFOUR-1-Ni	N.A.	47	29	22[a]	1.17	37.4	Anion	47
Co^{2+}-CPM-6	0.6, 0.75	80	28	9.3[a]	1.18	25.9	Cation	48

	PSD	Uptake		Selectivity	Density	Q_{st}	Strategies	Ref.
		1 bar	0.2 bar					
	nm	$cm^3 cm^{-3}$	$cm^3 cm^{-3}$		$g\ cm^{-3}$	$kJ\ mol^{-1}$		
NU-1106	1.0	58	28	10[d]	1.52	N.A.		49
MOF-303	0.87	92	**28**	**6.6**[a]	0.99	23.7	**Metalation**	This chapter
CPM-6	0.6, 0.70	72	28	7.3[a]	1.11	25.1	Cation	48
UTSA-74	1.0	81	28	8.4[a]	1.34	24.4	Open metal site	50
ZIF-69	0.72, 0.44	71	27	8.35[d]	1.30	24.9	Ultramicropore	51
CPM-5	0.6, 0.75	62	25	7.1[a]	1.13	25.0	Cation	48
CROFOUR-2-Ni	N.A.	46	24	15.5[a]	1.27	30.5	Anion	47
SCU-11	~2.3	72	22	5.7[d]	1.02	N.A.	Open metal site	52
UIO-66	0.93, 1.21	56	20	5.9[a]	1.26	24.6		43
SIFSIX-3-Ni	0.37	65	17	N.A.	1.63	18.9	Ultramicropore	41
Y-csq-MOF-1	0.64, 1.1, 1.6	38	17	10.7[b]	0.87	33.8	Open metal site	53
NU-403	0.95	54	16	2.84[a]	1.42	22.0		46
$Sr_4(TCPE)_2$	0.52	25	11	7[a]	1.32	19.4	Ultramicropore	54
ZU-62	0.5	137	7	N.A.	1.62	N.A.	Dynamic gating	55
MOF-5 Cage	0.88	29	4	2.4[f]	0.59	11.1		56
CC3	0.44	53	36	20.4[e]	0.97	31.3	Ultramicropore	57
Noria	0.5-0.7	N.A.	N.A.	9.4[a]	N.A.	26.9	Ultramicropore	58
Zeolite Ag@ZSM-5	N.A.	N.A.	N.A.	50[a]	N.A.	65.0	Ag nanoparticles	59

2.4.7 Breakthrough Measurements

Dynamic Xe/Kr column breakthrough measurement was carried out using an automated breakthrough analyzer-ABR systems (Scheme S3, manufactured by Hiden Isochema, Warrington, U.K.). There are four inlet gas lines, one is the purge gas (Ar) and the others are working gas. Firstly, the four-way valve is on position B to control the purge gas passing through the column to activate the sample, then the four-way valve is switched to position A to direct the working gas flow into the sample. The stream at the outlet of the column is monitored by an online mass spectrometry. The sample holder is a stainless steel column with a length of 7 cm and an internal diameter of 0.6 cm (V_{column} = 2.1 cm^3). Between the cycles the sample was reactivated by Ar flow (10 mL min^{-1}) for 25 min. 543 mg of powder MOF-303, 540 mg of powder Ag-MOF-303, or 461 mg of powder Cu-MOF-303 were used for dynamic gas breakthrough measurements. The flow rate was set to Xe/Kr = 0.8/3.2 (total flow rate = 4 mL min^{-1}).



Scheme S2.1. Apparatus setup of cycling packed column gas adsorption breakthrough experiments.

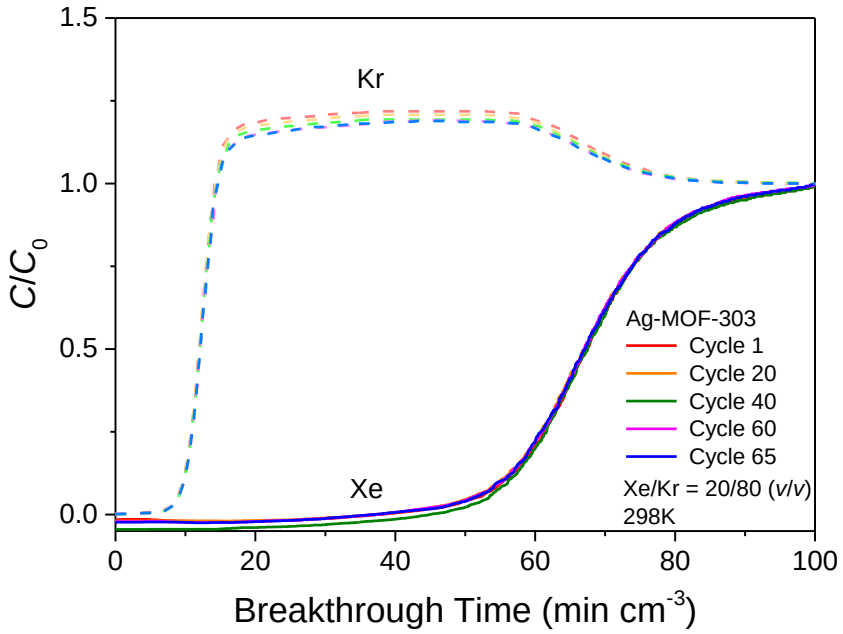


Figure S2.48. Cycling breakthrough curves of Ag-MOF-303 for Xe/Kr [20/80 (*v*/*v*)] mixed gas at 298 K with a flow rate of 4 mL min^{-1}, between the cycles the sample was regenerated by a 25-min purge with Ar of 10.0 mL min^{-1} at 298 K. Solid and dashed lines refer to Xe and Kr, respectively.

2.4.8 ^{129}Xe NMR Measurements

Xenon (Xe) with the natural abundance (26.4%) of the isotope ^{129}Xe was used for all the experiments. The MOF-303, Cu-, and Ag-MOF-303 samples were packed into glass tubes (outside diameter: 6 mm). The height of the samples in the glass tubes was about 20 mm. The samples were heated to 393 K with a heating rate of 1 K min^{-1} and kept at 393 K for 12 hours under vacuum to remove water and other organic solvents. Upon cooling, the samples were condensed with a known amount of xenon under the liquid N_2 condition. The tubes were then flame-fused for ^{129}Xe NMR investigation.

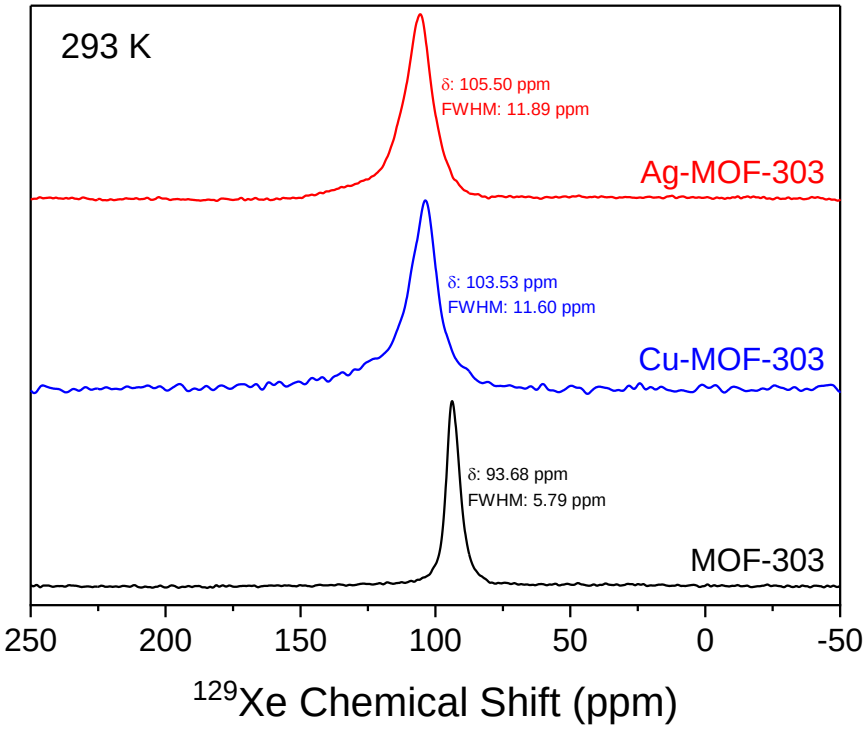


Figure S49. ^{129}Xe NMR spectra of MOF-303, Cu-, and Ag-MOF-303.

2.5 References

1. Yaghi, O. M.; Kalmutzki, M. J.; Diercks, C. S. *Introduction to Reticular Chemistry: Metal-Organic Frameworks and Covalent Organic Frameworks*, Wiley-VCH, Weinheim, **2019**.

2. a) Mulfort, K. L.; Farha, O. K.; Stern, C. L.; Sarjeant, A. A.; Hupp, J. T. *J. Am. Chem. Soc.* **2009**, *131*, 3866–3868; b) Ma, L.; Falkowski, J. M.; Abney, C.; Lin, W. *Nat. Chem.* **2010**, *2*, 838–847; c) Beyzavi, M. H.; Vermeulen, N. A.; Howarth, A. J.; Tussupbayev, S.; League, A. B.; Schweitzer, N. M.; Hupp, J.; Farha, O. K. *J. Am. Chem. Soc.* **2015**, *137*, 13624–13631; d) Baek, J.; Rungtaweevoranit, B.; Pei, X.; Park, M.; Fakra, S. C.; Liu, Y.; Matheu, R.; Alshmimri, S. A.; Alshehri, S.; Trickett, C. A.; Somorjai, G. A.; Yaghi, O. M. *J. Am. Chem. Soc.* **2018**, *140*, 18208–18216; e) Pi, W.; Feng, X.; Song, Y.; Xu, Z.; Li, Z.; Lin, W. *J. Am. Chem. Soc.* **2020**, *142*, 10302–10307; f) Peralta, R. A.; Huxley, M. T.; Evans, J. D.; Fallon, T.; Cao, H.; He, M.; Zhao, X.; Agnoli, S.; Sumby, C. J.; Doonan, C. J. *J. Am. Chem. Soc.* **2020**, *142*, 13533–13543.

3. a) Mondloch, J. E.; Bury, W.; Fairen-Jimenez, D.; Kwon, S.; DeMarco, E. J.; Weston, M. H.; Sarjeant, A. A.; Nguyen, S. T.; Stair, P. C.; Snurr, R. Q.; Farha, O. K.; Hupp, J. T.; *J. Am. Chem. Soc.* **2013**, *135*, 10294–10297; b) Yuan, S.; Chen, Y. P.; Qin, J.; Lu, W.; Wang, X.; Zhang, Q.; Zhou, H. C. *Angew. Chem. Int. Ed.* **2015**, *54*, 14696–14700; c) Kim, I. S.; Borycz, J.; Platero-Prats, A. E.; Tussupbayev, S.; Wang, T. C.; Farha, O. K.; Hupp, J. T.; Gagliardi, L.; Chapman, K. W.; Cramer, C. J.; Martinson, A. B. F. *Chem. Mater.* **2015**, *27*, 4772–4778; d) Li, Z.; Schweitzer, N. M.; League, A. B.; Bernales, V.; Peters, A. W.; Getsoian, A. B.; Wang, T. C.; Miller, J. T.; Vjunov, A.; Fulton, J. L.; Lercher, J. A.; Cramer, C. J.; Gagliardi, L.; Hupp, J. T.; Farha, O. K. *J. Am. Chem. Soc.* **2016**, *138*, 1977–1982; e) Abdel-Mageed, A. M.; Rungtaweevoranit, B.; Parlinska-Wojtan, M.; Pei, X.; Yaghi, O. M.; Behm, R. J. *J. Am. Chem. Soc.* **2019**, *141*, 5201–5210.

4. Evans, J. D.; Sumby, C. J.; Doonan, C. J. *Chem. Soc. Rev.* **2014**, *43*, 5933–5951.

5. a) Bloch, E. D.; Britt, D.; Doonan, C. J.; Uribe-Romo, F. J.; Furukawa, H.; Long, J. R.; Yaghi, O. M. *J. Am. Chem. Soc.* **2010**, *132*, 14382–14384; b) Shultz, A. M.; Sarjeant, A. A.; Farha, O. K.; Hupp, J. T.; Nguyen, S. T. *J. Am. Chem. Soc.* **2011**, *133*, 13252–13255; c) Morris, W.; Volosskiy, B.; Demir, S.; Gándara, F.; McGrier, P. L.; Furukawa, H.; Cascio, D.; Stoddart, J. F.; Yaghi, O. M. *Inorg. Chem.*, **2012**, *51*, 6443–6445. d) Bloch, W. M.; Burgun, A.; Coghlan, C. J.; Lee, R.; Coote, M. L.; Doonan, C. J.; Sumby, C. J. *Nat. Chem.* **2014**, *6*, 906–912.; e) Manna, K.; Zhang, T.; Lin, W. *J. Am. Chem. Soc.* **2014**, *136*, 6566–6569; f) Fei, H.; Cohen, S. M. *J. Am. Chem. Soc.* **2015**, *137*, 2191–2194.

6. a) Ingleson, M. J.; Barrio, J. P.; Guilbaud, J.-B.; Khimyak, Y. Z.; Rosseinsky, M. J. *Chem. Commun.* **2008**, 2680–2682; b) Doonan, C. J.; Morris, W.; Furukawa, H.; Yaghi, O. M. *J. Am. Chem. Soc.* **2009**, *131*, 9492–9493; c) Tanabe, K. K.; Cohen, S. M. *Angew. Chem., Int. Ed.* **2009**, *48*, 7424–7427; d) Gadzikwa, T.; Farha, O. K.; Mulfort, K. L.; Hupp, J. T.; Nguyen, S. T. *Chem. Commun.* **2009**, 3720–3722.

7. a) Wang, Y.; Liu, Q.; Zhang, Q.; Peng, B.; Deng, H. *Angew. Chem. Int. Ed.* **2018**, *57*, 7120–7125; b) Yan, W.; Li, S.; Yang, T.; Xia, Y.; Zhang, X.; Wang, C.; Yan, Z.; Deng, F.; Zhou, Q.; Deng, H. *J. Am. Chem. Soc.* **2020**, *142*, 16182–16187.

8. Karlin, K. D. *Science* **1993**, *261*, 701–708.

9. a) Fathieh, F.; Kalmutzki, M. J.; Kapustin, E. A.; Waller, P. J.; Yang, J.; Yaghi, O. M. *Sci. Adv.* **2018**, *4*, eaat3198; b) Hanikel, N.; Prévot, M. S.; Fathieh, F.; Kapustin, E. A.; Lyu, H.; Wang, H.; Diercks, N. J.; Glover, T. G.; Yaghi, O. M. *ACS Cent. Sci.* **2019**, *5*, 1699–1706.

10. a) Kolb, U.; Gorelik, T.; Kübel, C.; Otten, M. T.; Hubert, D. *Ultramicroscopy* **2007**, *107*, 507–513; b) Zhang, D.; Oleynikov, P.; Hovmöller, S.; Zou, X. *Z. Kristallogr.* **2010**, *225*, 94–102; c) Lu, H.; Miyasaka, K.; Terasaki, O.; Electron Diffraction. In Structure from Diffraction Methods, Eds.: Bruce, D. W.; O'Hare, D.; Walton, R. I. Wiley, **2014**, pp. 216–229; d) Huang, Z.; Grape, E. S.; Li, J.; Inge, A. K.; Zou, X. *Coordin. Chem. Rev.* **2021**, *427*, 213583.

11. a) Sun, T.; Wei, L.; Chen, Y.; Ma, Y.; Zhang, Y.-B. *J. Am. Chem. Soc.* **2019**, *141*, 10962–10966; b) Sun, T.; Lei, W.; Ma, Y.; Zhang, Y.-B. *Chin. J. Chem.* **2020**, *38*, 1153–1166.

12. Kau, L.-S.; Spira-Solomon, D. J.; Penner-Hahn, J. E.; Hodgson, K. O.; Solomon, E. I. *J. Am. Chem. Soc.* **1987**, *109*, 6433–6442.

13. a) Zhu, A.-X.; Xu, Q.-Q.; Liu, F.-Y.; Li, Z.; Qi, X.-L. *Inorg. Chim. Acta*, **2011**, *370*, 333–339; b) Chen, Y.; Li, L.; Cao, Y.; Wu, J.; Cao, Q.; Li, Y.; Hu, H.; Liu, W.; Liu, Y.; Kang, Z.; Li, J. *CrystEngComm*, **2013**, *15*, 2675–2681; c) Beheshtia, A.; Mousavifarda, E. S.; Noorizadeha, S.; Mayerb, P.; Woźniak, K. *Inorg. Chim. Acta*, **2019**, *497*, 119082.

14. a) Kerry, F. G. *Industrial Gas Handbook: Gas Separation and Puri-fication*, CRC Press, **2007**; b) Banerjee, D.; Cairns, A. J.; Liu, J.; Motkuri, R. K.; Nune, S. K.; Fernandez, C. A.; Krishna, R.; Strachan, D. M.; Thallapally, P. K. s*Acc. Chem. Res.* **2015**, *48*, 211–219.

15. a) Gücüyener, C.; van den Bergh, J.; Gascon, J.; Kapteijn, F. *J. Am. Chem. Soc.* **2010**, *132*, 17704–17706; b) Bloch, E. D.; Queen, W. L.; Krishna, R.; Zadrozny, J. M.; Brown, C. M.; Long, J. R. *Science* **2012**, *335*, 1606–1610; c) Cadiau, A.; Adil, K.; Bhatt, P. M.; Belmabkhout, Y.; Eddaoudi, M. *Science* **2016**, *353*, 137–140; d) Li, L.; Lin, R.-B.; Krishna, R.; Li, H.; Xiang, S.; Wu, H.; Li, J.; Zhou, W.; Chen, B. *Science* **2018**, *362*, 443–446; e) Banerjee, D.; Simon, C. M.; Elsaidi, S. K.; Haranczyk, M.; Thallapally, P. K. *Chem* **2018**, *4*, 466–494; f) Lin, R.; Xiang, S.; Zhou, W.; Chen, B. *Chem* **2020**, *6*, 337–363.

16. Li, J. R.; Kuppler, R. J.; Zhou, H. C. *Chem. Soc. Rev.* **2009**, *38*, 1477–1504.

17. a) Meek, S. T.; Teich-McGoldrick, S. L.; Perry, J. J.; Greathouse, J. A.; Allendorf, M. D. *J. Phys. Chem. C* **2012**, *116*, 19765–19772; b) Chen, X.; Plonka, A. M.; Banerjee, D.; Krishna, R.; Schaef, H. T.; Ghose, S.; Thallapally, P. K.; Parise, J. B. *J. Am. Chem. Soc.* **2015**, *137*, 7007–7010; c) Lee, S.-J.; Kim, S.; Kim, E.-J.; Kim, M.; Bae, Y.-S. *Chem. Eng. J.* **2018**, *335*, 345–351; d) Li, L.; Guo, L.; Zhang, Z.; Yang, Q.; Yang, Y.; Bao, Z.; Ren, Q.; Li, J. *J. Am. Chem. Soc.* **2019**, *141*, 9358–9364.

18. a) Mohamed, M. H.; Elsaidi, S. K.; Pham, T.; Forrest, K. A.; Schaef, H. T.; Hogan, A.; Wojtas, L.; Xu, W.; Space, B.; Zaworotko, M. J.; Thallapally, P. K. *Angew. Chem. Int. Ed.* **2016**, *55*, 8285–8289; b) Elsaidi, S. K.; Mohamed, M. H.; Simon, C. M.; Braun, E.; Pham, T.; Forrest, K. A.; Xu, W.; Banerjee, D.; Space, B.; Zaworotko, M. J.; Thallapally, P. K. *Chem. Sci.* **2017**, *8*, 2373–2380; c) Wang, Q.; Ke, T.; Yang, L.; Zhang, Z.; Cui, X.; Bao, Z.; Ren, Q.; Yang, Q.; Xing, H. *Angew. Chem. Int. Ed.* **2020**, *59*, 3423–3428.

19. a) Kuznicki, S. M.; Ansón, A.; Koenig, A.; Kuznicki, T. M.; Haastrup, T.; Eyring, E. M.; Hunter, D. *J. Phys. Chem. C* **2007**, *111*, 1560–1562; b) Daniel, C.; Elbaraoui, A.; Aguado, S.; Springuel-Huet, M.-A.; Nossov, A.; Fontaine, J.-P.; Topin, S.; Taffary, T.; Deliere, L.;

Schuurman, Y.; Farrusseng, D. *J. Phys. Chem. C* **2013**, *117*, 15122–15129; c) Perry, J. J.; Teich-McGoldrick, S. L.; Meek, S. T.; Greathouse, J. A.; Haranczyk, M.; Allendorf, M. D. *J. Phys. Chem. C* **2014**, *118*, 11685–11698; d) Kapelewski, M. T.; Oktawiec, J.; Runčevski, T.; Gonzalez, M. I.; Long, J. R. *Isr. J. Chem.* **2018**, *58*, 1138–1143; e) Wang, Y.; Liu, W.; Bai, Z.; Zheng, T.; Silver, M. A.; Li, Y.; Wang, Y.; Wang, X.; Diwu, J.; Chai, Z.; Wang, S. *Angew. Chem. Int. Ed.* **2018**, *57*, 5783–5787.

20. Karle, J.; Hauptman, H. *Acta Cryst.* **1950**, *3*, 181.
21. Burla, M. C.; Caliandro, R.; Carrozzini, B.; Cascarano, G. L.; Cuocci, C.; Giacovazzo, C.; Mallamo, M.; Mazzone, A.; Polidori, G. *J. Appl. Cryst*. **2015**, *48*, 306–309.
22. Sheldrick, G. M. A short history of SHELX. *IUCr* **2008**, *64*, 112–122.
23. Dolomanov, O. V.; Bourhis, L. J.; Gildea, R. J.; Howard, J. A. K.; Puschmann, H. OLEX2: a complete structure solution, refinement and analysis program. *J. Appl. Cryst.* **2009**, *42*, 339–341.
24. Marcus M.; MacDowell A.; Celestre R.; Manceau A.; Miller T.; Padmore H.; Sublett R. Beamline 10.3.2 at ALS: A Hard X-ray Microprobe for Environmental and Materials Sciences. *J. Synchrotron Radiat.* **2004**, *11*, 239–247.
25. Kraft, S.; Stümpel, J.; Becker, P.; Kuetgens, U. High Resolution X-ray Absorption Spectroscopy with Absolute Energy Calibration for the Determination of Absorption Edge Energies. *Rev. Sci. Instrum.* **1996**, *67*, 681–687.
26. Kelly, S.; Hesterberg, D.; Ravel, B. Analysis of Soils and Minerals Using X-ray Absorption Spectroscopy. *Methods of soil analysis. Part 5. Mineralogical methods;* Soil Science Society of America: Madison, WI, **2008**; pp 367–463.
27. Ravel, B.; Newville, M. ATHENA, ARTEMIS, HEPHAESTUS: Data Analysis for X-ray Absorption Spectroscopy Using IFEFFIT. *J. Synchrotron Radiat.* **2005**, *12*, 537–541.
28. Newville, M. IFEFFIT: Interactive XAFS Analysis and FEFF fitting. *J. Synchrotron Radiat.* **2001**, *8*, 322–324.
29. Tóth, J. Uniform Interpretation of Gas/Solid Adsorption. *Adv. Colloid Interface Sci.* **1995**, *55*, 1–239.
30. Tóth, J. State Equation of the Solid-Gas Interface Layers. *Acta Chim. Acad. Sci. Hung.* **1971**, *69*, 311–317.
31. Xiong, S.; Gong, Y.; Hu, S.; Wu, X.; Li, W.; He, Y.; Chen, B.; Wang, X. *J. Mater. Chem. A* **2018**, *6*, 4752–4758.
32. Yu, L.; Xiong, S.; Lin, Y.; Li, L.; Peng, J.; Liu, W.; Huang, X.; Wang, H.; Li, J. *Inorg. Chem.* **2019**, *58*, 15025–15028.
33. Kapelewski, M. T.; Oktawiec, J.; Runčevski, T.; Gonzalez, M. I.; Long, J. R. *Isr. J. Chem.* **2018**, *58*, 1138–1143.
34. Liu, Y.; Liu, J.; Hu, J. *BMC Chem. Eng.* **2019**, *1*, 3.
35. Li, L.; Guo, L.; Zhang, Z.; Yang, Q.; Yang, Y.; Bao, Z.; Ren, Q.; Li, J. *J. Am. Chem. Soc.* **2019**, *141*, 9358–9364.

36. Wang, H.; Yao, K.; Zhang, Z.; Jagiello, J.; Gong, Q.; Han, Y.; Li, J. *Chem. Sci.* **2014**, *5*, 620–624.

37. Liu, J.; Strachan, D. M.; Thallapally, P. K. *Chem. Commun. (Cambridge, U. K.)* **2014**, *50*, 466–468.

38. Wang, T.; Peng, Y.-L.; Lin, E.; Niu, Z.; Li, P.; Ma, S.; Zhao, P.; Chen, Y.; Cheng, P.; Zhang, Z. *Inorg. Chem.* **2020**, *59*, 4868–4873.

39. Zhang, P.; Zhong, Y.; Yao, Q.; Liu, X.; Zhang, Y.; Wang, J.; Deng, Q.; Zeng, Z.; Deng, S. *J. Chem. Eng. Data* **2020**, *65*, 4018–4023.

40. Bae, Y.-S.; Hauser, B. G.; Colón, Y. J.; Hupp, J. T.; Farha, O. K.; Snurr, R. Q. *Microporous Mesoporous Mater.* **2013**, *169*, 176–179.

41. Elsaidi, S. K.; Mohamed, M. H.; Simon, C. M.; Braun, E.; Pham, T.; Forrest, K. A.; Xu, W.; Banerjee, D.; Space, B.; Zaworotko, M. J.; Thallapally, P. K. *Chem. Sci.* **2017**, *8*, 2373–2380.

42. Yu, G.; Liu, Y.; Zou, X.; Zhao, N.; Rong, H.; Zhu, G. *J. Mater. Chem. A* **2018**, *6*, 11797–11803.

43. Yan, Z.; Gong, Y.; Chen, B.; Wu, X.; liu, Q.; Cui, L.; Xiong, S.; Peng, S. *Sep. Purif. Technol.* **2020**, *239*, 116514.

44. Chen, X.; Plonka, A. M.; Banerjee, D.; Krishna, R.; Schaef, H. T.; Ghose, S.; Thallapally, P. K.; Parise, J. B. *J. Am. Chem. Soc.* **2015**, *137*, 7007–7010.

45. Elsaidi, S. K.; Mohamed, M. H.; Helal, A. S.; Galanek, M.; Pham, T.; Suepaul, S.; Space, B.; Hopkinson, D.; Thallapally, P. K.; Li, J. *Nat. Commun.* **2020**, *11*, 3103.

46. Idrees, K. B.; Chen, Z.; Zhang, X.; Mian, M. R.; Drout, R. J.; Islamoglu, T.; Farha, O. K. *Chem. Mater.* **2020**, *32*, 3776–3782.

47. Mohamed, M. H.; Elsaidi, S. K.; Pham, T.; Forrest, K. A.; Schaef, H. T.; Hogan, A.; Wojtas, L.; Xu, W.; Space, B.; Zaworotko, M. J.; Thallapally, P. K. *Angew. Chem. Int. Ed.* **2016**, *55*, 8285–8289.

48. Liu, B.-y.; Gong, Y.-j.; Wu, X.-n.; Liu, Q.; Li, W.; Xiong, S.-s.; Hu, S.; Wang, X.-l. *RSC Advances* **2017**, *7*, 55012–55019.

49. Maldonado, R. R.; Zhang, X.; Hanna, S.; Gong, X.; Gianneschi, N. C.; Hupp, J. T.; Farha, O. K. *Dalton Trans.* **2020**, *49*, 6553–6556.

50. Tao, Y.; Fan, Y.; Xu, Z.; Feng, X.; Krishna, R.; Luo, F. *Inorg. Chem.* **2020**, *59*, 11793–11800.

51. Luo, S.; Ma, F.; Wang, X.; Yuan, M.; Chen, L.; Qiu, S.; Tang, Q.; Wang, S. *J. Radioanal. Nucl. Chem.* **2020**, *324*, 1275–1281.

52. Wang, Y.; Liu, W.; Bai, Z.; Zheng, T.; Silver, M. A.; Li, Y.; Wang, Y.; Wang, X.; Diwu, J.; Chai, Z.; Wang, S. *Angew. Chem. Int. Ed.* **2018**, *57*, 5783–5787.

53. Angeli, G. K.; Sartsidou, C.; Vlachaki, S.; Spanopoulos, I.; Tsangarakis, C.; Kourtellaris, A.; Klontzas, E.; Froudakis, G. E.; Tasiopoulos, A.; Trikalitis, P. N. *ACS Appl. Mater. Interfaces* **2017**, *9*, 44560–44566.

54. Xiong, J.; Li, A.; Fan, Y.; Xu, Z.; Feng, H.; Gao, Q.; Fan, Q.; He, Y.; Gao, Z.; Luo, F. *J. Solid State Chem.* **2020**, *288*, 121337.

55. Wang, T.; Ke, T.; Yang, L.; Zhang, Z.; Cui, X.; Bao, Z.; Ren, Q.; Yang, Q.; Xing, H. *Angew. Chem. Int. Ed.* **2020**, *59*, 3423–3428.

56. Greathouse, J. A.; Kinnibrugh, T. L.; Allendorf, M. D. *Ind. Eng. Chem. Res.* **2009**, *48*, 3425–3431.

57. Chen, L.; Reiss, P. S.; Chong, S. Y.; Holden, D.; Jelfs, K. E.; Hasell, T.; Little, M. A.; Kewley, A.; Briggs, M. E.; Stephenson, A.; Thomas, K. M.; Armstrong, J. A.; Bell, J.; Busto, J.; Noel, R.; Liu, J.; Strachan, D. M.; Thallapally, P. K.; Cooper, A. I. *Nat. Mater.* **2014**, *13*, 954–960.

58. Patil, R. S.; Banerjee, D.; Simon, C. M.; Atwood, J. L.; Thallapally, P. K. *Chem. Eur. J.* **2016**, *22*, 12618–12623.

59. Deliere, L.; Coasne, B.; Topin, S.; Gréau, C.; Moulin, C.; Farrusseng, D. *Chem. Eur. J.* **2016**, *22*, 9660–9666.

Chapter 3. Design of MOFs with Absolute Structures

Portions of this chapter have been published in:
Wang, H.; Pei, X.; Proserpio D. M.; Yaghi, O. M. *Isr. J. Chem.* **2021**, *61*, 774–781.

3.1 Introduction

Metal-organic frameworks (MOFs) are crystalline porous structures constructed by joining metal-containing units [secondary building units (SBUs)] with organic linkers by strong bonds.[1] In the past twenty five years, MOFs have attracted great attention with exponential growth of research, owing to their tunable chemical environment for applications in areas such as gas separation and catalysis.[2–4] These applications are dependent on the choice of building blocks and synthetic procedures, size and shape of pores in MOFs and the interactions between guests and frameworks. In particular, the stereochemistry of the framework plays a vital role in determining properties of MOFs and has wide applications in asymmetric catalysis, enantioselective separation, and structure determinations of small molecules with absolute configurations.[5–17] Thus, the study of MOFs with absolute structures is important in the field of MOF chemistry.

Absolute structures are divided into two categories: chiral structures, and achiral but non-centrosymmetric structures.[18] While the MOFs of the second kind haven't been systematically studied, chiral MOFs are of broad interest and many attempts toward the syntheses of chiral MOFs have been reported. The synthetic strategies of obtaining such MOFs include: (i) direct synthesis of MOFs by using chiral ligands,[19–22] (ii) post-synthetic modification of achiral MOFs with chiral auxiliaries,[23–26] (iii) chiral induction of MOFs with achiral building units by using chiral templates.[27–29] These synthetic methods have been extensively developed, however, most require the use of chiral species. Compared with using chiral ligands or templates, it is more challenging to synthesize chiral MOFs from achiral starting materials since the chirality of MOFs is relatively unpredictable during the synthesis. As there are limited reports in this research topic,[30–32] this is also an important topic as enantiopure compounds are not always easy to obtain.

Here, we report the synthesis and structure of a new Al-based MOF with absolute structure, MOF-829 [$Al_3(\mu_3\text{-}O)(OH)(H_2O)_2(BTB)_2$, BTB = 1,3,5-benzenetribenzoate]. By comparing it with a reported chiral MOF, MOF-520 [$Al_8(\mu\text{-}OH)_8(HCOO)_4(BTB)_4$], we analyze the role of building units (SBUs and linkers) and topology in producing MOFs with absolute structures, and further the influence of synthetic procedures on obtaining such MOFs without the need of auxiliary chiral inducers. These two MOFs are synthesized from the same metal ions and organic linkers, however, careful tuning of the modulators in the synthesis leads to the formation of different SBUs with and without intrinsic chirality, and thus directing the formation of MOFs with distinct structures.

3.2 Experimental Section

3.2.1 Materials and Methods

Aluminum chloride ($AlCl_3$) and formic acid were obtained from Acros Organics. 1,3,5-benzenetribenzoic acid (H_3BTB) and *N*,*N*-diethylformamide (DEF) were purchased from TCI America. All chemicals were used without further purification.

The topology of MOF-829 was analyzed by the following procedure: (1) for checking the topology in RCSR database,[33] the single-crystal structure of MOF-829 was first reduced by substituting SBUs and linkers with atoms at their centers-of-gravity. The connectivity was then calculated in ToposPro[34] based on close contact. The obtained adjacent matrix was further rectified to make sure it matches the chemical connectivity in the original MOF structure. The established reduced structure was exported into .cgd file and then imported into Systre[35] for topology analysis. (2) To check the underlying net of MOF-829 in the TTD database,[36] the CIF file was analyzed by ToposPro[34] and TopCryst.[37]

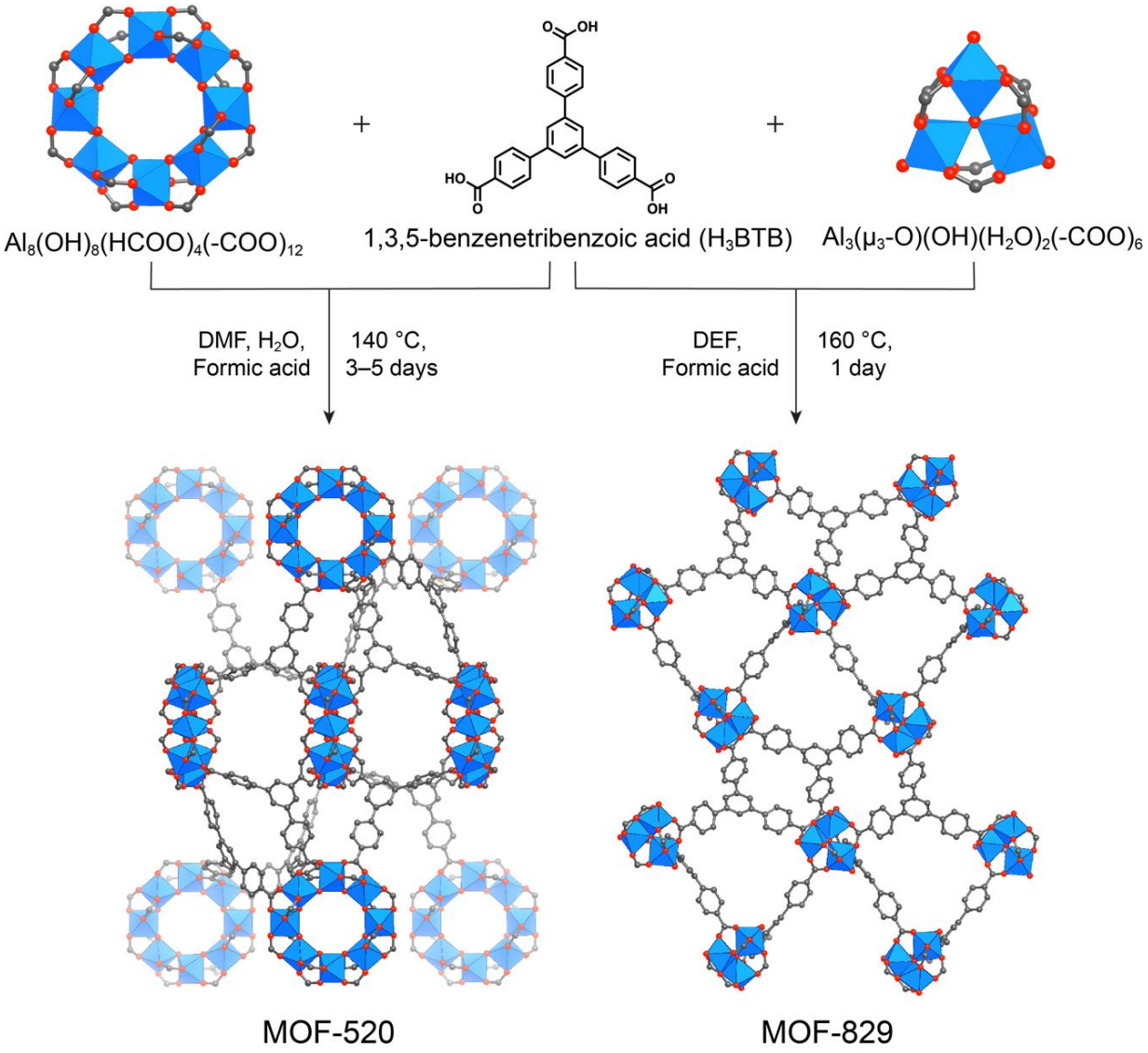


Figure 3.1 Synthesis and structures of MOF-520 and MOF-829 (CCDC deposition number: 1488944, 1488951 and 2101022. The two structures of MOF-520 are with different chiralities, which will be discussed in detail in Section 3.3.2). MOF-520 is built from SBU $[Al_8(OH)_8(HCOO)_4(\text{-}COO)_{12}]$ and BTB linker. Each SBU is linked by twelve BTB linkers, and each BTB linker is bound to three different SBUs. The structure of MOF-520 is formed in 3,12-connected fon topology. MOF-829 is comprised of the SBU, $[Al_3(\mu_3\text{-}O)(OH)(H_2O)_2(\text{-}COO)_6]$, and BTB linker. Each SBU is connected to six carboxylate groups from six BTB linkers, forming the extended structure in 3,6-connected 3,3,3,3,6,6T23 net. Color code: Al, blue; O, red; C, gray. H atoms are omitted for clarity.

3.2.2 Synthetic Procedure

Preparation of MOF-829: $AlCl_3$ (3.3 mg, 0.0251 mmol) and H_3BTB (7.4 mg, 0.0168 mmol) were dissolved in a solvent mixture of DEF/formic acid (1.788 mL/0.112 mL) in a 4 mL pressure tube. The mixture was heated at 160 °C for one day and block colorless crystals were obtained.

3.2.3 Determination and Refinement of the Single-Crystal X-ray Structure

The single-crystal X-ray structure of MOF-829 was measured on a Rigaku XtaLAB P200 equipped with a MicroMax 007HF rotating anode and a Pilatus 200K hybrid pixel array detector. A single crystal of MOF-829 of 0.22 × 0.16 × 0.15 mm was mounted on a capillary base and placed in a 150 K nitrogen cold stream (slightly above the melting by Cu Kα radiation with omega scans. The data was integrated using CrysAlis Pro software package and scaled by the SCALE3 ABSPACK.[38] The space group was determined to be *Pca*2_1. The primary structure solution was obtained using SHELXT-2018/02[39] and the full-matrix least-square refinement on F^2 was done by SHELXL-2018/03,[40] both using the Olex2[41] software package. All the non-hydrogen atoms were refined anisotropically and hydrogens were placed at geometrically-calculated positions. The structure was refined as an inversion twin (detailed discussion in section 3.3). Olex2 solvent mask procedure[42] was applied; the masked volume and total number of masked electrons are 22408.0 $Å^3$ and 6666.9 e^-, respectively. The percentage of void space is 76.8%. Weighing scheme was refined to converge at the end. Detailed statistics on the data quality and the quality of structure solution are summarized in **Table 1**. The crystallographic information file (CIF) of the structure can be accessed from Cambridge Structure Database (CSD) via deposition number 2101022.

Table 3.1 Measurement details, data quality and refinement quality of the single-crystal structure of MOF-829.

	Before SQUEEZE	After SQUEEZE
Formula	$Al_6C_{108}O_{32}H_{70}$·x(DMF)	$Al_6C_{108}O_{32}H_{70}$
Formula weight	2041.52 + x(DMF)	2041.52
Temperature/K	150	150
Crystal system	orthorhombic	orthorhombic
Space group	*Pca*2_1	*Pca*2_1
a/Å	34.5751(3)	34.5751(3)
b/Å	18.3942(2)	18.3942(2)
c/Å	45.8595(4)	45.8595(4)
Volume/$Å^3$	29165.8(5)	29165.8(5)
Z	4	4
ρ_{calc} (g/cm^3)	0.465	0.465
μ/mm^{-1}	0.450	0.450
F(000)	4208.0	4208.0
Crystal size/mm^3	0.22 × 0.16 × 0.15	0.22 × 0.16 × 0.15
Radiation	Cu Kα (λ = 1.54178 Å)	Cu Kα (λ = 1.54178 Å)
2θ range for data collection/°	5.774 to 139.052	5.774 to 139.052
Index ranges	-41 ≤ h ≤ 42 -22 ≤ k ≤ 22 -54 ≤ l ≤ 55	-41 ≤ h ≤ 42 -22 ≤ k ≤ 22 -54 ≤ l ≤ 55
Reflections collected	795662	795662

Independent reflections	54113 (R_{int} = 0.0685, R_{sigma} = 0.0274)	54113 (R_{int} = 0.0685, R_{sigma} = 0.0274)
Restrains and parameters	1/1316	1/1316
Goodness-of-fit on F^2	1.670	0.960
Final R indexes [I>=2σ (I)]	R_1 = 0.1629 wR_2 = 0.3663	R_1 = 0.0295 wR_2 = 0.0761
Final R indexes [all data]	R_1 = 0.1780 wR_2 = 0.3753	R_1 = 0.0364 wR_2 = 0.0792
Largest diff. peak/hole / e $Å^{-3}$	1.79/-0.74	0.38/-0.31
Flack parameter	0.40(5)[a]	0.434(11)
Hooft parameter		0.425(2)
Parsons parameter		0.441(4)

[a] The parameters before SQUEEZE intrisically contains errors caused by solvent scattering. The values and their standard uncertainties should be viewed critically.

3.3 Results and Discussions

3.3.1 Synthesis and Structure of MOF-829 and MOF-520

MOF-829 is built from a trinuclear SBU $[Al_3(\mu_3\text{-}O)(OH)(H_2O)_2(\text{-}COO)_6]$: One of the six corners in each AlO_6 octahedron is shared with the other two octahedra through a μ_3-oxygen atom, four of corners are bridged by carboxylate groups with adjacent aluminum ions, and the last corner is capped by either OH^- or H_2O (the number of hydrogen is derived based on charge balance). Each SBU is connected to six carboxylate groups from six linkers, forming the extended structure in the newly identified 3,6-connected net (Figure 3.1 and 3.4b).

MOF-520 was obtained from the same metal ions [Al(III)] and linkers (BTB) as MOF-829 however different synthetic conditions.[10] The metal source used in this synthesis is $Al(NO_3)_3 \cdot 9H_2O$, with more water of hydration compared to the anhydrous $AlCl_3$ used for MOF-829. Finely-tuned trace amount of water was also added to match the required water content for producing MOF-520. With a lower reaction temperature (140 °C) and the presence of higher water content in the synthetic media, the Al^{3+} ions likely went through a milder hydrolysis process and longer aggregation time.[43,44] As a result, the SBUs of MOF-520 are larger and composed of eight circularly-arranged aluminum octahedra. Every two adjacent aluminum atoms share corners through μ-OH groups, and in addition are bridged by two carboxylate groups. The total of sixteen bridging carboxylate groups of each SBU come from both formate and BTB linkers. Each SBU is linked by twelve BTB linkers, and each BTB linker binds to three different SBUs. The structure of MOF-520 is therefore formed in the 3,12-connected **fon** topology (Figure 3.1 and 3.4a).[45]

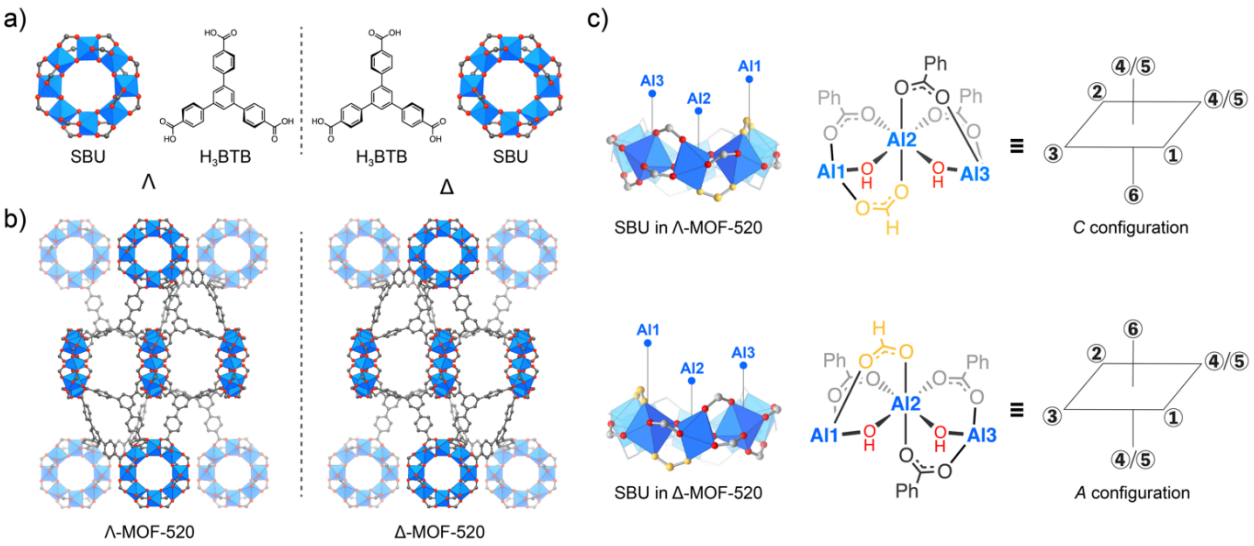


Figure 3.2 a) Illustration of the SBUs and BTB linkers in Λ- and Δ-MOF-520. b) The structure of Λ- and Δ-MOF-520. Color code: Al, blue; O, red; C, gray. H atoms are omitted for clarity. Dashed lines in (a) and (b) indicates configurations are mirrored to each other. c) Left: Al ions of different chemical environments and their locations in SBU. Middle: the coordination octahedra of Al2 in both MOFs, formate groups are highlighted in yellow and the linkers on the back are colored in gray. Right: the ligand priority of the two kinds of Al2 octahedron determined by the CIP rule are numbered in corresponding schemes. Structures of Δ- and Λ-MOF-520 can be accessed from CSD via deposition number 1488944 and 1488951, respectively.

3.3.2 Absolute Structure of MOF-520

As a MOF that crystallizes in enantiopure single crystals, the absolute configurations of MOF-520 have already been reported in our previous study[8,10] and demonstrated great application in facilitating the single-crystal structure determination of complex chiral compounds. The notation of the enantiomorphs of MOF-520 in the previous work was simply based on the conformations of the BTB linkers (Λ and Δ; Figure 3.2a,b) as the achiral H_3BTB molecules adopt chiral atomic arrangements in MOF-520 crystals, however, the chirality of SBUs was not discussed. The origin of the absolute configuration of the SBUs in MOF-520 can be understood from two aspects. The first is the arrangement of the coordinating formate groups: it follows the chiral site symmetry of the SBU, 222 (D_2) without having additional local symmetry operations.[46] On the second aspect, the chiral arrangement of formate groups and other carboxylate from linkers decides the coordination asymmetry of the aluminum octahedra, thus allowing the notation of the absolute configuration of the SBUs through the nomenclature for octahedral chiral complexes (Figure 3.2c, left). A traditional approach for analyzing the stereochemistry of coordination centers was performed based on IUPAC recommendation.[47] As a result, there are three kinds of aluminum octahedra in the crystal structure: the coordination spheres of Al1 and Al3 contain mirror planes (not considering the absolute geometry of the ligands) thus no absolute configuration, while the sequence of ligand arrangement [assigned by Cahn-Ingold-Prelog (CIP) convention] determines the chirality to Al2 octahedron (Figure 3.2c, middle and right). It is found that only *A* configuration of Al2 exists in Λ-MOF-520, meanwhile only *C* configuration of Al2 exists in Δ-MOF-520. Therefore, the chirality of a MOF-520 crystal is not only determined by the conformation of the linker, but also the absolute configuration of the SBU.

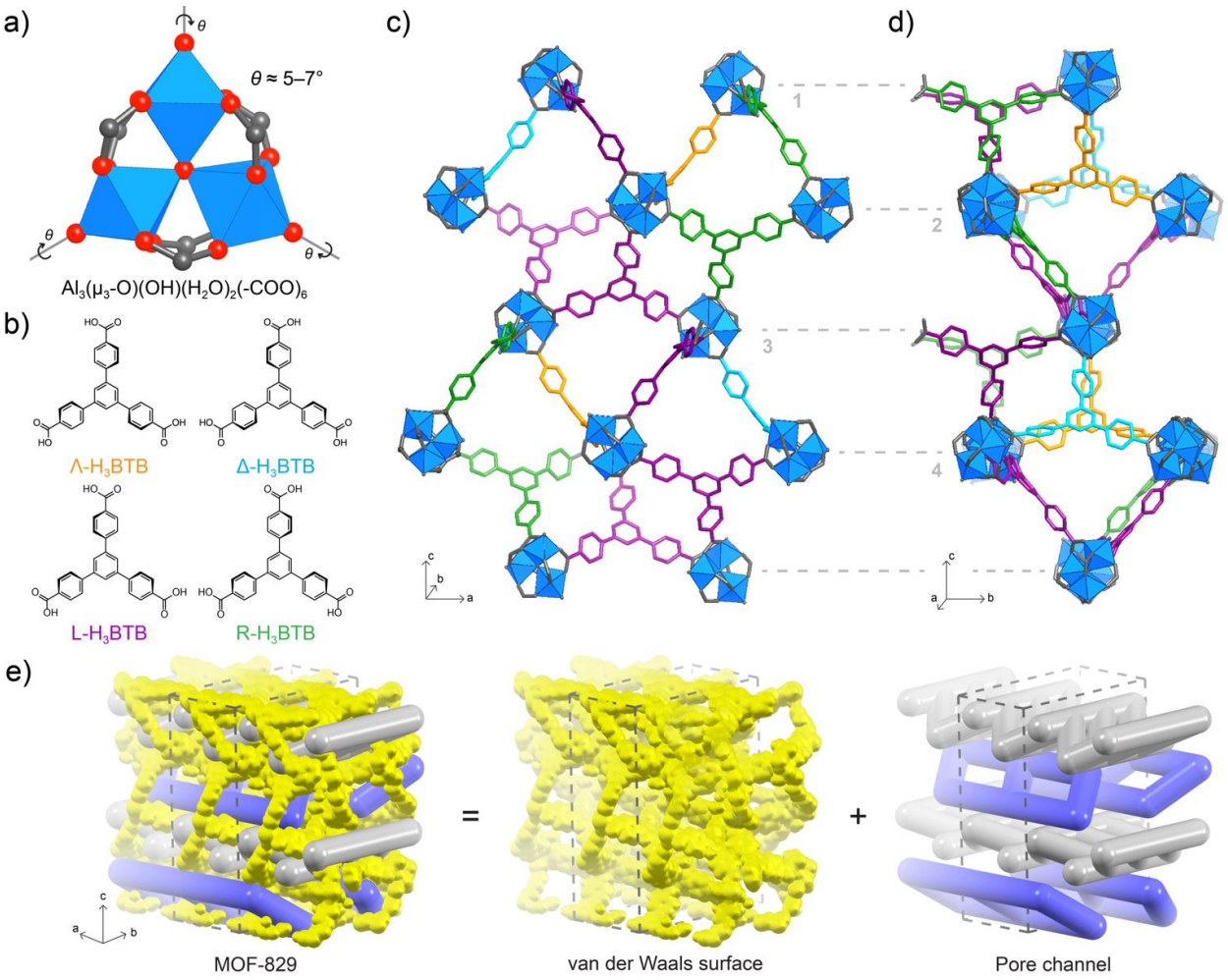


Figure 3.3 a) The tri-aluminum SBU in MOF-829. (CSD deposition number 2101022.) b) The BTB linker adopts four kind of conformations (Λ, Δ, L, and R) in MOF-829. c) The arrangement of Λ-, Δ-, L-, and R-H_3BTB linkers in MOF-829 viewed along the *b* axis. The linkers are arranged in four layers separated by Al SBUs, where the first and the third layers consist of all four conformations of the linkers, while the second and the fourth layers only comprise L- and R-BTB linkers. (d) The arrangement of Λ-, Δ-, L-, and R-BTB linkers in MOF-829 viewed along the *a* axis. Color code: Al, blue; O, red in (a), gray in (c) and (d); C, gray. Λ-BTB linker, light orange; Δ-BTB linker, sky blue; L-BTB linker, violet; R-BTB linker, green. H atoms are omitted for clarity. e) Illustration of the pore channel structures of MOF-829. Grey cylinders represent the interconnected pore channels in layer 1 and layer 3, while violet cylinders represent the interconnected pore channels in layer 2 and 4. The diameter of the cylinders is *ca.* 7.5 Å. The grey and violet channels further connect at where the cylinder surfaces intersect, forming a 3D channel framework. Dashed lines outline the unit cell.

3.3.3 Absolute Structure of MOF-829

Unlike the SBU of MOF-520, the tri-aluminum SBU is traditionally viewed as an centrosymmetric unit with point symmetry of $\bar{6}2m$ (D_{3h}). Although there is a slight deviation on the geometry of the SBUs in MOF-829 that the aluminum octahedra all rotates clockwise/anticlockwise for 5–7 degrees around the μ_3-O–Al axes (Figure 3.3a), they are still close to their ideal geometry and the

SBU is thus considered as pseudo-centrosymmetric. The BTB linker in the crystal structure of MOF-829 appears in four kinds of conformations (Figure 3.3b). While two of them are of the same propeller-shape as in MOF-520 (Λ and Δ), there are two additional chiral conformations that can be regarded as one of the propeller blades flipping to the opposite orientation (annotated as L and R in the following text). Despite having two pairs of enantiomers, all of the four conformations of BTB present in the same crystal of MOF-829 due to the existence of glide planes in the space group. The combination of racemic linkers conformations and pseudo-centrosymmetric SBUs derives the achiral structure of MOF-829. However, the non-centrosymmetric space group ($Pca2_1$) indicates that it still has an absolute structure, although there are no enantiomorphs.[48]

Determination of the absolute structure was carefully performed. The diffraction data collections at shorter X-ray wavelengths indicated that such energies cannot generate sufficient anomalous scattering to differentiate the intensities of Friedel pairs (FRIEDIF = 38 at λ = 0.7288 Å, calcualted by PLATON),[49,50] therefore, longer wavelengths (Cu Kα) were chosen to obtained the reported dataset (FRIEDIF = 166).[51] Additionally, the data collection strategy covered full sphere of reciprocal space so that it ensured a Friedel coverage of 98% for a Flack parameter with reliable standard uncertainty.[18a] The correct determination of the Flack parameter is also confirmed by its agreement with the Hooft and the Parsons parameters (Table 3.1).[52] The relatively small standard uncertainty obtained with good measurement rules out the possibility of that the absolute structure is ambigious,[18a,53] furthermore the obtained structure was carefully inspected and no additional symmetry (especially inversion symmetry) was found. Thus, the structure is not a centrosymmetric structure wrongly solved in non-centrosymmetric space group, and the relatively large Flack parameter is a result of inversion twinning. In fact, the non-centrosymmetric structural feature can be thoroughly understood from the arrangement of the building units along the *c* axis, the polar axis of $Pca2_1$. A structure fragment in one unit cell range representing these features is illustrated in Figure 3.3c and 3.3d. When viewing from the *b* axis, the linkers are arranged in four layers separated by Al SBUs, where the first and the third layers consist of all four conformations of the linkers, while the second and the fourth layers only comprise L- and R-BTBs (Figure 3.3c). The L-/R-BTB linkers are aligned in "V" shapes when viewing along *a* axis, and inverted V shapes aren't present in the structure (Figure 3.3d). Similarly, the Λ-/Δ-BTB linkers are uniformly directly along the *c* axis, while all the L-/R-BTB linkers align to the opposite direction. The different alignment of the BTB linkers further creates two sets of 2D pore channel networks, arranging in a non-centrosymmetic fashion (Figure 3.3e, illustrated by grey and violet cylinders). The 2D networks futher interconnect to form the 3D pore channel framework of MOF-829. As a conclusion, the collective arrangement of the linkers with absolute conformations determines the absolute structure of MOF-829, unlike in MOF-520 that it is the presence of one in the pair of enantiomers that determines the absolute configuration of the MOF.

3.3.4 The Relationship between the Topologies and the Absolute Structures

The arrangement of linkers and SBUs inside a MOF can be well-described by the concept of topology in reticular chemistry. Therefore, we further investigate the topology of both MOFs searching for a possible relation with the formation of MOFs with absolute structures. Although the topology of MOF-829 was not included in the RCSR database, we analyzed the structure following IUPAC guidelines[54] with Systre and ToposPro: the cluster representation gives a known underlying net with point symbol $(4\cdot6^2)(4\cdot6^9\cdot8^5)(6^3)$ named 3,3,3,3,6,6T23 (Figure 4.4b). The Samara Topological Data Center[36,37] shows four isoreticular compounds with refcodes TOVJAR,[55] OYEWEW,[56] MUKDUU,[57] LURJUG.[58] The net is composed of six kinds of nodes (two 6-connected and four 3-connected) and twelve kinds of edges. The maximum symmetry

embedding of the 3,3,3,3,6,6T23 net is determined to be $Pca2_1$, the same as for MOF-829. As the structures possessing one topology can only lie in a space group that is the subgroup of the highest possible symmetry, any MOF with this topology must be in a non-centrosymmetric space group as there is no inversion center in the space group $Pca2_1$ and any of the subgroups. Although there are many cases of centrosymmetric molecules crystallizing in non-centrosymmetric space groups,[59,60] it cannot happen to MOFs as the inversion center will become global symmetry once it appears in a periodically extended structure. Therefore, we conclude that it is the net topology of MOF-829 that determines the formation of this MOF with an absolute structure.

In comparison, the **fon** topology of MOF-520 has the maximum embedding symmetry of $P4_2/nmc$, a centrosymmetric space group (Figure 3.4a).[33, 61] The constructing units therefore have to be carefully chosen if a chiral structure is desired. H_3BTB is likely insufficient to act as the only strong structure-directing linker as it can possess many flexible conformations, but the presence of a chiral SBU at the same time increase the chance of forming a chiral structure. Indeed, there is still possibility that a meso compound can be formed even though building units with absolute configurations are chosen. In this case, the dimensions of the building units and the angles between them when forming a structure are also critical for the formation of an enantiopure structure.

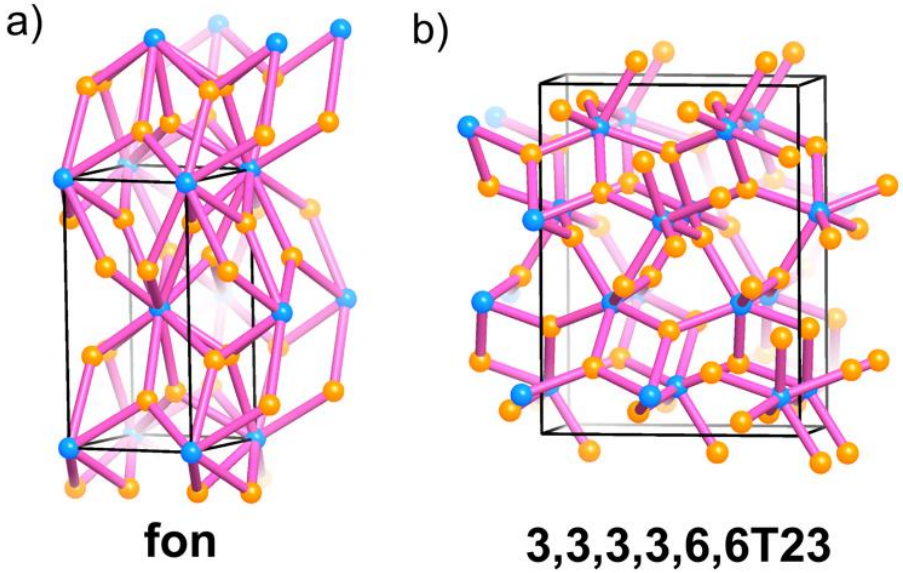


Figure 3.4 a) Illustration of the **fon** topology in its maximum embedding symmetry ($P4_2/nmc$). The 3-connected and 12-connected nodes are colored in yellow and blue, respectively. b) Illustration of the 3,3,3,3,6,6T23 net in its maximum embedding symmetry ($Pca2_1$). The 3-connected and 6-connected nodes are colored in yellow and blue, respectively. All kinds of edges in both topologies are uniformly colored in magenta.

3.4 Conclusion

From this comparative study between MOF-829 and MOF-520, we conclude that the underlying topology can determine the formation of a MOF with absolute structure if the topology itself is already non-centrosymmetric or chiral. If the topology itself is centrosymmetric, building units with potential absolute configurations have to be chosen. The choice of organic linkers with potential absolute conformations is rather straightforward, but the choice of SBUs with absolute structures from careful tuning of synthetic conditions hasn't been pursued. However, there are still rich SBU chemistry to be explored, especially for ions that can undergo complicated controlled

hydrolysis such as Al and Ti. A large number of ion-oxo clusters of these elements have been reported that can be potential SBUs of MOFs,[43, 62–66] meanwhile, there are also SBUs such as the octa-aluminum SBU in MOF-520 that never had such chiral configurations reported in individual clusters. Therefore, we envision that there is significant potential in pure synthetic-driven formation of SBUs with absolute configurations yet with no chiral auxiliary.

3.5 References

1. Yaghi, O. M.; Kalmutzki, M. J.; Diercks, C. S. *Introduction to Reticular Chemistry: Metal-Organic Frameworks and Covalent Organic Frameworks*, Wiley-VCH, Weinheim, **2019**.
2. Furukawa, H.; Cordova, K. E.; O'Keeffe, M.; Yaghi, O. M. *Science* **2013**, *341*, 1230444.
3. Lee, J.; Farha, O. K.; Roberts, J.; Scheidt, K. A.; Nguyen, S. T.; Hupp, J. T. *Chem. Soc. Rev.* **2009**, *38*, 1450–1459.
4. Wang, H.; Shi, Z.; Yang, J.; Sun, T.; Rungtaweevoranit, B.; Lyu, H.; Zhang, Y.-B.; Yaghi, O. M. *Angew. Chem. Int. Ed.* **2021**, *133*, 3459–3463.
5. Nuzhdin, A. L.; Dybtsev, D. N.; Bryliakov, K. P.; Talsi, E. P.; Fedin, V. P. *J. Am. Chem. Soc.* **2007**, *129*, 12958–12959.
6. Ma, L.; Abney, C.; Lin, W. *Chem. Soc. Rev.* **2009**, *38*, 1248–1256.
7. Liu, Y.; Xuan, W.; Cui, Y. *Adv. Mater.* **2010**, *22*, 4112–4135.
8. Lee, S.; Kapustin, E.; Yaghi, O. M.; *Science* **2016**, *353*, 808–811.
9. Inokuma, Y.; Yoshioka, S.; Ariyoshi, J.; Arai, T.; Hitora, Y.; Takada, K.; Matsunaga, S.; Rissanen, K.; Fujita, M. *Nature* **2013**, *495*, 461–466.
10. Pei, X.; Bürgi, H.-B.; Kapustin, E. A.; Liu, Y.; Yaghi, O. M. *J. Am. Chem. Soc.* **2019**, *141*, 18862–18869.
11. Vaidhyanathan, R.; Iremonger, S. S.; Shimizu, G. K. H.; Boyd, P. G.; Alavi, S.; Woo, T. K. *Science* **2010**, *330*, 650–653.
12. Cadiau, A.; Adil, K.; Bhatt, P.; Belmabkhout, Y.; Eddaoudi, M. *Science* **2016**, *353*, 137–140.
13. Li, L.; Lin, R.; Krishna, R.; Li, H.; Xiang, S.; Wu, H.; Li, J.; Zhou, W.; Chen, B. *Science* **2018**, *362*, 443–446.
14. Mohamed, M. H.; Yang, Y.; Li, L.; Zhang, S.; Ruffley, J. P.; Jarvi, A.; Saxena, S.; Veser, G.; Johnson, J.; Rosi, N. L. *J. Am. Chem. Soc.* **2019**, *141*, 13003–13007.
15. Lee, J.; Farha, O. K.; Roberts, J.; Scheidt, K. A.; Nguyen, S. T.; Hupp, J. T. *Chem. Soc. Rev.* **2009**, *38*, 1450–1459.
16. Manna, K.; Zhang, T.; Lin, W. *J. Am. Chem. Soc.* **2014**, *136*, 6566–6569.
17. Wei, Y.-S.; Zhang, M.; Zou, R.; Xu, Q. *Chem. Rev.* **2020**, *120*, 12089–12174.
18. a) Flack, H. D. *Helv. Chim. Acta* **2003**, *86*, 905–921; b) Flack, H. D.; Barnerdinelli, G. *Chirality* **2008**, *20*, 681–690.
19. Seo, J. S.; Whang, D.; Lee, H.; Jun, S.; Oh, J.; Jeon, Y.; Kim, K. *Nature* **2000**, *404*, 982–986.
20. Ma, L.; Falkowski, J. M.; Abney, C.; Lin, W. *Nat. Chem.* **2010**, *2*, 838–846.
21. Wanderley, M. M.; Wang, C.; Wu, C.; Lin, W. *J. Am. Chem. Soc.* **2012**, *134*, 9050–9053.
22. Gu, Z.; Zhan, C.; Zhang, J.; Bu, X. *Chem. Soc. Rev.* **2016**, *45*, 3122–3144.
23. Banerjee, M.; Das, S.; Yoon, M.; Choi, H. J.; Hyun, M. H.; Park, S. M.; Seo, G.; Kim, K. *J. Am. Chem. Soc.* **2009**, *131*, 7524–7525.

24. Garibay, S. J.; Wang, Z.; Tanabe, K. K.; Cohen, S. M. *Inorg. Chem.* **2009**, *48*, 7341–7349.

25. Jones, S. C.; Bauer, C. A. *J. Am. Chem. Soc.* **2009**, *131*, 12516–12517.

26. Marshall, R. J.; Griffin, S. L.; Wilson, C.; Forgan, R. S. *Chem. - Eur. J.* **2016**, *22*, 4870–4877.

27. Kepert, C. J.; Prior, T. J.; Rosseinsky, M. J. *J. Am. Chem. Soc.* **2000**, *122*, 5158–5168.

28. Lin, Z.; Slawin, A. M. Z.; Morris, R. E. *J. Am. Chem. Soc.* **2007**, *129*, 4880–4881.

29. Zhang, S. Y.; Li, D.; Guo, D.; Zhang, H.; Shi, W.; Cheng, P.; Wojtas, L.; Zaworotko, M. J. *J. Am. Chem. Soc.* **2015**, *137*, 15406–15409.

30. di Gregorio, M. C.; Shimon, L. J. W.; Brumfeld, V.; Houben, L.; Lahav, M.; van der Boom, M. E. *Nat. Commun.* **2020**, *11*, 380.

31. a) McDonald, T. M.; Lee, W. R.; Mason, J. A.; Wiers, B. M.; Hong, C. S.; Long, J. R. *J. Am. Chem. Soc.* **2012**, *134*, 7056–7065; b) Martell, J. D.; Porter-Zasada, L. B.; Forse, A. C.; Siegelman, R. L.; Gonzalez, M. I.; Oktawiec, J.; Runčevski, T.; Xu, J.; Srebro-Hooper, M.; Milner, P. J.; Colwell, K. A.; Autschbach, J.; Reimer, J. A.; Long, J. R. *J. Am. Chem. Soc.* **2017**, *139*, 16000–16012.

32. Castillo-Blas, C.; de la Peña-O'Shea, V. A.; Puente-Orench, I.; de Paz, J. R.; Sáez-Puche, R.; Gutiérrez-Puebla, E.; Gándara, F.; Monge, Á. *Sci. Adv.* **2017**, *3*, e1700773.

33. O'Keeffe, M.; Peskov, M. A.; Ramsden, S. J.; Yaghi, O. M. *Acc. Chem. Res.* **2008**, *41*, 1782–1789.

34. Blatov, V. A.; Shevchenko, A. P.; Proserpio, D. A. *Cryst. Growth Des.* **2014**, *14*, 3576–3586.

35. Delgado-Friedrichs, O.; O'Keeffe, M. *Acta Crystallogr., Sect. A: Found. Adv.* **2003**, *59*, 351–360.

36. Alexandrov, E. V.; Shevchenko, A. P.; Blatov, V. A. *Cryst. Growth Des.* **2019**, *19*, 2604–2614.

37. *TopCryst - The Samara Topological Data Center* (**2020**) [online]. Available from: https://topcryst.com [accessed Aug 5, 2021].

38. CrysAlis Pro 1.171.40.53, Rigaku Oxford Diffraction, **2019**.

39. Sheldrick, G. M. Acta Crystallogr., Sect. A: Found. Adv. **2015**, 71, 3–8.

40. Sheldrick, G. M. Acta Crystallogr., Sect. C: Struct. Chem. **2015**, 71, 3–8.

41. Dolomanov, O. V.; Bourhis, L. J.; Gildea, R. J.; Howard, J. A. K.; Puschmann, H. *J. Appl. Crystallogr.* **2009**, *42*, 339–341.

42. van der Sluis, P.; Spek, A. L. Acta Crystallogr., Sect. A: Found. Crystallogr. **1990**, 46, 194–201.

43. Fang, W. H.; Zhang, L.; Zhang, J. *Chem. Soc. Rev.* **2018**, *47*, 404–421.

44. Geng, L.; Liu, C.-H.; Wang, S.-T.; Fang, W.-H.; Zhang, J. *Angew. Chem. Int. Ed.* **2020**, *59*, 16735–16740.

45. Kapustin, E. A.; Lee, S.; Alshammari, A. S.; Yaghi, O. M. *ACS Cent. Sci.* **2017**, *3*, 662–667.

46. *International Tables for Crystallography Vol. A* (Eds.: M. I. Aroyo), Wiley-VCH, Weinheim **2016**, pp. 410–411.

47. *Nomenclature of Inorganic Chemistry - IUPAC Recommendations* (Eds.: Connelly, N. G.; Damhus, T.; Hartshorn, R. M.; Hutton, A. T.), Royal Society of Chemistry, Cambridge **2005**, pp. 189–190.

48. *Online Dictionary of Crystallography, Absolute structure* (**2017**) [online]. Available from: https://dictionary.iucr.org/Absolute_structure [Accessed June 29, 2021].

49. Spek, A. L. *J. Appl. Cryst.* **2003**, *36*, 7–13.

50. Flack, H. D.; Barnerdinelli, G. *Acta Crystallogr., Sect. A: Found. Crystallogr.* **2008**, *64*, 484–493.

51. Parsons, S. *Tetrahedron: Asymmetry* **2017**, *28*, 1304–1313.

52. Watkin, D. J.; Cooper, R. I. Acta Crystallogr., Sect. B: Struct. Sci., Cryst. Eng. Mater. **2016**, 72, 661–683.

53. Watkin, D. J.; Cooper, R. I. *Chemistry (Basel, Switz.)* **2020**, *2*, 796–804.

54. Bonneau, C.; O'Keeffe, M.; Proserpio, D. M.; Blatov, V. A.; Batten, S. R.; Bourne, S. A.; Lah, M. S.; Eon, J.-G.; Hyde, S. T.; Wiggin, S. B.; Öhrström, L. *Cryst. Growth Des.* **2018**, *18*, 3411–3418.

55. Feng, D.; Wang, K.; Wei, Z.; Chen, Y.-P.; Simon, C. M.; Arvapally, R.; Martin, R. L.; Bosch, M.; Liu, T.-F.; Fordham, S.; Yuan, D.; Omary, M. A.; Haranczyk, M.; Smit, B.; Zhou, H.-C. *Nat. Commun.* **2014**, *5:5723*, doi: 10.1038/ncomms6723.

56. a) Tian, J. *CSD Communication*, **2016**; b) Liu, C.-S.; Sun, C.-X.; Tian, J.-Y.; Wang, Z.-W.; Ji, H.-F.; Song, Y.-P.; Zhang, S.; Zhang, Z.-H.; He, L.-H.; Du, M. *Biosens. Bioelectron.* **2017**, *91*, 804–810.

57. Dong, L.-Z.; Zhang, L.; Liu, J.; Huang, Q.; Lu, M.; Ji, W.-X.; Lan, Y.-Q. *Angew. Chem. Int. Ed.* **2020**, *59*, 2659–2663.

58. Lv, H.-J.; Li, Y.-P.; Xue, Y.-Y.; Jiang, Y.-C.; Li, S.-N.; Hu, M.-C.; Zhai, Q.-G. *Inorg.Chem.* **2020**, *59*, 4825–4834.

59. Herbstein, F. H.; Schoening, F. R. L. *Acta Crystallogr.* **1957**, *10*, 657–663.

60. Pidcock, E. *Chem. Commum.* **2005**, 3457–3459.

61. Delgado-Friedrichs, O.; O'Keeffe, M. *RCSR database: fon topology.* Available from: http://rcsr.net/nets/fon [Accessed June 31, 2021].

62. Murugavel, R.; Kuppuswamy, S. *Angew. Chem. Int. Ed.* **2006**, *45*, 7022–7026.

63. Rong, C.; Yu, Z.; Wang, Q.; Zheng, S.-T.; Pan, C.-Y.; Deng, F.; Yang, G.-Y. *Inorg. Chem.* **2009**, *48*, 3650–3659.

64. Lokare, K. S.; Frank, N.; Braun-Cula, B.; Goikoetxea, I.; Sauer, J.; Limberg, C. *Angew. Chem. Int. Ed.* **2016**, *55*, 12325–12329.

65. Xuan, W.; Ye, C.; Zhang, M.; Chen, Z.; Cui, Y. *Chem. Sci.* **2013**, *4*, 3154–3159.

66. Sun, Y.; Lu, D.-F.; Sun, Y.; Gao, M.-Y.; Zheng, N.; Gu, C.; Wang, F.; Zhang, J. *ACS Mater. Lett.* **2021**, *3*, 64–68.

Chapter 4. Large Cages of Zeolitic Imidazolate Frameworks

Portions of this chapter have been published in:
Wang, H.; Pei, X.; Kalmutzki, M. J.; Yang, J.; Yaghi, O. M. *Acc. Chem. Res.* **2022**, *55*, 707–721.

4.1 Introduction

The design and synthesis of permanently porous materials with extended cage structures is a long-standing challenge in chemistry. In this chapter, we highlight the unique role of zeolitic imidazolate frameworks (ZIFs), a subclass of MOFs materials built from tetrahedral nodes connected through imidazolate linkers, in meeting this challenge, and illustrate specific features that set ZIFs apart from other porous materials. The structures of ZIFs are characteristic of a variety of large, zeolite-like cages that are covalently connected with neighboring cages and fused in 3-dimensional space and these structures are discussed in this chapter.

Our fascination with cage compounds stems from their beauty and the promise that the space encompassed by these cages can be used to manipulate and transform confined molecules in ways not possible otherwise.[5] Fundamental to this vision is the ability to create cages that are (a) architecturally stable to withstand the passage of gases and molecules in and out of such cages, and (b) thermally and chemically stable to allow chemistry to be carried out within these cages as well as on these cages themselves. In the 1970s, the idea that weak non-covalent interactions can be used to direct the assembly of large structures yielded the first cage-like compounds.[6,7] Their unique properties with respect to molecular recognition processes sparked the interest in further exploring the chemistry of this class of materials. Thus far, a myriad of metal-organic coordination cages, formed through the assembly of typical neutral organic linker molecules (e.g., pyridyl-based linkers) and single metal nodes, has been reported.[8–13] However, they generally suffer from inherent architectural instability. This makes it impossible to remove guest molecules from within these cages without collapsing them, thus limiting their applications.[14]

When charged linkers, such as carboxylates, are used to join the metal ions into cages, multi-metallic units known as secondary building units (SBUs) become the vertices leading to formation of metal-organic polyhedra (MOPs).[15] Although a less known fact, it is these MOPs that were proven to have combined architectural, thermal, and chemical stability. We note that architectural stability is evidenced by the measurement of nitrogen adsorption isotherms at 77 K and low pressure, which was demonstrated to be possible on MOP-50 for the first time in cage-like structures.[16] Although the solution host-guest chemistry of coordination cages is well-known, neither their gas adsorption isotherms nor their thermal and chemical stability have been directly evaluated prior to MOP-50.

All molecular porous entities, regardless of their chemical composition, suffer a significant inherent drawback. Although the cages themselves have defined connectivity, their spatial arrangements are impacted more by solvation status in solution states or interactions with guest molecules in solid states. This leads to the perspective of comparing coordination cages with a class of unique cage structures, zeolitic imidazolate frameworks (ZIFs). ZIFs are porous framework materials that feature a wide range of large, zeolite-like cages formed by linking single metal ion vertices and ditopic imidazole-based linkers.[17–20] The cages in ZIFs are fused in 3-dimensional space, resulting in extraordinary architectural and chemical stability that surpasses other cage-like structures. The thus-obtained well-defined spatial arrangement and alignment of cages in extended structures enabled the vast potential of ZIFs in applications related to catalysis, gas storage, and gas separation, among others.[21–25] These ultimate extended cage compounds, in comparison to isostructural zeolites, have shown more diversified and ultra-large pore structures, resulting in a rich yet relatively unexplored field of reticular chemistry. As such, it is essential to evaluate existing ZIF structures from cage chemistry perspective for the rational design of new cage structures.

In light of the emergence of ZIFs, it is worthwhile to examine discrete coordination cage chemistry and compare it to that of ZIFs. In this account, we focus on the chemistry of coordination cages and ZIFs. Both classes of materials possess cage structures that are made up of single metal vertices with bridging linkers. The fundamental difference between the two is that in coordination cages, the individual cages are isolated. Whereas in ZIFs, the cages are covalently coupled to neighboring cages. Furthermore, coordination cages are usually made of neutral pyridyl linkers, while ZIFs are made of charged imidazolate linkers. We will discuss how the structural chemistry of ZIFs fundamentally endows themselves with structural diversity and tunability, and outstanding architectural, chemical, and thermal stability. We also note that as methods for making nano-sized ZIF crystals become available and more developed, it is unclear, aside from the point of view of aesthetics and pure scientific inquiry, how the chemistry of coordination cages might diverge from that of *poly*-cages present in ZIFs.

4.2 Origins of the Stability of Extended Tetrahedral Structures

Architectural stability is a prerequisite for permanent porosity. Its origin is found in two structural features of reticular compounds: the rigidity of the individual building units and an arrangement of links around individual nodes that results in zero stress at the node itself. Framework structures built from rigid organic linkers and polynuclear SBUs often combine the rigidity of the individual building units and structural arrangements that allow all external forces to be canceled out at the nodes.[26] This is not possible for structures built from single metal nodes because the coordination geometry of these nodes is not as rigid as that of the SBUs in MOFs, for instance, the displacement of the metal ions perpendicular to the plane of two-dimensional coordination geometries (e.g., trigonal, square) is easy. Consequently, coordination cages generally suffer from low architectural stability (Figure 4.1A). The architectural instability originating from the single metal nodes can be circumvented by fusing individual cages into three-dimensional framework structures. Links connecting individual cages can be envisioned as braces that counter external forces acting on the cage upon mechanical stress. As a result, all forces exerted on the framework cancel out at the 4-c tetrahedral node (points of 'zero stress') (Figure 4.1B). The permanent porosity of zeolites is due to these structural features – tetrahedral nodes connected by short linkers – and the structural similarity with ZIF suggests that their stability is of the same origin.

Aside from architectural stability, chemical stability is another critical factor when considering the application of porous materials. Many studies have shown that ZIF possesses outstanding chemical stability.[27] This is ascribed to the fact that charged imidazolate linkers form strong bonds with metal ions. Compared with the neutral ligands utilized in constructing discrete coordination cages, charged linkers in ZIFs increase the strengths of N-metal bonds and balance the charge of cationic metal ions, allowing the formation of a stable charge neutral framework, meanwhile retaining high porosity without counter ions filling the pores. In addition, the imidazolate linkers lead to hydrophobic and chemically inert pore surfaces. It makes the polar species hardly attack the N-metal bonds, mitigating linker replacement and framework degradation.[20] These considerations are supported by the finding that ZIFs retain both crystallinity and porosity when refluxed in water, alkaline solutions, or organic solvents over an extended time.[27]

ZIFs are well-known for high thermal stability compared to other inorganic-organic hybrid materials. They generally remain stable until around 500 °C in thermal gravimetric analyses (TGA), while MOFs usually start to decompose at around 300 °C because of decarboxylation reactions. Interestingly, a TGA-mass spectrometry (MS) analysis of ZIF-8 reported that the thermal transformation of ZIF-8 started at 400 °C was originated from the leaving of CH_3 groups,

while the imidazole rings bridging metals remained to be intact and the skeleton of the framework was preserved.[28] The complete decomposition of the ZIF-8 framework occurs after 600 °C, during which the imidazole rings are disintegrated.[29]

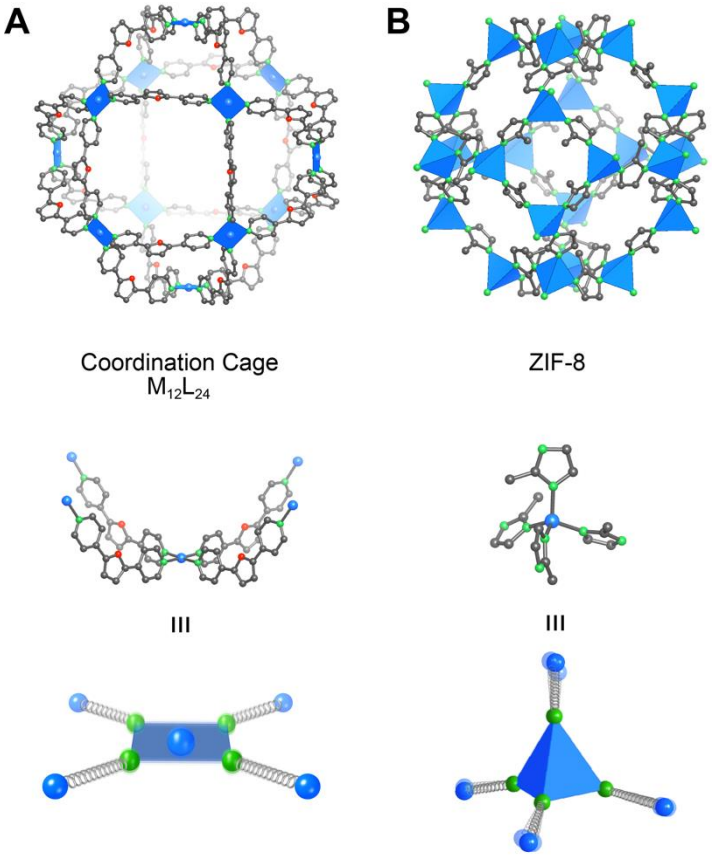


Figure 4.1. Comparison of the architectural stability of the planar nodes of coordination cages and tetrahedral nodes of ZIFs. A: The planar coordination leaves one degree of freedom perpendicular to the plane for the complex, thus rendering the resulting construct architecturally unstable. B: In extended structures built from tetrahedral nodes, this degree of freedom is removed, and the displacement of the metal center is strongly aggravated. Mechanical stress acting on these nodes is more evenly distributed, rendering materials with tetrahedral topologies architectural stability. The use of the short imidazolate linkers in ZIFs results in additional stiffening of the overall structure. Color code: Zn, Pd, blue (tetrahedron, square or atom); O, red; N, green; C, dark gray. Hydrogen atoms are omitted for clarity.

Because porous ZIFs are metastable phases, they can transform into denser and thermodynamically more stable phases when exposed to external stimuli such as pressure or temperature. A number of ZIFs can undergo glassification when glass transition temperatures are lower than decomposition temperature.[30,31] Mechanistic studies indicated that the coordination distortion of tetrahedral metal ions and ultrafast ligand exchange drove the amorphization at the melting stage, such that the metals in solidified glass remained their tetrahedral coordination geometry.[32,33] Nevertheless, the ZIFs are not considered to be decomposed but collapsed in such cases.

The effects of temperature and pressure on the solvothermal and mechanochemical synthesis of ZIFs are also evident. For instance, the reaction of $Co(NO_3)_2 \cdot 6H_2O$ and 2-nitroimidazole (nIM) in DEF at 120 °C for 12 hours yields the kinetic product with **rho** net. Prolonged heating leads to a

structural transformation into a thermodynamically more stable product with **sod** net.[34] Mechanical energy can also induce phase transitions as illustrated by the mechanochemical synthesis of ZIF: a low-density structure is often formed first, then evolves into increasingly dense structures in a stepwise mechanism resembling Ostwald's rule of stage.[35,36]

ZIFs have demonstrated certain degrees of stability that is desirable to render them suitable for catalysis, gas storage, and gas separation processes. In a manner akin to other functional materials, the properties of ZIFs are strongly correlated to the structure and chemical nature of their building units. Thus, designing their structures rationally is critical in developing high-performance materials.

4.3 Design of ZIFs Through Link-Link Interactions

The reticular syntheses of metal-organic frameworks rely mainly on the use of secondary building units with pre-defined geometries, and their principles based on geometric consideration – such as the concept of minimal transitivity – have been proposed.[37,38] In contrast, ZIFs are solely built from imidazolate linkers and tetrahedral metals nodes, meaning that the framework structures must be determined by other interactions. Such interaction may result from the building units and the solvents used, structure-directing agents, and structural fragments formed throughout the synthesis.

Consequently, early synthetic explorations of ZIFs relied heavily on a trial-and-error approach and the use of high-throughput methods.[3,27] This resulted in the rather serendipitous discovery of ZIF structures (Figure 4.5; Scheme S4.1) such as ZIF-10 (**mer** net) with *mer* cages [$Zn_{32}(IM)_{48}$, where IM = imidazolate], ZIF-8 (**sod** net) with *sod* cages [$Zn_{24}(mIM)_{36}$, where mIM = 2-methylimidazolate], or ZIF-11 (**rho** net) and ZIF-20 (**lta** net), whose structures both contain *lta* cages [$Zn_{48}(bIM)_{72}$ and $Zn_{48}(Pur)_{72}$, where bIM = benzimidazolate and Pur = purinate].[3,4,27,39] The use of progressively larger imidazole-based linkers such as 5,6-dimethylbenzimidazole (HdmbIM) and 5-chlorobenzimidazole (HcbIM) was found to lead to the formation of ZIFs with larger cages: **zea** TIF-1 with *zea* cages [$Zn_{64}(dmbIM)_{96}$], **poz** ZIF-95 with *poz* A [$Zn_{48}(cbIM)_{72}$], *poz* B [$Zn_{80}(cbIM)_{120}$], and *poz* C [$Zn_{24}(cbIM)_{32}$] cages, and **moz** ZIF-100 with *moz* cages [$Zn_{264}(cbIM)_{396}$].[2,40] While appending short side chains onto the backbones of organic linkers in MOFs has little influence on their reticulation [*e.g.*, the isoreticular functionalization of MOF-5][41], the above examples highlight the sensitivity of ZIF formation to the steric demand and chemical nature of additional substituents appended to the imidazolate linkers.

The observed profound impact of linker substitution patterns on the net of the resulting framework is attributed to link-link interactions, including hydrogen bonding, dipole-dipole interaction, π···π attractions, and steric repulsion.[4] In contrast to MOFs, where the general applicability of the isoreticular principle in expanding a given structure has been proved, such expansions are rarely possible in ZIFs. This is attributed to the fact that the angle between adjacent nodes need to remain roughly 145° in zeolite and ZIF topologies, however, it is challenging to design isoreticular expansion of imidazolate linkers matching the required angle. How these interactions direct the formation of ZIFs becomes evident when investigating structural intermediates. Framework formation is initiated by the deprotonation of the imidazole linker to yield an ionic N-donor that binds to a metal ion. Synchrotron X-ray atomic pair distribution function (PDF) analysis combined with mass spectrometry, electron microscopy, and density functional theory (DFT) calculations carried out on ZIF-8 [$Zn(mIM)_2$, where mIM = 2-methylimidazolate] revealed that initially high concentrations of $Zn(mIM)_4$ units are formed that persist over a long time (Figure 4.2).[42] The

formation of these moieties increases the acidity of the remaining N–H bonds, thus speeding up their deprotonation. As a result, an amorphous phase was formed that shows structural resemblance to the structure of ZIF-8 and possibly acts as an intermediate to crystalline ZIF-8. In basic solution, ZIFs typically precipitate almost instantaneously as highly insoluble powders, making it necessary to slow down the reaction by liquid diffusion, solvothermal methods, or the addition of coordination buffers in order to yield crystalline materials.

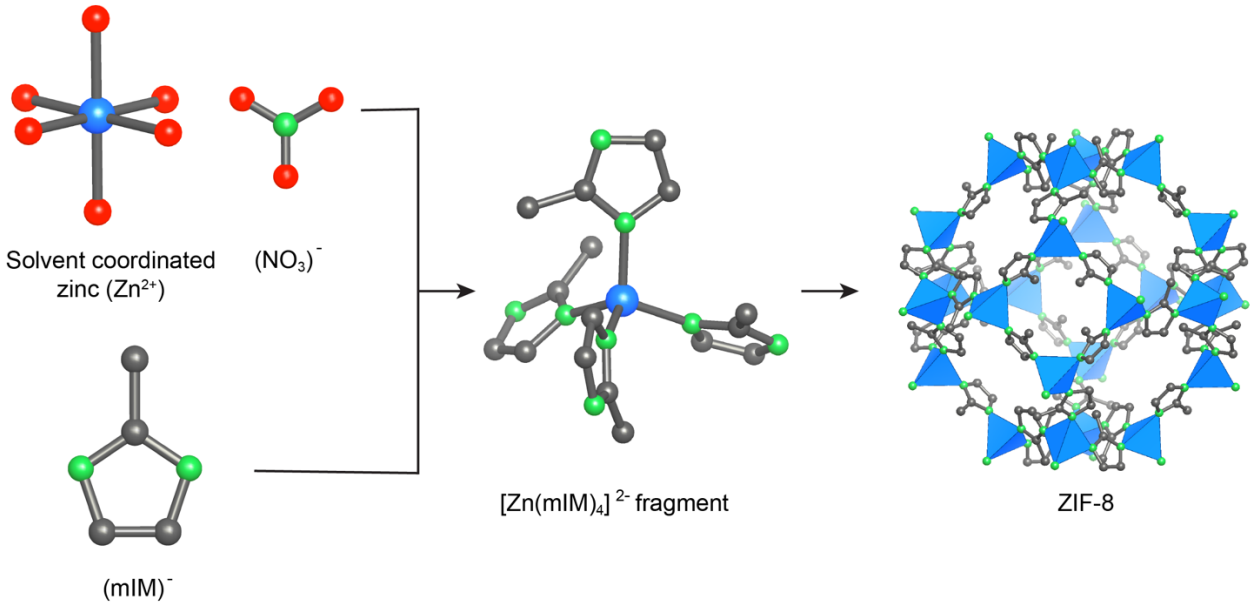


Figure 4.2. The formation mechanism of ZIFs exampled by ZIF-8. Tetrahedral $Zn(mIM)_4$ units are initially formed in high concentrations and persist throughout the formation of crystalline product, highlighting the influence of link-link interactions in the reticulation process. Color code: Zn, blue (tetrahedron or atom); O, red; N, green; C, dark gray. Hydrogen atoms are omitted for clarity.

A general growth mechanism of ZIFs is thus deduced. It is initiated by the formation of small entities (i.e., clusters) by a coagulation reaction. These clusters coalesce by adding monomers to form amorphous particles, a monomer-addition that subsequently transforms into the crystalline structure by particle reorganization induced by intra-particle nucleation. The initial formation of $M(IM)_4$ clusters highlights the effect that substituent appended to the imidazole linker can exert on the way these units will link up and eventually transform into the final framework structure. Interactions between adjacent linkers can either be attractive or repulsive, leading to either the formation of smaller or larger rings, respectively. An example for the occurrence of attractive forces between neighboring linkers is the formation of **lta** frameworks over **dia**, **sod**, and **rho** frameworks using purinate, 5-azabanzimidazolate (5-abIM), 4-azabanzimidazolate (4-abIM), and benzimidazolate (bIM) linkers (Scheme S4.1).[27] While repulsive forces are dominant for bIM and 4-abIM, the C–N bonds of both Pur and 5-abIM linkers can undergo attractive dipole-dipole interactions. As a result, these linkers assemble into small 4-membered rings that subsequently form the cubic *lta* cages necessary for the construction of **lta** frameworks. In the case of bIM and 4-abIM linkers, repulsive forces direct the self-assembly process, leading to the preferential formation of large rings and thus **sod** or **rho**, and **dia** frameworks, respectively (Figure 4.5). While the influence of attractive dipole-dipole interactions is hard to predict, the degree of steric repulsion between differently sized imidazolate-based linkers can be quantified using the steric index δ.[1] δ

is calculated according to equation 1 by multiplying the van der Waals volume of the linker molecule (V) and a distance (l) that is defined by the largest substituent. Since imidazole can be functionalized in two distinct positions – the 2-position and the 4- or 5-position – the two distance l_2 and $l_{4,5}$ have been defined (Figure 4.3A).

$$\delta = V \times l \qquad \text{Eq. 1}$$

The steric index δ can be used to predict the size of the cages and pore openings of ZIF structures and explains the structural diversity accessible through the mixed-linker approach. Selected examples of imidazolate-based linkers alongside values of their steric indices are given in Figure 4.3B. The steric index of linkers used in the construction of ZIFs can give information about the size of rings formed, and thus to some degree, the size of cages constructed from these rings. This is possible based on systematic patterns found for the orientation of differently substituted imidazole-based linkers with respect to the rings formed by linking these molecules: (i) Substituents appended to the 2-position of the imidazole linker generally point into the small (mostly 4-membered) rings. (ii) Substituents appended to the 4- and 5-position of the imidazole linker are typically oriented towards the center of 8-membered and larger rings. (iii) Both substituents appended to the 2- or 4-/5- positions of the imidazole linker can point into 6-membered rings. More general principles can be derived using these findings. Increasing the size of substituents in the 4-/5-position will inevitably lead to the formation of large rings, but the simultaneous formation of smaller rings is not precluded since the sterically less demanding 2-position can point towards the center of the small rings.

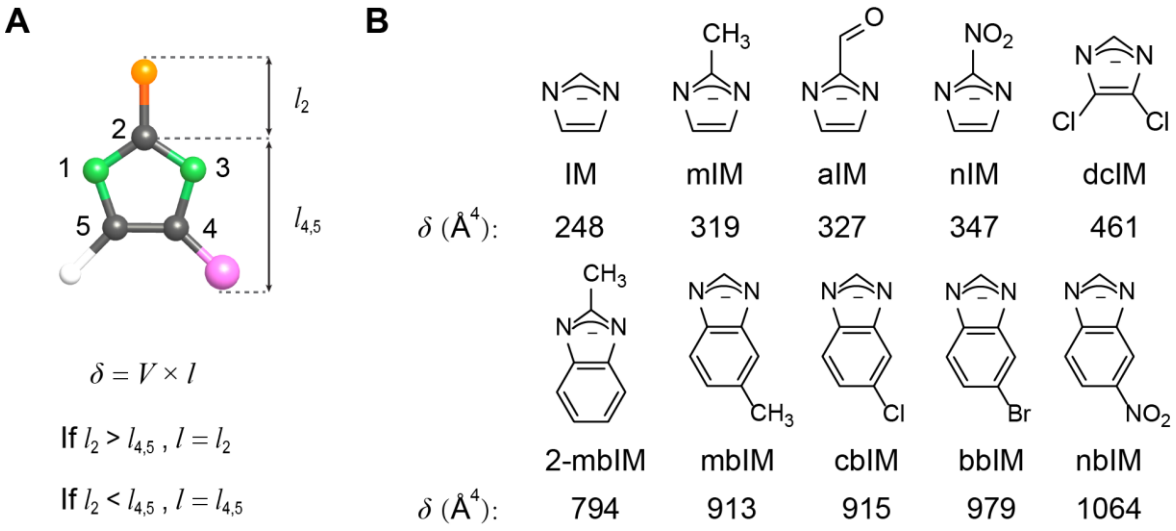


Figure 4.3. Link-link interactions as a design tool for ZIFs. A. Definition of the steric index (δ). Two distances – l_2 and $l_{4,5}$ – are defined, of which only the larger value is used for the calculation of the steric index. B. Compilation of imidazole and benzimidazole derivative alongside the respective δ values. Color code: N, green; C, gray; substituents in the 2-, 4-, and 5-position are shown in yellow, pink, and white, respectively.

Similarly, the use of imidazole-based linkers with large δ due to a large value of $l_{4,5}$ does not necessarily result in large cages because the formation of large cages (or large internal pores) in tetrahedral structures relies on a combination of both large and small rings. Accordingly, ZIF structures containing large cages are realized when both linkers with small and large δ are mixed

in an appropriate ratio. This statement can be illustrated by comparing the largest cages in the structures of ZIF-68 [Zn(bIM)(nIM), where nIM = 2-nitroimiazolate] and ZIF-412 [$Zn(bIM)_{1.13}(nIM)_{0.62}(IM)_{0.25}$].[1,3] While both structures contain the same 8- and 12-membered rings as a result of the high steric index of the bIM (δ = 679 Å^4) and nIM (δ = 347 Å^4) linkers, the *gme* cage in ZIF-68 is only half the size of the *ucb* cage in ZIF-412. This finding can be attributed to the larger number of small rings formed by the additional comparatively small IM linkers (δ = 248 Å^4) (Figure 4.3B and Figure 4.5).

Interestingly, multinary mixtures do not necessarily yield only one structure, but different mixtures with varying ratios of the same linkers result in the formation of frameworks with ring and pore sizes of any value up to a maximum value. The larger the number of different imidazole-based linkers incorporated into a single framework structure, the more potent this principle gets, highlighting that the number of structures accessible by linking tetrahedra is close to infinite. This statement is underpinned by the finding that reaction of Zn^{2+} ions with mixtures of nbIM (δ = 1064 Å^4), mIM (δ = 319 Å^4), and IM linkers (δ = 248 Å^4) in different ratios yields three topologically distinct ZIFs; ZIF-486 [$Zn(nbIM)_{0.20}(mIM)_{0.65}(IM)_{1.15}$, **gme**), ZIF-376 ($Zn(nbIM)_{0.25}(mIM)_{0.25}(IM)_{1.5}$, **lta**), and ZIF-414 [$Zn(nbIM)_{0.91}(mIM)_{0.62}(IM)_{0.47}$, **ucb**] with cages-sizes between 22.6, 27.5, and 45.8 Å, respectively (Figure 4.5).[1]

Because link-link interactions are relatively weak, the reaction medium [i.e., solvents or other structure directing agents (SDA)] may very well play a pivotal role in directing the reticulation of ZIFs, however, it is difficult to quantify these effects. Employing SDAs such as bulky amides solvents can lead to the formation of multiple structures from the very same mixture of building units. For instance, the reaction of Zn^{2+} and HIM leads to the formation of a ZIF in **can** net (CAN-[$Zn_{18}(IM)_{21}$]) when *N*,*N*-dibutylformamide (DBF) is used, but a ZIF in **afi** net (AFI-[$Zn_{24}(IM)_{30}$]) forms in the presence of *N*,*N*-dipropylformamide (DPF).[43] Single-crystal structure of **can** ZIF revealed that the DBF molecules reside orderly in the *can channel*, indicating that they serve as a template during ZIF formation.

More recent efficient syntheses of ZIF by liquid-assisted grinding (LAG) and ion- and liquid-assisted grinding (ILAG) were reported as well as other non-traditional synthesis routes such as sonochemical and dry-gel conversion (DGL).[36,44] Gas sorption experiments indicate the formation of highly porous materials with specific surface areas similar to those of materials prepared by traditional solvothermal reactions. In contrast to other methods, mechanochemistry provides a tool to study the phase diagram of ZIFs, giving access to both kinetic, highly porous phases and thermodynamically more stable, dense phases. In addition, mechanochemistry allows the synthesis of ZIF phases not accessible using solvothermal methods.[35] In line with solvothermal synthesis, the mechanochemical reaction of ZnO and HmIM leads to the formation of ZIF-8 (**sod** net), which shows amorphization upon prolonged LAG. Further grinding results in the formation of a ZIF with **kat** net – not accessible under solvothermal conditions – and eventually a ZIF of **dia** net. These transformations follow the order of increasing *T*/*V* ratio (2.4, 3.8, and 4.2 nm^{-3}, respectively) and thus increasing thermodynamic stability.

While design principles based on a deeper understanding of the link-link interactions are useful in designing new ZIFs, they also outline the limits of direct synthesis of functionalized ZIFs. In contrast to MOFs, where isoreticular functionalization is generally applicable, for ZIFs a specific structure can only be formed from certain combinations of metal ions and linkers, thus often precluding the formation of functionalized isoreticular derivatives via direct synthesis. This, however, does not limit the structural chemistry of ZIFs since the organic nature of the imidazole-

based linkers enables their modification via post-synthetic methods.[45] An early example of a post-synthetic modification (PSM) carried out on the organic backbone of a ZIF is the functionalization of the aIM (1H-imidazole-2-carbaldehyde) linkers in ZIF-90 [$Zn(aIM)_2$] by imine condensation with ethanolamine to yield ZIF-92, and its selective reduction using $NaBH_4$ to yield an alcohol group (ZIF-91).[46] In both cases, the crystallinity and porosity of the parent ZIF-90 are fully retained (Figure 4.4A). Alternative to their covalent modification, the imidazole-based linkers in ZIFs can be exchanged post-synthetically (Figure 4.4B). These aspects further enrichen the structural diversity of ZIFs.

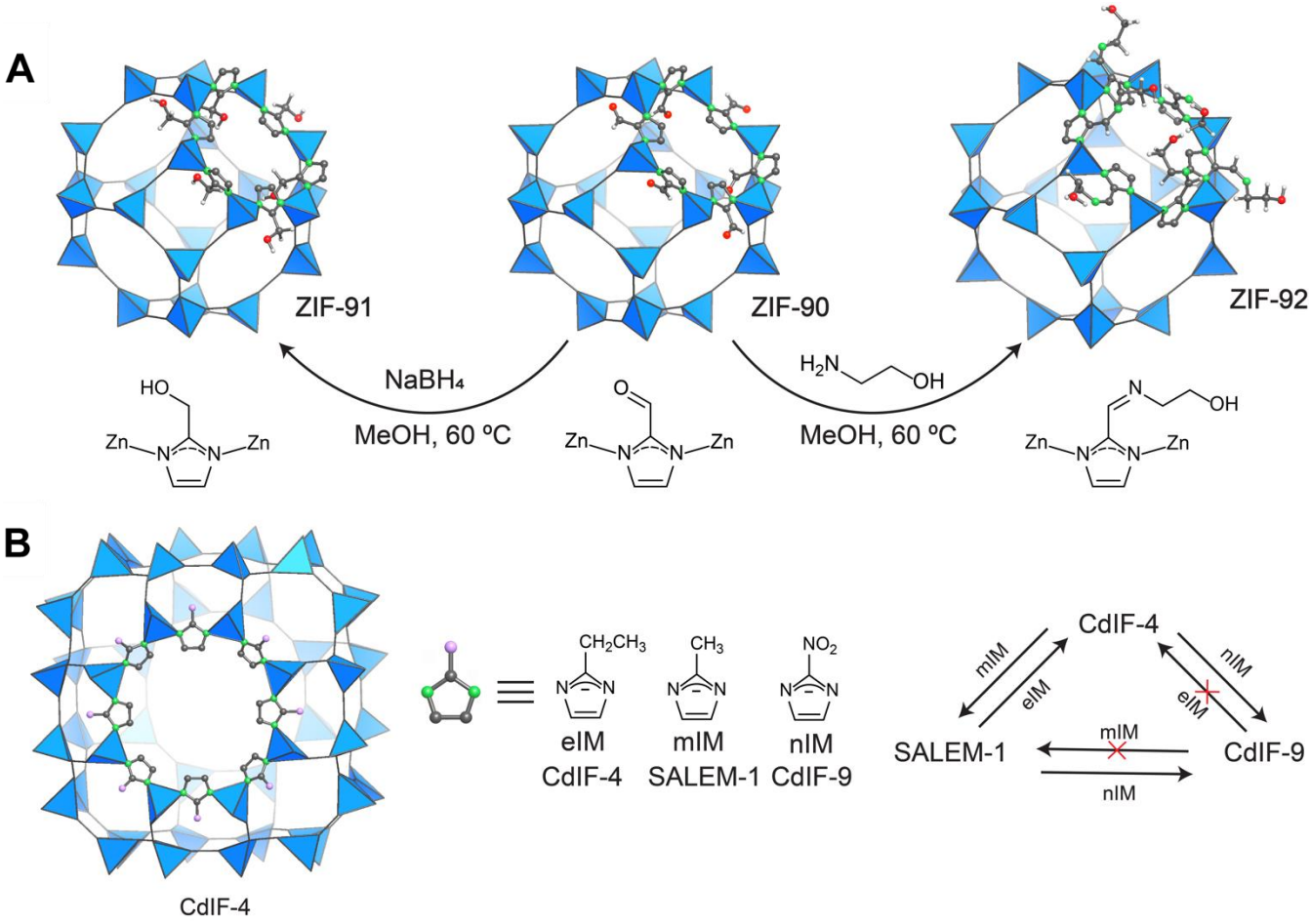


Figure 4.4. Post-synthetic modification of ZIFs. A. Covalent organic modification of the organic backbone of ZIF-90. The aldehyde functionality of the aIM linker can react with an amine to give the corresponding imine (right) or reduced to give the corresponding alcohol (left). B. Linker exchange reactions in CdIF-4. The eIM linker in CdIF-4 can be exchanged to give CdIF-9 and SALEM-1. Color code: Zn, Cd, blue (tetrahedron); O, red; N, green; C, dark gray; H, light gray; substituents in the 2-position of linkers are shown in light purple.

4.4 Diversity of ZIFs Structures and Cages

While only 255 zeolite structures have been reported after more than 150 years of research in this field,[47] since the first report of ZIF in the early 2000s, ZIFs adopting more than 40 different topologies have been reported.[1,19,20] Although composed of similar building units, ZIFs adopt many more topologies not known in zeolite chemistry. One of the reasons being that ZIFs allow

multiple kinds of linkers to co-exist in the same structure. This allows for one additional parameter to be for tuned, a parameter not accessible for discrete coordination cages that don't allow for this degree of structural complexity. In the following section the structural diversity of ZIFs will be discussed with respect to composition, topologies, and pore metrics.

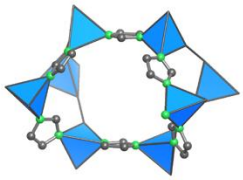
The report of the binary mixed-linker ZIFs demonstrates the potential of the multi-linker approach (see Table S4.1). Selecting different combinations of linkers leads to the formation of different types of rings that assemble into cages. For example, while mIM linkers, when reacted with Zn^{2+} ions, tend to form only *sod* cages and thus frameworks of **sod** net, mixing these linkers with 5-cbIM leads to the formation of both *sod* and *cub* cages, resulting in the construction of an **lta** structure (ZIF-76) (Figure 4.5).

The mixed linker approach has recently been pushed to the next level by employing up to three different imidazole-based linkers simultaneously, leading to the discovery of fifteen ZIFs (ZIF-303, 360, 365, 376, 386, 408, 410, 412, 413, 414, 486, 516, 586, 615, and 725).[1] This strategy facilitates the formation of ZIFs with ten different nets – among them previously unreported nets such as **kfi**, **afx**, **ucb**, **ykh**, **gcc**, and **bam** – from a selection of only ten different linkers. Such structural complexity can only be achieved by mixing multiple linkers within one structure and has seldom been observed in any other cage compounds or cage-containing materials. The mixed linker approach does, however, not preclude the formation of simple structures previously realized in binary systems, such as ZIF-303 [$Zn(cbIM)_{0.70}(nIM)_{0.30}(IM)_{1.00}$, **cha** net], ZIF-376 [$Zn(nbIM)_{0.25}(mIM)_{0.25}(IM)_{1.50}$, **lta** net], and ZIF-410 [$Zn(cbIM)_{1.10}(aIM)_{0.90}$ **gme** net] and ZIF-486 [$Zn(nbIM)_{0.20}(mIM)_{0.65}(IM)_{1.15}$, **gme** net].

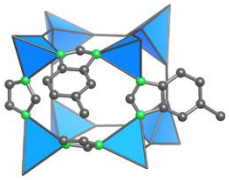
The vast number of accessible structures entails the prospect of precisely tailored pore metrics (cage size and aperture size) and shapes. These features are of key importance not only for the preparation of highly porous materials for gas storage applications, but also for selective trapping of molecules in separation processes, catalysis, and drug capture/release processes to name a few. The cages in ZIF structures are commonly referred to with their net acronym as given in the RCSR database (lower case three-letter code, italicized), or, more intuitively, their face symbols. The face symbol […n^m…] provides information on the types and connections of rings giving the number (m) of n-membered rings (MRs) found on the surface of the cage.[48] In contrast to molecular cages that are most often built from only small rings (e.g., 3-, 4-, 5-, and 6-MRs), the library of accessible rings is much larger in ZIFs, where 8-, 10-, 12-, 14-, 18-, and even 24-MRs are frequently encountered. The combination of many rings of different sizes is the key to constructing giant cages such as the *ucb* cage in ZIF-412 having the face symbol [$4^{36}.6^{24}.8^{6}.12^{8}$]. Each *ucb* cage is composed of thirty-six 4-MRs, twenty-four 6-MRs, six 8-MRs, and eight 12-MRs. The *ucb* cage represents the largest cages ever achieved in porous tetrahedral crystals; one single *ucb* cage can store as many as 121 octane or 146 p-xylene molecules at 298 K. A list of reported ZIF compositions along with information on their nets and the cages their structures are built from can be found in Table S4.1.

With respect to selective capture or release processes, not only the size, but also the precise shape of the pores is of pivotal importance. Forty-six different porous cages with various shapes and pore openings have been identified in ZIFs (Figure 4.5). Depending on their shape, these cages can be classified as (i) nearly spherical, (ii) ellipsoidal, (iii) irregular, and (iv) channels. Cages of regular spherical shape are referred to as '*nearly spherical cages*' and include *sod*, *cha*, *lta*, *fau*, *moz*, and *ucb* cages. The high point symmetry of these cages typically imparts a high symmetry onto the framework itself. For instance, the *fau* and *ucb* cages found in **ucb** ZIF-412 ($Fm\bar{3}m$) have point

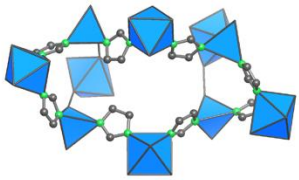
symmetries of $4\bar{3}m$ and $m\bar{3}m$, respectively, and the *lta* cages found in LTA ($Pm\bar{3}m$), RHO ($Pm\bar{3}m$), KFI ($Im\bar{3}m$), and **ucb** ($Fm\bar{3}m$) ZIFs and have a point symmetry of $m\bar{3}m$. The highly symmetric cages in ZIFs are almost 'isotropic' and their indistinguishable subcomponents/faces help to minimize the surface energy and distribute local strain equally throughout the assembly.[49] In combination with the fact that each vertex of these cages is linked to another cage this results in the outstanding architectural stability of ZIFs. As a result, the cage sizes and the complexity of their architecture exceed those of the most sophisticated discrete molecular cage compound ever made ($Pd_{48}L_{96}$ with 48 Pd nodes and 96 linkers)[13] by far: A single cage built from up to 264 nodes that are connected by 396 linkers as in the case of the *moz* cage.[2] The immense structural diversity found in the realm of ZIFs known today is most likely only the tip of the iceberg and it can be expected that the further development of the multi linker approach will give rise to a myriad of new ZIF structures.



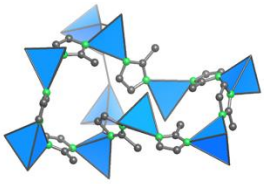
lov [$4^2.6^2$]
$Zn_8(IM)_{10}$



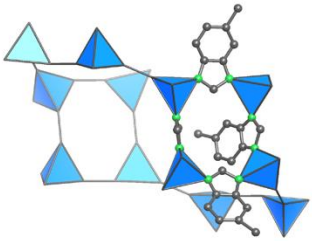
cub [4^6]
$Zn_8(mIM)_{12}$



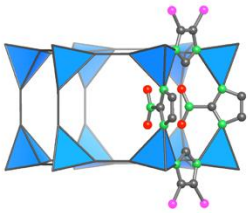
kds [$4^2.8^2$]
$Zn_2In_6(IM)_{12}$



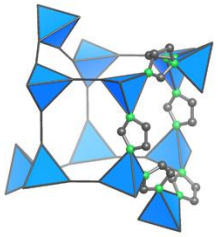
ict [$6\ .8^2$]
$Cd_{10}(mIM)_{11}$



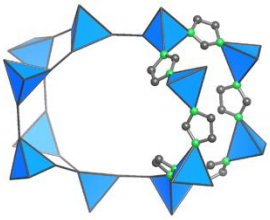
zeb B [$4^2.10^2$]
$Zn_{12}(mbIM)_{14}$



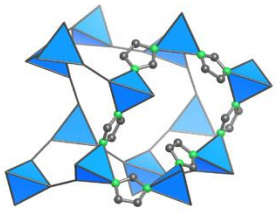
hpr [$4^6.6^2$]
$Zn_{12}(nIM)_6(dClIM)_{12}$



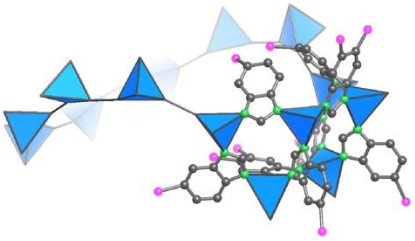
lau [$4^2.6^4$]
$Zn_{12}(IM)_{16}$



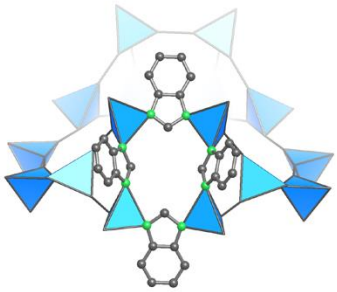
kaa [$6^2\ .8^2$]
$Zn_{12}(IM)_{14}$



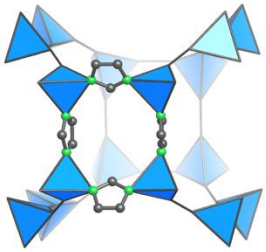
neb [6^6]
$Zn_{14}(IM)_{18}$



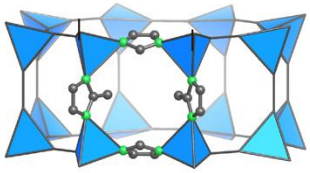
moz D [$3^2.4.12^2$]
$Zn_{14}(cbIM)_{17}$



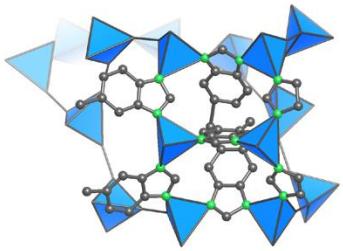
ykh C [$3^4.4^2.12^2$]
$Zn_{16}(mbIM)_{22}$



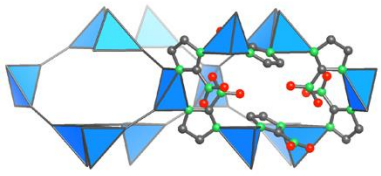
ste [$4^2.8^4$]
$Zn_{16}(IM)_{20}$



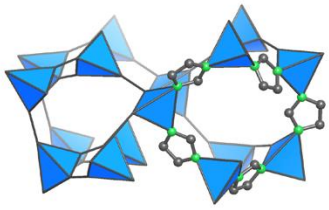
opr [$4^8.8^2$]
$Zn_{16}(mIM)_{24}$



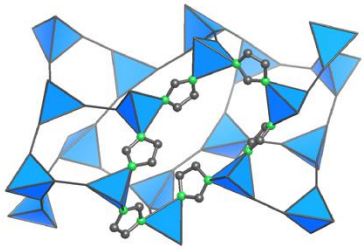
zeb A [$4^2.6^2.10^2$]
$Zn_{16}(mbIM)_{20}$



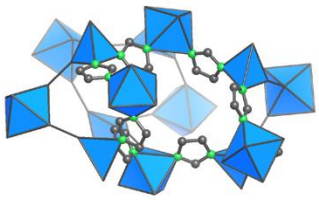
mog [$6^4.8^2$]
$Zn_{16}(nIM)_{20}$



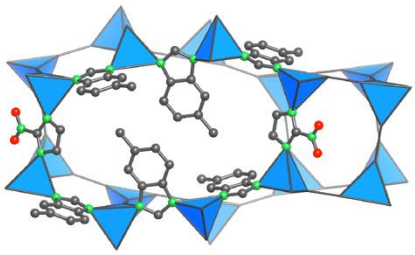
nog B [$5^4.6.8^2$]
$Zn_{16}(IM)_{22}$



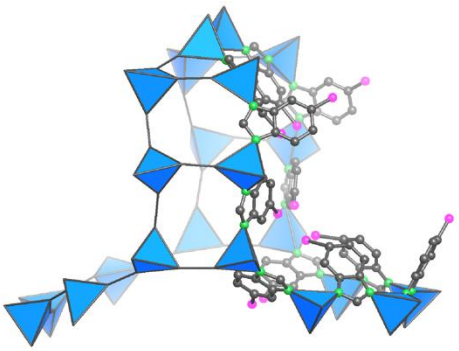
fsi [$4^2.6^8$]
$Zn_{20}(IM)_{28}$



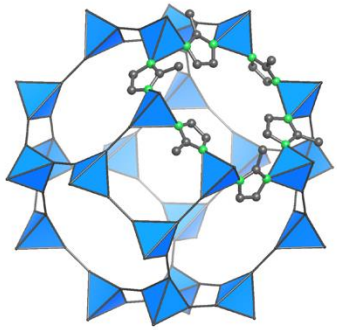
gar [$4^3.8^3$]
$Zn_{20}In_8(IM)_{18}$



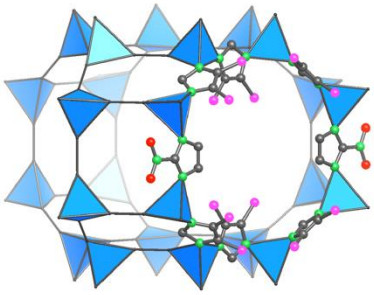
gsm [$4^6.8^4$]
$Zn_{20}(nIM)_{12}(mbIM)_{16}$



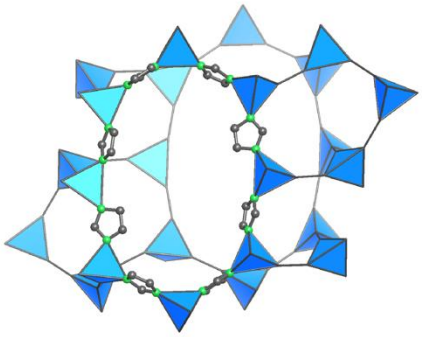
moz C [$3^2.4^4.12^3$]
$Zn_{22}(cbIM)_{32}$



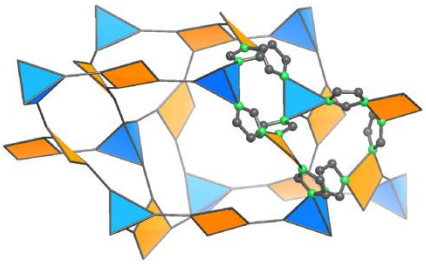
sod [$4^6.6^8$]
$Zn_{24}(mIM)_{36}$



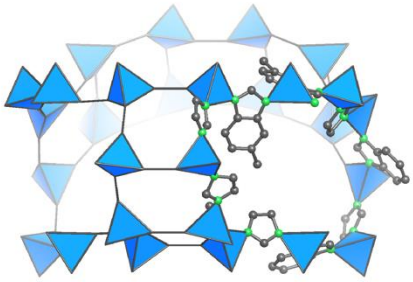
gme [$4^9.6^2.8^3$]
$Zn_{24}(nIM)_{18}(dClIM)_{18}$



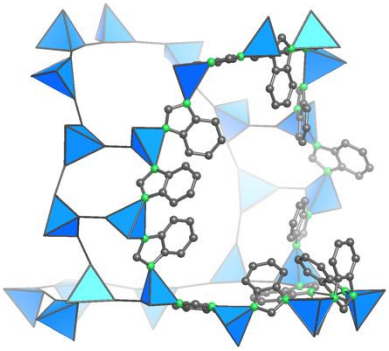
nog A [$5^4.6^2.8^4$]
$Zn_{24}(IM)_{32}$



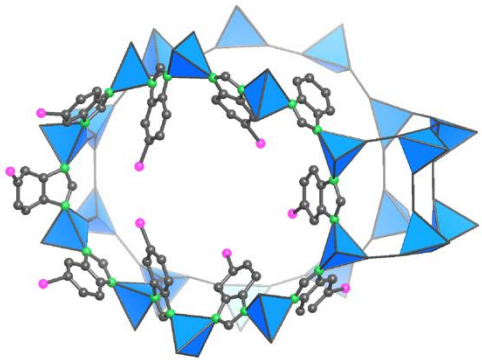
ntn [$4^2.5^4.6^4.8^2$]
$Zn_{10}Cu_{14}(IM)_{35}$



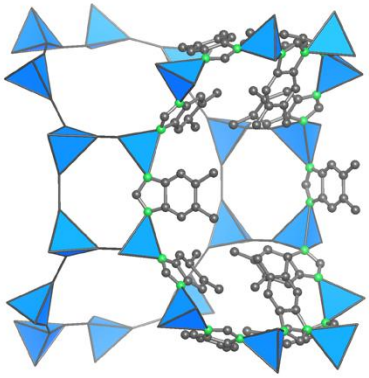
zeb channel [$4^8.10^2.12^2$]
$Zn_{28}(IM)_9(bIM)_{29}$



ykh B [$4^4.12^2.14^2$]
$Zn_{28}(mbIM)_{34}$

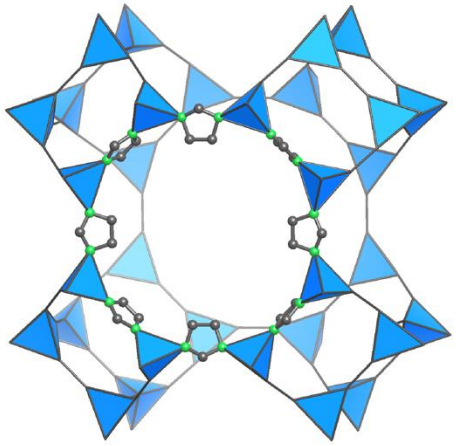


poz C [$4^6.10^4$]
$Zn_{24}(cbIM)_{32}$

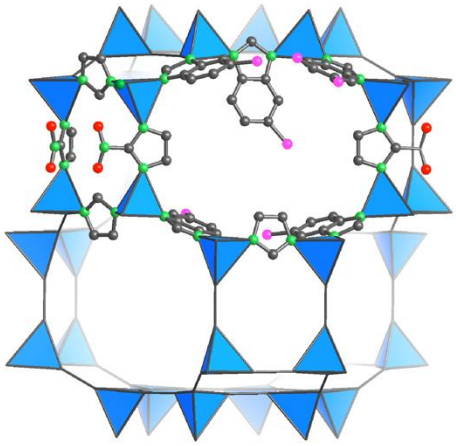


zea B [$4^2.12^4$]
$Zn_{24}(dmbIM)_{28}$

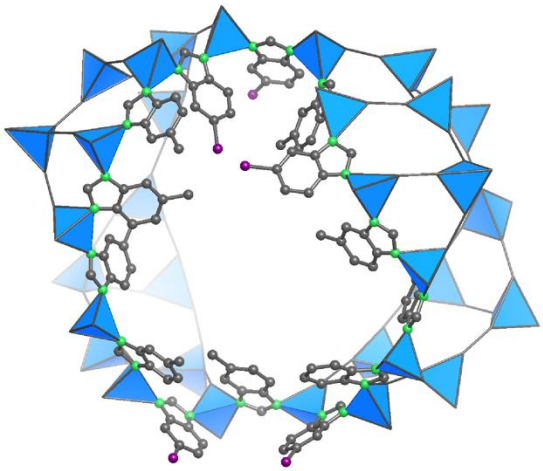




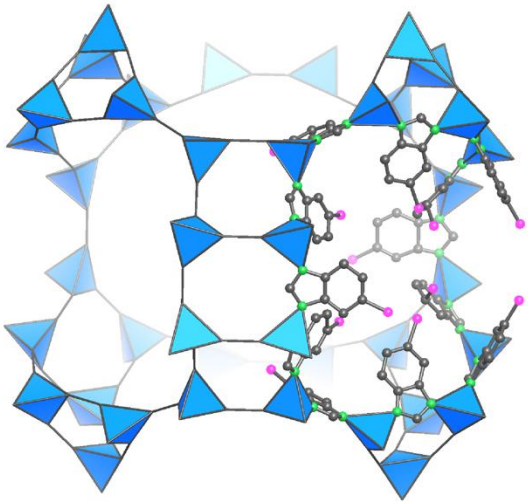
mer [$4^{12}.8^{6}$]
$Zn_{32}(IM)_{48}$



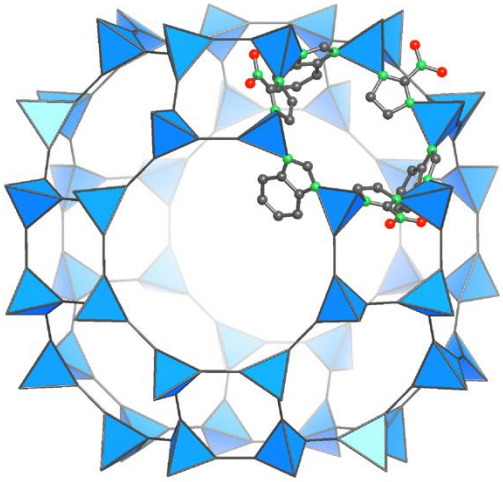
cha [$4^{12}.6^{2}.8^{6}$]
$Zn_{36}(nIM)_{6}(cbIM)_{12}(IM)_{36}$



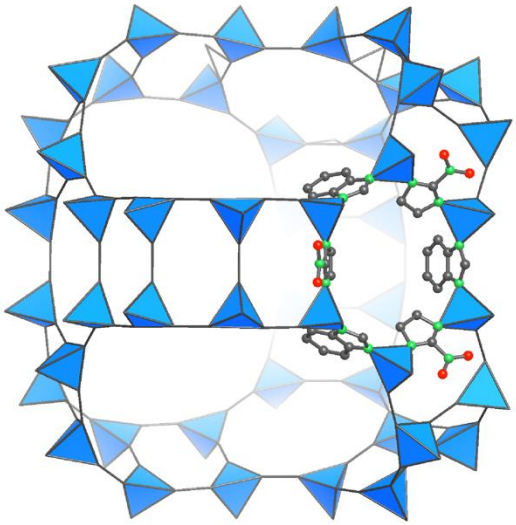
ykh [$3^{4}.4^{8}.10^{2}.14^{2}$]
$Zn_{32}(mbIM)_{29.52}(bbIM)_{18.48}$



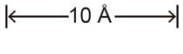
moz B [$3^{4}.4^{11}.12^{5}$]
$Zn_{40}(cbIM)_{58}$

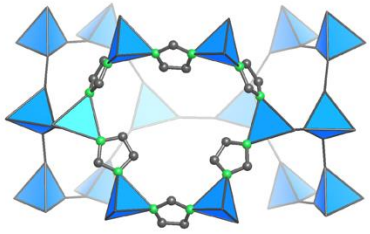


lta [$4^{12}.6^{8}.8^{6}$]
$Zn_{48}(IM)_{12}(nIM)_{24}(bIM)_{36}$

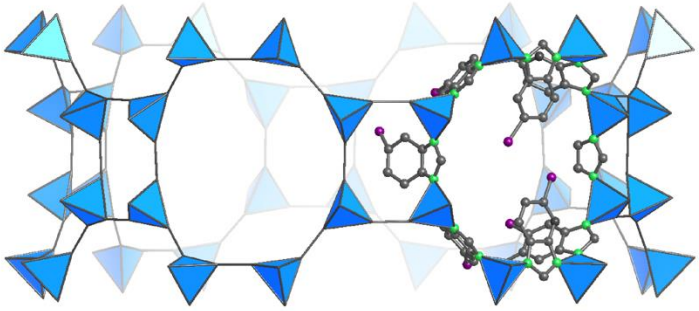


fau [$4^{18}.6^{4}.12^{4}$]
$Zn_{48}(nIM)_{12}(IM)_{16.8}(bIM)_{43.2}$

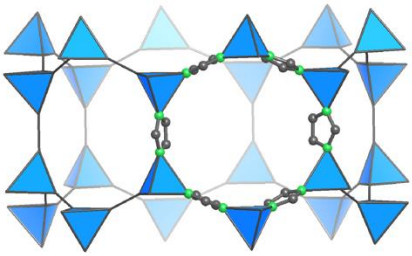




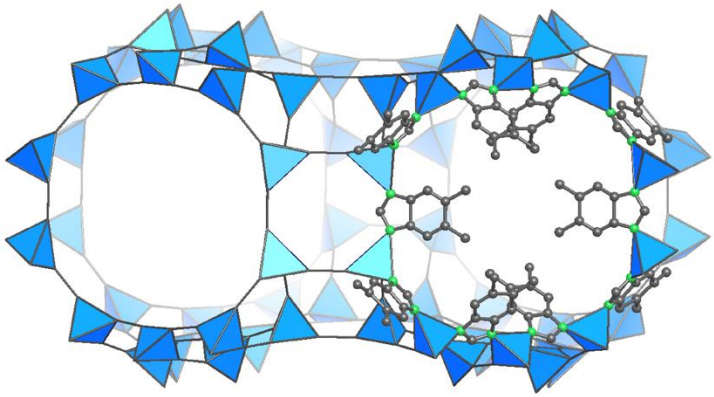
can channel [$6^3.12^2$]
$Zn_{18}(IM)_{21}$



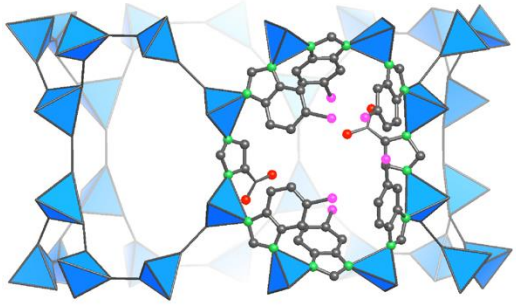
bam channel [$4^6.8^6.24^2$]
$Zn_{48}(IM)_6(bbIM)_{54}$



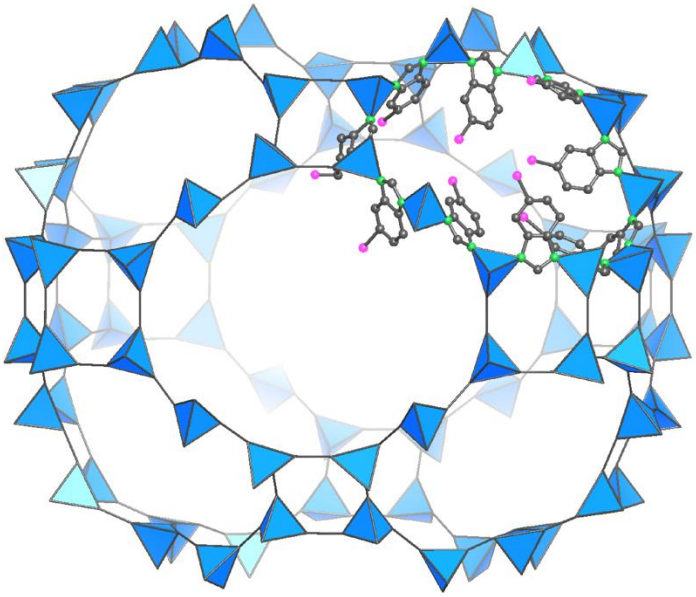
afi channel [$6^6.12^2$]
$Zn_{24}(IM)_{30}$



zea [$3^8.4^{22}.10^4.12^4$]
$Zn_{64}(dmbIM)_{96}$

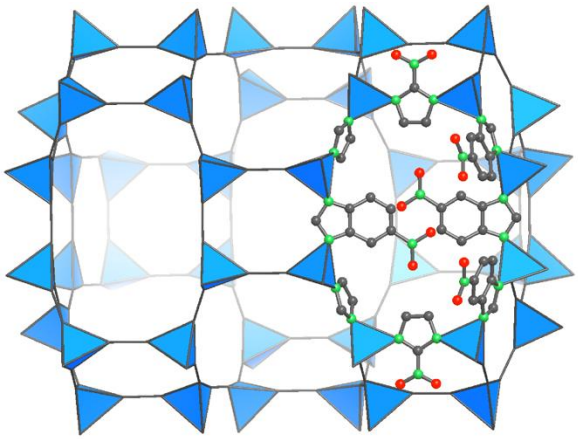


gcc channel [$8^6.18^2$]
$Zn_{36}(4\text{-}nIM)_{18}(cbIM)_{24}$

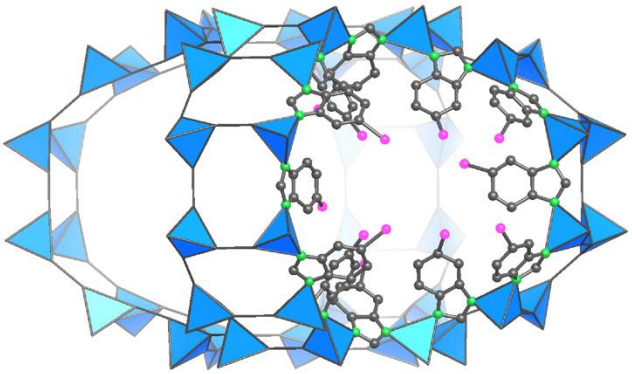


poz B [$4.8^2.10^8.12^4$]
$Zn_{80}(cbIM)_{120}$

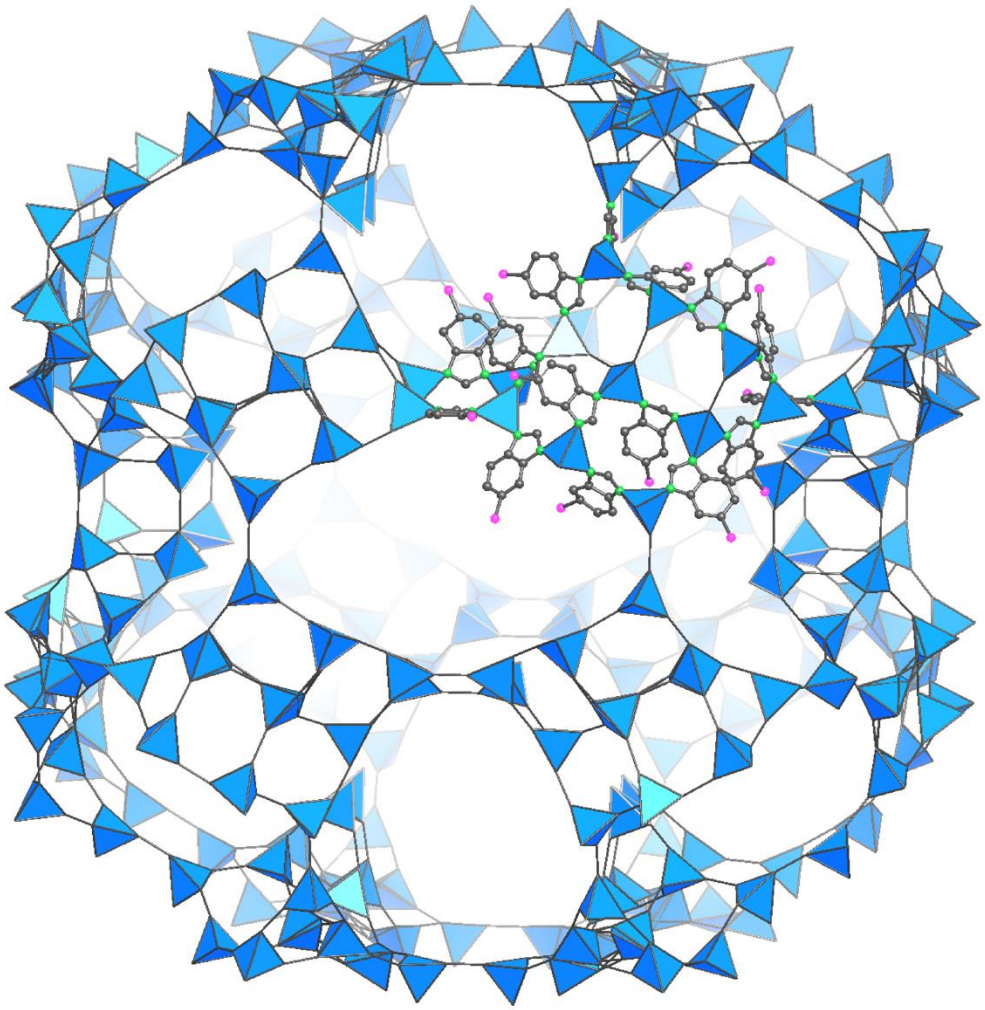




aft [$4^{15}.6^{2}.8^{9}$]
$Zn_{48}(IM)_{12}(nIM)_{24}(nbIM)_{32}$



poz A [$4^{20}.8^{2}.12^{4}$]
$Zn_{48}(cbIM)_{72}$



moz [$3^{48}.4^{108}.12^{26}$]
$Zn_{264}(cbIM)_{396}$

10 Å

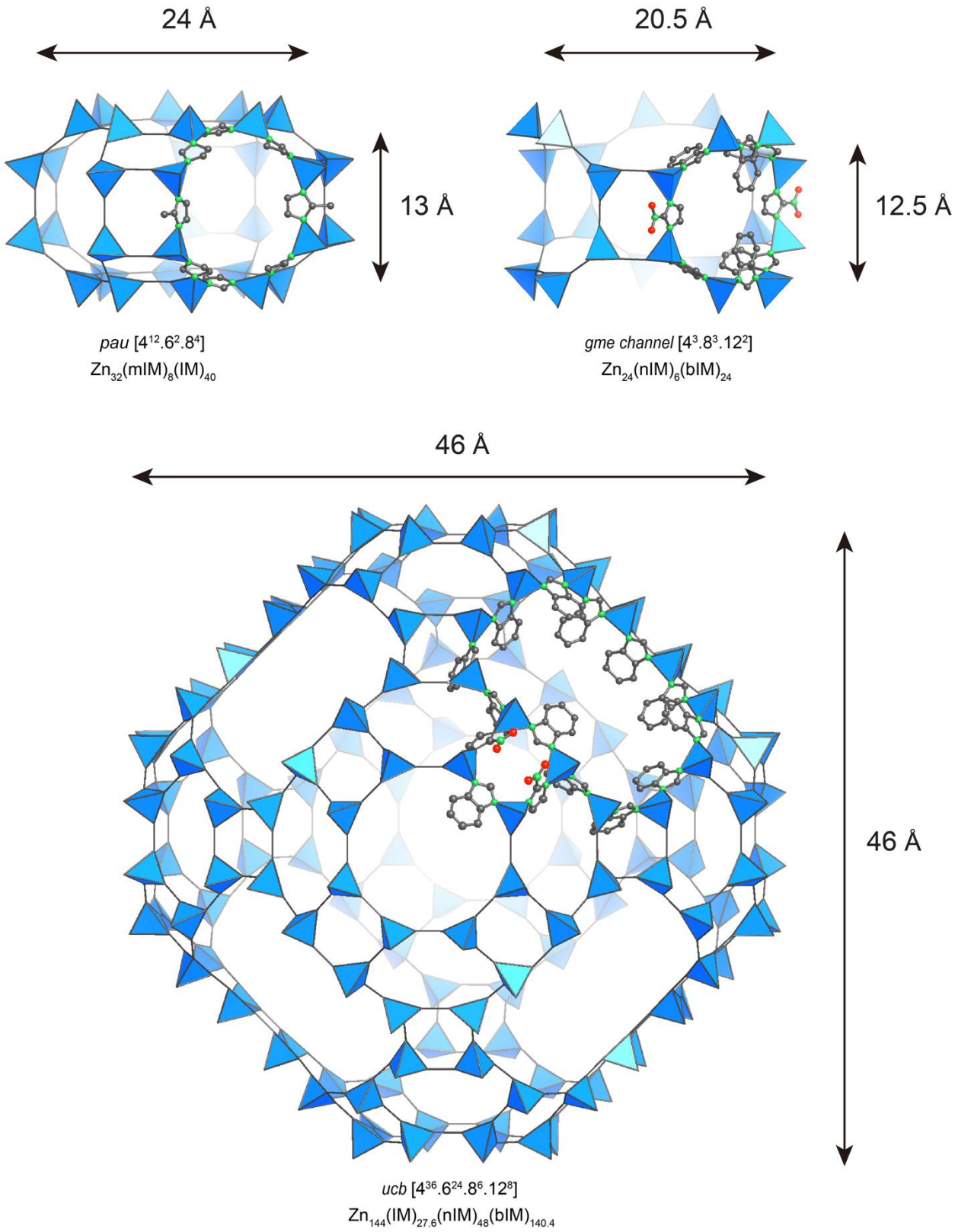


Figure 4.5. Cages identified in ZIFs. Color code: Zn, blue (tetrahedron); Cu, orange (square); O, red; N, green; C, dark gray; Cl, pink, Br, purple. Hydrogen atoms are omitted for clarity.

4.5 Intrinsic Advantages of Fused Cages

Extended structures built from fused cages present the following advantages: the chemical and architectural stability from the interconnected vertices, and the fact of being able to connect a variety of cages with different chemical environments in closely confined spaces in a well-defined spatial arrangement. These two features, together with the large surface area and tunable pore size, provide ZIFs with unique potentials among cage-like materials with respect to their future development and application.

The benefit of excellent stability of ZIFs has been demonstrated in several applications, such as being effective heterogeneous catalysts for several reactions. For example, ZIF-8, ZIF-9, and ZIF-10 exhibited outstanding performance in catalyzing the Knoevenagel reaction between benzaldehyde and malononitrile, without showing structural degradation in the basic reaction media.[50] Hupp *et al.* exchanged the mIM linker of ZIF-8 into imidazolate (IM) followed by the treatment with *n*-butyl lithium,[51] targeting at the formation of a solid-state Brønsted base catalyst. It is not only a clear example of the chemical stability of ZIF-8 toward strong nucleophilic bases, but also of the architectural stability of being able to bear linker exchange without degrading into other topologies.

Multivariate systems, *i.e.* structures built from a combination of multiple interchangeable linkers bearing identical binding groups but being chemically distinct promise even greater potential.[52] It was shown that the performance of MTV-MOFs often surpass that of corresponding individual non-MTV-MOFs due to synergy effects.[53] A mixed-linker ZIF-8 composed of 2-methylimidazole (HmIM) and 1,2,4-triazole (Hmtz) can be viewed as the simplest model of a MTV-ZIF.[54] The two kinds of linkers were found to be randomly distributed throughout the crystals, and varying the linker ratios allowed the fine tuning of the threshold pressure of capillary condensation of their water sorption isotherms. Although MTV-ZIFs with more than two kinds of linkers have not been reported, it is anticipated that a higher complexity and better performances will be achieved when increasing the type of linkers in MTV-ZIFs.

Fusing cages into extended structures allows several different cages to co-exist in the same crystal, creating a complex platform joining distinct chemical environments in an ordered spatial arrangement. In contrast to discrete cage systems, the different cages in ZIFs are connected in a face sharing manner, allowing the guest molecules to travel through the cages on a predefined path given by the spatial arrangement of the cages with respect to each other, which is not possible for individual molecular cages. Additionaly, the imidazolate linkers can guide molecules through the pore system by directing them *via* steric effects. A study on ZIF-8 revealed that the mass transport within the cages occurs by ~10^2 times (at 200 K) than between cages, while the gate opening effect allows for the cross-cage migration to be tuned at higher pressures and temperatures.[55]

Looking at ZIFs as individual but fused cages, they can be viewed as compartmentalized not only in terms of space and geometry, but also in terms of function. Their cages have varying chemical compositions and geometries and thus possess different properties such as polarities, resulting in different behavior in physical processes. For example, the *in situ* X-ray diffraction experiment on ZIF-412 found that its cages were sequentially filled during the gas sorption process: first the *lta* cage, then the *fau* cage, and eventually the largest *ucb* cage.[56] This concept can be applied to the design of materials where each individual cage have a specific function as can be envision for ZIF-reactors: cascade reactions are carried out in the individual cages and the substrate is guided from one cage-reactor to another until the final product is formed. Such materials provide chemists with

the opportunity to carry out complex multi-step reaction within a single material. This prospect is unique to ZIFs because they are the only group of compounds featuring a fixed spatial arrangement of cages that are interconnected through small apertures, which is not possible for MOFs or arrangements of MOPs as both MOFs and MOPs feature pores without wall, rather than cages.

Fast guest molecule diffusion is indeed the basis of the application of ZIFs in gas storage and separation. Arranging various linkers in ZIFs provide the opportunity to fabricate remarkably large and complex cages, which benefit the removal of large volatile organic compounds (e.g., octane and p-xylene) in particular,[1] in addition increase the diffusion speed of guests across the crystal. Engineering approaches can further help to improve the mass transport in ZIFs by making ZIFs into nano-sized particles,[57] thin films,[58] or permeable nanostructures.[59] Combining the hierarchical pore structure and material fabrication techniques will be able to optimize the performances of this solid-state porous material to the greatest extent.

4.6 Conclusion and Outlook

ZIFs are a unique class of materials that combine the advantages of cages and architecturally stable extended structures. Over the last decades, dozens of cages with various composition, size and shape have been discovered, exhibiting a level of complexity that cannot be realized in molecular cages. Their unique architecture, high mechanical, chemical, and thermal stability combined with the possibility of post-synthetic modification renders them a highly promising class of materials for a wide range of applications including but not limited to gas storage, gas separation, and catalysis. The potential of ZIFs with respect to structural complexity has, however, not been realized to its full extend.[60] While the link-link interactions play a pivotal role in understanding ZIF formation, further research is required to fully understand the mechanism of ZIF formation and thus deduce principles allowing for the design of synthesis of ZIFs with ever growing complexity. This will eventually allow for the in silico design of high performance ZIFs and a profound understanding of structure-property relationships even for highly complex multinary structures. The combination of traits of different classes of materials with those of ZIFs will further enrichen the realm of ZIF chemistry, as was recently shown for Z-MOFs – materials implementing elements of ZIF and MOF chemistry. Therefore, the progress made in ZIF chemistry over the course of the last decade represents only a glimpse of their vast largely unexplored potential.

4.7 Supporting Information

Scheme S4.1. Common linkers in ZIFs and their name abbreviations.

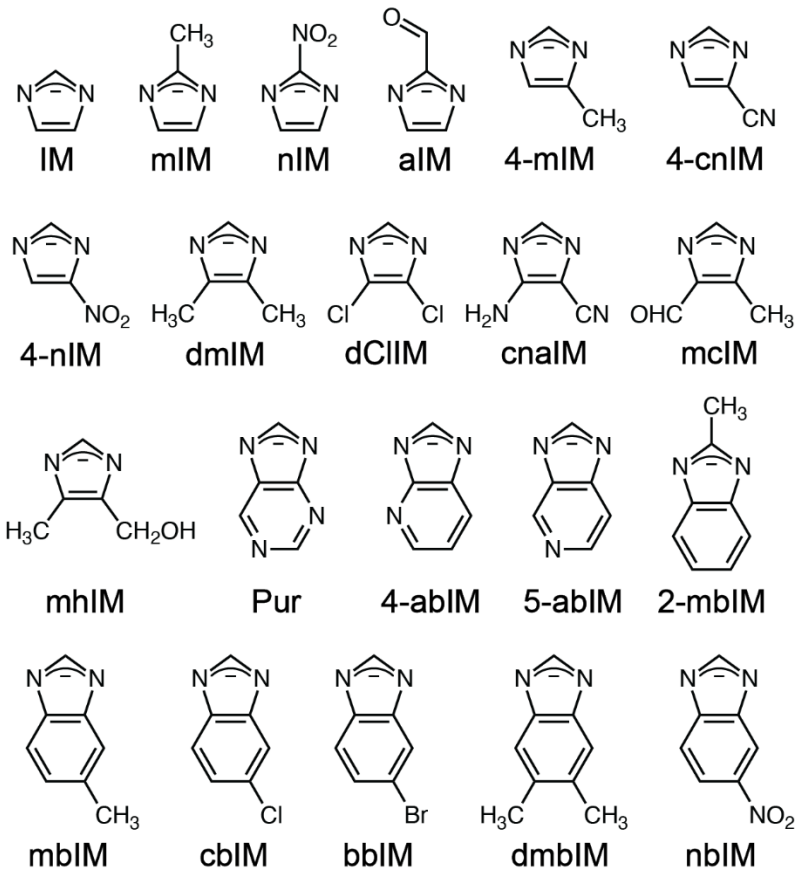


Table S4.1. The table is arranged by what nets can be formed by varying the combination of linkers. For each net, the information is listed as: **net** (*cages*): exemplar ZIF (metal salt used to synthesize the ZIF).

	IM	mIM	aIM	nIM	4-cnIM	dCIIM	dmIM	4-nIM	cnaIM	mcIM	mhIM	Pur	4-abIM	5-abIM	bIM	2-mbIM	mbIM	cbIM	bbIM	dmbIM	nbIM
IM	**crb** (*lau, kaa*): ZIF-1 ($Zn(NO_3)_2$), ZIF-2 ($Zn(NO_3)_2$), ZIF-64 ($Zn(NO_3)_2$); **dft** (*lov, ste, kaa*): ZIF-3 ($Zn(NO_3)_2$); **cag** (*fsl*): ZIF-4 ($Zn(NO_3)_2$); **mer** (*pau, opr, ste*): ZIF-10 ($Zn(NO_3)_2$); **gar**(*kds, gar*): ZIF-5 ($Zn(NO_3)_2$, $In(NO_3)_3$); **gis** (*gsm*): ZIF-6 ($Zn(NO_3)_2$); **moc** (*kds, krr*): ZIF-moc; **neb** (*neb*) ZIF-nnb; **nog** (*kds, nog A, nog B*); ZIF-nog; **qtz** (*kaa*): MAF-32 (ZnO/Zn(OH)$_2$); **ntn** (*ntn*): ZIF-003 ($Cu(NO_3)2$, $Zn(OAc)_2$); **thl** (*thl*): ZIF-204($Cu(NO_3)_2$, $Zn(AcO)_2$)	**mer** (*pau, opr, ste*): ZIF-60 ($Zn(NO_3)_2$); **zni** (*lov, zni*): ZIF-61 ($Zn(NO_3)_2$); **lct** (*ict, afi*): CdIF-5 ($Cd(NO_3)_2$/$Cd(OAc)_2$) (52)		**gme** (*hpr, gme*): ZIF-70 ($Zn(NO_3)_2$)				**gme** (*hpr, gme*): ZIF-70 ($Zn(NO_3)_2$)							**cag** (*fsl*): ZIF-62 ($Zn(NO_3)_2$)	**pcb** (*cub, ste*): TIF-3 ($Zn(OAc)_2$)	**cha** (*hpr, cha*): ZIF-302 ($Zn(NO_3)_2$); **zeb** (*cub, zeb channel, zeb A, zeb B*): TIF-2 ($Zn(OAc)_2$)	**cha** (*hpr, cha*): ZIF-301 ($Zn(NO_3)_2$)	**cha** (*hpr, cha*): ZIF-300 ($Zn(NO_3)_2$)		
mIM		**sod** (*sod*): ZIF-8 ($Zn(NO_3)_2$), ZIF-67 ($Co(NO_3)_2$); **dia** (*ada*): MAF-31 (ZnO/Zn(OH)$_2$)(47), **mog** (*kds, mog*): ZIF-CO3-1 ($Zn(NO_3)_2$)																			
aIM			**sod** (*sod*): ZIF-90 ($Zn(NO_3)_2$)															**gme** (*hpr, gme*): ZIF-410 ($Zn(CF_3SO_3)_2$)				
nIM				**fri** (*mog, xvi*): ZIF-77 ($Zn(NO_3)_2$); **sod** (*sod*): ZIF-65 ($Co(NO_3)_2$)	**gme** (*hpr, gme*): ZIF-82 ($Zn(NO_3)_2$)	**gme** (*hpr, gme*): ZIF-80 ($Zn(NO_3)_2$)									**gme** (*hpr, gme*): ZIF-68 ($Zn(NO_3)_2$)		**gis** (*gma*): ZIF-74 ($Zn(NO_3)_2$), ZIF-75 ($Co(NO_3)_2$); **fri** (*mog, xvi*): ZIF-73 ($Zn(NO_3)_2$), **gme** (*hpr, gme*): ZIF-79 ($Zn(NO_3)_2$)	**gme** (*hpr, gme*): ZIF-69 ($Zn(NO_3)_2$)	**gme** (*hpr, gme*): ZIF-81 ($Zn(NO_3)_2$)		**gme** (*hpr, gme*): ZIF-78 ($Zn(NO_3)_2$)
dCIIM						**rho** (*opr, ita*): ZIF-71 ($Zn(OAc)_2$); **lcs** (*afi*): ZIF-72 ($Zn(NO_3)_2$)															
dmIM							**rho** (*opr, ita*): ZIF-25 ($Zn(OAc)_2$)														
4-nIM																		**gcc** (*cub, gme, gcc channel*): ZIF-615 ($Zn(NO_3)_2$)			
cnaIM									**rho** (*opr, ita*): ZIF-96 ($Zn(OAc)2$)												
mcIM										**rho** (*opr, ita*): ZIF-93 ($Zn(OAc)_2$); **sod** (*sod*): ZIF-94 ($Zn(NO_3)_2$)										
mhIM											**rho** (*opr, ita*): ZIF-97 ($Zn(OAc)_2$)										
Pur												**ita** (*sod, cub, ita*): ZIF-20 ($Zn(NO_3)_2$), ZIF-21 ($Co(NO_3)_2$)									
4-abIM													**dia** (*ada*): ZIF-23 ($Zn(NO_3)_2$)								
5-abIM														**ita** (*sod, cub, ita*): ZIF-22 ($Zn(NO_3)_2$)							
bIM															**sod** (*sod*): ZIF-7 ($Zn(NO_3)_2$), ZIF-9 ($Co(NO_3)_2$); **rho** (*opr, ita*): ZIF-11 ($Zn(NO_3)_2$), ZIF-12 ($Co(NO_3)_2$)						
2-mbIM																	**ykh** (*ykh, ykh B, ykh C*): ZIF-586 ($Zn(NO_3)_2$)				
mbIM																			**ykh** (*ykh, ykh B, ykh C*): ZIF-516 ($Zn(NO_3)_2$)		
cbIM																		**poz** (*poz A, poz B, poz C, cub*): ZIF-95 ($Zn(NO_3)_2$); **moz** (*moz, moz B, ykh C, zea B, moz C, moz D*): ZIF-100 ($Zn(O_3SCF_3)_2$)			
dmbIM																				**zea** (*zea, ykh C, zea B*): TIF-1Zn ($Zn(OAc)_2$)	

	cbIM, nIM	bIM, nIM	nbIM, mIM	nbIM, nIM	bbIM, nIM	mbIM, nIM
IM	**cha** (*hpr, cha*): ZIF-303 ($Zn(NO_3)_2$), **kfi** (*hpr, pau, grc*): ZIF-365 ($Zn(NO_3)_2$)	**kfi** (*hpr, pau, grc*): ZIF-360 ($Zn(NO_3)_2$), **ucb** (*cub, hpr, fau, grc, ucb*): ZIF-412 ($Zn(NO_3)_2$)	**lta** (*sod, cub, grc*): ZIF-376 ($Zn(NO_3)_2$), **gme** (*hpr, gme*): ZIF-486 ($Zn(NO_3)_2$), **ucb** (*cub, hpr, fau, grc, ucb*): ZIF-414 ($Zn(NO_3)_2$)	**afx** (*hpr, gme, afi*): ZIF-386 ($Zn(NO_3)_2$)	**bam** (*cub, hpr, opr, gme, bam*): ZIF-725 ($Zn(NO_3)_2$)	**ucb** (*cub, hpr, fau, grc, ucb*): ZIF-413 ($Zn(NO_3)_2$)

Table S4.2. Cages that are only found in ZIFs.

Cage Label	Face Symbol	Highest Point Symmetry	ZIF nets that contain the cage
gar	$4^3.8^3$-b	-62m	**gar**
mog	$6^4.8^2$-c	mmm	**mog**, **frl**
neb	6^6-b	1	**neb**
nog A	$5^4.6^2.8^4$	2/m	**nog**
nog B	$5^4.6.8^2$	2/m	**nog**
ict	6.8^2	1	**ict**
ntn	$4^2.5^4.6^4.8^2$	2	**ntn**
thl	$4^2.5^4.6^2.7^4$	2	**thl**
ant	8^3	-62m	**ant**
tet	3^4	-43m	**crs**
tte-b	$3^4.6^4$	-43m	**crs**
zni	$6^3.12^2$	1	**zni**
zea	$3^8.4^{22}.10^4.12^4$	mmm	**zea**
zea B	$4^2.12^4$	4/mmm	**zea, moz**
ykh	$3^4.4^8.10^2.14^2$	2/m	**ykh**
ykh B	$4^4.12^2.14^2$	mm2	**ykh**
ykh C	$3^4.4^2.12^2$	mmm	**ykh, zea, moz**
zeb channel	$4^8.10^2.12^2$	m	**zeb**
zeb A	$4^2.6^2.10^2$-b	mm2	**zeb**
zeb B	$4^2.10^2$	m	**zeb**
poz A	$4^{20}.8^2.12^4$	4/mmm	**poz**
poz B	$4.8^2.10^8.12^4$	4/mmm	**poz**
poz C	$4^6.10^4$	-42m	**poz**
moz	$3^{48}.4^{108}.12^{26}$	m-3	**moz**
moz B	$3^4.4^{11}.12^5$	mm2	**moz**
moz C	$3^2.4^4.12^3$	mm2	**moz**
moz D	$3^2.4.12^2$	mm2	**moz**
ucb	$4^{36}.6^{24}.8^6.12^8$	m-3m	**ucb**
bam channel	$4^6.8^6.24^2$	6mm	**bam**
gcc channel	$8^6.18^2$	6mm	**gcc**

* Structures that containing these cages can be retrieved from Table S4.1. For the cages that hasn't been identified and named in ZIFs, it was firstly referenced to cages in zeolites[61] for naming. If no such cage was found in zeolites, the name of the cage follows the tradition[2] of adding uppercase letters after the name of the net.

4.8 References

1. Yang, J.; Zhang, Y.-B.; Liu, Q.; Trickett, C. A.; Gutiérrez-Puebla, E.; Monge, M. A.; Cong, H.; Aldossary, A.; Deng, H.; Yaghi, O. M. *J. Am. Chem. Soc.* **2017**, *139*, 6448–6455.
2. Wang, B.; Côté, A. P.; Furukawa, H.; O'Keeffe, M.; Yaghi, O. M. *Nature* **2008**, *453*, 207–211.
3. Banerjee, R.; Phan, A.; Wang, B.; Knobler, C.; Furukawa, H.; O'Keeffe, M.; Yaghi, O. M. *Science* **2008**, *319*, 939–943.
4. Hayashi, H.; Côté, A. P.; Furukawa, H.; O'Keeffe, M.; Yaghi, O. M. *Nat. Mater.* **2007**, *6*, 501–506.
5. Chakrabarty, R.; Mukherjee, P. S.; Stang, P. J. *Chem. Rev.* **2011**, *111*, 6810–6918.
6. Pedersen, C. J. *J. Am. Chem. Soc.* **1967**, *89*, 7017–7036.
7. Dietrich, B.; Lehn, J. M.; Sauvage, J. P.; Blanzat, J. *Tetrahedron* **1973**, *29*, 1629–1645.
8. Fujita, M.; Oguro, D.; Miyazawa, M.; Oka, H.; Yamaguchi, K.; Ogura, K. *Nature* **1995**, *378*, 469–471.
9. Fujita, M.; Ogura, K. *Bull. Chem. Soc. Jpn.* **1996**, *69*, 1471–1482.
10. Takeda, N.; Umemoto, K.; Yamaguchi, K.; Fujita, M. *Nature* **1999**, *398*, 794–796.
11. Tominaga, M.; Suzuki, K.; Kawano, M.; Kusukawa, T.; Ozeki, T.; Sakamoto, S.; Yamaguchi, K.; Fujita, M. *Angew. Chem. Int. Ed.* **2004**, *43*, 5621–5625.
12. Sun, Q.-F.; Iwasa, J.; Ogawa, D.; Ishido, Y.; Sato, S.; Ozeki, T.; Sei, Y.; Yamaguchi, K.; Fujita, M. *Science* **2010**, *328*, 1144–1147.
13. Fujita, D.; Ueda, Y.; Sato, S.; Mizuno, N.; Kumasaka, T.; Fujita, M. *Nature* **2016**, *540*, 563–566.
14. Ueda, Y.; Ito, H.; Fujita, D.; Fujita, M. *J. Am. Chem. Soc.* **2017**, *139*, 6090–6093.
15. Tranchemontagne, D. J.; Ni, Z.; O'Keeffe, M.; Yaghi, O. M. *Angew. Chem. Int. Ed.* **2008**, *47*, 5136–5147.
16. Sudik, A. C.; Millward, A. R.; Ockwig, N. W.; Côté, A. P.; Kim, J.; Yaghi, O. M. *J. Am. Chem. Soc.* **2005**, *127*, 7110–7118.
17. Chen, B.; Yang, Z.; Zhu, Y.; Xia, Y. *J. Mater. Chem. A* **2014**, *2*, 16811–16831.
18. Tan, J. C.; Bennett, T. D.; Cheetham, A. K. *Proc. Natl. Acad. Sci. U. S. A.* **2010**, *107*, 9938–9943.
19. Phan, A.; Doonan, C. J.; Uribe-Romo, F. J.; Knobler, C. B.; O'Keeffe, M.; Yaghi, O. M. *Acc. Chem. Res.* **2010**, *43*, 58–67.
20. Zhang, J.-P.; Zhang, Y.-B.; Lin, J.-B.; Chen, X.-M. *Chem. Rev.* **2012**, *112*, 1001–1033.
21. Melgar, V. M. A.; Kim, J.; Othman, M. R. *J Ind Eng Chem* **2015**, *28*, 1–15.
22. Lai, L. S.; Yeong, Y. F.; Lau, K. K.; Azmi, M. S. *Separ Sci Technol* **2014**, *49*, 1490–1508.
23. Barkholtz, H. M.; Liu, D.-J. *Mater Horizons* **2017**, *4*, 20–37.
24. Mottillo, C.; Friščić, T. *Angew. Chem., Int. Ed.* **2014**, *53*, 7471–7474.

25. Pimentel, B. R.; Parulkar, A.; Zhou, E.; Brunelli, N. A.; Lively, R. P. *Chemsuschem* **2014**, *7*, 3202–3240.

26. Yaghi, O. M.; O'Keeffe, M.; Ockwig, N. W.; Chae, H. K.; Eddaoudi, M.; Kim, J. *Nature* **2003**, *423*, 705–714.

27. Park, K. S.; Ni, Z.; Côté, A. P.; Choi, J. Y.; Huang, R.; Uribe-Romo, F. J.; Chae, H. K.; O'Keeffe, M.; Yaghi, O. M. *Proc. Natl. Acad. Sci. U. S. A.* **2006**, *103*, 10186–10191.

28. Gadipelli, S.; Travis, W.; Zhou, W.; Guo, Z. *Energ. Environ. Sci.* **2014**, *7*, 2232–2238.

29. Gadipelli, S.; Guo, Z. X. *ChemSusChem* **2015**, *8*, 2123–2132.

30. Bennett, T. D.; Goodwin, A. L.; Dove, M. T.; Keen, D. A.; Tucker, M. G.; Barney, E. R.; Soper, A. K.; Bithell, E. G.; Tan, J.-C.; Cheetham, A. K. *Phys. Rev. Lett.* **2010**, *104*, 115503.

31. Bennett, T. D.; Cheetham, A. K. *Acc. Chem. Res.* **2014**, *47*, 1555–1562.

32. Gaillac, R.; Pullumbi, P.; Beyer, K. A.; Chapman, K. W.; Keen, D. A.; Bennett, T. D.; Coudert, F.-X. *Nat. Mater.* **2017**, *16*, 1149–1154.

33. Bennett, T. D.; Tan, J.-C.; Yue, Y.; Baxter, E.; Ducati, C.; Terrill, N. J.; Yeung, H. H.-M.; Zhou, Z.; Chen, W.; Henke, S.; Cheetham, A. K.; Greaves, G. N. *Nat. Commun.* **2015**, *6*, 8079.

34. Biswal, B. P.; Panda, T.; Banerjee, R. *Chem. Commun.* **2012**, *48*, 11868–11870.

35. Katsenis, A. D.; Puškarić, A.; Štrukil, V.; Mottillo, C.; Julien, P. A.; Užarević, K.; Pham, M.-H.; Do, T.-O.; Kimber, S. A. J.; Lazić, P.; Magdysyuk, O.; Dinnebier, R. E.; Halasz, I.; Friščić, T. *Nat. Commun.* **2015**, *6*, 6662.

36. Do, J.-L.; Friščić, T. *ACS Cent. Sci.* **2017**, *3*, 13–19.

37. Yaghi, O. M.; O'Keeffe, M.; Ockwig, N. W.; Chae, H. K.; Eddaoudi, M.; Kim, J. *Nature* **2003**, *423*, 705–714.

38. Kalmutzki, M. J.; Hanikel, N.; Yaghi, O. M. *Sci. Adv.* **2018**, *4*, eaat9180.

39. Huang, X.; Zhang, J.; Chen, X. *Chin. Sci. Bull.* **2003**, *48*, 1531–1534.

40. Wu, T.; Bu, X.; Liu, R.; Lin, Z.; Zhang, J.; Feng, P. *Chem. - Eur. J.* **2008**, *14*, 7771–7773.

41. Eddaoudi, M.; Kim, J.; Rosi, N.; Vodak, D.; Wachter, J.; O'Keeffe, M.; Yaghi, O. M. *Science* **2002**, *295*, 469–472.

42. Terban, M. W.; Banerjee, D.; Ghose, S.; Medasani, B.; Shukla, A.; Legg, B. A.; Zhou, Y.; Zhu, Z.; Sushko, M. L.; Yoreo, J. J. D.; Liu, J.; Thallapally, P. K.; Billinge, S. J. L. *Nanoscale* **2018**, *10*, 4291–4300.

43. Shi, Q.; Xu, W.-J.; Huang, R.-K.; Zhang, W.-X.; Li, Y.; Wang, P.; Shi, F.-N.; Li, L.; Li, J.; Dong, J. *J. Am. Chem. Soc.* **2016**, *138*, 16232–16235.

44. Lee, Y.-R.; Jang, M.-S.; Cho, H.-Y.; Kwon, H.-J.; Kim, S.; Ahn, W.-S. *Chem Eng J* **2015**, *271*, 276–280.

45. Wang, Z.; Cohen, S. M. *Chem. Soc. Rev.* **2009**, *38*, 1315–1329.

46. Morris, W.; Doonan, C. J.; Furukawa, H.; Banerjee, R.; Yaghi, O. M. *J. Am. Chem. Soc.* **2008**, *130*, 12626–12627.

47. Zeolite Framework Types. https://asia.iza-structure.org/IZA-SC/ftc_table.php (accessed 2021 -09 -27).

48. Blatov, V. A.; O'Keeffe, M.; Proserpio, D. M. *CrystEngComm* **2009**, *12*, 44–48.

49. Beuerle, F. *Nature* **2016**, *540*, 529–530.

50. Tran, U. P. N.; Le, K. K. A.; Phan, N. T. S. *ACS Catal.* **2011**, *1*, 120–127.

51. Karagiaridi, O.; Lalonde, M. B.; Bury, W.; Sarjeant, A. A.; Farha, O. K.; Hupp, J. T. *J. Am. Chem. Soc.* **2012**, *134*, 18790–18796.

52. Deng, H.; Doonan, C. J.; Furukawa, H.; Ferreira, R. B.; Towne, J.; Knobler, C. B.; Wang, B.; Yaghi, O. M. *Science* **2010**, *327*, 846–850.

53. Dong, Z.; Sun, Y.; Chu, J.; Zhang, X.; Deng, H. *J. Am. Chem. Soc.* **2017**, *139*, 14209–14216.

54. Zhang, J.; Zhu, A.; Lin, R.; Qi, X.; Chen, X. *Adv. Mater.* **2011**, *23*, 1268–1271.

55. Jobic, H.; Kolokolov, D. I.; Stepanov, A. G.; Koza, M. M.; Ollivier, J. *J. Phys. Chem. C* **2015**, *119*, 16115–16120.

56. Cho, H. S.; Yang, J.; Gong, X.; Zhang, Y.-B.; Momma, K.; Weckhuysen, B. M.; Deng, H.; Kang, J. K.; Yaghi, O. M.; Terasaki, O. *Nat. Chem.* **2019**, *11*, 562–570.

57. Nune, S. K.; Thallapally, P. K.; Dohnalkova, A.; Wang, C.; Liu, J.; Exarhos, G. J. *Chem. Commun.* **2010**, *46*, 4878–4880.

58. Huang, A.; Chen, Y.; Wang, N.; Hu, Z.; Jiang, J.; Caro, J. *Chem. Commun.* **2012**, *48*, 10981–10983.

59. Shen, K.; Zhang, L.; Chen, X.; Liu, L.; Zhang, D.; Han, Y.; Chen, J.; Long, J.; Luque, R.; Li, Y.; Chen, B. *Science* **2018**, *359*, 206–210.

60. Atlas of Prospective Zeolite Structures. http://www.hypotheticalzeolites.net (accessed 2021 -09 -27).

61. Smith, J. V.; Polyhedral Units. In *Microporous and other Framework Materials with Zeolite-Type Structures*; Baur, W. H., Fischer, R. X., Eds.; New Series; Springer-Verlag: Berlin, Heidelberg, New York, 2000; Subvolume A: Tetrahedral Frameworks of Zeolites, Clathrates, and Related Materials, 65–131.

Chapter 5. Water Harvesting at the Single Crystal Level

Portions of this chapter have been published in:
Fuchs, A.; Wang, H.; Ji, Z.; Wuttke, S.; Yaghi, O. M.; Ploetz, E. **2022**, submitted.

5.1 Introduction

Knowing the upper limit of an intrinsic property for a material is critically important in realizing its full potential. For example, determination of all the adsorptive sites in metal-organic frameworks (MOFs) has led to the design of structures with exceptionally high surface areas.[1] Recently, MOFs have been shown to be useful in harvesting water from desert air,[2-10] where the water productivity depends on how fast water can move in and out of the pores. While such cycling kinetics of water sorption could be measured experimentally in bulk,[4] this has yet to be done on the single crystal level, leaving unanswered the question of what is the upper limit for how much water can be harvested in a given time. Herein, we present a general strategy to quantitatively determine the water sorption isotherm and the kinetics of uptake and release within a single crystal by Raman spectroscopy. We found that for a MOF-801 crystal, water moves ~20 times faster than in the bulk.[11] This represents the upper limit for MOF-801, and indicates that water harvesting devices could produce up to 3.8 L of water per hour per kilogram of MOF, a vast improvement over the previously reported 2.8 L per day.[4,11]

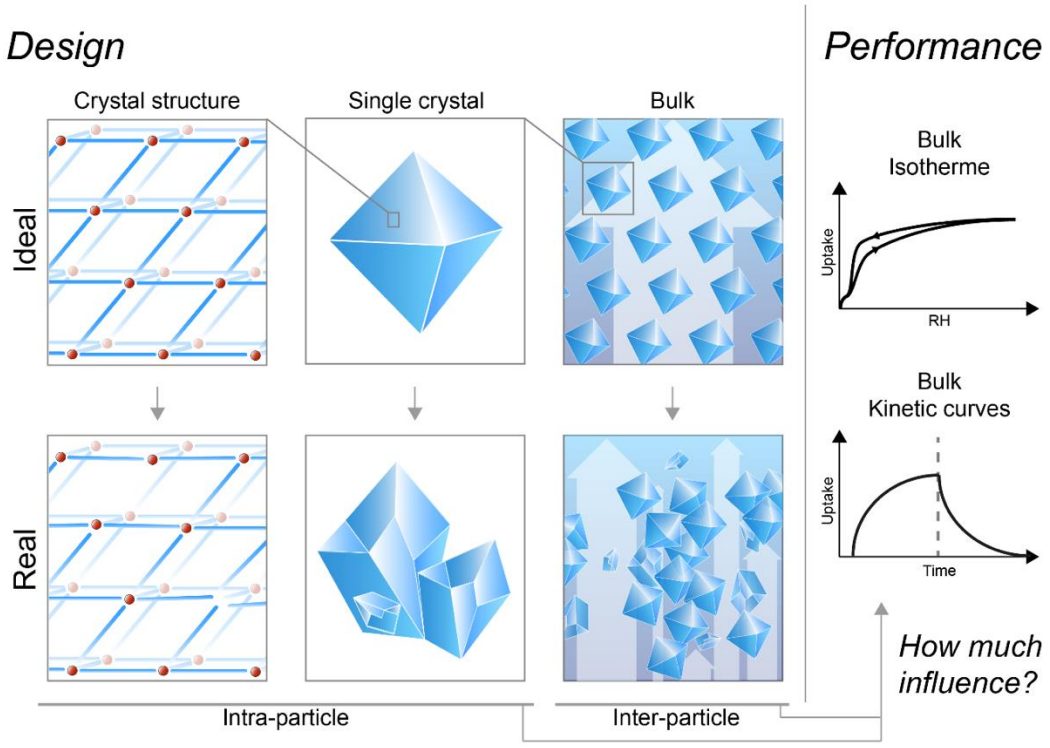


Figure 5.1: Design and performance evaluation of atmospheric water harvesting MOF materials. Comparing the influence of intra- and inter-particle effects on the bulk performance of sorbent systems for an ideal (single crystal) and real (bulk) material.

5.2 Methods and Results

The uptake performance of porous materials is usually determined by measuring bulk properties using mass gravimetric methods,[8] and described by the total uptake, the uptake mechanism (hence isotherm type), and the kinetic behavior. However, metal-organic frameworks (MOF) materials feature – like all crystalline materials – diverse defect sites (Figure 5.1), resulting in the disturbance

of their crystallinity due to macropores, mechanical deformations, or inter-crystal growth. The latter leads to particles with multiple crystalline zones or amorphous areas. In addition to defects (even if ideally grown), single crystals interfere with each other's uptake behavior many-fold, such as shielding neighboring particles from adsorbing guest molecules in the surrounding airflow and, hence, reducing the accessibility to pores or (*ii*) by creating condensation pockets between them.[12] Measuring the performance of the sorbent material alone, without the interference of intra- and inter-particle effects, would require a spatially resolved, quantitative method for monitoring the uptake.

5.2.1 Determine Water Uptake in MOF-801 Crystals via Raman spectroscopy

We report an optical methodology based on Raman spectroscopy (Section 5.3.1-5.3.2) to quantitatively determine isotherm and kinetic curves with sub-micron spatial resolutions, effectively probing the water uptake performance (total uptake, isotherm, and kinetics) of single crystals (SC). We study MOF-801, an important and well-studied MOF for atmospheric water harvesting (AWH)[2] that emerges as octagonal-shaped crystals with triangular faces (Figure 5.2a) and sizes of up 10 µm. They are formed by Zirconium-oxide / -hydroxide clusters linked with fumarate dianions. We implemented Raman spectroscopy for the label-free, 3D characterization of the chemical composition and background-free detection of water inside MOF-801. The water signature (characterized by the broad OH-stretch vibration around 3300 cm^{-1}) and MOF-801 are spectrally well separated (Figure 5.2b). We employed this spectral orthogonality in combination with the linear signal dependence on the amount of water to follow water uptake *in situ* with a spatial resolution of ~ 270 nm provided by the confocal microscope. Therefore, the probed volume is significantly lower than the average MOF-801 crystal size.

Firstly, we employed Raman spectroscopy to confirm the known water uptake mechanism by Furukawa and Coworkers[2] originally derived from single-crystal X-ray diffraction. A detailed description of the model is given in Section 5.5.1.2. We monitored the Raman signature of water in MOF-801 in terms of position and shape of the OH-stretch vibration, with increasing relative humidity (RH). MOF-801 features a multi-step mechanism for water uptake with known binding sites in tetrahedral and octahedral cages within the asymmetric unit cell of MOF-801 (Figure 5.2c). In the dry state with no water molecules bound, only the Zr: μ_3-OH stretch vibration of the metal-bound hydroxyl ligand at 3682 cm^{-1} was detectable (Figure 5.2b). This sharp, defined resonance gives clear evidence of the crystalline nature of this Zr: μ_3-OH hydroxyl group and the absence of guest molecules. The binding of water molecules is expected to happen first in the tetrahedral binding cavity to Zr: μ_3-O units (purple water molecules, Figure 5.2c). Indeed, we observed already at 2% RH a rising contribution of the OH-stretch resonance of water molecules between 3400 to 3700 cm^{-1} due to the incorporation of guest water molecules. As predicted, the Zr: μ_3-OH sites were unaffected and showed an identical Raman intensity with that in the dry state (Figure 5.2c). Between 2 to 6% RH, water is also adsorbed at the Zr: μ_3-OH sites (turquoise water molecules, Figure 5.2c), altering and diminishing the free vibration of the hydroxyl OH stretch Raman band at 3682 cm^{-1}, until it vanished. At 8% RH, the hydroxyl Raman peak was no longer detectable, while the adsorbed water led to a further intensity increase in the OH-stretch Raman signal between 3400 to 3700 cm^{-1}.

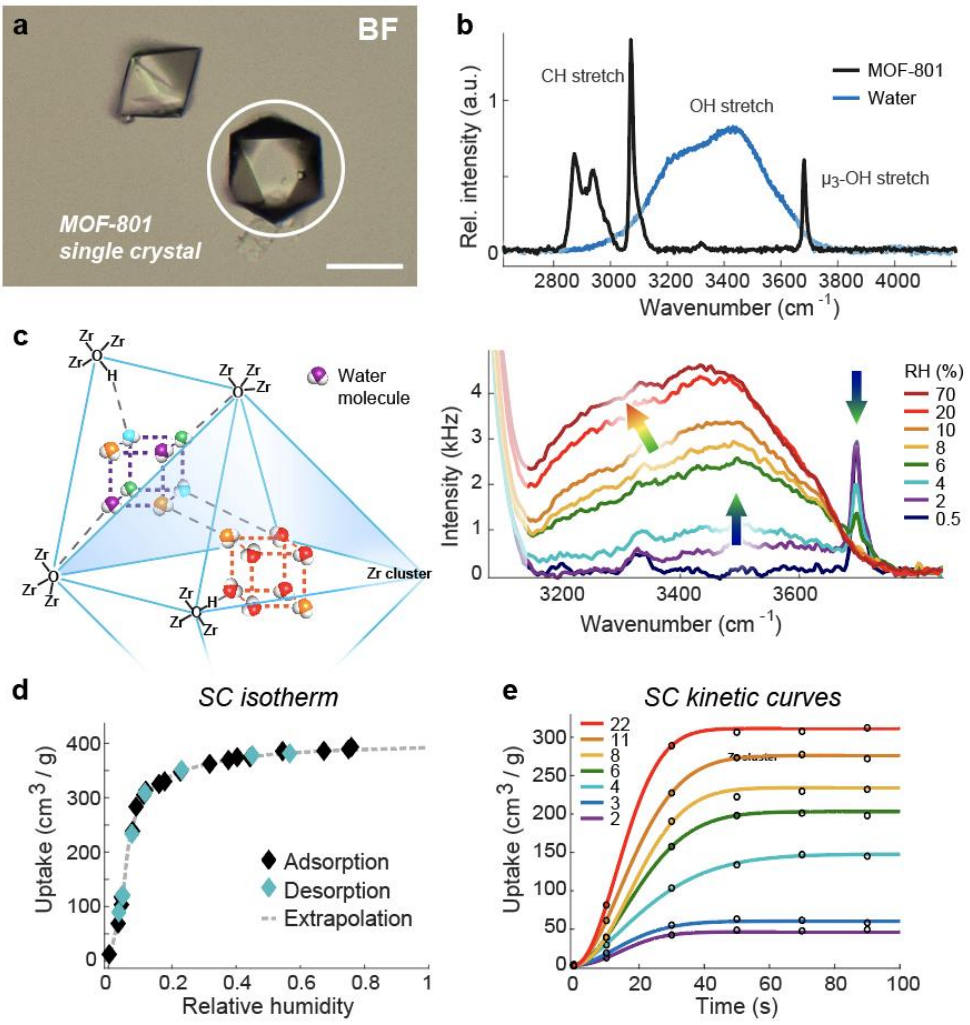


Figure 5.2: Water uptake in single, isolated MOF-801 crystals monitored by Raman spectroscopy. a) The bright-field image of MOF-801 shows isolated single crystals. Scale bar: 50 µm. b) Raman spectra of dry MOF-801 and liquid, double-distilled water. c) Raman spectroscopy of MOF-801 at increasing relative humidity (RH) confirms consecutive binding of water molecules in the tetrahedral (purple dotted cube) and octahedral (red dotted cube) binding cavities of the crystal structure. Coloring of water molecules (starting from blue over purple, cyan, green, and orange to red) indicates the binding order according to the reported uptake mechanism[2] for MOF-801. Arrows indicate spectral changes between corresponding humidities. Abbreviations: Zr: Zirconium; O: Oxygen; H: Hydrogen atoms. d) Absolute water uptake of single crystal (SC) MOF-801 derived from the ratiometric Raman analysis at varying humidities. Adsorption (black) and desorption (cyan) are reversible. The dotted line indicates the underlying isotherm, extrapolated to 100% RH. e) Kinetic of water uptake within the same crystal after exposure to selected relative humidities. The uptake saturates in ca. 50 s. Colored lines represent single-step Avrami fits, black dots show the data points.

In parallel, the OH peak maximum shifted to lower wavenumbers, indicating increased damping due to consecutive hydrogen bond formation to neighboring water molecules (green and orange water molecules, Figure 5.2c). After saturation in the tetrahedral cavities, the octahedral cavities are occupied by water molecules until saturation is reached (red water molecules, Figure 5.2c). Saturation starts above 20% RH with only a small amplitude increase still up to 70% RH. With increasing relative humidity, every new water molecule is further away from the metal clusters

and shielded from the host material. The spectral shape of the OH-stretch water peak in MOF-801 starts resembling the Raman signature of liquid water (Figure 5.2c; Figure 5.3a), as water guest molecules fill up the pores of MOF-801 only gradually. Humidity-dependent Raman spectra clearly support the published uptake mechanism in MOF-801.

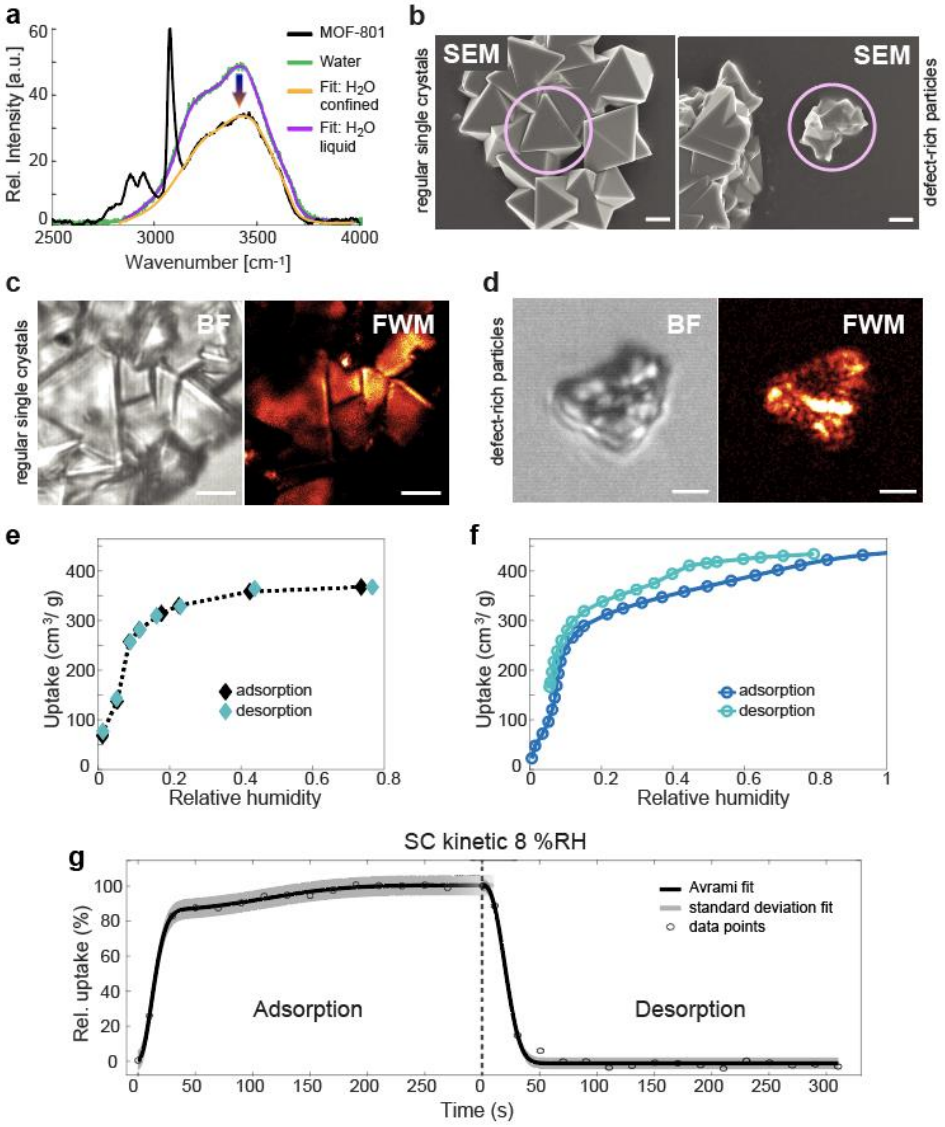


Figure 5.3. a) Raman spectra of water and MOF-801 under saturating humidity. At high relative humidity, the adsorbed water molecule do not sense the surrounding host material. Their Raman signature equals the one of liquid water. **b)** Scanning electron microscopy (SEM) of regular crystals and polycrystalline particles. Scale bars 5 µm. **c, d)** Bright-field (BF) and four-wave mixing (FWM) images of (c) regular single crystals and (d) polycrystalline particles. Scale bars 5 µm. Measurement details can be found in **Material section 5**. **e, f**) Adsorption and desorption Isotherms of MOF-801 determined (e) at the SC level and (f) in bulk via TGA. Measurement details can be found in **Material section 3 and 4. g)** Time course of water attachment after switching from 0 to 8% RH or reverse on a time window of 300 s. Time point 0 represents the exposure to the altered relative humidity. Both data sets represent the mean and standard deviation over 5 crystals.

Given the good agreement between the spectroscopic data and model, we next derived a theory-supported method to quantify the adsorbed water at the single crystal level (Section 5.3.1 and Section 5.5.2). The volume water uptake $\frac{V_{H2O}}{m_{MOF}}$ (in cm^3 g^{-1} of MOF) can be expressed via the density of the water-free host material ρ_{MOF} and the ratiometric expression $\frac{A_{OH}}{A_{CH}}$ linking the Raman intensity of the OH-stretch vibration of water to the CH-stretch vibration of MOF-801.

$$\frac{V_{H2O}}{m_{MOF}} = \frac{A_{OH}}{A_{CH}} \cdot \frac{1}{\rho_{MOF}} \cdot \Gamma \qquad \text{Eq. (1)}$$

The scaling factor Γ (Section 5.3 and Section 5.5.1.2) can be experimentally calibrated or theoretically modeled from the predicted number of water molecules $N_{H2O}(RH)$ in the asymmetric unit cell of MOF-801 at a given relative humidity. With this, we can quantify the water uptake at the SC level by converting the ratiometric ratio of measured OH to CH stretch Raman intensity.

We consecutively evaluated the inherent material performance of MOF-801 for taking up water without the interference of intra- or inter-particle effects using a series of Raman spectra inside of homogeneous, single crystals (SC). These were recorded as a function of relative humidity (*i.e.,* as isotherm curves) or as a function of the time after exposure to a given humidity (*i.e.,* kinetic curves). Figure 5.2d displays the SC isotherm for MOF-801 at 23.3 °C with a sub-micron resolution. The isotherm is characterized by a three-step behavior: after a steep uptake increase below ~8% RH, it features a second phase with slower adsorption behavior until 20% RH and slow saturation as the last phase above 20% RH. In contrast to bulk experiments,[2] no hysteresis could be observed, as expected for regular single crystals based on the pore size. Monitoring the temporal behavior of water uptake by MOF-801 at different relative humidities between 2 and 20% RH (Figure 5.2e) shows a nearly instantaneous uptake within the first tenth of seconds and the built-up of a constant plateau identical to the total amount of water observed in the SC isotherm. By modeling the kinetics by an Avrami model,[13] we found a saturation time around ~ 50 s (Section 5.5.1.1**)**.

5.2.2 Determine Water Uptake in MOF-801 Crystals via Raman spectroscopy

For water harvesting applications, MOF-801 is usually grown in monocrystalline, regular single crystals (Type 1). For about 10% of the particles, however, we found MOF-801 particles without crystalline faces (Type 2); see SEM images in Figure 5.3b). While regular crystals possess strongly reflecting surfaces with defined triangular shapes, Type 2 crystals display a complex inner structure as seen already by bright-field microscopy (Figure 5.3c-d). We verified the associated, higher level of defects by four-wave mixing (FWM) imaging, which is susceptible to defect sites and irregularities.[14] In contrast to the regularly formed, homogenous MOF-801 crystals**,** we found inhomogeneous substructures in defect-rich particles (Figure 5.3d) with localized, enhanced FWM signals indicating open metal sites inside the material.[14] SC X-ray diffraction on Type 1 and 2 crystals further confirmed the monocrystalline or polycrystalline nature of the material (Section 5.5.3), respectively. While Type 1 crystals possessed the expected cubic unit cell[2] with space group *Pn*-3, Type 2 particles were composed of multiple MOF-801 unit cell patterns with different orientations in the same crystal, hence representing defect-rich crystals with sub-crystallization zones.

Next, we set out to answer how intra-particle effects in defect-rich particles influence the SC performance compared to monocrystalline MOF-801. Figure 5.4a depicts the mean SC isotherm

of regular single crystals (blue; standard deviation as blue shade; cf. Figure S5.12) at 23.3 °C. We found a type IV isotherm with a clear step around 7% RH, a fast saturation below 20% RH, and maximum uptake of about 379 cm^3 g^{-1} (± 16.5 cm^3 g^{-1}) at ~77% RH.

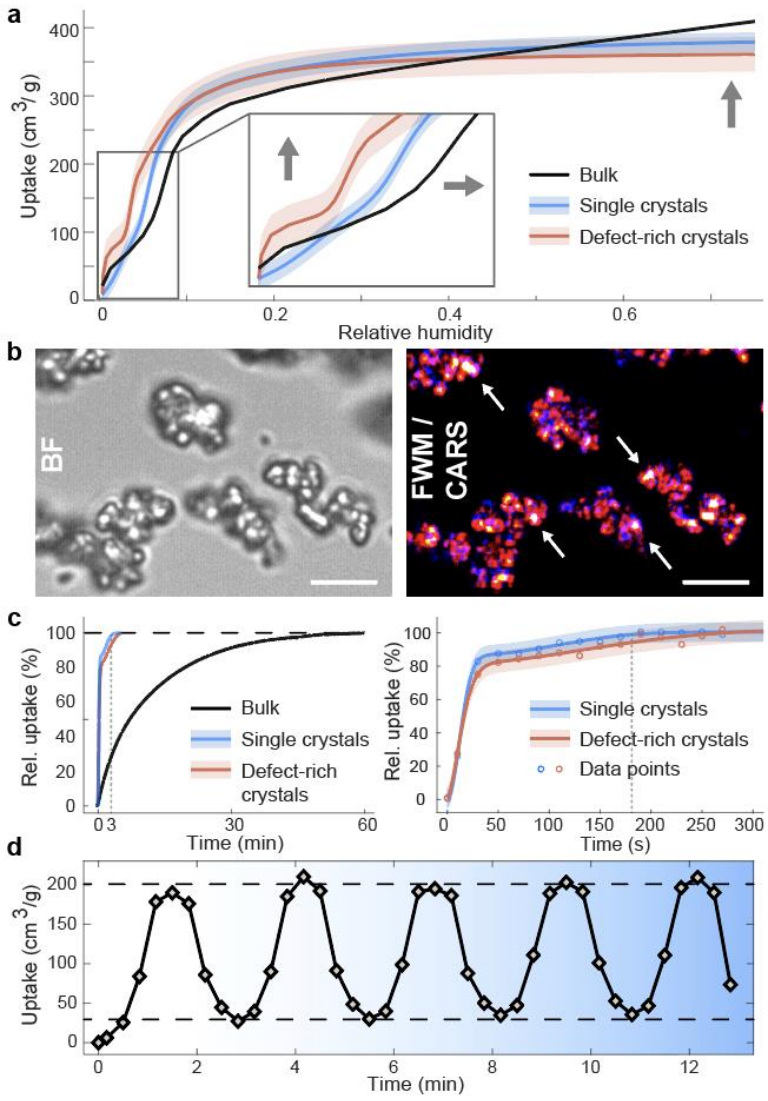


Figure 5.4. Influence of intra- and inter-particle effects in MOF-801 on SC isotherms and water kinetics. a) Isotherms of the bulk, the regular, single and defect-rich MOF-801 crystals. The colored lines represent the mean fit curve of SC (N = 7) and defect-rich (N = 5) particles. The shaded areas represent the corresponding standard deviation. b) Bright-field (BF, left panel) and label-free imaging based on FWM (red hot) and CARS (blue) microscopy to monitor the morphology and position of particle clusters with respect to uptaken water at 30% RH after saturation at ~70% RH for 5 minutes. CARS imaging based on the Raman resonance around 3400 cm^{-1}, *i.e.* 612 nm, shows the distribution of water within the material. While, some defect sites coincide with enhanced uptake (white spots, marked by arrows), we found a dominating contribution of inter-particle adsorption of water. Scale bar 2 µm. c) Bulk and average SC adsorption kinetic of dry MOF-801 (N = 5) after exposure to nitrogen with 8% RH, described by a customized Avrami fit function. While even a thin layer of bulk material needs about 1 h until saturation, single crystals saturate in 3-4 minutes (left panel). Dotted lines mark the 3 min time point. Even defect-rich particles take up >80% of the total amount in less than 60 s (right panel). Circles mark the center of the 20 s

long detection window per point. The standard deviation (shaded area) was derived per data point. d) Relative SC uptake when switching the RH that surrounds the sample between 0 and 8% RH every 80 s.

While the mean isotherm of defect-rich particles (orange) resembled the overall performance of regular crystal isotherms, it displayed three major differences: (*i*) Firstly, the standard deviation was significantly higher, reflecting the high variance of the underlying defects in the selected particles. (*ii*) Secondly, a faster uptake at low relative humidities was seen for isotherms in type 2 particles. The accompanying shift of the isotherm step towards lower RH confirms a higher amount of primary water molecules in the structure, as well as macropores created by missing cluster defects as observed by FWM imaging (Figure 5.4b). (*iii*) Thirdly, the average maximum uptake is decreased compared to regular crystals, meaning the inner surface per volume of defect-rich particles was found to be lower.

The bulk isotherm showed a higher uptake compared to the regular SC isotherm at very low RH, indicating open metal sites as observed for defect-rich particles. Below 10% RH, the bulk isotherm rises less steeply than the SC isotherm, causing a shift of the infliction point toward higher RH. Above 10% RH, the SC and the defect-rich isotherm show a strong and distinct saturation, while it still increases linearly in bulk. At RH over ~60%, this results in more water per bulk material than in single crystals alone.

Next, we approached the question of which effects are responsible for the different uptake behavior in bulk and at the SC level. In bulk, water molecules can condensate in the inter-particle space between crystals leading to an additional uptake. As defects like cracks or macropores can equally contribute to water incorporation and hysteresis, we employed a combination of FWM and Coherent Anti-Stokes Raman Scattering (CARS) imaging to visualize the morphology and position of MOF-801 in comparison to the distribution of uptaken water. FWM monitors the distribution of MOF-801 material and especially open metal sites,[14] while CARS localizes and quantifies uptaken water. Figure 5.4b displays the overlay of an FWM (red) and a CARS (blue) image over the same region at 20.8% RH, measured after saturating the system at 70% RH for about 5 minutes. Areas, where local water clusters are caused by defect sites, appear white in the image (examples marked with arrows). We found that the water signal was mostly anti-correlated to the FWM signal, indicating liquid water between and around the crystals. It explains the larger amount of uptaken water and the missing hysteresis in SC isotherms of regular single crystals compared to bulk (Figure 5.3e, f).

Due to interparticle adsorption, also the bulk kinetic differs significantly from the SC kinetic behavior (Figure 5.4c**)**. While the SC isotherms of MOF-801 were saturated within less than 3 min after a change in RH around the sample, the uptake in bulk saturated after 1h. The kinetic response of dry, regular MOF-801 crystals (8% RH) revealed a fast uptake, reaching > 85% within the first 60 s. The datasets were approximated by a dual-step Avrami model (Section 5.5.1.1; Figure S5.13). It revealed a second uptake step between 100 and 200 s, probably due to consecutive filling of the octahedral cavities in MOF-801. The kinetic behavior of Type 2 particles (Figure 5.4c; orange curve) followed the Type 1 curve very closely. When modeling the liquidation of water within MOF-801 by a dual-step Avrami fit, more than 80% uptake was found to occur within the first minute, while the successive filling process was observed around 100 to 200 s. Overall, water uptake by Type 2 particles was found to happen slower than that in regular crystals. This might be caused by the complex inner structure, hindering the fast transport to the inside of the particles. It could also be that defect sites on the outer perimeter of the particle spawn fast water clusters, which are blocking the diffusion of water molecules further inside.[15]

Since the desorption time of single crystals are in the same regime as the adsorption (Figure 5.3g), the inherent cycle time for MOF-801 itself is significantly faster than currently possible in water harvesting devices due to inter-particle contributions. To demonstrate the maximum capabilities of the undisturbed MOF-801 framework, we selected a regular single crystal and cycled the RH between 0 and 8% with a cycle time of 160 s (Figure 5.4d). The sample was first completely dried with nitrogen (Methods Section 5.3.3**)**. Next, the RH of the gas stream over the sample was changed from 0 to 8% RH (or back) every 80 s while the uptake was monitored. The first desorption is not returning to the ground level at t = 0 s, which could be caused by primary bound water molecules that are not desorbing on the selected time scale. During the recorded cycle, we found a total difference in relative uptake (maximum – minimum per cycle) of 851 ± 13.3 cm^3 g^{-1} MOF over five cycles, i.e., a possible harvest of ~170 cm^3 g^{-1} MOF (12.6 wt%) every 160 s. In comparison, MOF-801 was implemented into a water harvesting device to test the practical water harvesting cycle (WHC). It can produce 2.8 L of water per kilogram of material daily.[11] The remarkable time difference of WHC indicates the upper limit of the material could be reached. It would be possible to harvest around 24 times more water compared to developed devices.

5.3 Materials and Characterizations

5.3.1 Hyperspectral Raman Imaging at A Controlled Relative Humidity

Static and dynamic Raman spectroscopy measurements were carried out on a home-built, confocal, multi-modal microscope[14] using a 532 nm CW laser source (Samba 100 04-01, Cobolt GmbH). The excitation power was 21 mW (measured at the entrance of the microscope backport) for all measurements. Spectra were recorded between 2300 and 4215 cm^{-1} probing the CH-stretch region of the MOF-801 material, and the OH-stretch vibrations of adsorbed water molecules, if not mentioned otherwise. The spatial resolution of the Raman mapping experiment was 0.27 µm in the lateral and 0.74 µm in the axial direction for a 60x water-immersion objective lens (1.2 NA). The scattered light at the sample was collected in epi-detection using a spectrometer (Kymera 328i, Andor Solis) equipped with a 300 lines mm^{-1} grating and a 512 x 512 pixel emCCD camera (iXon 897, Andor Solis). This instrumental configuration enables a spectral resolution of ~15 cm^{-1}. The spectral acquisition was controlled by *Andor Solis for Imaging V4.30* (Oxford Instruments). For image acquisition, areas with 500 nm step-size were raster-scanned while full Raman spectra were recorded at each pixel of the image. The acquisition time per pixel was set to 5 s.

For monitoring adsorbed water molecules in MOF-801 *in situ*, we installed a relative humidity control unit (Figure 5.5a) on the confocal setup. The MOF sample is located in a channel slide (µ-Slide I Luer Glass Bottom, Ibidi) on top of the XYZ scanning stage of the microscope and connected to the flow system. Dry nitrogen serves as the reference and carrier gas for extracting water molecules from the MOF materials through constant flow. A three-way vault can switch between this drying line and the ‘wet line’ containing nitrogen with a specific relative humidity. The latter can be adjusted by the flow ratio regulated by two mass flow controllers (MFC, D-6311-FGD-33-AV-99-0-S-DR, Wagner Mess- und Regeltechnik GmbH): the nitrogen in the ‘wet line’ is enriched with water vapor by diffusing through a double-distilled, water-filled vessel. The relative humidity is controlled directly after mixing and at the sample chamber, as marked by RH in Figure 5.5a. The laboratory temperature was set to 23.3 °C, and the total mass flow was held constant at 1 standard liter nitrogen per minute for all experiments.

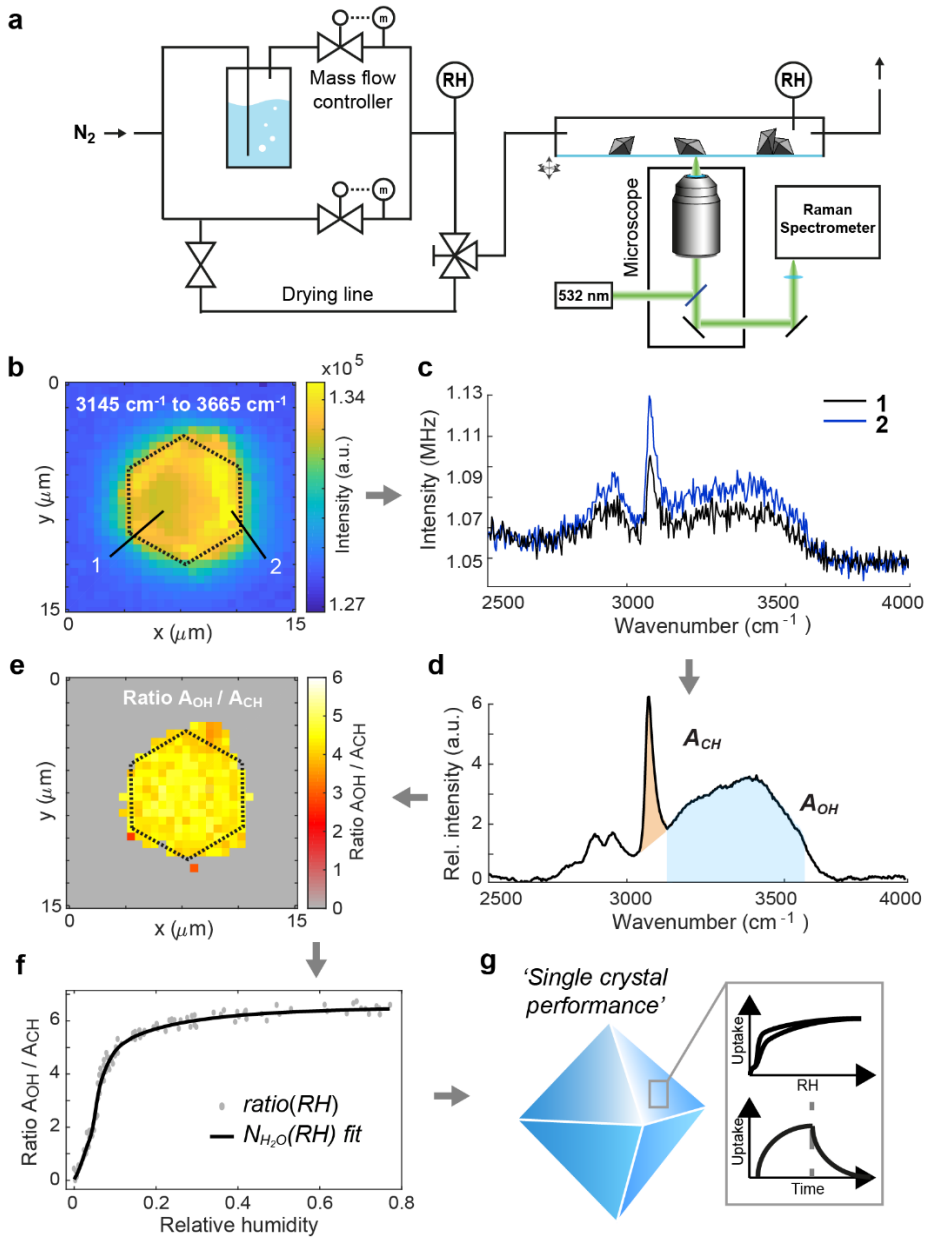


Figure 5.5. Quantification of water uptake in MOF-801 at the single crystal level by Raman spectroscopy. a) Schematics of the micro-spectroscopy setup with the unit for controlling the relative humidity over the sample. RH: relative humidity measuring stations. b) Univariate analysis of a hyperspectral Raman data set in the water OH—stretch region reveals an irregular water distribution in a regular single crystal of MOF-801. Crystal border at measurement plane is indicated as dotted line. Raman mapping was carried out at 5 s integration time. The scanning range was 20 x 20 µm with 40 pixels per line. c) Raman spectra of selected pixels marked in (a). d) Background corrected, mean spectrum over all pixels inside the crystal border. The strength of the CH- (orange) and the OH-stretch vibration (blue) is indicated as area under the graph. e) The ratiometric representation A_{OH} / A_{CH} of the HRI data set in (a) shows a uniform water distribution. f) Ratio A_{OH} / A_{CH} at varying relative humidities between 0 and 77% RH recorded for 7 regular single crystals (grey points) allows for determining number of water molecules per unit cell, i.e. $N_{H2O}(RH)$. g) Schematic of the single crystal performance methodology.

5.3.2 Quantification of Water Uptake

The local uptake and distribution of water were quantified based on the linear dependence of Raman scattering on the number of scattering molecules in the confocal volume (Section 5.5.2.31). To ensure that water is evenly distributed in uniformly grown MOF-801 crystals, we first used hyperspectral Raman imaging (HRI) within a region of interest and recorded Raman spectra at each pixel. We visualized the water content in MOF-801 crystals first by univariate data analysis and derived the Raman intensity A_{OH} of the OH stretch vibration of water between 3145 and 3665 cm^{-1} as a function of the position within the crystal

$$A_{OH}(x,y) = \int_{3145\ cm^{-1}}^{3665\ cm^{-1}} I_{Raman}(\tilde{\nu},x,y)\ d\tilde{\nu} \qquad \text{Eq. (1)}$$

Figure 5.5b depicts an exemplary water distribution at ~38% RH. The apparent hexagonal shape of the crystal clearly confirms the sectioning capabilities of HRI and the correct positioning for imaging the particle: the image plane was successfully selected at around 50% height of the octahedral crystal (Figure S5.15) for monitoring the water content inside the crystal center. The HRI image shows a continuous water distribution throughout the whole crystal with apparently increased water content at the surface boundaries, in addition to an intensity gradient from left to right. This apparent increase at the edges would indicate that saturation inside the crystal would not have been reached yet, even after 1 h of equilibration at ~38% RH. For a regularly shaped crystal, we would expect an even distribution of adsorbed water per MOF material within minutes due to fast intra-crystalline diffusion,[12] contrary to the experimental findings.

Deviations in apparent water uptake are caused by a combination of light scattering at the edges and a varying amount of MOF material inside of the detection volume due to defects and the 3D nature of the particles. Both effects lead to a variation in local excitation power and detection efficiency, an incomplete filling of the confocal volume, and concomitantly to a change in absolute amplitude of the recorded Raman spectra, as for example seen for areas within the interior (Position 1) and at the edge (Position 2) in MOF-801 (Figure 5.5c).

To prevent any influence of these effects on the quantification of the water uptake in MOF-801, we introduced a ratiometric approach that quantifies the amount of detected, water-associated OH-stretch intensity in comparison to the observed CH-stretch signal reporting on MOF-801 and hence the amount of surrounding host material present. Here, the water uptake relates not to A_{OH} alone but to the ratio of A_{OH} / A_{CH}. Figure 5.5d shows the background-corrected, mean spectrum over all pixels inside the crystal. The strength of the OH-stretch band A_{OH} is marked in blue, the CH-stretch A_{CH} is in orange. To correct against the spectral overlap between the water-based OH-stretch and MOF-801-associated CH-stretch resonance below 3150 cm^{-1}, modeling and deconvolution of the water peak from the MOF-signature (Section 5.5.2.2) was employed, resulting in the area marked in orange. Using the ratiometric representation, i.e., when plotting the peak ratio A_{OH} / A_{CH} as a function of position, the interior displays an even signal (Figure 5.5e), representing the expected uniform, saturated uptake of water inside the crystal.

To convert the ratiometric Raman ratio into a quantitative measure, i.e., into water volume per mass of MOF-801, three interrelations need to be considered:

(1) The uptake can be related to the density of water ρ_{H2O}, the respective molecular weight M_x, as well as the amount of material n_x in the confocal volume and hence the Raman intensity of the OH and CH stretch vibration

$$\frac{V_{H2O}}{m_{MOF}} = \frac{n_{H2O} \cdot \frac{M_{H2O}}{\rho_{H2O}}}{n_{MOF} \cdot M_{MOF}} = \frac{A_{OH}}{A_{CH}} \cdot \frac{cf_{OH}}{cf_{CH}} \cdot \frac{M_{H2O}}{\rho_{H2O} \cdot M_{MOF}} \qquad \text{Eq. (2)}$$

The latter formula takes into account that the detected intensities of both Raman resonances A_x are proportional to the quantity of guest and host species

$$n_{H2O} = cf_{OH} \cdot A_{OH} \,/\, N_A \qquad \text{and} \qquad n_{MOF} = cf_{CH} \cdot A_{CH} \,/\, N_A \qquad \text{Eq. (3)}$$

(2) The conversion factors can be determined either experimentally or theoretically. Experimental calibration was carried out in pure water and dry MOF-801 material. Knowing the density of the host and guest material allows for calculating the number of Raman active species in the confocal volume in the first step, irrespective of the absolute Raman intensities. The conversion factors of dry MOF-801 and water under excitation intensity would amount to

$$cf_{OH} = \frac{n_{H2O,cal}}{A_{OH,cal}} = \frac{\rho_{H2O} \cdot V_{confocal}}{A_{OH,cal} \cdot M_{H2O}} \qquad \text{Eq. (4a)}$$

$$cf_{CH} = \frac{n_{MOF,cal}}{A_{CH,cal}} = \frac{\rho_{MOF} \cdot V_{confocal}}{A_{CH,cal} \cdot M_{MOF}} \qquad \text{Eq. (4b)}$$

with $A_{x,cal}$ referring to the peak strength of the OH- or CH-stretch vibration for the host and guest material. When combining eq. 4-5, the expression for water uptake shortens to

$$\frac{V_{H2O}}{m_{MOF}} = \frac{A_{OH}}{A_{CH}} \cdot \frac{A_{CH,cal}}{A_{OH,cal}} \cdot \frac{1}{\rho_{MOF}} \qquad \text{Eq. (5)}$$

For identical measurement conditions of the calibration measurements, the ratio $\frac{A_{CH,cal}}{A_{OH,cal}} := \Gamma$ of calibrated Raman intensities remains constant and can be treated as a scaling factor

$$\frac{V_{H2O}}{m_{MOF}} = \frac{A_{OH}}{A_{CH}} \cdot \Gamma \cdot \frac{1}{\rho_{MOF}} \qquad \text{Eq. (6)}$$

As laid out in Section 5.5.2**,** the measurement conditions for calibrations of host and guest molecules-associated scaling factors differ due to variations in excitation intensity induced by scattering in the detection volume. While no polarization dependency in MOF-801 was found for the CH and the OH-stretch Raman peak (Figure S5.6), we need to incorporate the reduction in excitation power and hence linearly decreased Raman signature of the detected CH stretch vibration and adopt the experimental scaling factor to

$$\Gamma_{exp} = \frac{A_{CH,cal}}{A_{OH,cal} \cdot L_{scatter}} \qquad \text{Eq. (7)}$$

We estimated the average scattering loss $L_{scatter}$ on MOF-801 compared to transparent water alone by determining the integrated transmission intensity of broadband white-light via brightfield microscopy (Figure S5.7). We experimentally obtained the scaling factor Γ_{exp} for MOF-801 as 0.0837 ± 0.0131.

(3) Since the experimental determination of Γ is challenging, we further modeled the number of water molecules in the asymmetric unit cell of MOF-801 as a function of the relative humidity $N_{H2O}(RH)$ based on the water uptake mechanism[2] in MOF-801. Modeling by an adapted Klotz model reveals that the volume water uptake in (cm^3 g^{-1} MOF) and relative humidity N_{H2O} are related by a linear scaling factor of 8.22 (Section 5.5.1.2).

$$\frac{V_{H2O}}{m_{MOF}} = N_{H2O}(RH) \cdot 8.22 \qquad \text{Eq. (8)}$$

Knowing that the ratio A_{OH} / A_{CH} describes the uptake as a function of relative humidity while being proportional to the number of water molecules $N_{H2O}(RH)$ by a constant factor f_{fit}

$$\frac{A_{OH}}{A_{CH}} = N_{H2O}(RH) \cdot f_{fit} \qquad \text{Eq. (9)}$$

we can theoretically derive an expression for the scaling factor Γ_{th} (insert eq. 9-10 in eq. 7), that is independent of the calibration procedure

$$\Gamma_{th} = \frac{8.22 \cdot \rho_{MOF}}{f_{fit}} \qquad \text{Eq. (10)}$$

With the theoretical model (Section 5.5.2.3) and eq. 10 at hand, we employ the SC isotherm data itself expressed as ratio A_{OH} / A_{CH} as a function of relative humidity and fit its course to the model function $N_{H2O}(RH)$ to determine the scaling factor Γ_{th}. Figure 5.5f depicts the ratio A_{OH} / A_{CH} at relative humidities between 0 and ~77% RH and the model fit function $N_{H2O}(RH)$ that determines the number of adsorbed water molecules per asymmetric unit cell. We found a model-supported scaling factor $\Gamma_{th} = 0.0938 \pm 0.0041$ with uncertainty that only depends on the intrinsic noise of the underlying Raman spectrum (Figure S5.8). It is in good agreement with the calibration-based scaling factor of $\Gamma_{exp} = 0.0837 \pm 0.0131$ (Figure S5.9) within the range of error (Section 5.5.2.4).

5.3.3 Raman-Based Single-Crystal Isotherms and Sorption Kinetics

MOF-801 powder was placed in a channel slide (µ-Slide I Luer Glass Bottom, Ibidi) on the microscope and dried under nitrogen flow until the RH reached 0.0% RH (for at least 1h). In the following, adsorption isotherm / kinetic curves refer to measurements with a prior increase in relative humidity, while desorption experiments refer to a prior decrease in RH. Crystals were selected in the bright field channel and measured in the midplane of the selected particles. The corresponding measurement parameters are summarized in Table 5.1. The laser power was 25 mW (measured in front of the microscope body) for all experiments.

For SC isotherms, we waited for equilibration of the system after a change in RH (at least 3 min) before starting the measurement of each data point. For SC adsorption/desorption isotherms, we

waited at least 10 minutes after the adsorption measurement before reducing the RH again to ensure full saturation with humid air at the upper turning point between adsorption and desorption isotherm.

For monitoring the SC adsorption kinetics, we dried the sample as described above and adjusted the RH in the disconnected wet line meanwhile to 8% RH. At t: = 0 s, a kinetic series in the Andor Solis software was started, and the three-way vault was applied to switch from the dry to the humid flow. The tube length between vault and channel slide was ca. 80 cm with an inner tube diameter of 2 mm, resulting in ca. 2.5 cm^3 volume. The channel slide has an inner volume of 60 µL. The constant flow of 1 standard liter $minute^{-1}$ (ca. 18 mL s^{-1}, i.e. 1080 mL min^{-1} for nitrogen at 23.3 °C) ensures a complete air exchange over the sample in less than 1 s. For the designed system and settings, we found, that the adsorption kinetics is not dominated by the flow rate (Figure S5.15).

For monitoring the SC desorption kinetics, the sample system was held at a fixed relative humidity, e.g., at 8% RH until t: = 0 s. Then, the mass flow controllers were set to 1 and 0 standard liter per minute, effectively exposing the sample with dry nitrogen only under a controlled flow at 1 standard liter per minute.

For cycling kinetic experiments, the ratio of the mass flow controllers was alternated every 80 s between only dry air and predefined values (e.g., 0.9 (dry) to 0.1 (humid) standard liter per minute for 8% RH).

Table 5.1: Measurement setting for monitoring the sorption isotherms, kinetics, and spatial distribution of water by Raman spectroscopy.

	Integration time (s)	Accumulation	EM Gain
SC isotherm	50	5	0
SC kinetic	20	1	100
Hyperspectral scan	5	1	100

5.3.4 MOF-801 synthesis and material characterization

5.3.4.1 MOF-801 Synthesis

5.3.4.1.1 Chemicals Used for Synthesis

Zirconium oxychloride octahydrate ($ZrOCl_2 \cdot 8H_2O$, purity ≥ 99.5%), fumaric acid, Sigmacote® siliconizing reagent were obtained from Sigma-Aldrich Co. *N*,*N*-Dimethylformamide (DMF), formic acid (purity ≥ 99.0%), and anhydrous methanol were obtained from EMD Millipore Chemicals. Anhydrous acetone was obtained from Acros Organics.

5.3.4.1.2 Preparation of Single MOF-801 crystals

For synthesizing monocrystalline SC-MOF-801 [$Zr_6O_4(OH)_4(fumarate)_6$], fumaric acid (0.027 g, 0.23 mmol) and $ZrOCl_2 \cdot 8H_2O$ (0.075 g, 0.23 mmol) were dissolved in DMF (11.67 ml) before adding formic acid (1.76 ml) to the solution. The solvent mixture was placed in a 20-ml vial, which was heated at 120 °C for two days. Octahedral colorless crystals were collected and washed with fresh DMF three times per day for three days. The crystals were subsequently washed with fresh methanol for three days, three times per day. The solid was then dried under dynamic vacuum at room temperature for 2 hours and at 120 °C for 24 hours to yield an activated sample.

5.3.4.1.3 Preparation of MOF-801 as Microcrystalline Powder

For synthesizing microcrystalline powder of MOF-801 [$Zr_6O_4(OH)_4$(fumarate)$_6$], fumaric acid (0.290 g, 2.50 mmol) and $ZrOCl_2 \cdot 8H_2O$ (0.805 g, 2.50 mmol) were dissolved in DMF (10.0 ml) before adding formic acid (3.50 ml) to the solution. The solvent mixture was placed in a 20-ml vial and heated at 130 °C for 6 hours. As-synthesized microcrystalline powder was collected and washed with fresh DMF three times per day for three days. The sample was then washed with fresh methanol three times per day for three days. The solid was afterward dried under dynamic vacuum at room temperature for 2 hours and at 120 °C for 24 hours to yield an activated sample.

To reduce the nucleation in the growth of MOF-801 samples, the inner surface of the 20-ml vial was rinsed with siliconizing reagent Sigmacote®, washed with acetone, and dried in the oven before use.

5.3.4.2 MOF-801 Characterization

5.3.4.2.1 Single-crystal X-ray diffraction (SC-XRD)

Single-crystal X-ray diffraction (SC-XRD) datasets were collected at the beamline 12.2.1 at the Advanced Light Source (Lawrence Berkeley National Laboratory, USA) using a radiation wavelength of $\lambda = 0.7288$ Å. Beamline 12.2.1 is equipped with a PHOTON-II CMOS detector operating in shutterless mode and a Si(111) monochromator. For the measurement, the crystalline sample was mounted on a Kapton® MiTeGen MicroMount™ in a minimal amount of Paratone® N oil and submerged in a cold gas stream generated by an Oxford Cryosystems 800 Series Cryostream.

5.3.4.2.2 Scanning Electron-Microscopy (SEM)

SEM measurements were carried out on an FEI Quanta 3D FEG scanning electron microscope using an accelerating voltage of 10 kV and a working distance of 10.4 mm. Prior to experiments, crystalline MOF-801 powder was thoroughly washed with DMF and methanol, activated under dynamic vacuum and afterward dispersed on a silicon wafer.

5.3.4.2.3 Sorption measurements for determining isotherms and kinetic curves in bulk

Low-pressure N_2 adsorption measurements were carried out on a Micromeritics ASAP 2420 surface area analyzer. Ultrahigh-purity-grade N_2 and He (99.999% purity) were used throughout adsorption experiments. MOF-801 samples were dried under dynamic vacuum at 120 °C for 12 hours prior to the analyses.

Kinetic water adsorption curves were conducted on 1.029 mg of MOF-801, uniformly distributed on a 6.35-mm diameter pan with the help of a thermogravimetric analyzer (TGA) under constant humidified nitrogen flow (200 mL min^{-1}). The water sorption dynamics measurements were conducted with a TA Instruments SDT Q600 series thermal gravimetric analyzer (TGA). The primary gas inlet was directly connected to a nitrogen tank (Praxair, ultrahigh purity, 99.999%). The secondary gas inlet was used to supply a humidified nitrogen feed by regulating the gas flow using a mass flow controller (Sierra SmartTrak 100) and passing the stream through a gas washing bottle (2 L). The temperature and RH were monitored using high-accuracy thermocouples and humidity sensors downstream of the TGA chamber. For the measurements in thin-layer geometry, ~1 mg of the microcrystalline powder sample of MOF-801 was loaded in the TGA pan. Prior to the adsorption measurement in the TGA, microcrystalline MOF-801 sample was activated under dry nitrogen flow (176 mL min^{-1}) at 150 °C, respectively, until the weights of MOFs do not have

noticeable changes. After activation, the samples were cooled down to 30 °C under dry nitrogen flow (176 mL min^{-1}). Immediately after 30 °C was reached, the adsorption measurement was started. The temperature during the adsorption was kept constant at 30 °C, and the RH was kept at 8%.

5.3.5 MOF-801 synthesis and material characterization

The water distribution between MOF-801 crystals was visualized by multimodal imaging using two microscopy techniques: four-wave mixing (FWM) and coherent anti-Stokes Raman scattering (CARS). For this, we previously coupled a pulsed near-infrared light source in a home-built scanning Raman microscope.[14] Briefly, two synchronized femtosecond laser pulse trains at ω_1 = 774 nm and ω_2 = 1053 nm serve to derive the pump and Stokes beams as third-order nonlinear excitation. The pump beam at 774 nm has a pulse duration of about 150 fs. The spectrally broadened Stokes beam was derived by super-continuum generation in a PCF at 1053 nm. Both pulse trains were recombined and coupled into the scanning microscope collinearly with the CW laser. The details on optical elements controlling the chirp, polarization, intensity, and beam shape have been outlined previously.[14] At given temporal and spatial overlap between both excitation sources within the MOF-801 sample, a nonlinear resonance at $2\omega_1 - \omega_2$ can be detected in epi-direction by decoupling the signal from the excitation via a dichroic mirror (zt532/NIRrpc; AHF, Germany) and spectral filtering via a bandpass filter (HQ 620/60 M; AHF, Germany) before avalanche photodiodes (Count Red; LaserComponents). Scanning of the sample is achieved using an XYZ piezo stage (BIO3.200; PiezoConcept).

FWM is a third-order nonlinear process that occurs independently of molecular transitions present in the sample. In presence of a vibrational or electronic resonance, the FWM signal is strongly enhanced and dominated by either coherent Raman scattering (CARS) or stimulated parametric emission, respectively. We employed polarization-dependent CARS (pCARS), to separate the vibrational response of the material from the unspecific FWM background by tuning the relative polarization angle between the linearly polarized exaction beams. An additional polarizer in front of the detector allows for selecting between CARS and FWM signal. To address the OH stretch band around 3400 cm^{-1}, we made use of spectral focusing[1] by chirping the Stokes beam within an 20 cm SF6 glass rod and temporally overlapping the pump beam with corresponding spectral components of the Stokes beam. FWM microscopy at ~ 612 nm used the temporal overlap with non-resonant components around 1050 nm.

Scan times per image were 180 s with an average beam power of 24 and 20 mW in front of the objective for pump and Stokes pulses respectively. CARS, as well as FWM images were scanned with 500 x 500 pixels, a step size of 180 µm and accumulated over 3 repeats.

5.4 Conclusion

In this chapter, we have demonstrated a methodology based on Raman spectroscopy for *in situ* measuring qualitative and quantitative water sorption with sub-micron resolution. By monitoring and understanding the intra- and inter-particle contribution of water uptake via adsorption-desorption isotherm and kinetic curves in MOF-801 at the single-crystal level, we found a striking difference in sorption behavior between single crystals and the bulk material. Before this work, it was assumed that the measured bulk sample was representative for each crystal when applying sorption isotherms, although crystals were not created equally nor possessed identical characteristics, such as size, morphology, or defect level. By measuring cyclic water sorption at the single-crystal level, which is the most perfect state of solid material, we determine the upper

limit of MOF-801 with a minimum cycle time below 3 minutes. This surprisingly fast cycle time enables a potential harvest of ~3.8 L water per hour per kilogram of MOF, a significant improvement over the previously reported 2.8 L per day.[4,11] Therefore, our approach could help to reveal the hidden upper limit of a material's inherent property to push technology advancement.

5.5 Supporting Information

5.5.1 Uptake Mechanism Description and Fit Model

5.5.1.1 Kinetic Curve Fit Model

For monitoring the water uptake over time in MOF-801, Raman spectra were taken in the center of single MOF-801 crystals. The kinetic series were recorded within a 20 s acquisition time window, with t = 0 s being the time point, at which the sample chamber is either exposed to humid air or to pure N_2. Since spectra at every frame represent the average over the kinetic process during the acquisition time, the respective time points are chosen as the midpoint between the start and end time point of the frame (Figure S5.1), while the first frame lasting from t = - 20 s to 0 s was exceptionally set as data point $t_{kinetic}$ = 0 s. The second frame time from 0-20 s was set as $t_{kinetic}$ = 10 s, the third frame time from t = 20 to 40 s as $t_{kinetic}$ = 30 s, etc., continuing until $t_{kinetic}$ = 250 s usually.

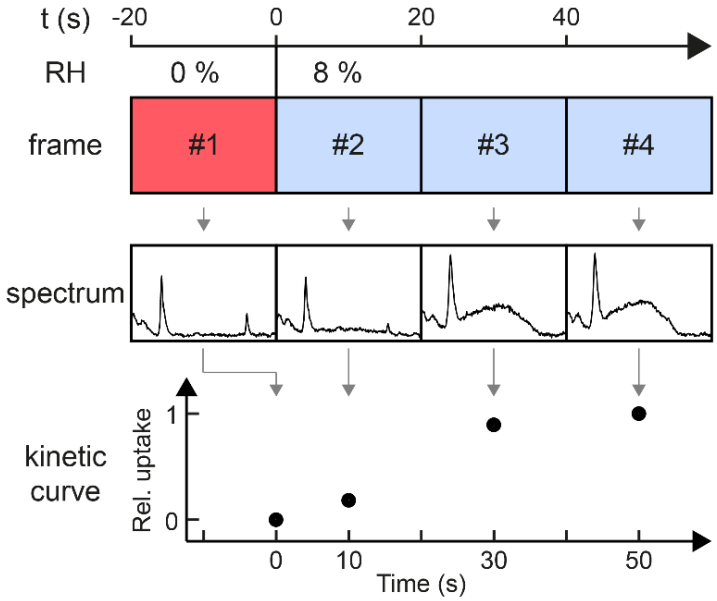


Figure S5.1 Data processing for kinetic series. Schematics of the data processing for determining the uptake kinetics in MOF-801 from a series of Raman spectra as function of time. The conversion of Raman spectra to quantitative amount of uptaken water is identical as described for the isotherm curves.

The kinetics (Figure 5.4c and d) of water uptake in type 1 and type 2 crystals was always determined for 5 single MOF-801 particles of both types each and represented as average increase plus standard deviation. The RH in the humid air flow deviated by 0.5 %RH maximally (e.g.., 8.0 ± 0.5 %RH) during kinetic measurements on different crystals, days, and slightly unbalanced changes in flow rate at the start of the measurement. All kinetic data sets were scaled between the minimum (relative uptake := 0 %) and maximum (relative uptake := 100 %). The average value and standard deviation per relative humidity were calculated for both types. The data were empirically fitted with a dual-step Avrami model [16-17] based on the findings of Martell et al.,[13]

taking the cooperative binding of water (Section 5.5.1.2) and transformation from gas to liquid phase into account:

For the desorption curve, the fit needed to be modified to a one-step Avrami model by fixing $w_2 := 0$ to address the more direct desorption behavior observed (Figure 5.3f). A more detailed study of the desorption mechanism will be the prospect of future research.

5.5.1.2 Water Adsorption Isotherm Curve Fit Model

MOF-801 features a multi-step mechanism for water uptake[2] with binding sites in tetrahedral and octahedral cages (Figure S5.2). The following paragraph describes the underlying modeling to quantify the total amount of water molecules N_{H2O} per asymmetric unit cells in MOF-801 in order to explain the observed adsorption isotherms and quantify the total uptake of water at the single-crystal level.

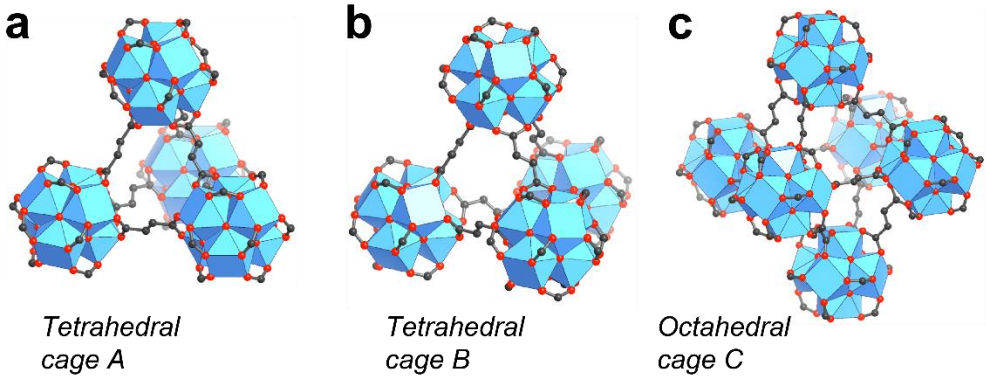


Figure S5.2 Water binding sites in tetrahedral cages (a, b) and the octahedral cage (c) in an asymmetric unit cell of MOF-801.

Based on SC-XRD, binding sites of water in an asymmetric unit cell were identified. Overall, the asymmetric unit cell contains two complete $Zr_2O_6(OH)_4$ clusters. Using these clusters as vertices, four tetrahedral cages (3 x Cage A and 1 x B) and two octahedral cages (Cage C) are formed (Figure S5.3). In cage B and C, 8 water molecules form a cubic cluster, while in cage A, 7 water molecules form an incomplete cube.

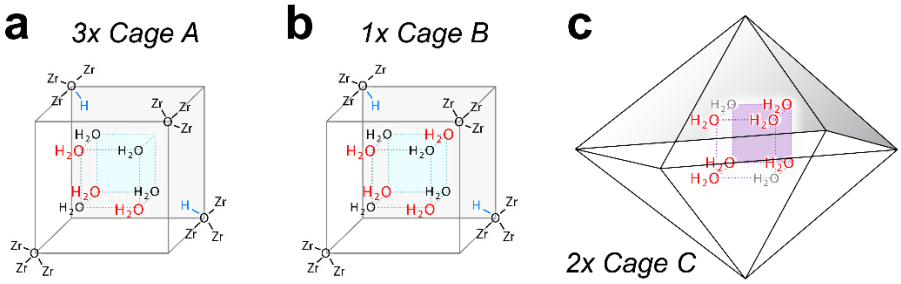


Figure S5.3. Overview of the water binding sites in the tetrahedral cages (a, b) and the octahedral cage (c) and their multiplicity per asymmetric unit cell.

Knowing about the number of binding sites as well as about the binding mechanism, we can express the number of adsorbed water molecules N_{H2O} per asymmetric unit cell as a function of the RH using the equilibrium constants. A model based on linear combinations of Klotz equations was created that can be used to fit MOF-801 isotherms. The Klotz equation was originally

developed to describe an adsorption process with N binding sites, where only the first binding step is different in binding constant.[18] The model was adapted to describe the binding in one asymmetric unit cell of MOF-801 with 31 distinct binding steps. First, the binding events were divided into the binding sites at cage A (tetrahedral) and the cages B and C (tetrahedral and octahedral). The water binding in cage A is described by 7 equilibrium constants (K_1 to K_7), each corresponding to a water in the incomplete cube. The binding in cage B is coupled with that in the two cage C according to the SC-XRD data, so there are 24 equilibrium constants (K_8 to K_{31}) describing 24 water molecules in the three cubes. The number of bound water in a cage A ($N_{H2O\,cageA}$) and in cage B+2C ($N_{H2O\,cageB,2C}$) can be expressed as:

$$N_{H2O\,cageA}(x) = \frac{K_1 x + 2K_1K_2x^2 + \cdots + 7(K_1K_2 \ldots K_7)x^7}{1 + K_1 x + K_1K_2x^2 + \cdots + (K_1K_2 \ldots K_7)x^7} \qquad \text{Eq. (S1.2)}$$

$$N_{H2O\,cageB,2C}(x) = \frac{K_8 x + 2K_8K_9x^2 + \cdots + 24(K_8K_9 \ldots K_{31})x^7}{1 + K_8 x + K_8K_9x^2 + \cdots + (K_8K_9 \ldots K_{31})x^7} \qquad \text{Eq. (S1.3)}$$

Here, x is the relative humidity of the surrounding air flow (between 0 and 1). To determine the total amount of water molecules N_{H2O} as a function of the RH, we need to add up all contributions to the four tetrahedral and 2 octahedral cluster. The number of water molecules $N_{H2O}(x)$ within the asymmetric unit cell as a function of the RH reads as

$$N_{H2O}(x) = 3 \cdot N_{H2O\,cageA}(x) + N_{H2O\,cageB,2C}(x) \qquad \text{Eq. (S1.4)}$$

However, creating a fit model with 31 open parameters using isotherms will suffer from overfitting issues. In order to simplify the model, we reduce the whole binding mechanism into 5 chemically distinct events (involving multiple binding of water molecules simultaneously), each has a unique value of K: The first three events comprise water binding to tetrahedral cage A and B: (1) binding to the metal-oxide cluster at the μ_3-O site ($K_{\mu3\text{-}O}$); (2) binding to metal bound hydroxyl groups, μ_3-OH($K_{\mu3\text{-}OH}$); and (3) bridging of the previous binding sites into cubes or incomplete cubes in the tetrahedral cages (K_{tc}). The next two events occur in the octahedral cage C: (4) nucleation (K_d) nearby cage B and (5) further growth into cubes (K_{dc}). (Table S5.1, Figure S5.4).

To convert the number of molecules per asymmetric unit cell into the uptake as volume water (cm^3) per mass MOF-801 (g), a scaling factor is calculated. Given that each asymmetric unit cell contains 2 metal clusters and 12 organic linkers, its chemical formula becomes $Zr_{16}O_{64}C_{48}H_{32}$ and the corresponding molecular weight is 2727.4 g/mol. Combining with the volume of water vapor (2.241×10^4 cm^3/mol), one water molecule bound to an asymmetric unit cell corresponds to a water uptake of 8.22 cm^3/g.

The model describes measured adsorption isotherms of MOF-801 with the five distinct equilibrium constants as fit parameters as Eq. S1.5:

$$\frac{V_{H2O}}{m_{MOF}} = N_{H2O}(RH) \cdot 8.22 \qquad \text{Eq. (S1.5)}$$

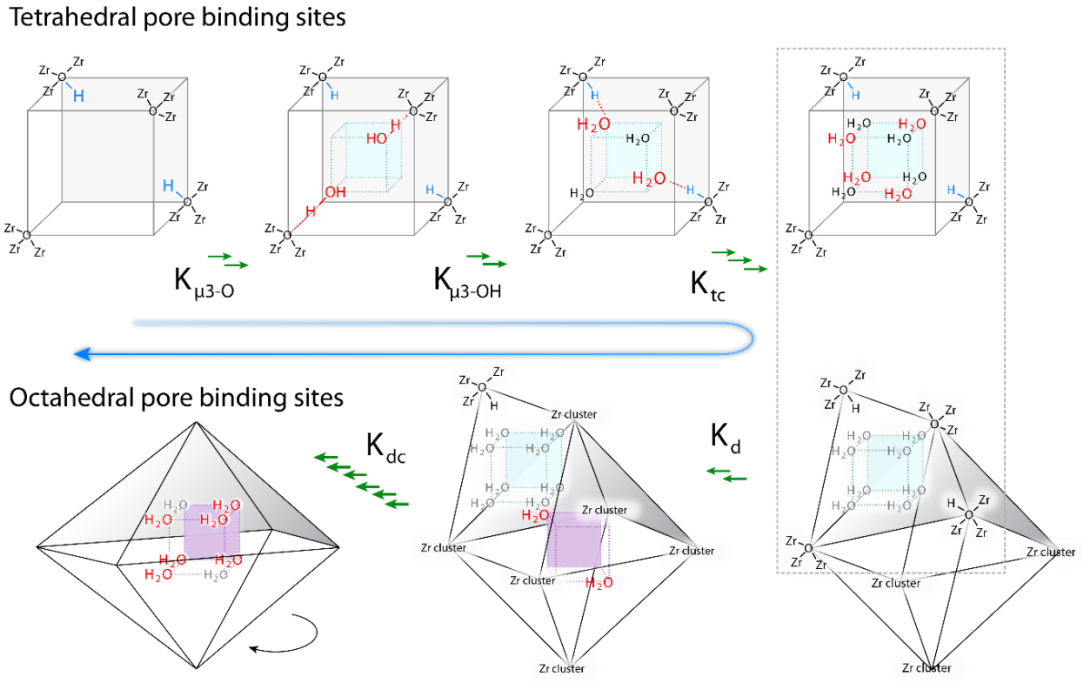


Figure S5.4. Schematic of the adsorption of water in MOF-801 crystals.[2] K_x describes the respective binding constant for the chemically distinct binding events per asymmetric unit cell.

Table S5.1: Equilibrium constants of the fit model describing water uptake in MOF-801 per asymmetric unit cell.

	$K_{\mu 3\text{-}O}$	$K_{\mu 3\text{-}OH}$	K_{tc}	K_d	K_{dc}
K_1	2				
K_2	1/2				
K_3		2			
K_4		1/2			
$K_5 - K_7$			1		
K_8	2				
K_9	1/2				
K_{10}		2			
K_{11}		1/2			
$K_{12} - K_{15}$			1		
K_{16}				4	
K_{17}				3/2	
K_{18}				2/3	
K_{19}				1/4	
$K_{20}/K_{24}/K_{28}$					4
$K_{21}/K_{25}/K_{29}$					3/2
$K_{22}/K_{26}/K_{30}$					2/3
$K_{23}/K_{27}/K_{31}$					1/4

5.5.2 Quantitative Water Uptake and Kinetics of MOF-801 via Raman Spectroscopy

Raman scattering provides detailed spectroscopic fingerprint information of the targeted material, but it is an inherently weak process.[19] Concomitantly, the recorded spectral signature of a Raman scattering process is often dominated by other processes, such as Rayleigh scattering, straight light, and/or autoluminescence by the investigated sample itself. Hence, measured spectra frequently show additional contributions, such as background and unstable baselines. The following paragraph describes the spectral background correction of recorded Raman spectra, the determination of uptaken water compared to MOF-801 within the detection volume, as well as their quantitative analysis. All data analysis was carried out using home-written Matlab scripts (Matlab 2018b, The MathWorks, Inc; Natick, MA, USA).

5.5.2.1 Initial Background Correction

Mathematical pre-processing was used to eliminate baseline drifts, offset, and background. First of all, recorded Raman spectra were corrected against cosmic rays by *Andor Solis for Imaging V4.30* (Oxford Instruments). Next, Rayleigh scattering and spurious background were removed by polynomial fitting. The background data was automatically approximated by a quadratic function in the region without Raman resonances between 2595 – 2620 cm^{-1} and 3760 – 4190 cm^{-1} and subtracted prior to further analysis (Figure S5.5a).

5.5.2.2 Determining the Intensity of Selected Raman Resonances

Spontaneous Raman scattering scales linearly with the number of Raman active molecules within the confocal volume [7]. Hence, Raman signatures of two species, such as water and MOF-801, add up linearly. For non-overlapping Raman resonances, the strength of a vibrational transition $A_{Raman\ Peak}$ is directly proportional to the sample concentration. It is given by the area under the background-corrected Raman spectrum and reads as (Eq. S2.1)

$$A_{Raman\ Peak} = \int_{\tilde{\nu}_1}^{\tilde{\nu}_2} I_{Raman}(\tilde{\nu})\ d\tilde{\nu} \qquad \text{Eq. (S2.1)}$$

with $\tilde{\nu}_1$ and $\tilde{\nu}_2$ being the lower and upper wavenumber of a selected peak. The uncorrected strength of the CH and OH stretch vibration is given by (Figure S5.5b)

$$A_{OH} = \int_{3145\ cm^{-1}}^{3665\ cm^{-1}} I_{Raman}(\tilde{\nu})\ d\tilde{\nu} \qquad \text{Eq. (S2.2)}$$

$$A_{CH,raw} = \int_{3130\ cm^{-1}}^{3145\ cm^{-1}} I_{Raman}(\tilde{\nu})\ d\tilde{\nu} \qquad \text{Eq. (S2.3)}$$

While the Raman signature of water above 3150 cm^{-1} is well separated from the characteristic peaks of MOF-801, it still overlaps with the CH stretch vibration around 3000 cm^{-1} (Figure 5.2b), leading to an increasing offset of the CH signature with increasing relative humidity (RH). We take this contribution into account by: (i) modeling the shape of the OH stretch vibration of pure water, (ii) approximating the Raman spectrum of humid MOF-801 in the spectral region above 3200 cm^{-1} by the model function, and (iii) determining and subtracting the background contribution of water to the CH stretch vibration of the material.

For modeling the Raman signature of pure water, we first approximated the shape of the OH stretch vibration by a linear combination of two Gaussian functions with a χ^2 of nearly 1 (Figure S5.5c).

$$f(\tilde{\nu}) = C \cdot \left(B_1 \cdot \exp\left(-\frac{(\tilde{\nu} - \mu_1)^2}{2w_1^2} \right) + B_2 \cdot \exp\left(-\frac{(\tilde{\nu} - \mu_2)^2}{2w_2^2} \right) \right) \quad \text{Eq. (S2.4)}$$

While keeping the model parameter, i.e., the Gaussian amplitudes B_i, center positions μ_i and widths w_i, fixed, we approximated the water content in MOF-801 afterward by linearly scaling the determined model function f with a factor C to the recorded Raman spectrum of the material. From the obtained fit-function $I_{fit,OH\ peak}$ describing the water contribution being present in MOF-801, we deduced its background contribution to the uncorrected CH signature $A_{CH,raw}$

$$A_{OH\ Bg,fit} = \int_{3130\ cm^{-1}}^{3145\ cm^{-1}} I_{fit,OH\ peak}(\tilde{\nu})\ d\tilde{\nu} \quad \text{Eq. (S2.5)}$$

$$A_{CH} = A_{CH,raw} - A_{OH\ Bg,fit} \quad \text{Eq. (S2.6)}$$

After subtraction, the corrected intensity of the CH stretch vibration A_{CH} can serve as a measure for the amount of the bare MOF material within the confocal volume. (Figure S5.5d).

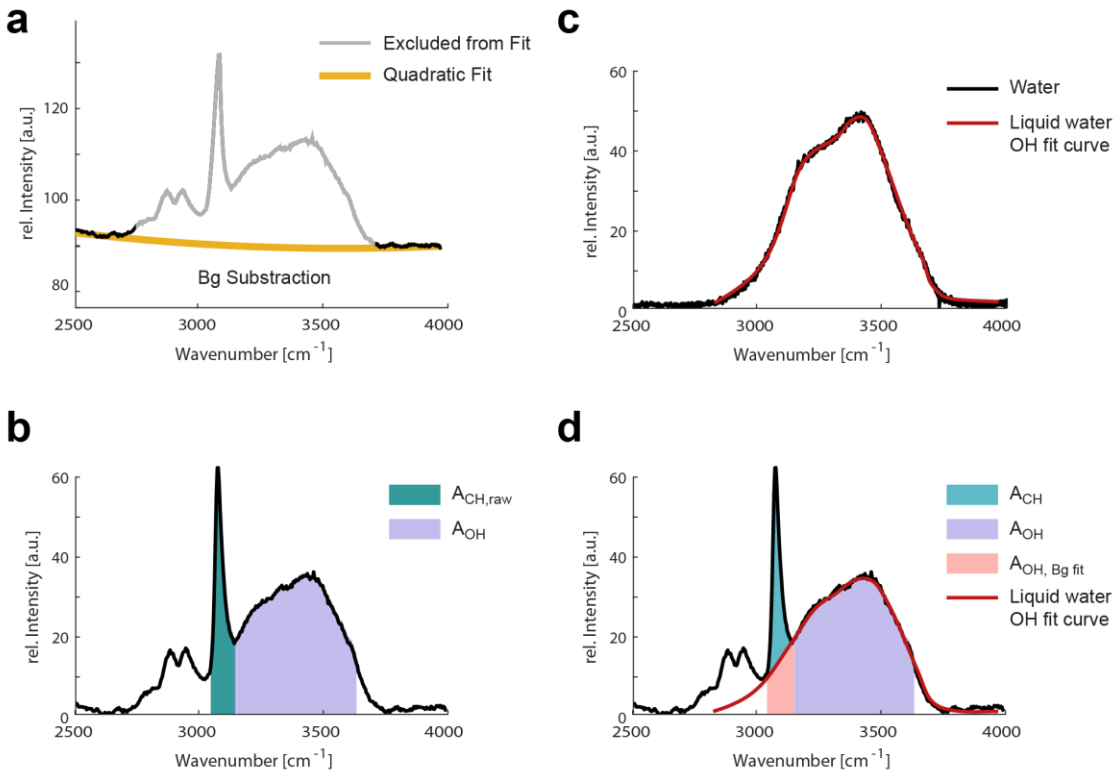


Figure S5.5. Schematic of the background correction and determination of selected Raman intensity a) The acquired spectra of MOF-801 are background-corrected by subtracting a quadratic background. b) The raw Raman peak strength of the OH stretch and the CH stretch vibration is calculated. c) To correct the CH-stretch vibration, a fit function modeling the liquid water OH-stretch peak is fitted to the spectrum. d) Using the fit function modeling the spectral shape of water, the contribution of the OH peak to the area under the CH peak is determined.

5.5.2.3 Quantification of Water Uptake in MOF-801 by Raman Spectroscopy

5.5.2.3.1 Connection between Raman Intensities and Quantitative Water Uptake

As Raman scattering scales linearly with the sample concentration, the observed Raman intensity A_{OH} due to OH-stretch resonance of water molecules within MOF-801 should directly relate to the total number of water molecules N_{H2O} inside the confocal volume. In general, the absolute Raman scattering intensity A (at the Stokes-Side) is proportional[20-21] to the number of scattering molecules N, the excitation intensity I_L, the reduced mass μ of vibrating atoms, the wavelength c/ν_L of the exciting light source, and the frequency ν of the observed Raman resonance. Moreover, it depends linearly on the temperature T following a Boltzmann distribution and quadratically on the vibration-induced change in polarizability $\frac{\partial \alpha}{\partial q}$ of the material, that can be related to the mean invariant ${\alpha'}_a$ and anisotropy invariant ${\gamma'}_a$ of the polarizability tensor. It describes the polarization-orientation dependency of the material, which is negligible for freely vibrating water molecules and frequently found to be phase independent.[22]

$$A \propto N \cdot \frac{I_L}{\mu} \cdot \frac{(\nu_L - \nu)^4}{\nu \cdot \left(1 - e^{-\frac{h\nu}{kT}}\right)} \cdot [45({\alpha'}_a)^2 + 7({\gamma'}_a)^2] \qquad \text{Eq. (S2.7)}$$

To automatically quantify the water uptake in MOF-801, we need a constant, calibrated conversion factor that relates the measured Raman intensity of the OH stretch vibration to the number of adsorbed water molecules. For constant experimental conditions, i.e., identical observation range, detection and excitation geometry, we can limit the dependencies on the OH-stretch signal according to Eq. S2.7 to 1) the temperature T, 2) the wavelength ν_L, 3) polarization P of the excitation laser / orientation of water molecules in the crystal, 4) the excitation intensity of the laser at the confocal volume I_L, and 5) the number of water molecules in the confocal volume N_{H2O}, which influence our experiment with different strength:

1) The laboratory is equipped with active temperature control, ensuring temperature stability of < 0.2 °C over 24 h. With an average lab temperature of 23.3 °C, the Boltzmann-associated scaling factor varies only on 33 digits after the comma for changes in lab temperature. The heating of the material by the visible, incident laser excitation at 532 nm was further on not observed as expected for the non-absorbing host material.[23]

2) The diode-pumped laser at 532 nm serving as excitation laser features a line width of < 1 MHz and wavelength stability of < 1 pm over 8 hours. Changes in excitation laser wavelength can hence be excluded.

3) MOF-801 has a cubic unit cell with space group $P_{n\text{-}3}$. It is highly symmetric, i.e., the effect of polarization of the incident laser light I_L on the linker Raman spectrum is expected to be little. Water molecules adsorbed inside the MOF framework have varying orientations and can rotate. Therefore, no influence of the polarization is expected on the OH-stretch vibration. Indeed, we found no significant shift in the spectrum of humid MOF-801 when the polarization of the excitation beam is rotated by 90° (Figure S5.6). Therefore, any influence of the incident laser polarization can be neglected.

4) The excitation intensity depends on the deposited laser power of the excitation laser within the confocal volume. Since the laser system features a low noise level (<0.25% RMS) and power

stability (< 0.3 %), the scattering by the MOF-801 crystal is the major source causing changes in the exciting laser intensity and detection efficiency. At the same time, a decrease in laser intensity also affects the signature height of the CH-stretch vibration, as expected with a linear dependency on the laser power:

$$A_{CH};\ A_{OH} \propto I_L \qquad \text{Eq. (S2.8)}$$

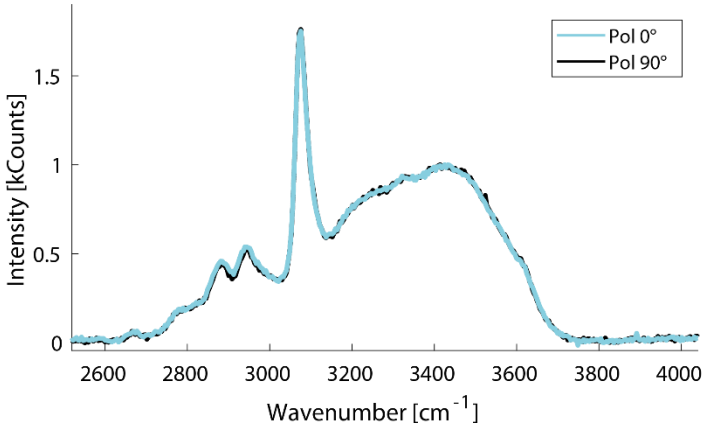


Figure S5.6. Polarization dependency of the OH and CH-stretch vibration in MOF-801. Raman spectrum of MOF-801 with p-polarization (blue) and s-polarization (black) after rotating the linear polarization of the excitation laser by 90° by a half-wave plate. Including a fixed detection geometry, both spectra are acquired under identical experimental settings otherwise. No polarization dependence for the OH- and CH-stretch vibrations are observed.

We, therefore, introduced a ratiometric approach (see below) to correlate the ratio of the Raman peaks A_{OH}/A_{CH} directly to the number of molecules in the confocal volume and correct for changes in absolute intensity.

5) The ratio of Raman peak strength of OH to CH-stretch vibration can be related to the uptake in cm^3 per gram of MOF-801. For the following, we take the laser intensity for all materials in the confocal volume as constant and will discuss the influence of scattering again for the calibration measurements (Section 5.5.2.3.3). We can relate the amount of a given material in the confocal volume, *i.e.*, the number of scattering molecules N_x to their corresponding Raman peak strength A_x by a conversion factor $\mathrm{c}f_{RamanPeak}$.

$$N_x = \mathrm{c}f_{RamanPeak} \cdot A_x \qquad \text{Eq. (S2.9)}$$

For ease of reading, we expressed the number of scattering particles N_x as the substance amount n_x by applying the Avogadro constant N_A in the following paragraph.

$$N_x = n_x \cdot N_A \qquad \text{Eq. (S2.10)}$$

For quantifying the water uptake, we describe the uptake as the amount of water volume per mass MOF-801, which again is a function of the substance amount n_x:

$$\frac{V_{H2O}}{m_{MOF}} = \frac{\frac{m_{H2O}}{\rho_{H2O}}}{m_{MOF}} = \frac{n_{H2O} \cdot \frac{M_{H2O}}{\rho_{H2O}}}{n_{MOF} \cdot M_{MOF}} \qquad \text{Eq. (S2.11)}$$

Here, M_x is the molecular weight of material x, and ρ_{H2O} is the density of water at the measurement temperature of 23.3 °C. For a given molecular weight and density of water-free MOF-801 ($\rho_{H2O} = 1.592$ mg/mm^3; see Ref. [2]), we can relate the volume per weight of MOF-801 to the Raman signatures of guest and host by combining Eq. S2.09 - 2.11 to

$$\frac{V_{H2O}}{m_{MOF}} = \frac{A_{OH}}{A_{CH}} \cdot \frac{cf_{H2O}}{cf_{MOF}} \cdot \frac{M_{H2O}}{\rho_{H2O} \cdot M_{MOF}} \qquad \text{Eq. (S2.12)}$$

Determining the conversion factors is the crucial step in calculating the quantitative water uptake from the Raman spectrum of MOF-801. For Raman spectra of MOF-801 and water that are collected on the same microscope, with the same excitation wavelength, and the same objective (as for all presented spectra), the conversion factors are only dependent on (1) the Raman band of the material and (2) the incident laser power. In a broader sense, the same material irradiated with the same laser power will always result in the same Raman spectrum (with the restrictions from above). The conversion factors cf_{H2O} and cf_{MOF} can be considered as constant for a fixed excitation laser power for water-free MOF-801 and liquid water. These conversion factors cf_{H2O} and cf_{MOF} can be theoretically determined with calibration measurements in dry MOF-801 and liquid water excited with the same laser power, based on Eq. S2.09 and Eq. S2.10:

$$cf_{H2O} = \frac{n_{H2O,cal}}{A_{OH,cal}} = \frac{\rho_{H2O} \cdot V_{confocal} \cdot N_A}{A_{OH,cal} \cdot M_{H2O}} \qquad \text{Eq. (S2.13a)}$$

$$cf_{MOF} = \frac{n_{MOF,cal}}{A_{CH,cal}} = \frac{\rho_{MOF} \cdot V_{confocal} \cdot N_A}{A_{CH,cal} \cdot M_{MOF}} \qquad \text{Eq. (S2.13b)}$$

Here, $A_{x,cal}$ is the Raman intensity of the peak x according to Eq. S2.2-2.6 from the calibration measurement. When combining Eq. S2.12 and S2.13, the expression shortens to:

$$\frac{V_{H2O}}{m_{MOF}} = \frac{A_{OH}}{A_{CH}} \cdot \frac{A_{CH,cal}}{A_{OH,cal}} \cdot \frac{1}{\rho_{MOF}} \qquad \text{Eq. (S2.14)}$$

For an equal excitation intensity, the ratio $\frac{A_{CH,cal}}{A_{OH,cal}}$ is constant between calibration measurements and can be expressed as a simple scaling factor leading to Eq. S2.15:

$$\frac{V_{H2O}}{m_{MOF}} = \frac{A_{OH}}{A_{CH}} \cdot \Gamma \cdot \frac{1}{\rho_{MOF}} \qquad \text{Eq. (S2.15)}$$

This scaling factor can be determined twofold with a fairly good agreement: (i) either by theoretical modeling of experimental data (section 5.5.2.3.2) or (ii) by using a series of calibration experiments (section 5.5.2.3.3). Both methodologies are compared in the following paragraph to highlight their strength and deviations for the SC isotherm determination. To distinguish between the results, we name them Γ_{th} and Γ_{exp}. Please note that both parameters yield a similar result.

5.5.2.3.2 Determination of Scaling Factor Γ_{th} by Theoretical Calculations and Fit

Knowing about the number and nature of binding sites in MOF-801 (Section 5.5.2) allowed us to describe the total number of adsorbed water molecules (N_{H2O}) per asymmetric unit cell as a function of RH via five different equilibrium constants. The uptake as volume water (mL) per mass MOF-801 (g) was modeled as a function of the RH Eq. S1.5 displays the relation as derived:

$$\frac{V_{H2O}}{m_{MOF}} = N_{H2O}(RH) \cdot 8.22 \qquad \text{Eq. (S2.16)}$$

Since the ratio $\frac{A_{OH}}{A_{CH}}$ is also only dependent on the RH with

$$\frac{V_{H2O}}{m_{MOF}} \propto N_{H2O}(RH) \propto \frac{A_{OH}}{A_{CH}} \qquad \text{Eq. (S2.17)}$$

the same fit model can be applied to approximate the measured ratio of Raman intensities

$$\frac{A_{OH}}{A_{CH}} = N_{H2O}(RH) \cdot f_{fit} \qquad \text{Eq. (S2.18)}$$

By inserting Eq 2.15-2.18, we can connect the theoretical and experimental approach

$$N_{H2O}(RH) \cdot 8.22 = N_{H2O}(RH) \cdot f_{fit} \cdot \Gamma_{th} \cdot \frac{1}{\rho_{MOF}} \qquad \text{Eq. (S2.19)}$$

and derive the following expression for Γ_{th}:

$$\Gamma_{th} = \frac{8.22 \cdot \rho_{MOF}}{f_{fit}} \qquad \text{Eq. (S2.20)}$$

As described in the material section accompanying Figure 5.5f, the ratio of A_{OH}/A_{CH} at different RH was measured on seven different crystals. All data points were combined in one data set. The resulting data were fitted (Eq. S2.18) to extract f_{fit}, and the standard deviation of the fit.

With this, Γ_{th} was determined as $\Gamma_{th} = 0.0938 \pm 0.0041$.

5.5.2.3.3 Determination of Scaling Factor Γ_{exp} by Calibration Measurement

In comparison to the modeling approach, we equally pursued an experimental determination using an external standard procedure. We measured five different areas in completely dry MOF-801 and liquid water under identical experimental conditions (section 5.3, SC isotherm). Next, we determined the Raman peak strength for the CH stretch vibration in MOF-801 without water and the OH-stretch vibration of liquid water (Section 5.5.2.2). For both samples completely occupying the confocal volume, which has an identical shape and size for both materials, we can derive the following linear scaling factor:

$$\Gamma^*_{exp} = \frac{A_{CH,cal}}{A_{OH,cal}} \qquad \text{Eq. (S2.22)}$$

Light, however, is significantly scattered at the interface between air and the MOF crystal while this effect is negligible within the water. Due to the extensive scattering, the intensity of the laser excitation within the MOF calibration sample is lower than anticipated. Since water,[24-26] as well as MOF-801,[23] barely absorb in the Vis/NIR range, we assign the decrease in transmission primarily to scattering and reflection. The incident laser light, as well as the created Raman photons, will be scattered differently, depending on their wavelength. This prohibits the estimation of the

scattering by Rayleigh photons alone. To estimate the correction factor against this loss we determined the integrated transmission intensity of a spectrally broad light source in MOF-801 compared to water for 15 different areas (Figure S5.7).

We derived the mean transmitted intensity per area $I_{mean,x}$ for both media and defined the correction factor $L_{scatter}$ between liquid water and MOF-801 as

$$L_{scatter} = \frac{I_{mean,MOF}}{I_{mean,H20}} \qquad \text{Eq. (S2.23)}$$

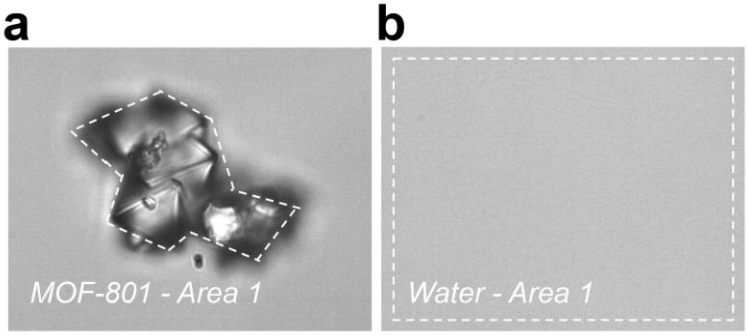


Figure S5.7: Example of the estimation of the loss in Raman signal intensity due to scattering in MOF-801 crystals. Bright-field images of (a) MOF-801 crystals and (b) water were acquired with the same settings (light source intensity, camera parameters, height over microscopy slide). The areas of interest were selected (inside of white dotted line), and the average intensity of the selected areas per pixel (I_{mean}) was calculated. In total, 15 areas for MOF-801 and 2 areas for water were analyzed.

The determined correction factor $L_{scatter}$ accounts for the reduction in excitation power and hence reduced amplitude of the linearly scaling Raman scattering process taking place in adsorbed water (when measured within MOF-801) compared to liquid water.

The measured scaling factor can therefore be described as

$$\Gamma_{exp} = \frac{A_{CH,cal}}{A_{OH,cal} \cdot L_{scatter}} \qquad \text{Eq. (S2.24)}$$

Since the scattering loss is inducing a significantly higher uncertainty compared to all other contributions, the standard deviation of the 15 areas selected to determine $I_{mean,MOF}$ alone was applied to estimate the uncertainty of Γ_{exp}.

With Eq. S2.24, we could calculate $\Gamma_{exp} = 0.0837 \pm 0.0131$.

5.5.2.4 Uncertainty of Water Quantification and Error Propagation

5.5.2.4.1 General uncertainty of Raman Intensity

To derive the experimental error when determining the water content in MOF-801, we took the mean of all background-corrected spectra of a series with the length *i* of spectral pixels. Under the assumption that the background is spectrally independent, we calculated the standard deviation for each spectrum $\sigma_S(i)$ against the mean within a selected spectral region sel, where no Raman

resonances are present ($x_{sel} = 2495 - 2625$ and $3760 - 4190$ cm^{-1} with $L(x_{sel})$ pixels; Figure S5.8):

$$\sigma_S(i) = \sqrt{\frac{1}{L(x_{sel}) - 1} \cdot \sum_{j=1}^{L(x_{sel})} \left| x_{sel}(j) - x_{sel,mean}(j) \right|^2} \qquad \text{Eq. (S2.25)}$$

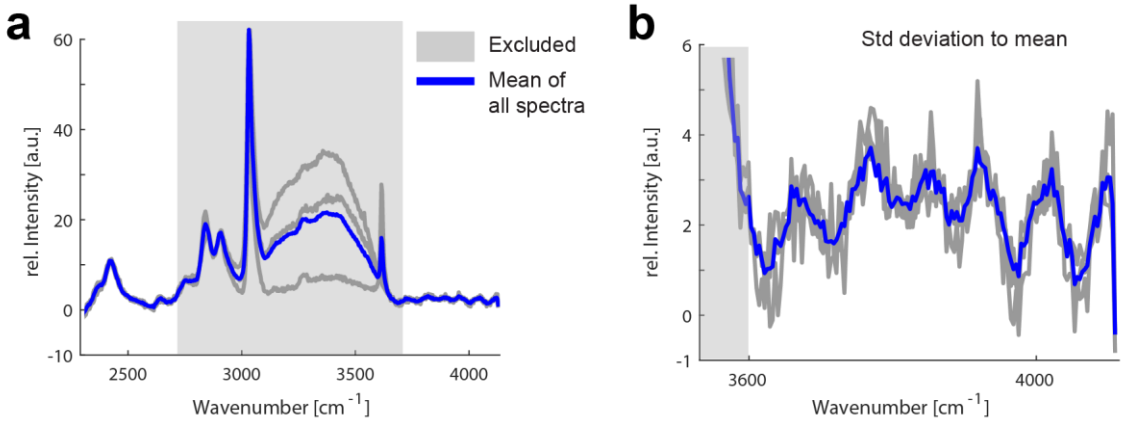


Figure S5.8. Estimation of the white noise-induced measurement uncertainty. a) Example series of Raman spectra for isotherm and kinetic curves (grey lines). While water significantly changes the Raman signature between 2800 and 3700 cm^{-1}, the spectral signature outside the grey area is hardly affected, only seen by changes in background level and structure. When calculating the mean of all spectra (blue), we derive the static background inherent to all spectra. b) When comparing the background region of every spectrum to the mean, we can approximate the white noise induced uncertainty as the standard deviation.

The intensity $A_{OH}(i)$ of the adsorbed water peak is given as integral over the Raman resonance, *i.e.*, the sum over Raman signal. The associated error for $A_{OH}(i)$, $\sigma_{OH}(i)$ is accumulating over the number of pixels N_{OH} in the integration range (*i.e.*, 3145 - 3665 cm^{-1}) and given using the constant, wavelength-independent error σ_S by

$$\sigma_{OH} = \sum_{i=3145\ cm^{-1}}^{3665\ cm^{-1}} \sigma_{OH}(i) = N_{OH} \cdot \sigma_S \qquad \text{Eq. (S2.26)}$$

The error σ_{CH} of the intensity $A_{CH}(i)$ of the CH vibration in MOF-801 can be derived accordingly.

$$\sigma_{CH} = N_{CH} \cdot \sigma_S \qquad \text{Eq. (S2.27)}$$

We assume no covariance between A_{OH} and A_{CH} yielding the propagated error σ_{noise} as[27]

$$\sigma_{noise} = \sigma_S \cdot \left| \frac{A_{OH}}{A_{CH}} \right| \cdot \sqrt{\left(\frac{N_{OH}}{A_{OH}} \right)^2 + \left(\frac{N_{CH}}{A_{CH}} \right)^2} \qquad \text{Eq. (S2.28)}$$

5.5.2.4.2 Comparison of $\sigma_{rel,H2O}$, Γ_{th}, $\sigma_{\Gamma_{th}}$, Γ_{exp} and $\sigma_{\Gamma_{exp}}$

When comparing the determined scaling factors Γ_{th} and Γ_{exp}, we found an agreement of both values within the margin of error (Figure S5.9a). This is a strong validation of the values since

both methods followed fundamentally different approaches. That said, the experimentally derived calibration factor is smaller with an about four times higher standard deviation due to the scattering loss approximation. When determining $L_{scatter}$ (Section 5.5.2.3.3), we found a roughly two-time higher transmission through the water compared to the MOF-801 crystals. The chosen method is likely overestimating the scattering, leading to the decreased scaling factor compared to the fit-derived value. But even a more precise estimation of the amount of scattered light would not significantly reduce the large standard deviation since every crystal has a wide variety of scattering possibilities, e.g., due to the exact measurement position in a crystal.

Therefore, the scaling factor used for the presented data of this work was the one derived from the theoretical approach:

$$\Gamma_{th} = 0.0938 \pm 0.0041. \qquad \text{Eq. (S2.29)}$$

To determine the origin of the uncertainty of this scaling factor, we compared the noise-induced standard deviation σ_{noise} (Section 5.5.2.4.1) for both scaling factors. For comparison, we expressed the values as uncertainty in percent of the respective data points:

$$\text{Uncertainty } \delta = (\text{standard deviation} / \text{data point value}) \cdot 100 \qquad \text{Eq. (S2.30)}$$

Since the noise-induced uncertainty can vary between data points, we plotted the mean over 37 data points from 6 different SC isotherms.

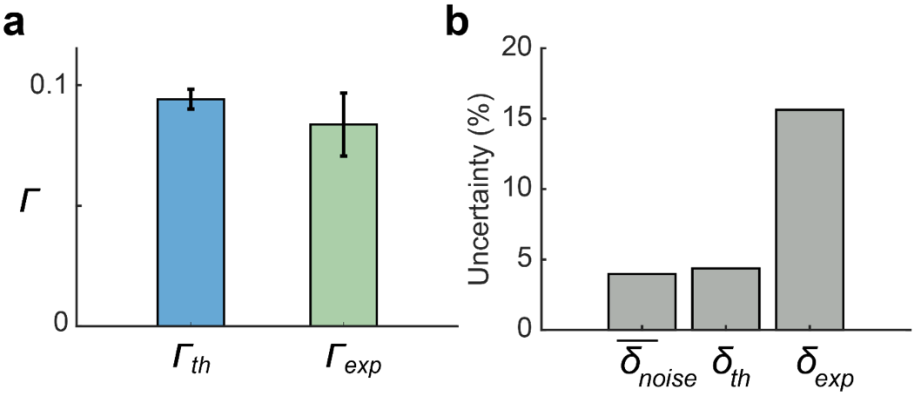


Figure S5.9: Reliabiity of conversion factor. a) Determination of the conversion factor Γ using the fit model (left) and calibration measurements (right). The error bars represent the mean value and standard deviation as specified in Section 5.5.2.3. b) Comparison of the uncertainty in determining the conversion factor Γ. From left to right: $\overline{\delta_{noise}}$ is the uncertainty induced by spectral noise for the uptake-averaged over 37 data points. δ_{th} denotes the uncertainty of the scaling factor derived by fitting, while δ_{exp} denotes the one derived from the calibration measurements.

It was found that the uncertainty of the approximated conversion factor Γ_{th} is nearly equal to the noise-induced uncertainty observed in Raman spectra, while the experimentally derived uncertainty Γ_{exp} is significantly higher (Figure S5.9b). For Γ_{th}, this is a good indication that the selected method for the fit is a valid interpretation of the Raman spectra and the underlying uptake mechanism. Furthermore, these findings give encouraging indications that additional noise reduction by advanced chemometric methods, such as principal component analysis,[28-29] can further enhance the robustness of our method.

5.5.3 SC-XRD on Polycrystalline MOF-801 Particles

Monocrystalline MOF-801. A MOF-801 single-crystal of 5 × 5 × 5 μm was taken from the synthesized batch and mounted on the diffractometer. The measured, raw data were processed with the Bruker APEX3 software package.[30] The data were first integrated using the SAINT V8.38A software and then corrected for absorption with SADABS 2016/2 routines.[31]

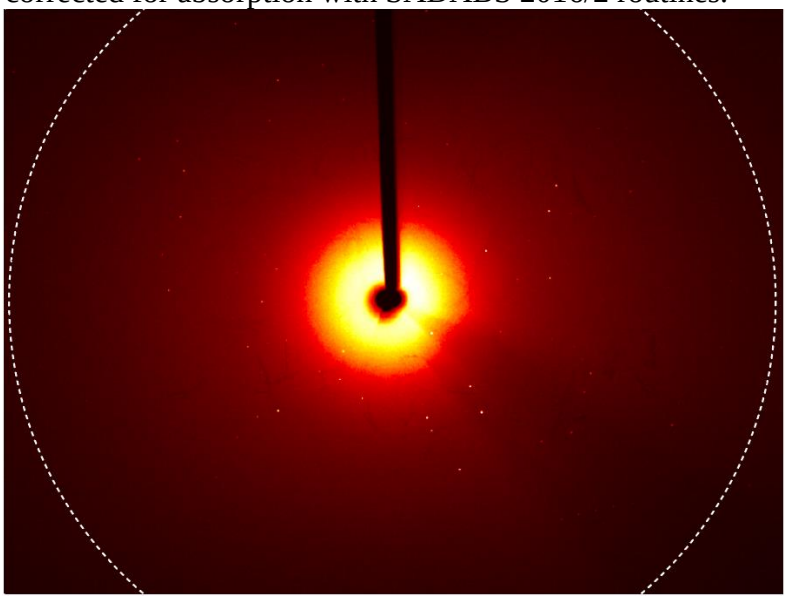


Figure S5.10. SC-XRD example of a regular MOF-801 crystal. The Circle represents the resolution of 0.8 Å.

The structures were solved by intrinsic phasing (SHELXT-2018/03) and the refinement was done by full-matrix least-squares on F^2 (SHELXL-2018/03), using the Olex2 software package.[32-34] In line with literature, MOF-801 has a cubic unit cell with space group P_{n-3}.

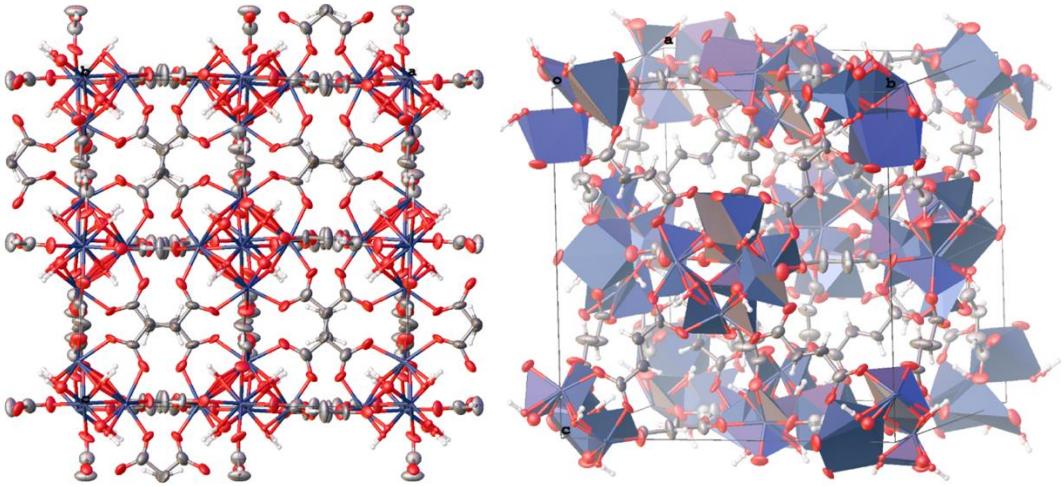


Figure S5.11. Structure of MOF-801 single crystal. Thermal Ellipsoids are drawn with 50% probability. Zr Oxide clusters are represented in dark blue, linker molecules in gray, and red elements sketch the oxygen atoms of the connecting carboxy groups of the fumarate linker.

The data quality was influenced by the limited diffraction ability from the crystal. The resolution was cut off to 1 Å, and the R_{int} of the full data was 16.64%. The atoms of MOF-801 was refined

anisotropically, except the μ-3 oxygen atoms always failed, mostly because the limited resolution is not able to distinguish the disorders clearly.[35] H5A and H6B were fixed by command HFIX 13 to fit the pseudo-tetrahedral geometry of oxygen. Despite the limited quality of the structural solution, the skeleton of the chemical structure clearly matched with the structure of MOF-801.

Polycrystalline Particles. A minor fraction of MOF-801 particles is polycrystalline (about 10% of particles per field of view in SEM). To characterize their nature, we carried out SXRD on several particles. Two representative examples are described in the following:

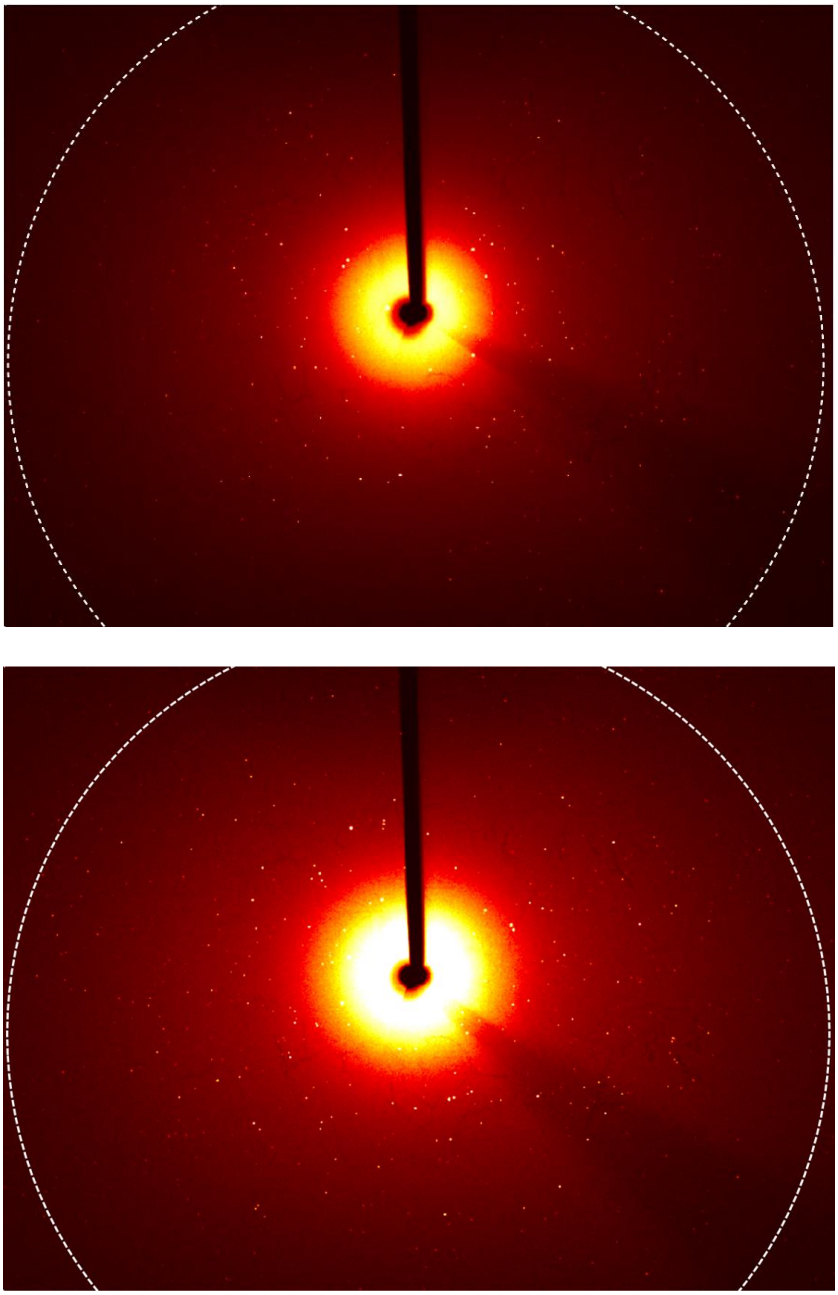


Figure S5.12. SXRD examples of polycrystalline particles. Electron diffraction pattern of polycrystalline sample 1 (top) and 2 (bottom) of MOF-801. The Circle represents the resolution of 0.8 Å.

Polycrystalline sample 1 of MOF-801 was around 2 × 3 × 2 μm in size. Its diffraction pattern showed discrete diffraction peaks in the frames (Figure S5.12, top), indicating that it was composed of a countable number of single-crystalline domains. The twin domains were searched with CELL_NOW and eventually, 8 domains of MOF-801 were identified (Table S5.2). The five largest domains had sufficient numbers of diffractions to determine the Bravais lattice followed by unit cell refinements, while the last three domains did not.

Table S5.2: Summary of parameters of polycrystalline sample 1 from the crystallographic data.

Domains	Bravais Lattice	Unit cell [*a*, *b*, *c* / Å; *α*, *β*, *γ* / °]	Figure of Merit	Rotation axis (relative to domain 1)	Angle of rotation / °
Domain 1	cP	*a* = 17.857(9)	0.230	-	-
Domain 2	cP	*a* = 17.836(5)	0.277	[-0.788 1.000 -0.954]	134.4
Domain 3	cP	*a* = 17.845(7)	0.281	[1.000 0.661 -0.378]	159.5
Domain 4	cP	*a* = 17.855(12)	0.328	[-0.505 1.000 0.507]	179.1
Domain 5	cP	*a* = 17.880(5)	0.366	[1.000 0.954 -0.584]	159.7
Domain 6	-	*a* = 17.799, *b* = 17.871, *c* = 17.871; *α* = 90.05, *β* = 89.72, *γ* = 90.28	0.431	[0.525 -0.984 1.000]	144.5
Domain 7	-	*a* = 17.799, b = 17.871, *c* = 17.871; *α* = 90.05, *β* = 89.72, *γ* = 90.28	0.504	[0.549 -0.832 1.000]	80.7
Domain 8	-	*a* = 17.799, *b* = 17.871, *c* = 17.871 *α* = 90.05, *β* = 89.72, *γ* = 90.28	0.192	0.926 -0.635 1.000	155.8

Polycrystalline sample 2 was around 8 × 3 × 2 μm in size and examined by SXRD. Similar to polycrystalline sample 1, the diffraction of polycrystalline sample 2 showed discrete diffraction peaks in the frames (Figure S5.12; bottom), indicating it was composed of a countable number of single-crystalline domains. The twin domains were searched with CELL_NOW, and eventually, 10 domains that all matched the unit cell of MOF-801 were identified. The five largest domains had sufficient numbers of diffractions to determine the Bravais lattice followed by unit cell refinements, while the last 5 domains did not (Table S5.3).

Table S5.3: Summary of parameters of polycrystalline sample 2 from the crystallographic data.

Domains	Bravais Lattice	Unit cell [*a*, *b*, *c* / Å; *α*, *β*, *γ* / °]	Figure of Merit	Rotation axis (relative to domain 1)	Angle of rotation / °
Domain 1	cP	*a* = 17.879(9)	0.294	-	-
Domain 2	cP	*a* = 17.876(7)	0.352	[-0.195 1.000 -0.195]	155.0
Domain 3	cP	*a* = 17.879(12)	0.277	[1.000 0.304 0.460]	144.2
Domain 4	cP	*a* = 17.897(6)	0.267	[1.000 0.854 0.080]	176.1

Domain 5	cP	a = 17.867(11)	0.302	[1.000 -0.314 0.943]	173.2
Domain 6	-	a = 17.846, b = 17.875, c = 17.917; α = 89.94, β = 90.13, γ = 90.01	0.335	[1.000 0.456 0.441]	147.0
Domain 7	-	a = 17.846, b = 17.875, c = 17.917; α = 89.94, β = 90.13, γ = 90.01	0.397	[0.042 0.794 1.000]	57.0
Domain 8	-	a = 17.846, b = 17.875, c = 17.917; α = 89.94, β = 90.13, γ = 90.01	0.350	[0.472 1.000 -0.152]	163.9
Domain 9	-	a = 17.846, b = 17.875, c = 17.917; α = 89.94, β = 90.13, γ = 90.01	0.389	[-0.084 1.000 -0.478]	138.1
Domain 10	-	a = 17.846, b = 17.875, c = 17.917; α = 89.94, β = 90.13, γ = 90.01	0.365	[0.625 -0.639 1.000]	178.7

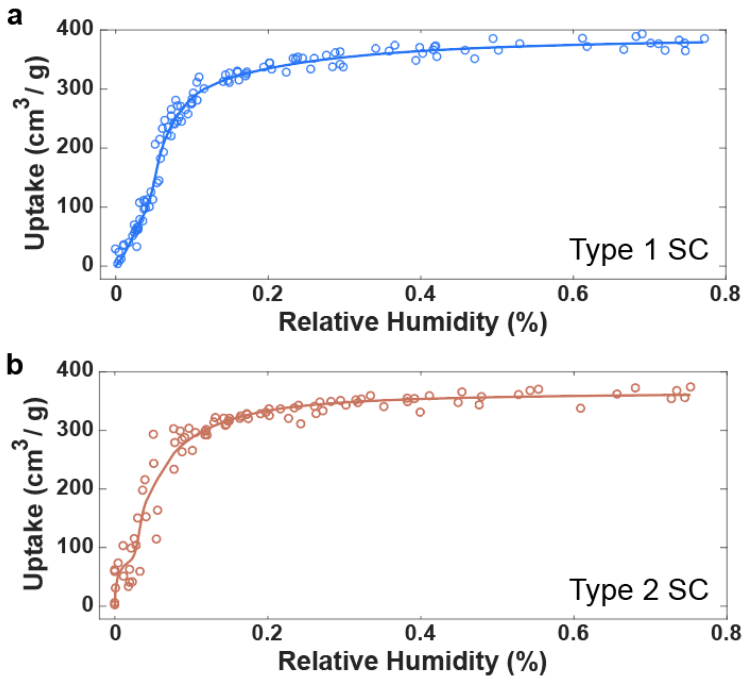


Figure S5.13. Data to Figure 5.4a. Overview plot of underlying data sets for SC isotherms of monocrystalline (Type 1) and polycrystalline (Type 2) MOF-801 particles. The colored lines represent the mean fit curve over N = 7 (Type 1) and N = 5 (Type 2) particles.

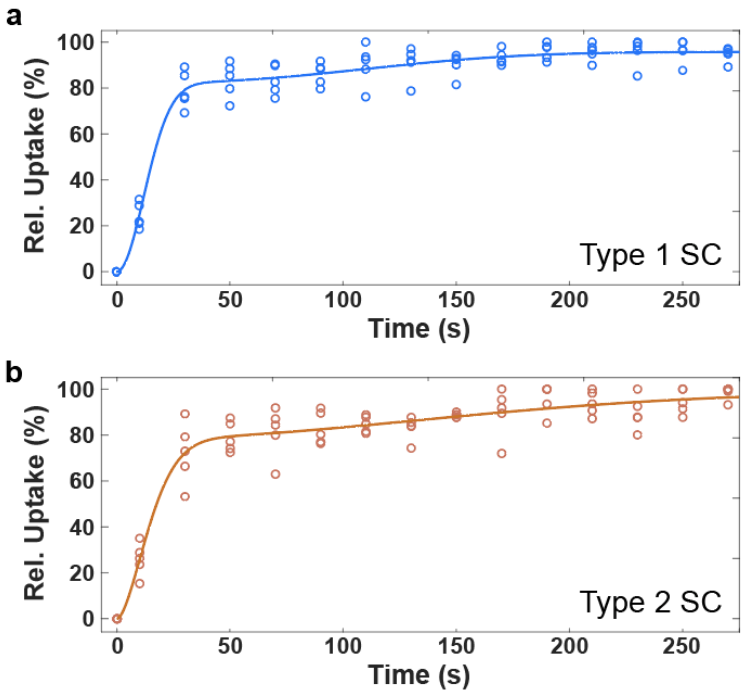


Figure S5.14. Data to Figure 5.4c. Overview plot of underlying data sets for SC kinetics data of monocrystalline (Type 1) and polycrystalline (Type 2) MOF-801 particles. The colored lines represent the mean fit curve over N = 5 particles each.

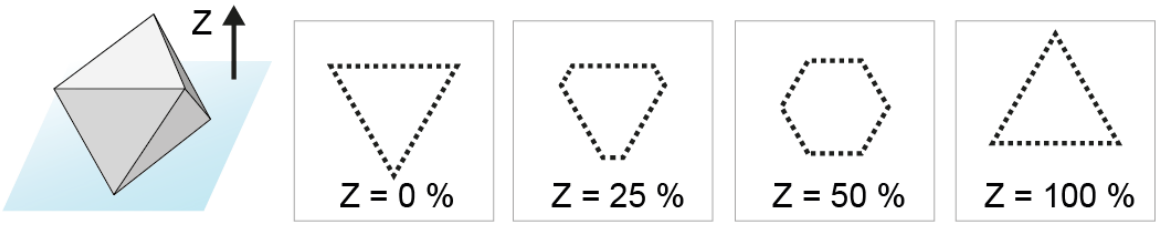


Figure S5.15: Apparent shape of an octahedral crystal at different imaging planes.

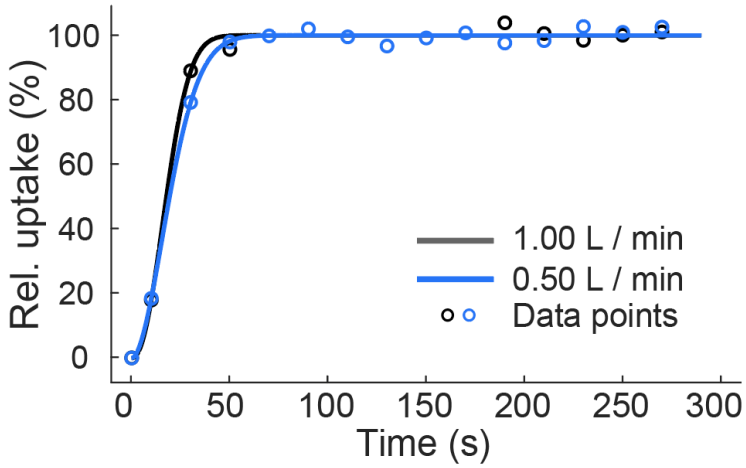


Figure S5.16: Adsorption at 8%RH for different flow rates. No significant difference in uptake kinetics was observed.

5.6 References

1. Chae, H. K.; Siberio-Perez, D. Y.; Kim, J.; Go, Y.-B.; Eddaoudi, M.; Matzger, A. J.; O'Keeffe, M.; Yaghi, O. M. *Nature* **2004**, *427*, 523–527.
2. Furukawa, H.; Gándara, F.; Zhang, Y.-B.; Jiang, J.; Queen, W. L.; Hudson, M. R.; Yaghi, O. M. *J. Am. Chem. Soc.* **2014**, *136*, 4369–4381.
3. Hanikel, N.; Pei, X.; Chheda, S.; Lyu, H.; Jeong, W.; Sauer, J.; Gagliardi, L.; Yaghi, O. M. *Science* **2021**, *374*, 454–459.
4. Kim, H.; Rao, S. R.; Kapustin, E. A.; Zhao, L.; Yang, S.; Yaghi, O. M.; Wang, E. N. *Nat. Commun.* **2018**, *9*, 1191.
5. LaPotin, A.; Zhong, Y.; Zhang, L.; Zhao, L.; Leroy, A.; Kim, H.; Rao, S. R.; Wang, E. N. *Joule* **2021**, *5*, 166–182.
6. Logan, M. W.; Langevin, S.; Xia, Z. *Sci Rep* **2020**, ***10***, 1492.
7. Wang, W.; Xie, S.; Pan, Q.; Dai, Y.; Wang, R.; Ge, T. *Renewable and Sustainable Energy Reviews* **2021**, *141*, 110802.
8. Xu, W.; Yaghi, O. M. *ACS Cent. Sci.* **2020**, *6*, 1348–1354.
9. Zhang, L.; Fang, W.-X.; Wang, C.; Dong, H.; Ma, S.-H.; Luo, Y.-H. *Inorg. Chem. Front.* **2021**, *8*, 898–913.
10. Zhou, X.; Lu, H.; Zhao, F.; Yu, G. *ACS Mater. Lett.* **2020**, *2*, 671–684.
11. Kim, H.; Yang, S.; Rao, S. R.; Narayanan, S.; Kapustin, E. A.; Furukawa, H.; Umans, A. S.; Yaghi, O. M.; Wang, E. N. *Science* **2017**, *356*, 430–434.
12. LaPotin, A.; Kim, H.; Rao, S. R.; Wang, E. N. *Acc. Chem. Res.* **2019**, *52*, 1588–1597.
13. Martell, J. D.; Milner, P. J.; Siegelman, R. L.; Long, J. R. *Chem. Sci.* **2020**, *11*, 6457–6471.
14. Fuchs, A.; Mannhardt, P.; Hirschle, P.; Wang, H.; Zaytseva, I.; Ji, Z.; Yaghi, O. M.; Wuttke, S.; Ploetz. E.; *Adv. Mater.*, **2022**, *34*, 2104530.
15. Muller, K.; Vankova, N.; Schottner, L.; Heine, T.; Heinke, L. *Chem Sci* **2019**, *10*, 153–160.
16. Avrami, M. The Journal of Chemical Physics **1940**, 8, 212–224.
17. Guo, B.; Wang, Y.; Shen, X.; Qiao, X.; Jia, L.; Xiang, J.; Jin, Y. *Materials* (*Basel, Switzerland*) **2020**, *13*, 877.
18. Buttersack, C. *Phys Chem Chem Phys* **2019**, *21*, 5614–5626.
19. Long, D. A. The Raman Effect: A Unified Treatment of the Theory of Raman Scattering by Molecules. (John Wiley & Sons, Ltd, 2002).
20. Pelletier, M. J. & Pelletier, C. C. in *Raman, Infrared, and Near-Infrared Chemical Imaging* **2020**, 1–20.
21. Placzek, G. in *Handbuch der Radiologie VI* Vol. 2 (ed E Marx) **1934**, 205 (Akademische Verlagsgesellschaft).
22. Nestor, J. R.; Lippincott, E. R. *Journal of Raman Spectroscopy* **1973**, ***1***, 305–318.

23. Fathieh, F.; Kalmutzki, M. J.; Kapustin, E. A.; Waller, P. J.; Yang, J.; Yaghi, O. M. *Sci. Adv.* **2018**, *4*, eaat3198.

24. Mason, J. D.; Cone, M. T.; Fry, E. S. *Appl. Opt.* **2016**, *55*, 7163–7172.

25. Pope, R. M.; Fry, E. S. *Appl. Opt.* **1997***, 36*, 8710–8723.

26. Curcio, J. A.; Petty, C. C. *J. Opt. Soc. Am.* **1951**, *41*, 302–304.

27. Goodman, L. A. Journal of the American Statistical Association **1960**, 55, 708–713.

28. Ramirez-Elias, M. G.; Alda, J.; Gonzalez, F. J. *Appl. Spectrosc.* **2012**, *66*, 650–655.

29. Zhang, X.; Chen, S.; Ling, Z.; Zhou, X.; Ding, D.-Y.; Kim, Y. S.; Xu, F. *Sci. Rep.* **2017**, *7*, 39891.

30. APEX3 V 8.38 v. 8.38 (Version 8.38, Madison, WI, **2018**).

31. SADABS V 2016/2 (Version 2016/2, Madison, WI, **2014**).

32. Sheldrick, G. M. *Acta Crystallogr A* **2008**, *64*, 112–122.

33. Sheldrick, G. M. Acta Crystallogr C Struct Chem **2015**, 71, 3–8.

34. Dolomanov, O. V.; Bourhis, L. J.; Gildea, R. J.; Howard, J. A. K.; Puschmann, H. *J. Appl. Crystallogr.* **2009**, *42*, 339–341.

35. Trickett, C. A.; Gagnon, K. J.; Lee, S.; Gándara, F.; Bürgi, H.-B.; Yaghi, O. M. *Angew. Chem. Int. Ed.* **2015**, *54*, 11162–11167.

Chapter 6. Evolution of MOFs: Living Solids

6.1 Introduction

Above chapters presented the design and functionalization strategy of MOFs,[1-11] where MOFs are treated as porous solid materials built from secondary building units (SBUs) and organic ligands. Normally, researchers view MOFs as solids that have fixed volumes and shapes with atoms that are bound tightly to each other that makes them resistant to change. Our recent research finds that components of MOFs can be changed, even after it formed. Ligands and composition of MOFs can be tuned and modified by post-synthetic procedures. Original MOFs can evolute to new MOFs with the introduction of new organic linkers and guest substrates. From this perspective, the framework can be viewed as a "solution" system, where building units of MOFs can move in and out of MOFs freely. Thus, MOFs are living solids. In this chapter, we use UiO-67 [$Zr_6O_4(OH)_4(C_{14}H_8O_4)_6$] which is composed of Zr-SBUs and 4,4'-biphenyldicarboxylate (BPDC) to illustrate this idea (Figure 6.1).

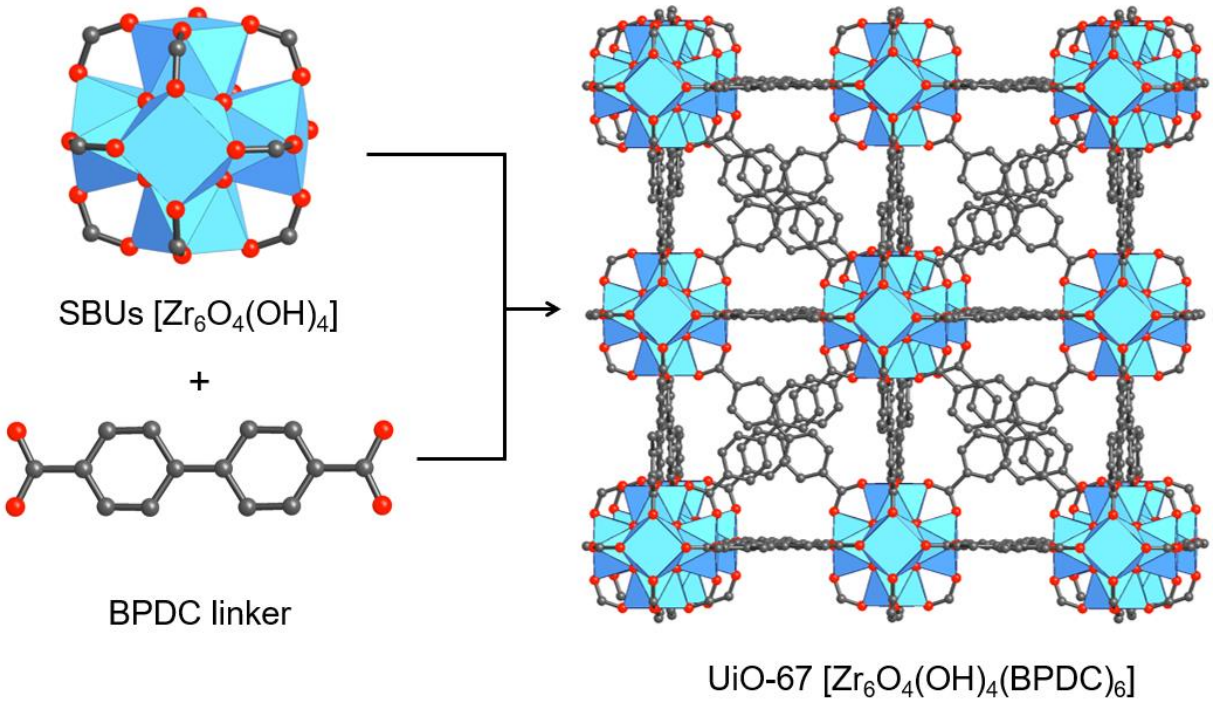


Figure 6.1. Structures and synthesis of UiO-67. Color code: Zr, blue; O, red; C, dark gray. Hydrogen atoms are omitted for clarity.

6.2 Results and Discussions

6.2.1 Synthesis of UiO-67 and organic linkers

UiO-67 was fabricated from the dimethyl formamide (DMF) solution of zirconium oxychloride octahydrate ($ZrOCl_2{\cdot}8H_2O$) and 4,4′-biphenyldicarboxylic acid (H_2BPDC) with the presence of benzoic acid. 3.4 g of BPDC and 51.2 g of benzoic acid were dissolved in 800 ml of DMF and the mixture was stirred at room temperature until the solution is clear. 4.52 g of $ZrOCl_2{\cdot}8H_2O$ was added to the solution and stirring to obtain a clear mixture. The mixture was heated at 120 °C for 2 days. White MOF solids were collected and washed by DMF three times per day for 3 days, and immersed in methanol for 3 days, during which time the methanol was replaced four times per day.

The solid was then dried at room temperature for 6 hours, 80 °C for 6 hours, and 120 °C for 12 hours to yield activated UiO-67.

For the evolution of UiO-67, six new linkers BPDC-NH_2, BPDC-COOH, BPDC-iVa, BPDC-OH, BPDC-Bz, and BPDC-Pyr were synthesized (Figure 6.2, Scheme 6.1).

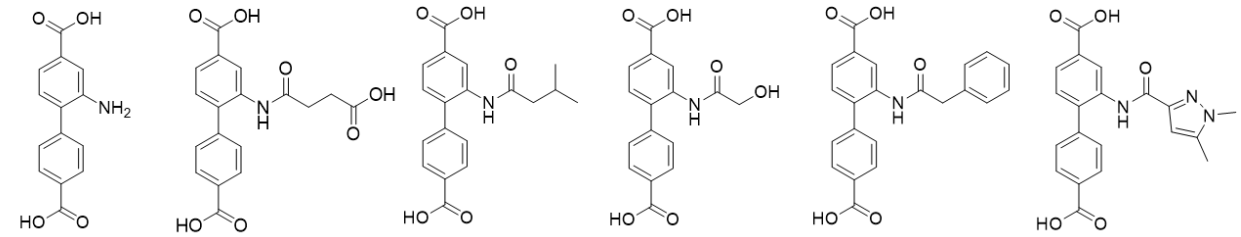


Figure 6.2. Structures of six organic linkers.

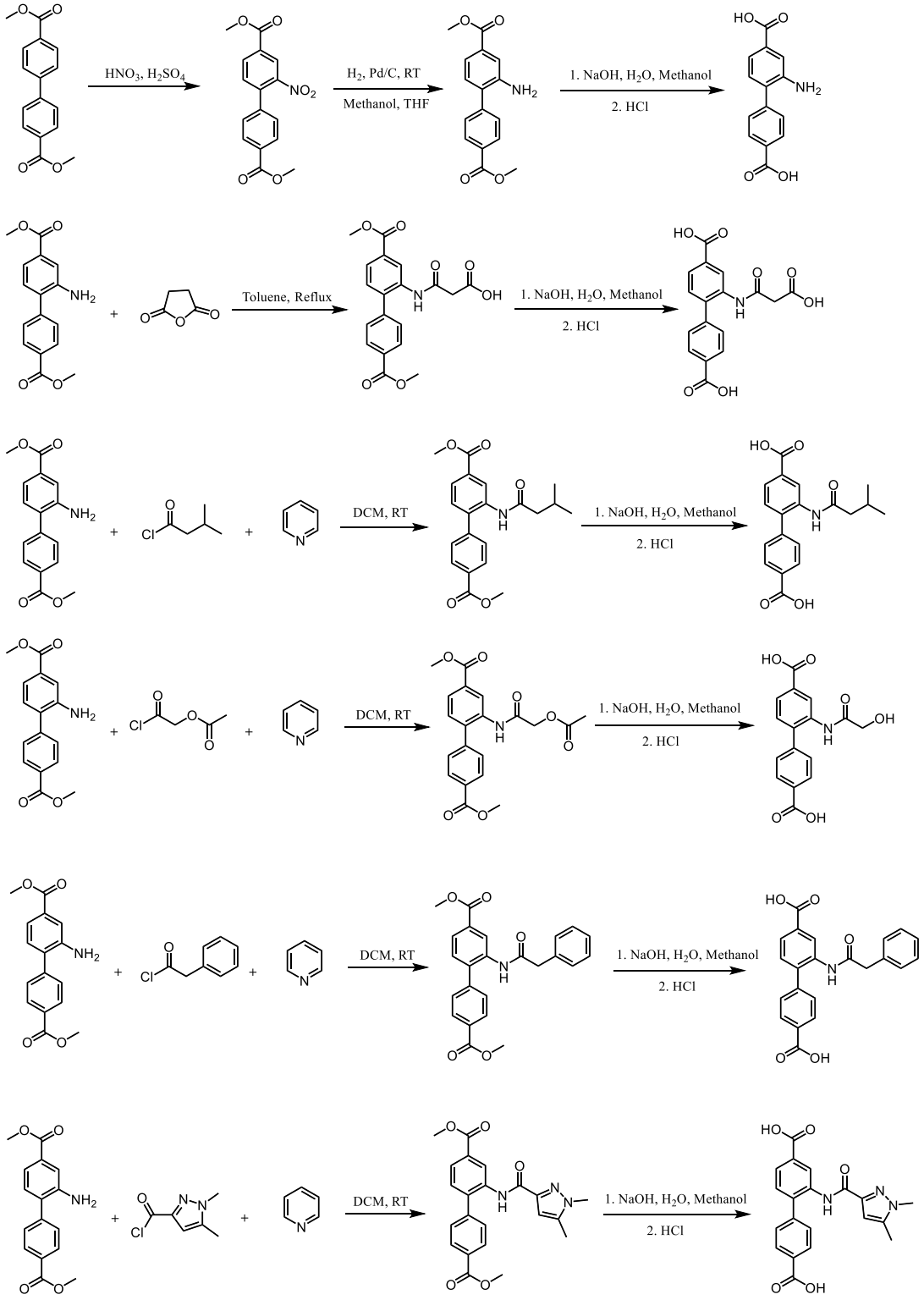
Synthesis of BPDC-NH_2: 10 g of dimethyl biphenyl-4,4′-dicarboxylate was dissolved in 100 ml of H_2SO_4 (98%) and the solution was cooled to 0 °C. 3.38 g of HNO_3 (69%) was mixed with 7.5 ml of H_2SO_4 and the mixture was added into dimethyl biphenyl-4,4′-dicarboxylate and H_2SO_4 solution drop-wisely over 30 minutes under stirring. The reaction was kept in 0-5 °C and stirred for 1 hour. 500 ml of H_2O was added to quench the reaction. The product was extracted by ethyl acetate, subsequently was washed by water and $NaHCO_3$ (7.5 W%) and dried by anhydrous Na_2SO_4. After evaporation of organic solvents and recrystallized by isopropanol, 11.8 g of dimethyl 2-nitro-[1,1'-biphenyl]-4,4'-dicarboxylate (dmBPDC-NO_2) was obtained. 5.29 g of dmBPDC-NO_2, 320 ml of methanol, and 640 ml of tetrahydrofuran (THF) were placed in a reaction flask and stirred. Then 1.57 g of palladium carbon (10 %) was added, and the air in the reaction flask was replaced with hydrogen to obtain a mixture. After stirring at room temperature for 22 hours, the palladium carbon was removed by filtration. The solvents were removed by evaporation to give 4.1 g of dimethyl 2-amino-[1,1'-biphenyl]-4,4'-dicarboxylate (dmBPDC-NH_2). dmBPDC-NH_2 was hydrolyzed with the presence of methanol and NaOH (1M, aqueous), neutralized by HCl (1M, aqueous) to yield organic ligand BPDC-NH_2. ^{1}H NMR (400 MHz, DMSO-d_6) δ 13.37–12.42 (m, 2H), 8.11–7.95 (m, 2H), 7.58 (dd, J = 8.5, 2.0 Hz, 2H), 7.41 (d, J = 1.9 Hz, 1H), 7.21 (dt, J = 7.9, 1.9 Hz, 1H), 7.12 (dd, J = 7.9, 1.8 Hz, 1H).

Synthesis of BPDC-COOH: 1.1 g of dmBPDC-NH_2 was mixed with succinic anhydride and dissolved in 200 ml of toluene. The reaction was refluxed under N_2 atmosphere for 12 hours. The product was filtrated, washed by H_2O, and dried. The obtained solid was hydrolyzed with the presence of methanol and NaOH (1M, aqueous), neutralized by HCl (1M, aqueous) to yield 1 g of organic ligand BPDC-COOH. ^{1}H NMR (400 MHz, DMSO-d_6) δ 9.52 (s, 1H), 8.14–7.94 (m, 3H), 7.84 (d, J = 8.1 Hz, 1H), 7.52 (dd, J = 24.1, 8.0 Hz, 3H).

Synthesis of BPDC-iVa: 400 mg of dmBPDC-NH_2 was dissolved in 40 ml of CH_2Cl_2 and stirring under the solution becomes clear. 186 mg of isovaleryl chloride was dissolved in 20 ml CH_2Cl_2 and added into dmBPDC-NH_2 solution drop-wisely. 120 mg of pyridine was added and the reaction was stirred at room temperature for 20 hours. The reactant was extracted with CH_2Cl_2, washed by HCl (1M, aqueous) and $NaHCO_3$ (5 wt %) subsequently. The obtained solution was dried by Na_2SO_4 and the solvents were removed by evaporation to yield precursor of BPDC-iVa. Then the precursor was hydrolyzed by the mixture of methanol and NaOH (1M, aqueous), neutralized by HCl (1M, aqueous) to give 390 mg of organic ligand BPDC-iVa. ^{1}H NMR (400

MHz, DMSO-d_6) δ 13.07 (s, 2H), 9.44 (s, 1H), 8.08–7.93 (m, 3H), 7.84 (dd, J = 8.0, 1.8 Hz, 1H), 7.54–7.43 (m, 3H), 2.05 (d, J = 7.1 Hz, 2H), 1.95 (dt, J = 13.4, 6.7 Hz, 1H), 0.83 (d, J = 6.4 Hz, 6H).

Scheme 6.1. Synthesis of six organic linkers



Synthesis of BPDC-OH: 400 mg of dmBPDC-NH_2 was dissolved in 40 ml of CH_2Cl_2 and stirring under the solution becomes clear. 210 mg of acetoxyacetyl chloride was dissolved in 20 ml CH_2Cl_2 and added into dmBPDC-NH_2 solution drop-wisely. 120 mg of pyridine was added and the reaction was stirred at room temperature for 20 hours. The reactant was extracted with CH_2Cl_2, washed by HCl (1M, aqueous) and $NaHCO_3$ (5 wt%) subsequently. The obtained solution was dried by Na_2SO_4 and the solvents were removed by evaporation to yield precursor of BPDC-OH. Then the precursor was hydrolyzed with the presence of methanol and NaOH (1M, aqueous), neutralized by HCl (1M, aqueous) to give 480 mg of organic ligand BPDC-OH. ^{1}H NMR (400 MHz, DMSO-d_6) δ 13.14 (s, 2H), 9.19 (s, 1H), 8.64 (d, J = 1.8 Hz, 1H), 8.05 (dd, J = 8.2, 1.7 Hz, 2H), 7.81 (dt, J = 8.0, 1.8 Hz, 1H), 7.63 – 7.54 (m, 2H), 7.46 (dd, J = 7.9, 1.6 Hz, 1H).

Synthesis of BPDC-Bz: 400 mg of dmBPDC-NH_2 was dissolved in 40 ml of CH_2Cl_2 and stirring under the solution becomes clear. 238 mg of Phenylacetyl chloride was dissolved in 20 ml CH_2Cl_2 and added into dmBPDC-NH_2 solution drop-wisely. 120 mg of pyridine was added and the reaction was stirred at room temperature for 20 hours. The reactant was extracted with CH_2Cl_2, washed by HCl (1M, aqueous) and $NaHCO_3$ (5 wt%) subsequently. The obtained solution was dried by Na_2SO_4 and the solvents were removed by evaporation to yield precursor of BPDC-Bz. Then the precursor was hydrolyzed with the presence of methanol and NaOH (1M, aqueous), neutralized by HCl (1M, aqueous) to give 550 mg of organic ligand BPDC-Bz. ^{1}H NMR (400 MHz, DMSO-d_6) δ 13.11 (d, J = 24.5 Hz, 2H), 9.63 (s, 1H), 8.07 (d, J = 7.9 Hz, 1H), 7.95–7.80 (m, 3H), 7.45 (dd, J = 19.5, 8.0 Hz, 3H), 7.33–7.12 (m, 5H), 3.53 (s, 2H).

Synthesis of BPDC-Pyr: 400 mg of dmBPDC-NH_2 was dissolved in 40 ml of CH_2Cl_2 and stirring under the solution becomes clear. 244 mg of 1,5-dimethyl-1H-pyrazole-3-carbonyl chloride was dissolved in 20 ml CH_2Cl_2 and added into dmBPDC-NH_2 solution drop-wisely. 120 mg of pyridine was added and the reaction was stirred at room temperature for 20 hours. The reactant was extracted with CH_2Cl_2, washed by HCl (1M, aqueous) and $NaHCO_3$ (5 wt%) subsequently. The obtained solution was dried by Na_2SO_4 and the solvents were removed by evaporation to yield precursor of BPDC-Pyr. Then the precursor was hydrolyzed with the presence of methanol and NaOH (1M, aqueous), neutralized by HCl (1M, aqueous) to give 540 mg of organic ligand BPDC-Pyr. ^{1}H NMR (600 MHz, DMSO-d_6) δ 13.45–12.71 (m, 2H), 9.41 (s, 1H), 8.48 (d, J = 1.7 Hz, 1H), 8.03 – 7.99 (m, 2H), 7.84 (dd, J = 7.9, 1.8 Hz, 1H), 7.62–7.54 (m, 2H), 7.49 (d, J = 7.9 Hz, 1H), 6.46 (d, J = 0.9 Hz, 1H), 3.70 (s, 3H), 2.25 (s, 3H).

6.2.2 Evolution of UiO-67

40 mg of activated UiO-67 solid was immersed in the mixture of H_2O, methanol, and THF with the volume ratio of 1.5: 2: 3. 38.5 mg of tryptophan was added as guest substrate. The mixture was placed on the shaker and kept shaking (160 rpm) for 1 day to disperse the guest substrate. 2.2 mg of BPDC-NH_2 linker, 2.9 mg of BPDC-COOH, 2.9 mg of BPDC-iVa, 2.7 mg of BPDC-OH, 3.2 mg of BPDC-Bz, and 3.2 mg of BPDC-Pyr were added into the mixture and kept shaking for 2 days. UiO-67 will evolute under the guidance of guest substrate and with newly introduced linkers to change the composition. On day 4, the mixture was centrifuged and the solvent was removed. Fresh solvent mixture (V_{H2O}: $V_{methanol}$: V_{THF}=1.5: 2: 3) and same quantity of organic linkers (2.2 mg of BPDC-NH_2 linker, 2.9 mg of BPDC-COOH, 2.9 mg of BPDC-iVa, 2.7 mg of BPDC-OH, 3.2 mg of BPDC-Bz, and 3.2 mg of BPDC-Pyr) were added. The obtained mixture was placed on the shaker and kept shaking for 2 days. On day 6, 8, and 10, the original solvents were removed by the centrifuge and fresh solvent mixture and organic linkers were added. The mixture was kept shaking until day 12. The MOFs solid obtained on day 12 was separated from the mixture and

washed by DMF three times per day for 3 days. Then the solid was washed by H_2O for 3 days, during which time the H_2O was replaced 3 times per day and finally exchanged with acetonitrile. After removing acetonitrile, the MOF solid was activated under vacuum at room temperature for 10 hours and at 120 °C for 2 hours to yield evoluted MOFs, living solid-1.

The control experiment was also conducted under the same condition however without the introduction of guest substrate. 40 mg of activated UiO-67 solid was immersed in the solvent mixture (V_{H2O}: $V_{methanol}$: V_{THF}=1.5: 2: 3) and placed on the shaker to shake for 1 day. On day 2, 2.2 mg of BPDC-NH_2 linker, 2.9 mg of BPDC-COOH, 2.9 mg of BPDC-iVa, 2.7 mg of BPDC-OH, 3.2 mg of BPDC-Bz, and 3.2 mg of BPDC-Pyr were added into the mixture and kept shaking for 2 days. On day 4, 6,8, and 10, the original solvents were removed after the centrifuge and fresh solvent mixture and same quantity of organic linkers were added to the system. The MOFs solid obtained on day 12 was separated from the mixture and washed by DMF three times per day for 3 days and then washed by H_2O three times per day for another 3 days and finally exchanged with acetonitrile. After removing acetonitrile, the MOF solid was activated under vacuum at room temperature for 10 hours and at 120 °C for 2 hours to yield evoluted MOFs, living solid-2.

6.2.3 Composition of MOFs after Evolution

The evoluted MOFs living solid-1 and living solid-2 were digested by the HF and dissolved in DMSO-d_6. Then ^{1}H NMR was performed on living solid-1 and living solid-2 to determine their compositions. After analyzing their digestion NMRs, we found that 47 % of original BPDC linkers of UiO-67 has been replaced by 6 newly introduced linkers in living soild-1. Specially, BPDC-NH_2, BPDC-COOH, BPDC-iVa, BPDC-OH, BPDC-Bz, and BPDC-Pyr made up for 14.1 %, 6.3 %, 9.7 %, 5.7 %, 8.7 %, and 2.5 % of all linkers, respectively. The chemical formula of living solid-1 was determined to be $[Zr_6O_4(OH)_4(BPDC)_{3.2}(BPDC\text{-}NH_2)_{0.8}(BPDC\text{-}COOH)_{0.4}(BPDC\text{-}iVa)_{0.6}(BPDC\text{-}OH)_{0.3}(BPDC\text{-}Bz)_{0.5}(BPDC\text{-}Pry)_{0.2}]$. In living solid-2, 52 % of original BPDC linkers has been replaced and BPDC-NH_2, BPDC-COOH, BPDC-iVa, BPDC-OH, BPDC-Bz, and BPDC-Pyr made up for 18.1 %, 7.1 %, 10.5 %, 5.5 %, 8.5 %, and 2.6 % of all linkers, respectively. The chemical formula of living solid-2 was determined to be $[Zr_6O_4(OH)_4(BPDC)_{2.9}(BPDC\text{-}NH_2)_{1.1}(BPDC\text{-}COOH)_{0.4}(BPDC\text{-}iVa)_{0.6}(BPDC\text{-}OH)_{0.3}(BPDC\text{-}Bz)_{0.5}(BPDC\text{-}Pry)_{0.2}]$.

6.2.4 Guest Selectivity in Living Solids

Living solid-1 was trained and experienced the evolution under the guidance of guest substrate. The pore environment was changed and optimized to bind guest templates accordingly. Thus, we performed the guest selectivity tests of living solids to study its binding affinity of the guest template. Activated living solid-1, living solid-2, and UiO-67 were added to H_2O/methanol/THF mixtures (V_{H2O}: $V_{methanol}$: V_{THF}=1.5: 2: 3). Equal mole of tryptophan (guest substrate) and phenylalanine was added to the mixtures. The systems were placed on the shaker and kept shaking (160 rpm) for 4 days to allow guests fully dispersed in the solution and pores of MOFs. Then MOFs materials were separated from the mixture and washed by H_2O for three times, during which time washing systems were placed on the shaker to remove guest molecules on the MOFs surface and loosely bounded. The resulting materials were digested with the presence of HF in DMSO-d_6 and ^{1}H NMRs were performed to determine the guest present in the MOFs. The results showed that the mole ratio among tryptophan, phenylalanine, and living solid-1 was 0.24: 0.048: 1.00. The corresponding values in living solid-2 and UiO-67 were determined to be 0.25: 0.075: 1.00 and 0.33: 0.16: 1.00, respectively. Thus, the selectivity between tryptophan and phenylalanine in living solid-1, living solid-2, and UiO-67 were 5.0, 3.3, and 2,0, respectively. Compared with living

soild-2 and UiO-67, the binding affinity between guest tryptophan and living solid-1 increased 52 % and 150 %, respectively.

6.3 Conclusion

In this chapter, we have demonstrated the tunability and "living" nature of MOFs. MOFs can respond to the external environments and the composition, pore chemistry, and even structure of MOFs evolute accordingly. We studied UiO-67 to illustrate this finding. The linkers composition of UiO-67 will change after the incorporation of 6 new linkers and guest substrates. With the guidance of guest substrate, the pore environment and structure of UiO-67 will evolute to optimize the binding affinity of the guest. Thus, the binding of guest tryptophan of living solid-1 is higher than those of evolved UiO-67 without the guest template and pure UiO-67. This expands the original understanding of MOFs as porous solid materials and give chemists opportunities to explore new chemistry and applications of MOFs and reticular chemistry.

6.4 References

1. Yaghi, O. M.; Kalmutzki, M. J.; Diercks, C. S. *Introduction to Reticular Chemistry: Metal-Organic Frameworks and Covalent Organic Frameworks*, Wiley-VCH, Weinheim, **2019**.
2. Furukawa, H.; Cordova, K. E.; O'Keeffe, M.; Yaghi, O. M. *Science* **2013**, *341*, 1230444.
3. Eddaoudi, M.; Kim, J.; Rosi, N.; Vodak, D.; Wachter, J.; O'Keeffe, M.; Yaghi, O. M. *Science* **2002**, *295*, 469–472.
4. Deng, H.; Grunder, S.; Cordova, K. E.; Valente, C.; Furukawa, H.; Hmadeh, M.; Gándara, F.; Whalley, A. C.; Liu, Z.; Asahina, S.; Kazumori, H.; O'Keeffe, M.; Terasaki, O.; Stoddart, J. F.; Yaghi, O. M. *Science* **2012**, *336*, 1018–1023.
5. Yaghi, O. M.; O'Keeffe, M.; Ockwig, N. W.; Chae, H. K.; Eddaoudi, M.; Kim, J. *Nature*, **2003**, *423*, 705–714.
6. Li, H.; Eddaoudi, M.; O'Keeffe, M.; Yaghi, O. M. *Nature* **1999**, *402*, 276–279.
7. Eddaoudi, M.; Moler, D.; Li, H.; Reineke, T. M.; O'Keeffe, M.; Yaghi, O. M. *Acc. Chem. Res.* **2001**, *34*, 319–330.
8. Wang, H.; Shi, Z.; Yang, J.; Sun, T.; Rungtaweevoranit, B.; Lyu, H.; Zhang, Y.-B.; Yaghi, O. M. *Angew. Chem. Int. Ed.*, **2021**, *60*, 3417–3421.
9. Ji, Z.; Wang, H.; Canossa, S.; Wuttke, S.; Yaghi, O. M. Pore Chemistry of Metal-Organic Frameworks. *Adv. Funct. Mater.*, **2020**, *30*, 202000238.
10. Wang, H.; Pei, X.; Proserpio D. M.; Yaghi, O. M. Design of MOFs with Absolute Structures: A Case Study. *Isr. J. Chem.*, **2021**, *61*, 774–781.
11. Wang, H.; Pei, X.; Kalmutzki, M. J.; Yang, J.; Yaghi, O. M. *Acc. Chem. Res.*, **2022**, *55*, 707–721.